

**A TECHNICAL METHODOLOGY FOR ESTABLISHING STRUCTURAL
LIMITATIONS OF SHIPS IN PACK ICE**

By

© John Robert Dolny

A thesis submitted to the

School of Graduate Studies in partial fulfillment of the requirements for the degree of

Master of Engineering

Faculty of Engineering and Applied Science

Memorial University of Newfoundland

May 2017

St. John's, Newfoundland and Labrador

Abstract

This thesis presents a technical methodology for determining operational limitations for ships in pack ice from a structural risk perspective. The methodology relies on mechanics of ship-ice interaction and direct analysis of structural response. The limitations are presented in the form of so-called “safe speed” curves derived by a set of calculations under specific technical assumptions. These operational envelopes are useful in understanding a ship’s structural capability in a variety of ice types beyond the notional description of an ice class notation or lack thereof. The work focuses on hull forms and structural arrangements which are not necessarily intended for dedicated or aggressive ice operations and explores consequences of different operational demands. Non-ice strengthened and light ice class structures that may operate in light to medium pack ice present new technical challenges that require modifications to the conventional mechanics that form the basis of existing models and approaches. This thesis proposes several modifications and offers two case studies to demonstrate the methodology and highlight the influence of key parameters.

Acknowledgements

This thesis could not have been successfully completed without the continued support and encouragement from several people and numerous organizations. First and foremost, I take this opportunity to express my never-ending gratitude to my wife, Liz, for her patience, support and understanding throughout this process. It has been a long journey and I dedicate this thesis to her and our growing family. I would also like to thank my parents for their encouragement and support throughout my life to pursue my goals and interests.

I would like to thank Dr. Claude Daley, my graduate advisor, for his direction and guidance. It has been a pleasure to work together on this topic and others for several years. I am inspired by his enthusiasm and refreshing approach to research.

My graduate studies were carried out part-time as a full-time employee of American Bureau of Shipping (ABS). I would like to thank Drs. Han Yu and Roger Basu and Mr. James Bond for allowing me to pursue a part-time graduate degree while continuing to work for ABS. It has been an incredibly rewarding experience and I greatly appreciate this opportunity.

This research also builds upon parallel work I've supported and managed at ABS with many collaborative partners and sponsors including United States Coast Guard (USCG), Office of Naval Research (ONR), Naval Surface Warfare Center – Carderock Division (NSWCCD), Ship Structures Committee (SSC), Defense Research and Development Canada (DRDC), VARD Marine Inc., and Transport Canada (TC). I would like to specifically acknowledge the support from Mr. Tim McAllister (USCG), Dr. Paul

Hess (ONR), Mr. Andrew Kendrick (VARD), Dr. Neil Pegg (DRDC), and Mr. Brad Spence (TC). Their support, feedback, and technical contributions are gratefully appreciated. I believe their continued financial and intellectual commitments to research in this field are advancing the state-of-the-art in Arctic vessel operational safety.

Lastly I would like to thank my friends and colleagues at Memorial University and ABS. You have made my time in St. John's an enjoyable and inspiring place to work and study.

Table of Contents

Abstract.....	2
Acknowledgements.....	3
Table of Contents.....	5
List of Tables.....	8
List of Figures	9
1. Introduction.....	14
2. Summary of Safe Speed Issues	22
2.1. Ice types	22
2.2. Concentration.....	24
2.3. Floe size	27
2.4. Ice Strength.....	27
2.4.1. Ice Crushing Strength	28
2.4.2. Ice Flexural Strength.....	29
2.4.3. Pressure-Area Models.....	30
2.5. Ice Class	31
2.5.1. Finnish-Swedish Ice Class Rules.....	32
2.5.2. IACS Polar Class Rules	32
2.5.3. Implied Capabilities of Ice Classes	34
2.6. Hull Form.....	35
2.7. Operations	37
3. Existing Approaches for Operational Limitations in Ice.....	38
3.1. Canadian Arctic Ice Regime Shipping System (AIRSS).....	38
3.2. IMO Polar Code – POLARIS	39
3.3. Safe Speed in Ice.....	46
3.3.1. Russian Ice Passport / Ice Certificate.....	46
3.3.2. Probabilistic Approaches	50
3.3.3. Recent Approaches	52
4. Technical Methodology for Defining Safe Speeds in Ice	63
4.1. DDePS.....	64
4.2. Case 2a Interaction Scenario.....	65
4.3. Impact Model and Collision Mechanics	66
4.4. Ice Crushing Forces Considering Rigid Structures	69
4.4.1. Modification for Steep Frame Angles.....	72
4.5. Ice Flexural Limit Model.....	77
4.5.1. Updated Flexural Failure Limit Model by Daley & Kendrick.....	78

4.5.2.	Updated Dynamic Effects based on work by Sazidy	82
4.6.	Structural Limit States and Speed Check Algorithm.....	84
4.6.1.	Polar Class Design Limit Load Criteria	84
4.6.2.	Direct Line Load Criteria	86
4.6.3.	Large Deflection Criteria	92
5.	Full Scale Data Comparison to the Ice Load Model	94
5.1.	USCG <i>POLAR SEA</i> Data.....	95
5.1.1.	USCG <i>POLAR SEA</i> Multi-year Floe Impacts.....	97
5.1.2.	USCG <i>POLAR SEA</i> Bering Sea Pack Ice Trials	105
5.2.	Varandey Arctic Shuttle Tanker Ice Load Monitoring Program	110
6.	Ice Crushing Forces Considering Deformable Structures	116
6.1.	Numerical Simulations	119
6.2.	Calibration of the Numerical Ice Model	122
7.	Case Study – Ice Class PC5 Patrol Vessel	133
7.1.	Hull Form	133
7.2.	Hull Structural Design.....	135
7.3.	Finite Element Model.....	136
7.4.	Structural Response to Various Patch Loads	138
7.5.	Safe Speed Assessment Considering Rigid Structure.....	142
7.5.1.	Example Outputs of the Mathematical Model	143
7.5.2.	Safe Speed Results.....	150
7.6.	Structural Response to Deformable Ice Model	153
8.	Case Study – Non-ice Strengthened Naval Combatant.....	157
8.1.	Hull Form	157
8.2.	Hull Structural Design.....	159
8.3.	Finite Element Model.....	161
8.4.	Structural Response to Various Patch Loads	162
8.5.	Safe Speed Assessment Considering Rigid Structure.....	166
8.5.1.	Example Outputs of the Mathematical Model	167
8.5.2.	Safe Speed Results.....	173
8.6.	Response of Compliant Structure to Deformable Ice Model	175
8.6.1.	Safe Speed Assessment Considering Deformable Structure.....	182
9.	Conclusions and Recommendations for Future Work	185
10.	References	190
Appendix A - Description of Popov Terms.....		195
A.1	Popov Terms for Ship	195
A.2	Popov Terms for Ice.....	199

Appendix B – Polar Sea Full Scale Data Cases	202
B.1 Beaufort Sea – Case 1	202
B.2 Beaufort Sea – Case 2	203
B.3 Beaufort Sea – Case 3	204
B.4 Chukchi Sea – Case 1.....	205
B.5 Chukchi Sea – Case 2.....	206
B.6 Chukchi Sea – Case 3.....	207
B.7 Bering Sea – Case 1	208
B.8 Bering Sea – Case 2	209
B.9 Bering Sea – Case 3	210
Appendix C Varandey Tanker Full Scale Data Cases.....	211
C.1 Varandey – Case 1	211
C.2 Varandey – Case 2	212
C.3 Varandey – Case 3	213
Appendix D – LS-Dyna K-files.....	214
D.1 Ice Calibration Simulations	215
D.2 Patch Load Analysis Simulation	218
D.3 Ice-structure Interaction Analysis Simulations	221

List of Tables

Table 2-1: Ice types according to WMO nomenclature.....	23
Table 2-2: Ice floe sizes	27
Table 2-3: Finnish-Swedish Ice Class Rules with nominal descriptions	32
Table 2-4: IACS Polar Class Rules with nominal descriptions	33
Table 3-1: POLARIS risk index outcome (RIO) criteria.....	42
Table 3-2: POLARIS recommended speed limits for 'elevated operational risk'.....	42
Table 5-1: USCG <i>POLAR SEA</i> ice impact trials.....	97
Table 5-2: Selected ice impact events	98
Table 5-3: Selected <i>POLAR SEA</i> impact events in the Bering Sea	106
Table 5-4: Selected Varandey Tanker impact events	112
Table 6-1: Factors and responses for ice calibration exercise.....	124
Table 6-2: Numerical ice calibration experiments and results – initial runs.....	130
Table 6-3: Numerical ice calibration experiments and results – verification runs	131
Table 7-1: Main particulars and hull data for Ice Class PC5 patrol vessel	134
Table 7-2: Scantlings of typical frame of Ice Class PC5 patrol vessel	136
Table 7-3: Assumed material properties and bilinear plastic-kinematic model parameters.....	138
Table 7-4: Patch load cases	139
Table 7-5: Initial safe speed assessment parameters	150
Table 7-6: Numerical simulations between Ice Class PC5 patrol vessel and deformable ice model	153
Table 8-1: Main particulars and hull data for naval combatant	158
Table 8-2: Scantlings of typical longitudinal and web frame for naval combatant	160
Table 8-3: Material properties and bilinear plastic-kinematic model parameters	162
Table 8-4: Patch load cases	163
Table 8-5: Safe speed assessment parameters	173
Table 8-6: Numerical simulations between naval combatant ship and deformable ice model.....	176

List of Figures

Figure 1-1: Arctic sea ice extent as of 4 December 2016 along with data from previous years [source: NSIDC (2016)]	14
Figure 1-2: CRYSTAL SERENITY in Cambridge Bay, NU [source: Chris Corday/CBC]	15
Figure 1-3: Infographic highlighting key safety regulations of the IMO Polar Code [source: IMO].....	17
Figure 1-4: USCGC STRATTON (WMSL-752) operating in the Arctic Ocean during Operation Arctic Shield, September 12, 2014 [source: USCG]	19
Figure 2-1: Ice concentrations [source: Canadian Coast Guard]	25
Figure 2-2: Example ice chart and egg code [source: Canadian Ice Service]	26
Figure 2-3: Example ice observation and egg code [IACS, Canada, & Finland, 2014]	26
Figure 2-4: Typical ice compressive strength testing methods - uniaxial crushing (left) and in-situ borehole tests (right) [from Timco & Weeks, 2010]	28
Figure 2-5: Ice compressive strength vs. temperature and strain rate [Timco & Weeks, 2010]	29
Figure 2-6: Typical ice crushing parameters	31
Figure 2-7: IACS Polar Rules design scenario - glancing impact with thick level ice edge.....	34
Figure 2-8: Level ice thickness limitations for various ice classes [IACS et al., 2014]	35
Figure 2-9: Sketches of different bow forms.....	35
Figure 2-10: Definitions of hull angles [ABS, 2016b].....	36
Figure 3-1: POLARIS risk values (RVs).....	41
Figure 3-2: Alaska regional ice charts [data source: US NIC].....	43
Figure 3-3: Chukchi Sea Ice Chart (29 October 2012) [source: US NIC].....	44
Figure 3-4: Monthly minimum POLARIS RIOs for non-ice classed ships, Alaska region [ABS, 2015].....	45
Figure 3-5: Sketch of safe speed diagram [from Maxutov and Popov (1981)].....	47
Figure 3-6: Kurdyumov-Khesin [1976] ice pressure model (left) and pressure-area model (right).....	49
Figure 3-7: Examples safe speed guidance from a Russian ice passport [source: CNIIMF]	50
Figure 3-8: Probabilistic concept for safe speed in ice [from Tunik et al. (1990)].....	51
Figure 3-9: Reflected collision scenarios (left) and computed safe speed limits for PC7 ships (right) [from Daley & Liu (2010)]	52
Figure 3-10: safe speed envelopes considering locally compliant structure [from Daley & Kim (2010)] ...	53
Figure 3-11: LS-Dyna model of shoulder collision with an ice edge on elastic foundation [Sazidy (2014)]	54
Figure 3-12: Cross-check of velocity dependant ice flexural failure model with full scale test data [from (Sazidy, 2014)]	55
Figure 3-13: Safe speed assessment concept by Kolari & Kurkela (2012).....	56
Figure 3-14: Example safe speed results demonstrating the sensitivities to ice strength and ice class [from VARD (2015)].....	57
Figure 3-15: Numerical simulation considering deformable structure and ice [from (ABS, 2015)]	58

Figure 3-16: Technical safe speeds for the USCG WMSL Class cutter impacting ‘cake’ ice floes.....	60
Figure 3-17: DRDC Notional Destroyer	60
Figure 3-18: Numerical simulations of ice-structure interaction [from Daley (2015)].....	61
Figure 3-19: Numerical simulations of ice-structure interaction [from Daley (2015)].....	61
Figure 3-20: Limit speeds corresponding to 10cm permanent deformations [Daley (2015)]	62
Figure 4-1: Building blocks of a safe speed technical methodology.....	63
Figure 4-2: Typical inputs and outputs for the mathematical model.....	64
Figure 4-3: DDePS collision scenarios	65
Figure 4-4: Ship-ice collision scenario.....	66
Figure 4-5: Diagram of ship-ice impact scenario for the mathematical model.....	68
Figure 4-6: General wedge edge interaction geometry	70
Figure 4-7: Translation and reduction of true contact surface to rectangular patch load.....	72
Figure 4-8: Interaction geometry for trapezoidal contact areas	73
Figure 4-9: Contact area vs. indentation considering corrected trapezoidal contact shape.....	76
Figure 4-10: Translation and reduction of trapezoidal contact surface to rectangular patch load.....	76
Figure 4-11: Geometry of flexural failure and ice cusp	78
Figure 4-12: Hull-ice Contact showing Normal and Frictional Forces	79
Figure 4-13: Simple ice wedge breaking pattern [Sazidy et al. (2014)]	82
Figure 4-14: Comparison of static and dynamic flexural failure limits.....	83
Figure 4-15: Description of PC design load criteria.....	86
Figure 4-16: Description of direct limit load criteria	87
Figure 4-17: Structural limit states for frames subjected to lateral patch loads	88
Figure 4-18: Sketch of ice load applied to transverse framing	89
Figure 4-19: Description of large deflection criteria.....	93
Figure 5-1: Sketch of ice load panel on <i>POLAR SEA</i> (left); Extract from SSC 340 Indicating Hull Angles (right).....	96
Figure 5-2: Sketch of USCG <i>POLAR SEA</i> and instrumented location.....	96
Figure 5-3: Summary of measured force events vs ship speed for <i>USCG POLAR SEA</i> Chukchi and Beaufort Sea trials.....	98
Figure 5-4: Force-time history and process P-A curve for selected <i>POLAR SEA</i> event (chuk3).....	99
Figure 5-5: Pressure distributions (in MPa) at 6 instances for selected Polar Sea event (chuk3)	100
Figure 5-6: Process pressure-area data for selected Polar Sea events from Beaufort and Chukchi Seas....	101
Figure 5-7: Assumed <i>POLAR SEA</i> MY ice impact scenarios	102
Figure 5-8: <i>DDePS</i> (wedge shape) calculation results – force vs. speed, <i>POLAR SEA</i> data superimposed	103
Figure 5-9: <i>DDePS</i> calculations results for wedge ice edge under various assumptions.....	104
Figure 5-10: <i>DDePS</i> calculations results for rounded ice edge under various assumptions	104

Figure 5-11: USCG <i>POLAR SEA</i> in the Bering Sea [photo credit: USCG].....	105
Figure 5-12: <i>POLAR SEA</i> Bering Sea Impact Data	106
Figure 5-13: Force-time history and process P-A curve for selected Polar Sea event (ber1)	107
Figure 5-14: Pressure distributions (in MPa) at 6 instances for selected Polar Sea event (ber1)	107
Figure 5-15: Process pressure-area data for selected <i>POLAR SEA</i> events from Bering Sea.....	108
Figure 5-16: <i>DDePS</i> calculations results for pack ice impacts (35m ice floes)	109
Figure 5-17: <i>DDePS</i> calculations results for pack ice impacts (20m ice floes)	109
Figure 5-18: <i>DDePS</i> calculations results for pack ice impacts (10m ice floes)	109
Figure 5-19: Main voyage route of the Varandey Tanker	110
Figure 5-20: Sketch of Varandey Tanker indicating location of bow instrumented panel	111
Figure 5-21: Varandey Tanker 2009 Impact Data	111
Figure 5-22: Force-time history and process P-A curve for selected Varandey Tanker event (var1)	113
Figure 5-23: Pressure distributions (in MPa) at 6 instances for selected Varandey Tanker event (var2) ...	113
Figure 5-24: Process pressure-area data for selected Varandey Tanker events	114
Figure 5-25: <i>DDePS</i> calculations results compared with Varandey Tanker data (2009 events).....	115
Figure 6-1: Concept sketch for compliant ship-ice collision model (from Daley & Kim, 2010).....	117
Figure 6-2: Sketch of interaction model for rigid (top) and deformable (bottom) structures.....	118
Figure 6-3: LS-Dyna analysis results for rigid and deformable structures crushing an ice edge	121
Figure 6-4: Measured pressures in STePS ² lab tests (Bruneau et al., 2013a)	123
Figure 6-5: Sketch of DOE problem for ice calibration	124
Figure 6-6: Stress-strain curve for elasto-plastic numerical ice material.....	125
Figure 6-7: Diagram of patch size reduction an effective P-A relationship.....	126
Figure 6-8: Numerical simulation setup for ice calibration simulation A_104.....	127
Figure 6-9: Interface pressures - ice calibration experiment A_101	128
Figure 6-10: Time histories of force and contact area - ice calibration experiment A_101	128
Figure 6-11: Process-pressure area curves - ice calibration experiment A_101	128
Figure 6-12: Interface pressures - ice calibration experiment A_104	129
Figure 6-13: Time histories of force and contact area - ice calibration experiment A_104.....	129
Figure 6-14: Process-pressure area curves - ice calibration experiment A_104	129
Figure 6-15: Regression predictions versus numerical simulation results for Po and ex	132
Figure 7-1: Lines plans showing bow hull angles for an Ice Class PC5 patrol vessel.....	134
Figure 7-2: Representative structural arrangement for bow region of Ice Class PC5 patrol vessel	135
Figure 7-3: Finite element model of representative bow structure – Ice Class PC5 patrol vessel.....	137
Figure 7-4: Load cases centered on transverse frame (left); Load cases centered on plating (right).....	139
Figure 7-5: Load cases centered on bulkhead.....	139

Figure 7-6: FEA results of structure response to various patch loads	140
Figure 7-7: FEA results of structure response to various patch loads	140
Figure 7-8: von-Mises stress distribution plots for cases P_004 (left) and P_008 (right) at the frame limit load	141
Figure 7-9: von-Mises stress distribution at point of web frame collapse – load case P_009.....	142
Figure 7-10: Sample DDePS calculation scenarios.....	144
Figure 7-11: Load vs. speed results varying floe size and ice thickness (expressed in line load)	145
Figure 7-12: Case 1 – mathematical model outputs.....	146
Figure 7-13: Case 2 - mathematical model outputs.....	147
Figure 7-14: Case 3 - mathematical model outputs.....	148
Figure 7-15: Case 4 - mathematical model outputs.....	149
Figure 7-16: Technical safe speeds vs ice thickness for different floe sizes.....	151
Figure 7-17: Summary plot of safe speed curves.....	152
Figure 7-18: Summary plot of safe speed curves (stronger ice - $P_o = 6$ MPa, $\sigma_f = 1.0$ MPa).....	152
Figure 7-19: Numerical simulation – 1.05m ice edge centered on transverse frame (P_103)	154
Figure 7-20: Pressure-area results – 1.05m ice edge centered on transverse frame (P_103)	154
Figure 7-21: Force vs deformation results – 1.05m ice edge centered on transverse frame (P_103)	155
Figure 7-22: Force vs deformation comparison with patch load analysis	156
Figure 7-23: Force vs total normal deformation for additional load cases	156
Figure 8-1: Naval combatant lines plans showing bow hull angles	158
Figure 8-2: Naval combatant representative bow structural design – typical sections	159
Figure 8-3: Naval combatant representative bow structural design – shell expansion and typical side shell longitudinal arrangement	160
Figure 8-4: Finite element model of the representative bow structure for the naval combatant	161
Figure 8-5: Central load cases on longitudinal (left); End load cases on longitudinal and load cases on plating (right).....	164
Figure 8-6: Load cases on web frame (left); Load cases on bulkhead (right).....	164
Figure 8-7: FEA results of structure response to various patch loads	165
Figure 8-8: FEA results of structure response to various patch loads	165
Figure 8-9: von-Mises stress distribution plots for cases N_001 (left) and N_008 (right) at the frame limit load.....	166
Figure 8-10: von-Mises stress distribution plots for cases N_012 (left) and N_016 (right) at web frame and bulkhead collapse points	166
Figure 8-11: Impact scenarios for naval combatant safe speed assessment.....	169
Figure 8-12: Force vs. speed results varying floe size and ice thickness.....	169
Figure 8-13: Case 1 - mathematical model outputs.....	170
Figure 8-14: Case 2 - mathematical model outputs.....	171

Figure 8-15: Case 3 - mathematical model outputs.....	172
Figure 8-16: Technical safe speeds vs ice thickness for different floe sizes.....	174
Figure 8-17: Summary plot of safe speed curves.....	174
Figure 8-18: Influence of ice crushing strength to technical safe speed.....	175
Figure 8-19: Numerical simulation – 35cm ice edge centered on longitudinal frame (N_101).....	177
Figure 8-20: Force vs deformation results – 35cm ice edge centered on longitudinal frame (N_101).....	177
Figure 8-21: Numerical simulation – 70cm ice edge centered on web frame (N_108).....	178
Figure 8-22: Force vs deformation results – 70cm ice edge centered on web frame (N_108).....	178
Figure 8-23: Numerical simulation results – force vs. total displacement (top), force vs. structural deformation (bottom)	179
Figure 8-24: Force vs. total normal displacement for longitudinal frame load cases.....	180
Figure 8-25: Force vs. structural deformation for longitudinal frame load cases	181
Figure 8-26: Parameters obtained from numerical simulations	181
Figure 8-27: Technical limit speeds considering different damage tolerances	183
Figure 8-28: Summary plot of 5cm deflection limit speed curves vs. ice thickness and floe size	183

1. Introduction

The Arctic has been a subject of considerable attention in recent years. Evidence of a long-term downward trend of ice cover is clear and its effect on the region is significant. In particular, the minimum extent of summer Arctic sea ice is declining year upon year, as much as 5-10% per decade by some measures (Fetterer et al., 2016). Thicknesses and concentrations of multi-year ice are also reducing. Figure 1-1 presents the Arctic sea ice extent as it recedes in the summer months and recovers in the early winter. The last five years (2012-2016) are compared with the average and two standard deviation band from a 20-year period (1981 – 2010). Three of the last five summers (2012, 2015, and 2016) have seen minimum ice extents outside the two standard deviation range.

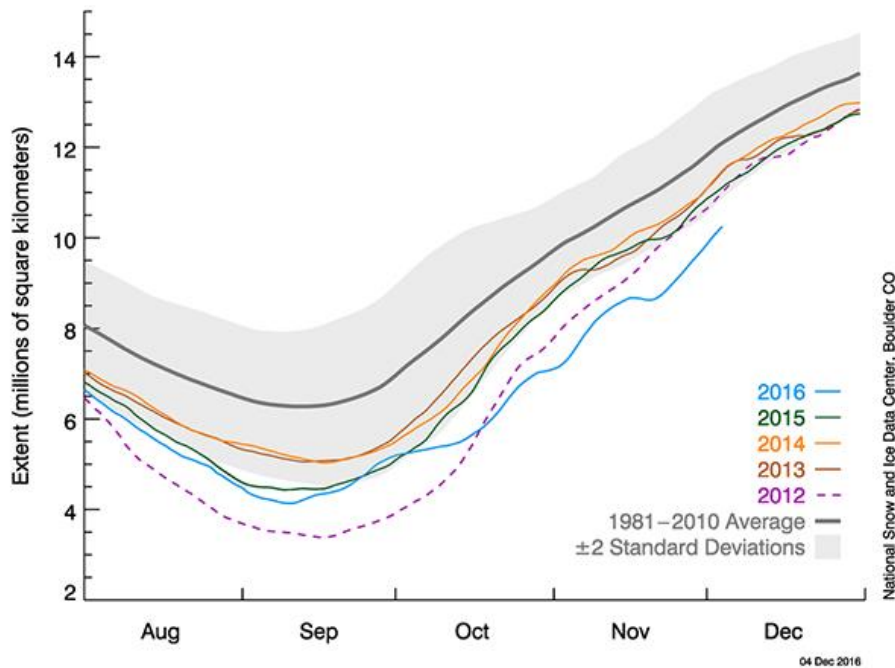


Figure 1-1: Arctic sea ice extent as of 4 December 2016 along with data from previous years [source: NSIDC (2016)]

The reduction of sea ice cover, combined with large estimates of natural resources, shorter transit routes, and new tourism opportunities, has led to a general speculation that

maritime traffic will dramatically increase in the region. While a surge in activity has yet to come to fruition, several notable events in recent years are signaling a potential for future growth.

Perhaps the most recent example is the summer 2016 transit of the large non-ice strengthened passenger ship, *CRYSTAL SERENITY* pictured in Figure 1-2, through the Canadian Northwest Passage (Brown, 2016). The success of this voyage will certainly attract more cruise line and adventure tourism companies to this frontier area. Commercial ship owners and operators are also attracted to the promise of shorter sea routes across the north and potential fuel savings as global shipping markets become increasingly competitive. The Northern Sea Route (NSR), which stretches across the Russian Arctic linking Asian and Northern European markets, typically becomes ice free in the summer months. Maritime traffic has started to develop at a modest pace along the NSR since the late 1990s, with nearly 5.4 million tons of cargo transported in 2015 (Belkin, 2016).



Figure 1-2: CRYSTAL SERENITY in Cambridge Bay, NU [source: Chris Corday/CBC]

It is well reported that the Arctic is rich with natural resources. In 2008, the United States Geological Survey (USGS) reported on enormous estimates of undiscovered oil and natural gas resources north of the Arctic Circle (Bird et al., 2008). In 2015, Shell carried

out a massive exploration campaign in the Alaskan Chukchi Sea which alone brought dozens of ships to the region. While the project was shelved due to low oil prices, the estimates for crude oil reserves are significant, and leases will undoubtedly be reconsidered if market and political conditions improve (Dlouhy, 2015). In the Russian Arctic, a new major gas field is under development on the Yamal peninsula, east of the Kara Sea. The project requires year-round infrastructure development which has brought cargo ships, heavy lift ships, and other various support fleets to the area. In addition a new fleet of high-ice class Arctic LNG carriers are currently under construction (Rowlands, 2016).

Arctic mining developments present another opportunity for wealth-generation driven by a global demand for raw materials and minerals. *Baffinland-Mary River* (Nunavut, Canada) is a high-grade iron ore project currently in advanced planning and development phases. The first shipment of ore from the mine was exported to Germany in 2015 (Eason, 2015). As the project comes online, bulk iron ore exports are expected to reach several millions of tons per year. On the northwest coast of Alaska, the Red Dog mine is one of the world's largest zinc mine. Product is stockpiled throughout the winter months and export shipments are made during summer seasons on the spot charter bulk market when the ports are ice-free.

An expansion of maritime activity in Arctic waters will inevitably increase the probability of an incident occurring in the region. Incidents can occur due to a variety of hazards associated with Arctic operations that are not present in other areas of the world. Some of the most critical hazards include structural damage from ice collisions, stability casualties due to ice accretion, equipment and machinery functionality in low air

temperatures, and grounding due to a general lack of accurate charting. The need for modern and effective regulation to mitigate these risks has been recognized at the international level. In 2015, the International Maritime Organization (IMO) formally adopted the Code for Ships Operating in Polar Waters (IMO Polar Code). The Polar Code, which entered into force in January 2017, introduces a broad spectrum of new binding regulations covering elements of ship design, construction, onboard equipment and machinery, operational procedures, training standards, and pollution prevention. Figure 1-3 highlights the key safety regulations of the code. One point of emphasis is on requirements for ships operating in Polar Waters to maintain documented information about their operational limitations in ice conditions.

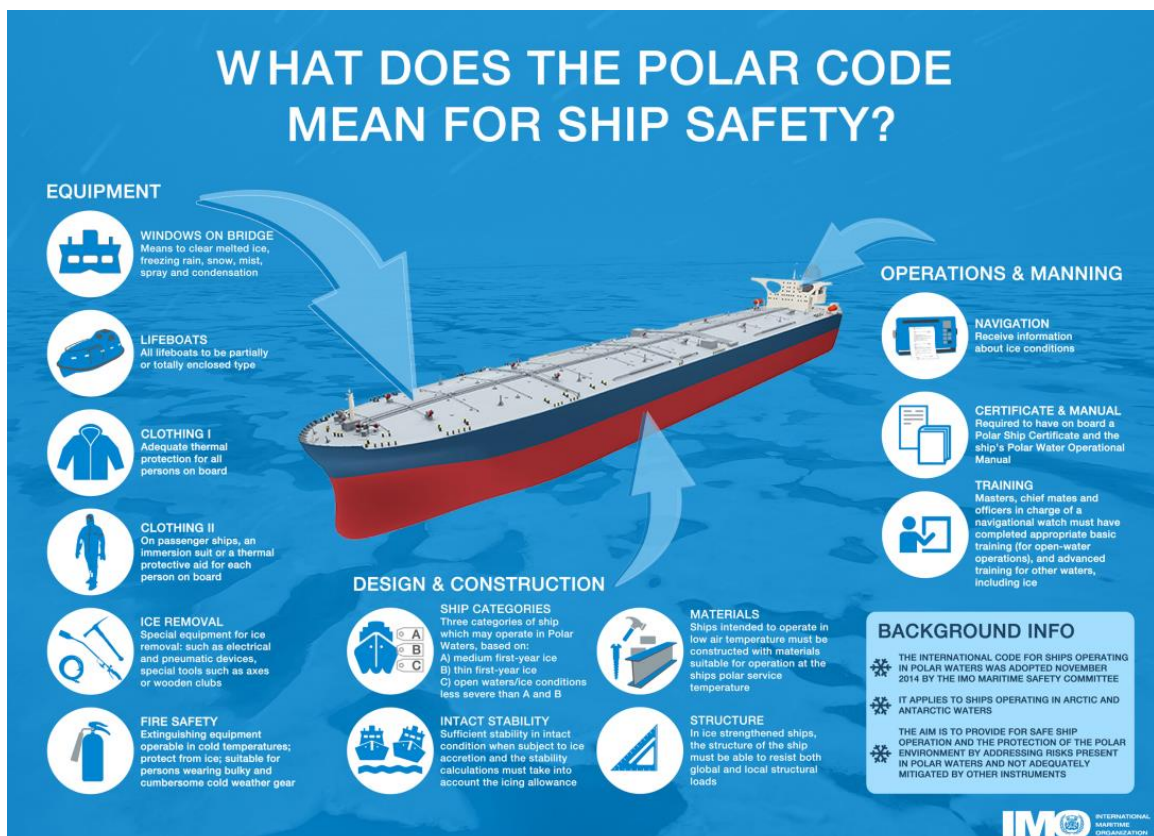


Figure 1-3: Infographic highlighting key safety regulations of the IMO Polar Code [source: IMO]

If a significant incident occurs, governments may be required to respond and provide assistance. In North America, it is widely recognized that the availability of heavy icebreakers is limited and the existing fleet is ageing quickly. In response, both American and Canadian governments have recently announced plans to modernize their icebreaker and Arctic fleets. In Canada, construction has recently started on a fleet of Arctic Offshore Patrol Ships (AOPS). Both American and Canadian Coast Guards have announced plans for replacement Polar icebreakers, however the acquisition programs are expected to take many years to complete; the most optimistic estimates suggest the early 2020s before first delivery (Berthiaume, 2016).

In the meantime there is a need to maintain an active presence in these regions with capabilities to support prevention, emergency response, search and rescue, and to address national sovereignty issues (US Navy Task Force Climate Change, 2014). This may result in the deployment of non-ice strengthened combatants (e.g. destroyer, frigate, and command and control ship) or lightly ice strengthened support and patrol ships. In fact in recent years, the USCG has conducted long-range summer patrols of Alaskan Arctic waters with the non-ice strengthened WMSL Class National Security Cutters (Figure 1-4). Despite the declining minimum extent of summer Arctic sea ice, there is still ice present throughout the year and these deployments may be in areas infested with ice.

Operators of these ships that may be deployed to the Arctic need a sound methodology to understand the limitations of their assets and evaluate operational risk for various ice conditions. The risk of structural damage to a ship operating in ice depends on many factors which include the ice conditions (thickness, strength, floe size and

concentration), the ship's structural particulars (shape of the hull, scantlings and structural arrangement) and the vessel's operational mode (speed and maneuvering). Operators rely on a combination of quality ice information, the ability to maneuver around/away from hazards, and adequate structural capacity to resist ice loads which arise in the form of forces and pressures on the hull.



Figure 1-4: USCGC STRATTON (WMSL-752) operating in the Arctic Ocean during Operation Arctic Shield, September 12, 2014 [source: USCG]

This thesis presents a technical methodology based on mechanics of ship-ice interaction and structural response that can be used to establish ship-specific operational limitations in ice conditions. The limitations are presented in the form of so-called “safe speed” curves but are referred throughout this thesis as “technical limit speeds”. As described by Daley (2015) this clarification is to emphasize that the speeds are derived by a set of calculations under specific technical assumptions. Actual operational safe speeds would need to take a variety of other factors into account, including various uncertainties, levels of training, field experience and organizational risk tolerance. The focus of this work is on hull forms and structural arrangements which are not necessarily intended for

dedicated ice operations. Government vessels such as coast guard and naval assets, for example, may be required to operate in light to medium pack ice conditions as part of an emergency response effort. Non-ice strengthened and light ice class structures present new technical challenges that require modification to the conventional mechanics that form the basis of existing models and approaches.

This thesis is organized into several chapters. Chapters 2 and 3 outline the principle issues that affect safe speeds in ice and a review several existing approaches for determining operational limitations is provided. A synthesized technical methodology is proposed in Chapter 4 along with the detailed derivation of an underlying mathematical model. The model builds on the technical background behind the IACS Polar Class Unified Requirements and introduces several key updates. Chapter 5 utilizes available full scale measurement data as a means to validate the model to an extent possible. It is noted however, that a comprehensive validation of the model is not currently achievable. Chapter 6 introduces a novel approach to modeling ship-ice interaction which takes into account the compliance of the local hull structure and its ability to absorb energy during a collision event. This modification to the model is shown to be particularly important for non-ice strengthened vessels. Finally, Chapters 7 and 8 demonstrate the methodology using two case studies – an Ice Class PC5 Patrol Vessel and a non-ice strengthened naval combatant. The case studies describe each step of the ice capability assessment procedure and highlight the influence of key parameters.

It is important to understand that local damage from ice is far more variable than say hull girder overload or grounding events. While most forms of structural failure lead

to sudden and critical problems, ice damage at the lower levels can be very limited in extent and with very minor consequences. So while no damage is ever desired, in the case of ice, the toleration of minor and inconsequential local denting can permit a significant increase in the operational window. In an emergency situation, the expansion of that window may be needed and justified. This thesis demonstrates methods that can help fully understand the issues and consequences.

2. Summary of Safe Speed Issues

The risks of structural damage to ships operating in ice depend on several factors. The most fundamental line of defense is to simply avoid ice. Ice avoidance requires quality information about the conditions, whether it be visual observation from the bridge, access to available ice charts, or the use of onboard radar and other ice detection technologies. If ice contact cannot be avoided, the ship itself should have proper materials and structural capacity to resist the ice loads. Ice class ships are strengthened specifically to increase the local structural resistance to ice impact loads. For extreme overload scenarios that lead to rupture of the shell plating, subdivision and damage stability reserve offer a final line of defense from a catastrophic breach of the hull.

Ship speed and vessel maneuvers are operational considerations that can reduce the risk of damage while operating in ice. The focus of this thesis is to develop a methodology which can quantify speeds that would bring a ship to defined rational structural limits. This Chapter describes several of the key factors that should be considered when establishing safe operational limitations for ships in ice including ice types, ice concentrations, ice floe size, ice strength, ship ice class, ship hull form, and operational modes.

2.1. Ice types

There are many different forms of ice and it is important to be able to distinguish between the different types that may be encountered. Ice cover is rarely uniform or homogeneous in nature. Sea ice is typically found as a mix of ice types, thicknesses and floe sizes at various total ice concentrations. Near the coast, ice may be ‘land fast’,

anchored in place by the shoreline or possibly grounded pressure ridges. Further offshore, pack ice typically consists of a mix of ice usually characterized as an ‘ice regime’.

Table 2-1 lists the standard nomenclature for sea ice ‘stage of development’ established by the World Meteorological Organization (WMO) and adopted by most national ice services (WMO, 2014). Each stage up to old ice has an associated nominal ice thickness range. The thickness generally increases as the ice is exposed to longer periods of cold temperatures (or Freezing Degree Days). Thicker ice also can become stronger in both compressive and flexural strengths. The codes are used in ice charts and ‘egg codes’ as a way to quickly reference each ice type. Egg codes are further discussed below.

Table 2-1: Ice types according to WMO nomenclature

Stage of Development	Thickness	Code	Stage of Development	Thickness	Code
New Ice	< 10 cm	1	Medium First Year Ice	70 - 120 cm	1•
Nilas, Ice Rind	< 10 cm	2	Thick First Year Ice	> 120 cm	4•
Young Ice	10 - 30 cm	3	Old Ice	--	7•
Grey Ice	10 - 15 cm	4	Second Year Ice	--	8•
Grey - White Ice	15 - 30 cm	5	Multi-Year Ice	--	9•
First Year Ice	30 - 200 cm	6	Ice of Land Origin (Glacial/Icebergs)	--	Δ•
Thin First Year Ice	30 - 70 cm	7	Undetermined/Unknown	--	X•
Thin First Year Stage 1	30 - 50 cm	8			
Thin First Year Stage 2	50 - 70 cm	9			

2.2. Concentration

Ice can be present in various concentrations usually expressed in tenths coverage. Lower concentrations mean there is more open water to maneuver around hazardous features and the probability of ice contact can be reduced. Higher concentrations initially make it more difficult to identify and differentiate between ice types. Contact with ice in high concentrations becomes unavoidable and ice interactions can hinder maneuverability, in particular for hull forms not optimized for icebreaking.

Winds, currents, and tides cause ice fields to converge and potentially create ridges as the ice buckles and fractures (i.e. deformed ice). This is known as ‘pressure’ and can persist at different severity levels. High pressure in the ice pack can pose a significant restriction to vessel movement and may ultimately lead to besetment.

Ice concentration is generally reported in terms of areal coverage in tenths. The scale of areal coverage can vary depending on the perspective of the reporting source. From the bridge of a ship, concentration is typically concerning the coverage of ice within the line of sight of the ship (up to several kilometers). Ice concentrations reported on ice charts relate to a much larger scale on the order of 10s of kilometers. Figure 2-1 is provided by the Canadian Coast Guard (2012) in the guide on *Ice Navigation in Canadian Waters* and depicts different concentrations of ice.

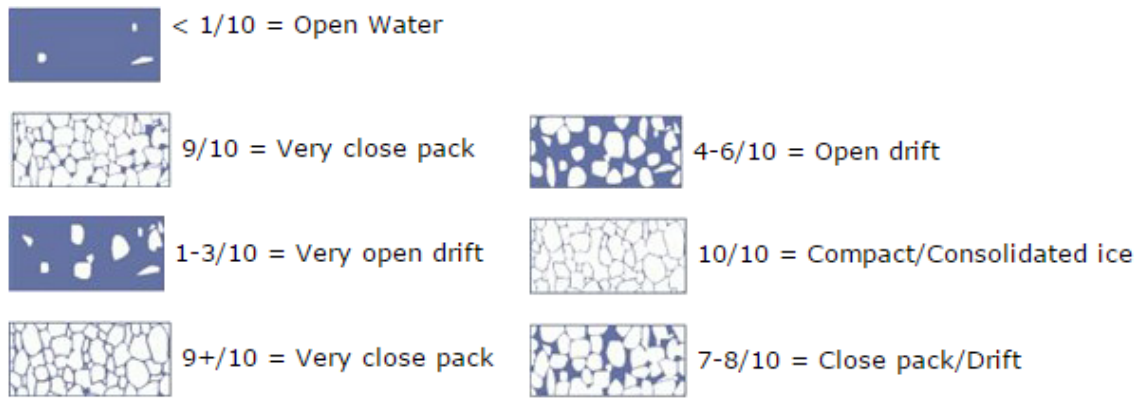


Figure 2-1: Ice concentrations [source: Canadian Coast Guard]

Ice charting services, for example the Canadian Ice Service (CIS) and the US Naval/National Ice Center (NIC) regularly produce ice charts for different geographical regions. The charts present an analysis of ice conditions based on an integration of data collected from satellite imagery, weather/oceanographic information, and visual observations from ship and aircraft. Charts are typically prepared on a daily, weekly or bi-weekly basis, depending on the region, and use a series of ‘Egg Codes’ to indicate concentration, stage of development, and form of ice (floe sizes). The charts can be used for planning of marine operations as well as for environmental research on the change and variability of ice conditions over time.

An example CIS ice chart is presented in Figure 2-2 for ‘Approaches to Resolute, mid-October’ in the northwestern part of Baffin Bay, Canada. The color codes represent different total concentrations. The ‘Egg Codes’ express concentration as a ratio in tenths describing the area of the water surface covered by ice as a fraction of the whole area. Total concentration includes all stages of development that are present while partial concentration refers to the amount of a particular stage or of a particular form of ice and represents only a part of the total. In this example, the total concentration of regime ‘L’ is

+9/10ths, or near 100%. The ice regime is comprised of 3/10ths multi-year ice, 5/10ths grey ice (10-15cm), and 1/10th new ice (<10cm) following the codes in Table 2-1.

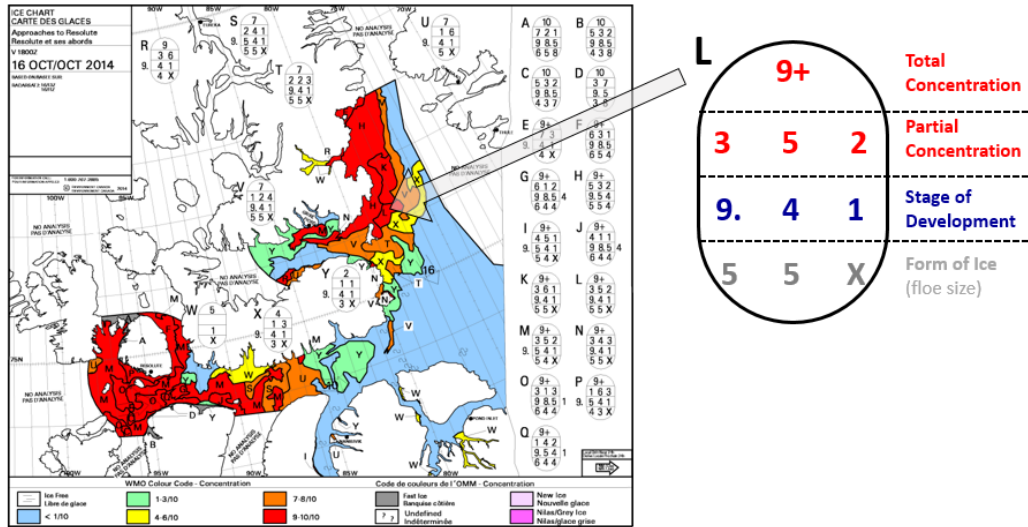


Figure 2-2: Example ice chart and egg code [source: Canadian Ice Service]

From the bridge of a ship, an ‘Egg Code’ can also be used to characterize an observation of ice conditions. Bridge observations can be subjective and the quality of the egg code description depends on the experience and skill level of the ice observer. Figure 2-3 is an example of an ice regime that is approximately 6/10ths total coverage with 4/10ths thick first-year ice (120-200cm), 1/10th second year ice, and 1/10th multi-year ice (note the dot applies to each ice type code listed to its left).

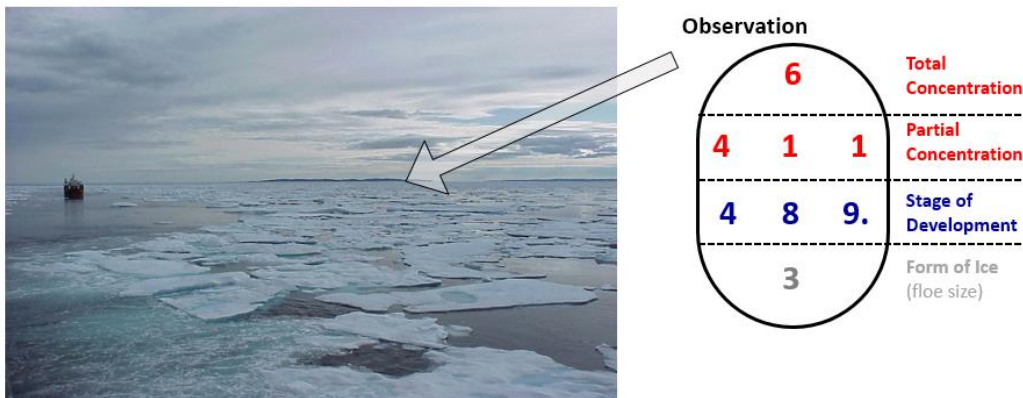


Figure 2-3: Example ice observation and egg code [IACS, Canada, & Finland, 2014]

2.3. Floe size

For operations in pack ice, the mass of the floe will have a direct effect on the loads acting on the ship hull. Floe mass depends on the area of the floe (size) and its thickness. WMO groups ice floe sizes into several categories as shown in Table 2-2. The range of floe widths for each category is fairly large, e.g. small floes are 20-100m, medium floes are 100-500m, and big floes are 500m – 2km. For most ships once floe sizes get to ~2-4x the ship’s length, the floes become effectively infinite. The categories and floe sizes specified by WMO are not really practical to vessel operations. As will be shown in later in this project, a smaller discretization of floe size is needed. The case studies presented in Chapters 7 and 8 show that floe size is a major factor that significantly effects the operational envelope of ships in pack ice, and perhaps even more important than thickness or ice strength, especially for naval hull forms.

Table 2-2: Ice floe sizes

Floe Sizes	Floe Width	Code
Pancake ice		0
Small ice cake; brash ice	< 2 m	1
Ice cake	2 - 20 m	2
Small floe	20 - 100 m	3
Medium floe	100 - 500 m	4
Big floe	500 - 2000 m	5
Vast floe	2 - 10 km	6
Giant floe	> 10 km	7
Fast ice, growlers, or floe-bergs		8
Icebergs		9
Undetermined or unknown		X

2.4. Ice Strength

Ice crushing strength and flexural strength can greatly influence the severity of ice loads on ships. Both terms are critical inputs to the mathematical model that is proposed

and applied in this thesis. Previous studies have highlighted the influence of ice strength on the local ice loads during impacts and the ultimate safe speed envelopes for different ship types (ABS, 2015; Dolny et al., 2013; VARD, 2015). It's important to consider realistic ice strength parameters when carrying out a ship-specific analysis.

2.4.1. Ice Crushing Strength

Various measurement data has been collected to study the variations in ice crushing strengths across different regions of the Arctic and for different types of ice. Unfortunately crushing strength is a challenge to define and measurement techniques can vary. Timco and Weeks (2010) provided a comprehensive review of the engineering properties of sea ice and assessed the state of knowledge of various physical and mechanical properties. Two common methods for measuring the crushing strength of sea ice include uniaxial compressive sample tests and in-situ borehole jack tests which measure the failure load (and stress) for ice under compression (see Figure 2-4). Test setups can vary and confining stresses can be introduced which can affect the strength results. Several researchers have studied the relationships between borehole and uniaxial tests. Kendrick & Daley (2011) offer a brief discussion of the different methods and how they relate to loads on ship hulls.



Figure 2-4: Typical ice compressive strength testing methods - uniaxial crushing (left) and in-situ borehole tests (right) [from Timco & Weeks, 2010]

One example plot taken from the Timco & Weeks paper presents the results of a mathematical expression for ice compressive strength that is based on data from field measurements. Figure 2-5 plots compressive strength of first-year ice as a function of air temperature and loading strain rate. Compressive strength values ranged from 0.4 MPa to about 5 MPa and were found to be strongly influence by the loading strain-rate.

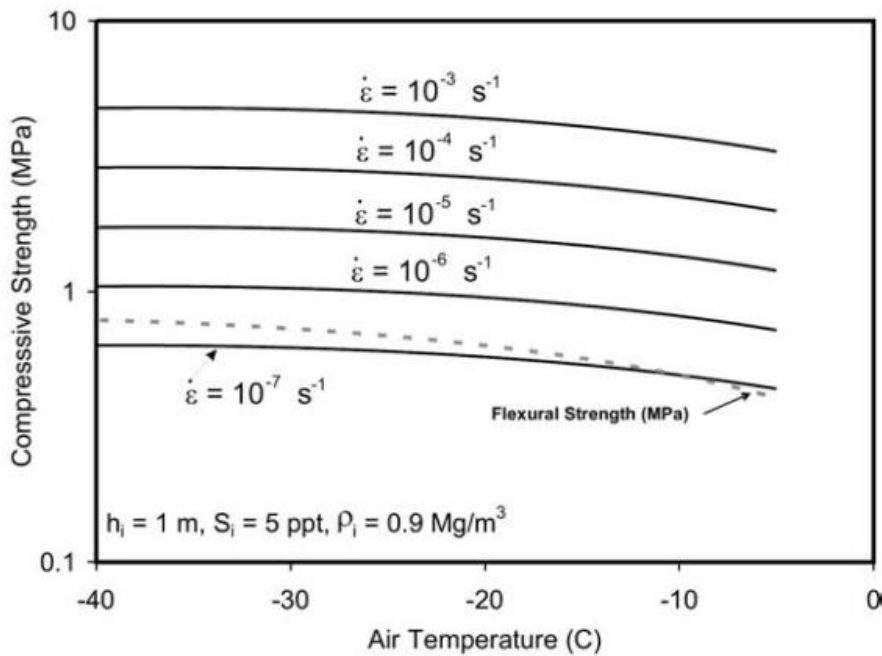


Figure 2-5: Ice compressive strength vs. temperature and strain rate [Timco & Weeks, 2010]

2.4.2. Ice Flexural Strength

Ice flexural strength is another practical parameter that is important to ice engineering problems, in particular ice loads on ship hulls. The basic concept of an icebreaking hull form is to introduce hull angles such that the flexural failure of an ice sheet limits the maximum ice crushing force on the hull. Flexural strength is typically measured using a simple beam bending or a cantilever beam tests. Typically for performance trials of icebreaking ships, target flexural bending strengths are between 0.5MPa – 0.75MPa.

2.4.3. Pressure-Area Models

The ice impact model used in the IACS Polar Rules (Daley, 2000) and the model used in the technical method proposed later in this thesis consider crushing strength as a nominal average pressure to crush ice on a contact area of 1m^2 , or P_0 , together with an inverse exponential function of area, $ex = -0.1$. This ‘process’ pressure-area representation of ice strength is empirically based on field measurements collected from instrumented ship panels. It is a practical approach for characterizing ice crushing strength as it lends itself to the development of an ice load pressure patch which is used to establish the minimum required structural scantlings in the rules. This is quite different from uniaxial strength values reported in the literature from field and laboratory experiments.

Frederking (1999) and Daley (2004) each describe two distinct types of pressure-area models. The ‘process’ P/A model describes how the average pressure relates to the total contact area, and is used to control the collision force during an ice indentation process. The ‘spatial’ P/A model is a description of how local peak pressures relate to zones within the total contact area. The ‘spatial’ model can be used to determine design loads on local structure, such as plating and framing. Both authors used data from measurement campaigns (*USCGC POLAR SEA* and *CCGS LOUIS S. ST-LAURENT*) to suggest a linkage between the two P/A curves when the effects are combined. Some of this data is revisited in Chapter 5.

Ice strength is highly variable and is not currently reported on ice charts. From the bridge of a ship, ice strength is also quite difficult to judge. In the deterministic methodology outlined in this thesis, conservative process-pressure area relationships are

selected for the crushing terms, with P_o values ranging from 3 – 6 MPa. Figure 2-6 shows a few different pressure area relationships compared with the strength models assumed for each IACS Polar Class. Chapter 5 presents sample data from several full scale ship instrumentation trails to benchmark the selected P-A models used in this thesis.

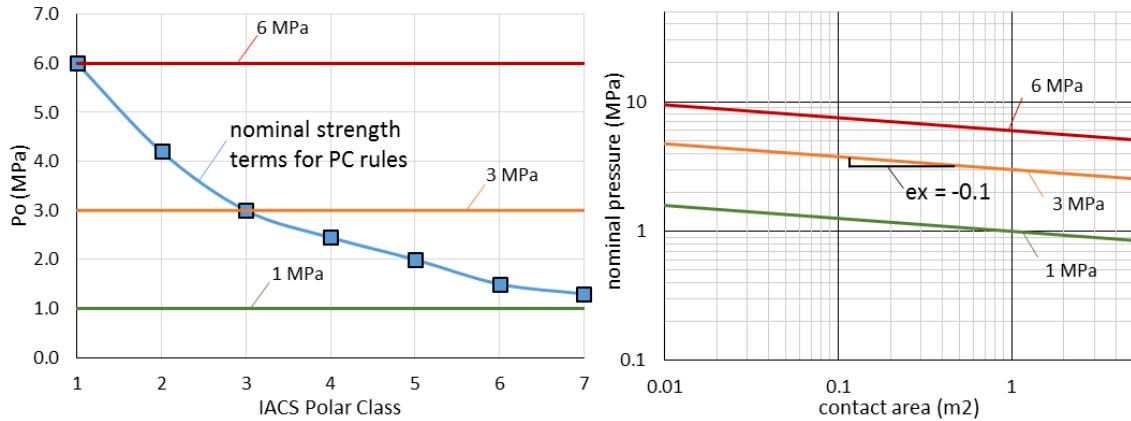


Figure 2-6: Typical ice crushing parameters

Other ice crushing models exist and have been used to determine ice loads on ship structures. For example section 3.3.1 briefly describes the Kheisin-Kurdyumov hydrodynamic model of ice-structure interaction that is utilized in the Russian rules and ice passport derivations.

2.5. Ice Class

Ice class requirements have been developed by classification societies and maritime authorities based on decades of service experience and history of ships operating in ice. Currently two principle sets of ice class rules are available and used in practice, 1) Finnish-Swedish Ice Class Rules (FSICR, or Baltic Rules) and 2) International Association of Classification Societies - Unified Requirements for Polar Ships (IACS Polar UR, or Polar Rules).

2.5.1. Finnish-Swedish Ice Class Rules

The FSICR were originally developed and primarily intended for winter navigation in the Baltic Sea although they are commonly used in several other areas where first-year sea ice is prevalent. Four (4) ice classes have been established by the Finnish and Swedish maritime authorities and are essential to the robust winter navigation system that exists in the region. The requirements for structural scantlings and machinery have been continuously calibrated over the years based on empirical data and service history. Table 2-3 describes each of Baltic ice classes along with the assumed level ice thickness used in the design point for structural strength.

Table 2-3: Finnish-Swedish Ice Class Rules with nominal descriptions

FS Ice Class	Description	Level Ice Thickness (for structural design)
IA Super	Navigating in difficult ice conditions without the assistance of icebreakers	1.0m
IA	Navigating in difficult ice conditions, with the assistance of icebreakers when necessary	0.8m
IB	Navigating in moderate ice conditions, with the assistance of icebreakers when necessary	0.6m
IC	Navigating in light ice conditions, with the assistance of icebreakers when necessary	0.4m

2.5.2. IACS Polar Class Rules

For many decades, classification societies each had their own unique set of ice classes for ships intended for Arctic operations. In 2008, the International Association of Classification Societies (IACS) finalized the Polar Class Unified Requirements, the result of a long term harmonization effort between IACS members and several coastal administrations. Seven (7) Polar Classes were defined based on descriptions of nominal ice conditions as shown in Table 2-4. The intent of the highest Polar Class PC1 is to offer

the capability for a ship to operate year-round in all Polar waters, subject to due caution by the crew. The lowest two Polar Classes, PC7 and PC6, were intentionally set to approximately correspond to FS Class 1A and 1A Super, respectively, however the Polar Rules consider old ice inclusions and their design points have been shown to slightly exceed those of the Baltic counterparts. Riska and Kämäräinen (2012) offer a detailed comparison of the background and history between the Polar Rules and FSICRs and their respective design points.

Table 2-4: IACS Polar Class Rules with nominal descriptions

Polar Class	Ice Description (based on WMO Sea Ice Nomenclature)
PC1	Year-round operation in all Polar waters
PC2	Year-round operation in moderate multi-year ice conditions
PC3	Year-round operation in second-year ice which may include multi-year ice inclusions.
PC4	Year-round operation in thick first-year ice which may include old ice inclusions
PC5	Year-round operation in medium first-year ice which may include old ice inclusions
PC6	Summer/autumn operation in medium first-year ice which may include old ice inclusions
PC7	Summer/autumn operation in thin first-year ice which may include old ice inclusions

One unique aspect of the IACS Polar Rules was the philosophy that the design ice load can be rationally linked to a design ship-ice interactions scenario. The selected design scenario is a glancing impact with a thick level ice edge and a mathematical model was developed for calculating ice load parameters for the bow region. The IACS Polar Rules model forms the basis of the technical methodology proposed later in this thesis.

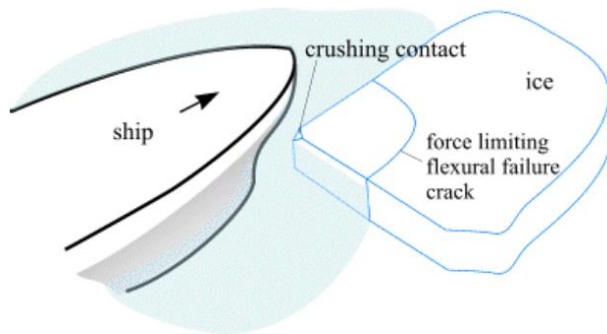


Figure 2-7: IACS Polar Rules design scenario - glancing impact with thick level ice edge

2.5.3. Implied Capabilities of Ice Classes

Any ship has some notional capacity to transit a certain amount of ice cover safely, though for a standard open water ship, the safe thickness is quite thin. As ice strengthening (i.e. ice class) is added to the hull, it becomes capable of handling thicker ice. Classification societies and regulatory administrations typically provide a basic nominal description of ice class notations based on their technical background and operational data obtained from service experience. For example, Figure 2-8 assembles the level ice thickness limitations for a variety of ice class notations as interpreted by various national administrations. This figure was produced by IACS during the development of the IMO Polar Code.

While there is general agreement between each administration for this simple metric (level ice thickness limitation), it is noted that compliance with an ice class does not provide a full representation of the ship's structural capabilities or limitations in various ice environments or operational modes. Additional analysis procedures are often sought by designers, builders and owners to quantitatively place bounds on the ships' structural capabilities. This thesis proposes a synthesized technical procedure to conduct such an analysis.

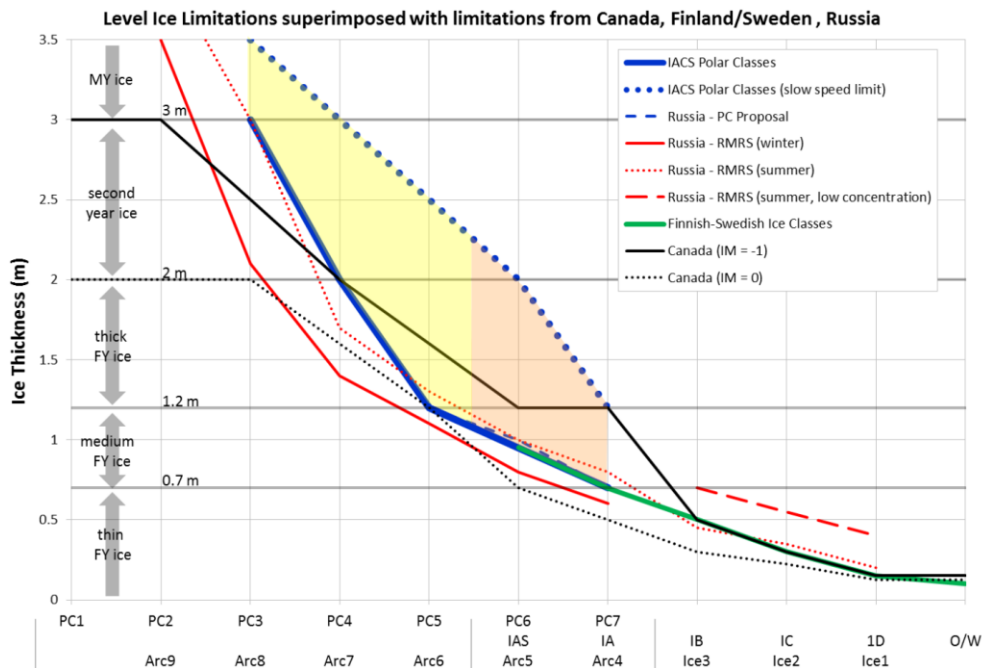


Figure 2-8: Level ice thickness limitations for various ice classes [IACS et al., 2014]

2.6. Hull Form

There is a vast range of potential ship hull forms and different bow shapes which have a strong influence on ice loads. Figure 2-9 presents sketches of four (4) different bow forms - a non-icebreaking form typical of naval platforms, a non-icebreaking form used traditionally for bulk cargo carriers, a moderate icebreaking form (in this example a Polar Class patrol vessel) and a heavy icebreaking bow (Polar Class cargo ship).

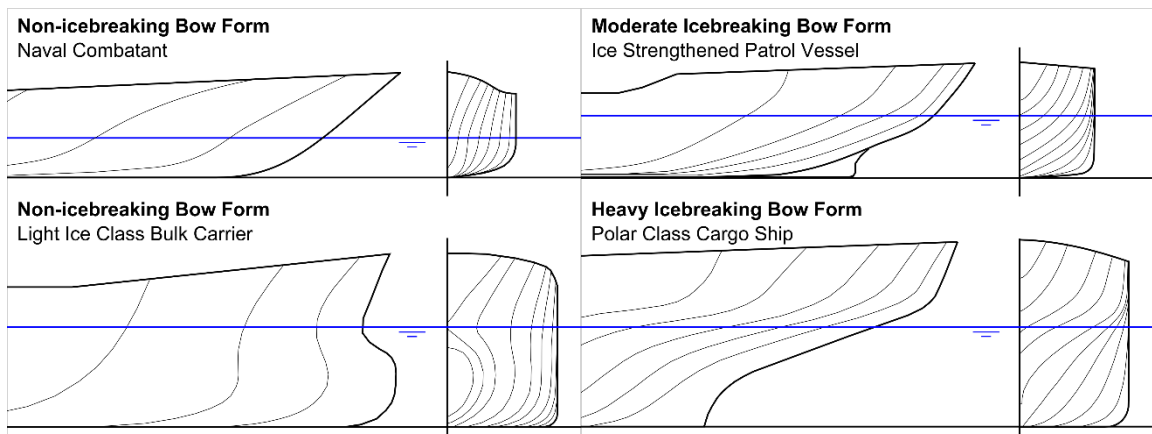
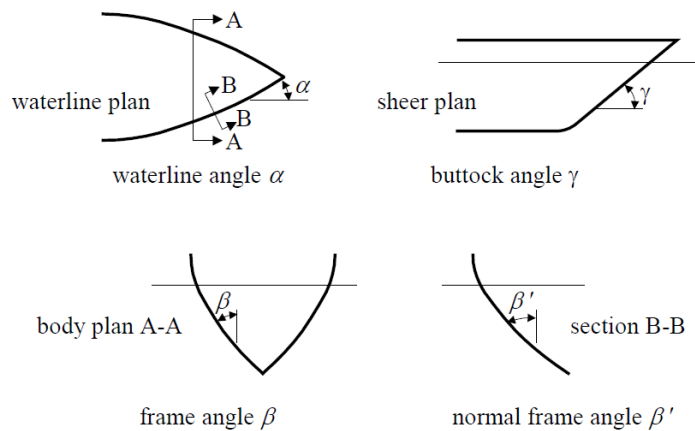


Figure 2-9: Sketches of different bow forms

Icebreaking bows are generally designed to promote ice failure in bending (i.e. flexural failure). During level icebreaking an icebreaking bow will ride over the ice and exert enough downward force to induced flexural failure. This tends to reduce the local loads on the ship compared with pure crushing of the ice. Icebreaking hull forms are also typically optimized to clear the ice away from propellers and underwater appendages and reduce frictional surface drag of the ice on the aft section of the hull.

Non-icebreaking bow forms are designed for open water performance. Typically at the waterline they have more vertically sided surfaces (i.e. low β angles) which result in promoting more crushing behavior. Some open water ships, e.g. naval platforms, tend to have fine waterline entrance geometries (low α angles). Others, e.g. large tankers or bulk carriers, may have very blunt bow forms which high α angles. These features can play a significant role on the nature of local ice pressures. Figure 2-10 is taken from the ABS Polar Class Rules (2016) and illustrates the definitions of these hull angles (α and β).



Note: β' = normal frame angle at upper ice waterline, degrees
 α = upper ice waterline angle, degrees
 γ = buttock angle at upper ice waterline (angle of buttock line measured from horizontal), degrees

Figure 2-10: Definitions of hull angles [ABS, 2016b]

2.7. Operations

Different modes of operation and different ice regimes will generate different magnitudes of ice impact forces. Ships that only encounter first-year ice will experience lower impact forces than a ship encountering old ice. Icebreakers with heavy ice strengthening that are required to ram ice features aggressively will obviously incur higher impact forces that would otherwise damage ships with lighter or no ice strengthening. The Canadian Coast Guard's publication on *Ice Navigation in Canadian Waters* (2012) offers some practical information about operations in ice and also includes guidance for non-icebreaking ships.

Speed is a fundamental operational consideration that can control the risk of damage to a ship. General guidance is to enter the ice pack at very low speeds to carefully receive the initial impacts. Once the vessel is into the pack, speed can be increased gradually to maintain headway and control of the ship, but the speed should not increase beyond the point at which the ship might suffer ice damage. The technical methodology presented in this thesis aims to offer quantitative guidance on estimating speeds that approach the limit of structural damage in different types of ice.

Additional guidance on ice operations typically focuses attention to the applied power in areas of weak ice or open leads, pools, etc. where the speed might unnoticeably increase to dangerous levels, posting extra lookouts on the bridge, the use of searchlights after dark, ballast control to protect a bulbous bow, rudders, propellers, etc., and turning in ice and in channels. All of these are critical to safe operations in ice and rely on competent and experienced ice navigators. However these topics are outside the scope of this work.

3. Existing Approaches for Operational Limitations in Ice

Different methods are available for determining operational limitations of ships in ice. One approach that has been applied by regulatory administrations, is the use of risk control methodologies and access control regimes. The Canadian Arctic Ice Regime Shipping System (AIRSS) and the IMO's POLARIS are two examples of risk-based control methodologies which link a vessel's ice class, or lack thereof, to actual ice conditions and provide guidance on whether or not it is safe to operate. These systems don't explicitly deal with safe operating speeds but offer a quick assessment of the risk level for operations in ice.

More specific safe speed analyses methods have also been proposed which link the ship's actual structural capacity to ice loads that arise from different operational impact scenarios. The methodology and mathematical model presented in Chapter 0 is a proposed synthesized approach that explicitly uses ship speed as a parameter for establishing operational limitations. This Chapter provides a review of several existing approaches to establish operational limitations for ships in ice.

3.1. Canadian Arctic Ice Regime Shipping System (AIRSS)

The Canadian Arctic Ice Regime Shipping System (AIRSS) was developed through collaborative efforts between Canadian government agencies and industry and introduced in the 1990s. AIRSS involves comparing the actual ice conditions along a route to the structural capability of the ship. The system recognizes that realistic ice conditions tend to manifest in an 'ice regime' which is composed of any mix or combination of ice types, including open water (Timco & Johnston, 2003).

Under AIRSS, the decision to enter a given ice regime is based on the quantity of dangerous ice present, and the ability of the vessel to avoid the dangerous ice along the route to (and from) its destination. Every ice type (including Open Water) has a numerical value which is dependent on the ice class of the vessel. This number is called the Ice Multiplier (IM). The value of the Ice Multiplier reflects the level of danger that the ice type poses to the particular category of vessel.

For any ice regime, an Ice Numeral (IN) is the sum of the products of the concentration (in tenths) of each Ice Type, and the Ice Multipliers relating to the Type or Class of the ship in question. These multiplications are repeated for as many Ice Types and each of their respective concentrations that may be present, including Open Water. Ice Numerals can be calculated from ice conditions observed on the bridge or from ice ‘egg codes’ typically found on ice charts. The Ice Numeral is therefore unique to the particular ice regime and ship operating within its boundaries. To use the system, the master or ice navigator needs to identify the ice types and concentrations along the route.

An Ice Numeral produced by AIRSS provides a binary go/no-go instruction to the operator. A negative IN means the vessel is restricted from operating while a positive IN permits vessel operations. No speed guidance is provided by AIRSS, although intuitively higher IN would generally permit higher safe speeds.

3.2. IMO Polar Code – POLARIS

The International Maritime Organization (IMO) recently developed a harmonized methodology for assessing operational limitations in ice called the *Polar Operational Limit Assessment Risk Indexing System* (POLARIS). POLARIS was published as a

recommendatory IMO Circular in 2016 (IMO, 2016) and is intended to be a supplement to the IMO International Code for Ships Operating in Polar Waters (Polar Code) (IMO, 2015). This system incorporates experience and best practices from the Canadian AIRSS system and additional input provided by several coastal administrations with experience regulating marine traffic in ice conditions. Similar to AIRSS, the basis of POLARIS is an evaluation of risk posed to the ship by ice conditions using the WMO nomenclature and the ship's assigned ice class (or lack thereof).

POLARIS can be used for voyage planning or on-board decision making in real time on the bridge although, as with any methodology, it is not intended to replace an experienced Master's judgment. POLARIS assesses ice conditions based on a Risk Index Outcome (RIO) determined by the following simple calculation (1):

$$RIO = (C_1 \cdot RV_1) + (C_2 \cdot RV_2) + (C_3 \cdot RV_3) + (C_4 \cdot RV_4) \quad (1)$$

Where;

$C_1 \dots C_4$: concentrations of ice types within ice regime

$RV_1 \dots RV_4$: corresponding risk index values for a given Ice Class (Figure 3-1)

The Risk Values (RV) are a function of ice class, season of operation, and operational state (i.e., independent operation or icebreaker escort). An example table of preliminary RVs for winter independent operations is shown in Figure 3-1. Risk levels are higher with increasing ice thickness and decreasing ice class. POLARIS establishes RVs for the seven (7) IACS Polar Classes, four (4) Finnish-Swedish Ice Classes, and non-ice strengthened ships.

Increasing Ice Thickness (severity) 												
ICE CLASS	Winter Risk Values (RVs)											
	ICE FREE	NEW ICE	GREY ICE	GREY WHITE ICE	THIN FIRST YEAR 1ST STAGE	THIN FIRST YEAR 2ND STAGE	MEDIUM FIRST YEAR 1ST STAGE	MEDIUM FIRST YEAR 2ND STAGE	THICK FIRST YEAR	SECOND YEAR	LIGHT MULTI YEAR	HEAVY MULTI YEAR
	--	0-10 cm	10-15 cm	15-30 cm	30-50 cm	50-70 cm	70-95 cm	95-120 cm	120-200 cm	200-250 cm	250-300 cm	300+ cm
PC1	3	3	3	3	2	2	2	2	2	2	1	1
PC2	3	3	3	3	2	2	2	2	2	1	1	0
PC3	3	3	3	3	2	2	2	2	2	1	0	-1
PC4	3	3	3	3	2	2	2	2	1	0	-1	-2
PC5	3	3	3	3	2	2	1	1	0	-1	-2	-2
PC6	3	2	2	2	2	1	1	0	-1	-2	-3	-3
PC7	3	2	2	2	1	1	0	-1	-2	-3	-3	-3
IA Super	3	2	2	2	2	1	0	-1	-2	-3	-4	-4
IA	3	2	2	2	1	0	-1	-2	-3	-4	-5	-5
IB	3	2	2	1	0	-1	-2	-3	-4	-5	-6	-6
IC	3	2	1	0	-1	-2	-3	-4	-5	-6	-7	-8
NO ICE CLASS	3	1	0	-1	-2	-3	-4	-5	-6	-7	-8	-8

Figure 3-1: POLARIS risk values (RVs)

A positive RIO indicates an acceptable level of risk where operations may proceed normally. A negative RIO indicates an increased risk level, potentially to unacceptable levels. Criteria is established, as shown in Table 3-1, for negative RIOs that suggest the operations should either stop to be reassessed or proceed cautiously with reduced speeds (IMO terminology is “subject to special consideration”).

Table 3-1: POLARIS risk index outcome (RIO) criteria

RIO_{SHIP}	Ice classes PC1-PC7	Ice classes below PC 7	Color Code
$20 \leq \text{RIO}$	Normal operation	Normal operation	
$10 \leq \text{RIO} < 20$			
$0 \leq \text{RIO} < 10$			
$-10 \leq \text{RIO} < 0$	Elevated operational risk	Operation subject to special consideration	
$-20 \leq \text{RIO} < -10$	Operation subject to special consideration	Operation subject to special consideration	
$-30 \leq \text{RIO} < -20$			

IMO has agreed on ‘recommended speed limits’ for POLARIS RIOs that fall into the ‘elevated operational risk’ category (i.e. RIOs between 0 and -10), however operations in such ice regimes are only permitted for Polar Class ships. These are not intended to be hard and fast speed limits and shipboard ice load measurement systems and/or ice trials can be used to calibrate the recommended speeds.

Table 3-2: POLARIS recommended speed limits for 'elevated operational risk'

Ice Class	Recommended Speed Limit
PC1	11 knots
PC2	8 knots
PC3-PC5	5 knots
Below PC5	3 knots

As an example demonstration, POLARIS is applied to consider the risks of a non-ice strengthened ship operating in the Alaska region using publically available ice chart data. This work was carried out by the author and was first presented in ABS (2015). Figure 3-2 shows four regional ice charts available for offshore Alaska (Chukchi, Beaufort, and Bering Seas). The charts are typically published several times per week. The black lines in the figure depict the superimposed ice regimes from all October charts between 2010 and 2015 (approximately 40 charts per region). An example of one Chukchi Sea regional ice chart for late October 2012, a relatively severe ice year, is shown in Figure 3-3.

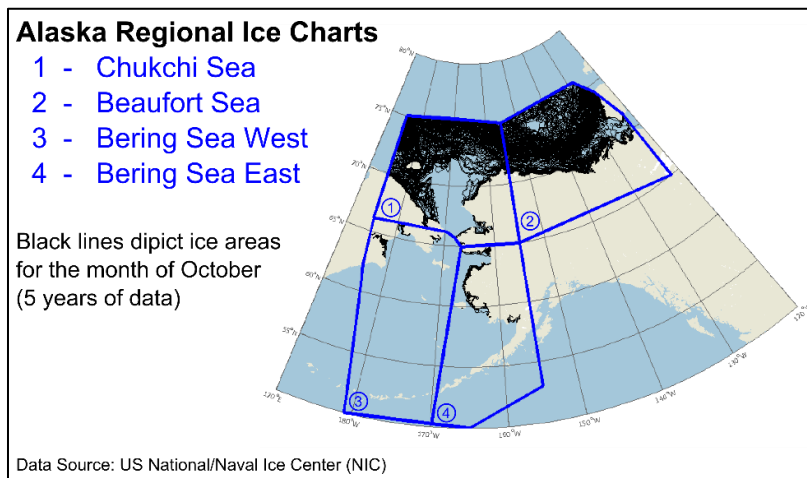


Figure 3-2: Alaska regional ice charts [data source: US NIC]

The maps in Figure 3-4 geographically present the results of POLARIS calculations using the historical ice charts from the US National/Naval Ice Center (NIC). The data was assembled and overlaid on a 0.5 x 0.5 latitude-longitude grid and processed on a monthly basis. ‘Minimum’ RIOs were computed based on the last 10 years of data (2004-2014) and plotted according to the color coded criteria scale described above. The outcomes highlight geographical areas in the Alaska region with elevated risk levels (orange and red areas indicate RIOs below -10) at different times of the year. It can be seen that there are large

areas of the Bering Sea and Arctic Alaskan waters where operations of non-ice classed ships in the summer months is permitted under POLARIS, even in the worst ice years. These ‘Minimum RIO’ plots reflect the worst ice conditions from the past 10 years.

POLARIS can be a useful tool for evaluating risks for ships operating in ice conditions and makes use of ice chart data that is publically available. However, the results are only dependent on ice thickness and concentration and don’t offer any practical guidance related to ship speed. The technical methodology presented and applied in this thesis takes into account more factors that contribute to the structural risk of ships in ice; namely floe size, ice strength, ship strength and ship speed.

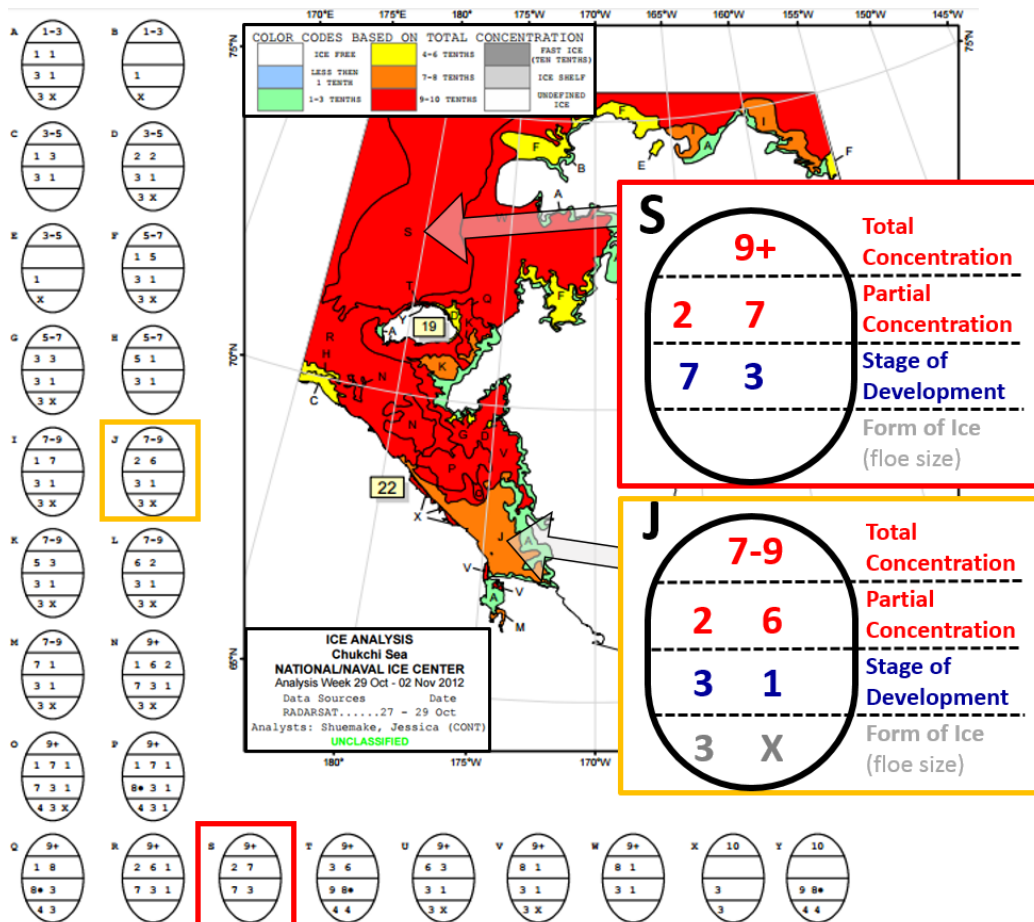


Figure 3-3: Chukchi Sea Ice Chart (29 October 2012) [source: US NIC]

Monthly **Minimum** POLARIS Risk Outcomes (10 years)

Non-ice classed ship

Ice data source: US National/Naval Ice Center (NIC)

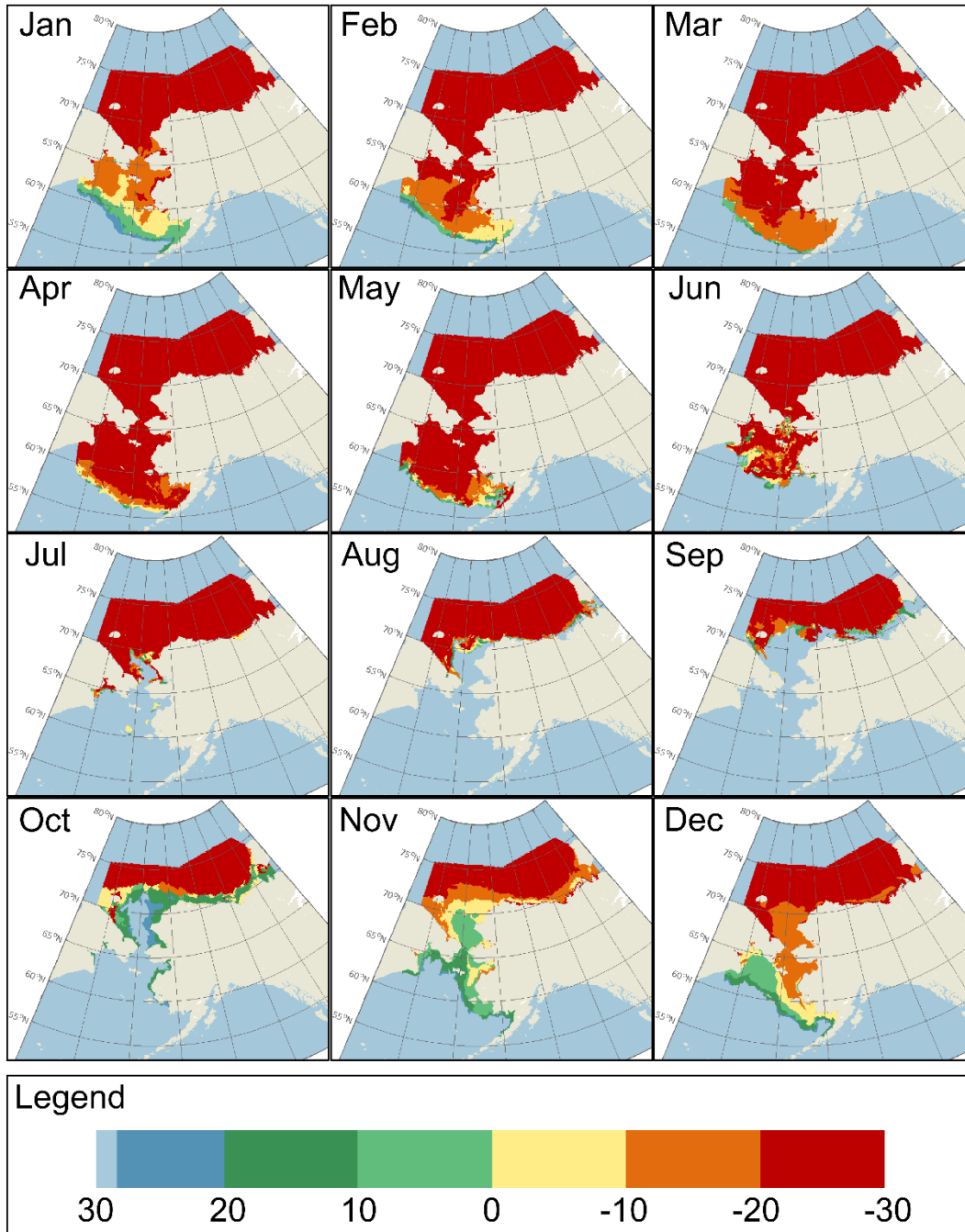


Figure 3-4: Monthly minimum POLARIS RIOs for non-ice classed ships, Alaska region [ABS, 2015]

3.3. Safe Speed in Ice

The idea of a ship-specific analysis procedure to determine safe navigating speeds in ice conditions is not novel. The earliest concepts of safe speeds were likely postulated by Russian scientists sometime in the 1960s and 1970s during the development of transportation regulations for ships operating in the Russian Arctic. The Ice Passport (often referred to as the Ice Certificate), was first introduced in the mid-1970s. One of its major components is the regulation of speed to mitigate the risk of hull damages due to ice. The Ice Passport contains safe speed guidance as a function of the ship's actual structural configuration and anticipated ice conditions. This is the only known existing regime which quantitatively considers the safe speed of ships in ice, however its full technical background is not widely available nor accepted.

Other technical approaches to the concept of safe speed also exist in the literature. Some are based on probabilistic approaches while others rely on purely deterministic analysis. Several recent efforts have adopted the ice-ship interaction model and structural response criteria used in the IACS Polar Rules with some modifications that permit safe speed assessments. An overview of available safe speed in ice technical approaches are described in the following sub-sections.

3.3.1. Russian Ice Passport / Ice Certificate

Maxutov and Popov (1981) provided a description of Ice Certificate requirements in one of the earliest available publications on its technical basis. They defined the safe limit speed as “the maximum speed under given ice conditions which ensures safe navigation”. This limit speed, depicted by simple diagrams (such as the one presented in

Figure 3-5), is determined by the available installed power and limitations in the hull structure. In addition to the limit speeds, other operational guidance is provided by the Ice Passport such as the minimum safe distance in the convoy and ice pressure resistance capabilities. The authors clearly note that while the Ice Certificate can provide the operator useful guidance, it cannot consider every possible ice condition or operating mode and the overall recommendation of operator due caution should be maintained.

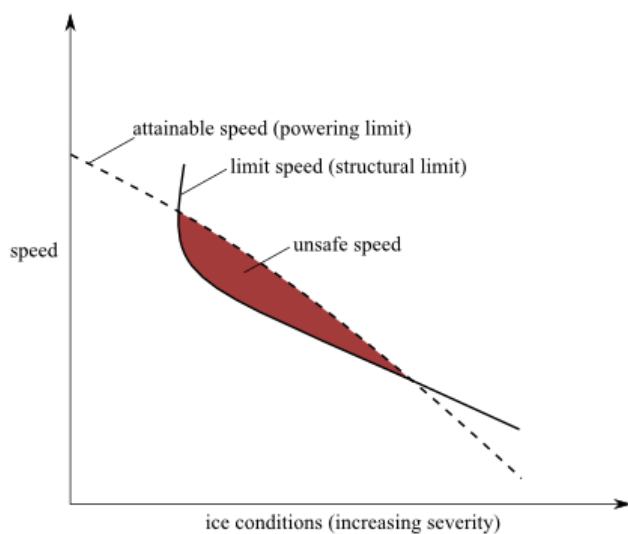


Figure 3-5. Sketch of safe speed diagram [from Maxutov and Popov (1981)]

In the late 1990s, at the request of Canadian authorities, a detailed report was prepared describing the scientific basis and methodology of the Ice Passport applied to *CCG PIERRE RADISSON* (Likhomanov et al., 1997; Likhomanov et al., 1998). The report included the ice load model procedures and the formulations to express the load-bearing capacity of framing members. The technical approach for safe speed guidance in the Ice Passport begins by establishing attainable (i.e. performance) speed curves in ice (v_{ship} vs. h_{ice}). Empirical and semi-empirical ice resistance formulations for level solid ice, hummocked ice covered in deep snow, high concentration pack ice, and cake ice are

formulated considering the full installed main engine power. These attainable speed curves may also be established by model tests or ice trials.

Critical state curves are developed to represent the load bearing capacity of local hull structural members. Expressed in terms of pressure, p , and load height, b , these limit states are derived using analytical beam theory or numerical finite element analyses (linear elastic and nonlinear static) of actual ship grillages. Two separate criteria are applied; first yield (zero plastic deformations) and the ultimate state (the formation of plastic hinges).

The ice load parameters used to develop safe speed curves in the ice passport are based on Kurdyumov and Kheisin's velocity-dependent hydrodynamic model for local contact pressure (1976) coupled with Popov-type collision mechanics (Popov et al., 1967). This was one of the first analytical models that produced the basic ice load parameters from a given set of input conditions. Kurdyumov and Kheisin modeled ice crushing using a concept of viscous extrusion and so-called "specific failure energy". It assumed that ice crushing involves the formation of a near-uniform layer of fine granular material that is then extruded. A viscous extrusion model was used to model the process and describe the pressures.

This crushing model presents two difficulties. The first, a practical challenge, is the need to numerically integrate the model to obtain a solution. This is because viscous extrusion includes velocity effects, which prevent the equations from being solved analytically by a closed-form solution. Another problem with the viscous extrusion model is that the pressure patterns it predicts are quite smooth, almost uniform. Empirical evidence from testing on ships and in labs has shown the ice pressure are highly non-

uniform, and typically contain peaks of very high pressures inside the contact zone. This is later shown in Chapter 5 with examples of full scale data measurements.

Figure 3-6 illustrates the difference between the Kurdyumov-Khesin (1976) model and the pressure-area model that is utilized in this thesis [Claude Daley, personal communication, March 2015]. With a pressure-area model the pressure is just a function of area which is just a function of the normal penetration. This permits the crushing energy to be expressed in terms of only one independent variable, the penetration. The Kurdyumov-Khesin model requires the time derivative as well, adding a significant level of difficulty to the problem. Further, it is widely felt by Canadian and European ice experts that the empirical evidence does not support the Kurdyumov-Khesin model.

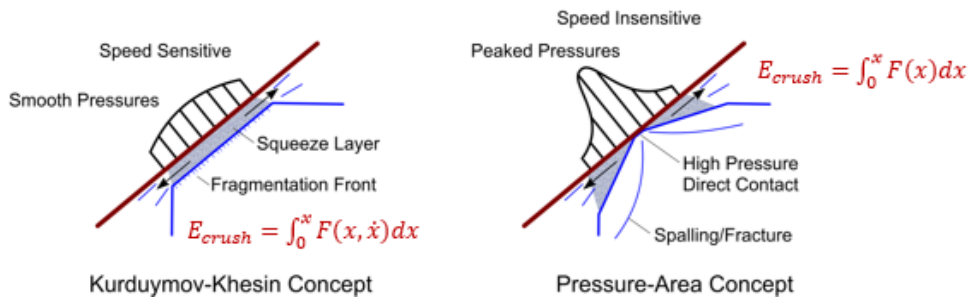


Figure 3-6: Kurdyumov-Khesin [1976] ice pressure model (left) and pressure-area model (right)

To develop the safe speed curves for an ice passport, the model described above is used to calculate the load parameters (p and b) over a range of ship speeds ($v_{ship} = 2- 20$ knots), ice thickness ($h_{ice} = 0.25 - 4.0$ m), floe size (50 m, 100 m, and infinite level ice), and impact locations (locations on the bow under two draft conditions). A solution scheme is devised to find the speed and ice thickness combinations corresponding to points on the critical state curves.

Examples of safe speed guidance found in a typical ice passport are provided in Figure 3-7. This example is for a Baltic 1C cargo ship. The left side graph is for 6/10ths concentration and the right is for +9/10ths. The safe speed curve (green) is the same in both cases, however the attainable speed (performance) is reduced for higher concentrations.

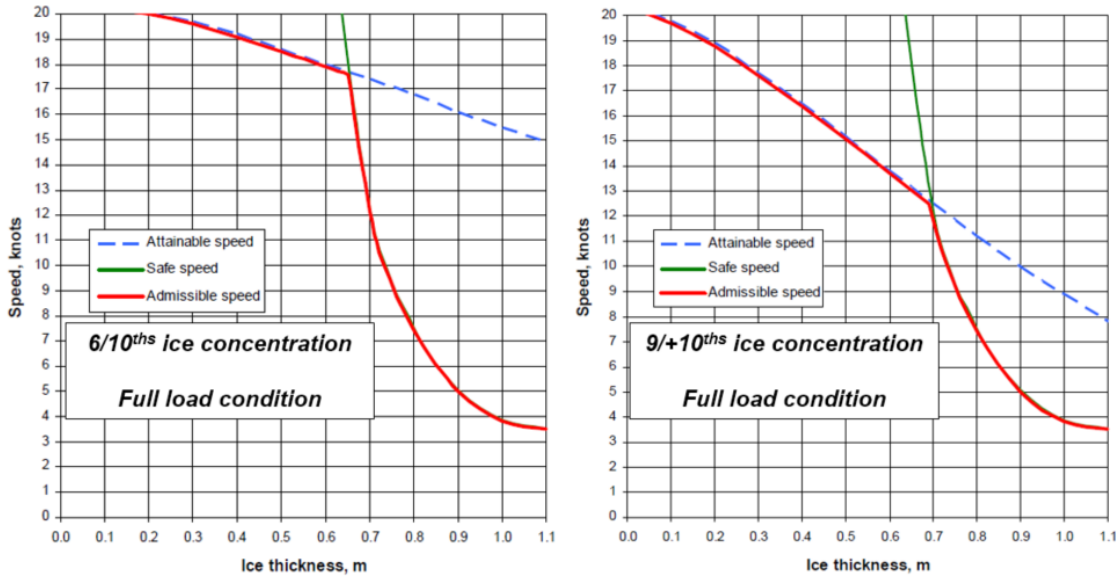


Figure 3-7: Examples safe speed guidance from a Russian ice passport [source: CNIIMF]

3.3.2. Probabilistic Approaches

Tunik et al. (1990) and Tunik (2000) recognized that the safe speed concepts applied in the Ice Passport hinged on pure deterministic analyses. He warned that compounding the most severe combinations of conservatively assumed critical parameters can ultimately lead to even higher levels of conservatism in the safe speeds. As an alternative, a conceptual probabilistic approach to safe speed analysis was offered. The approach is described in Figure 3-8. The impact location on the hull and the environmental ice parameters are treated as random variables and an analysis procedure is proposed to find the probability of load levels which exceed different structural damage levels.

Available distributions of ice concentrations, thickness, floe size and mechanical properties are utilized; however, it is noted that the parameters can vary significantly between regions.

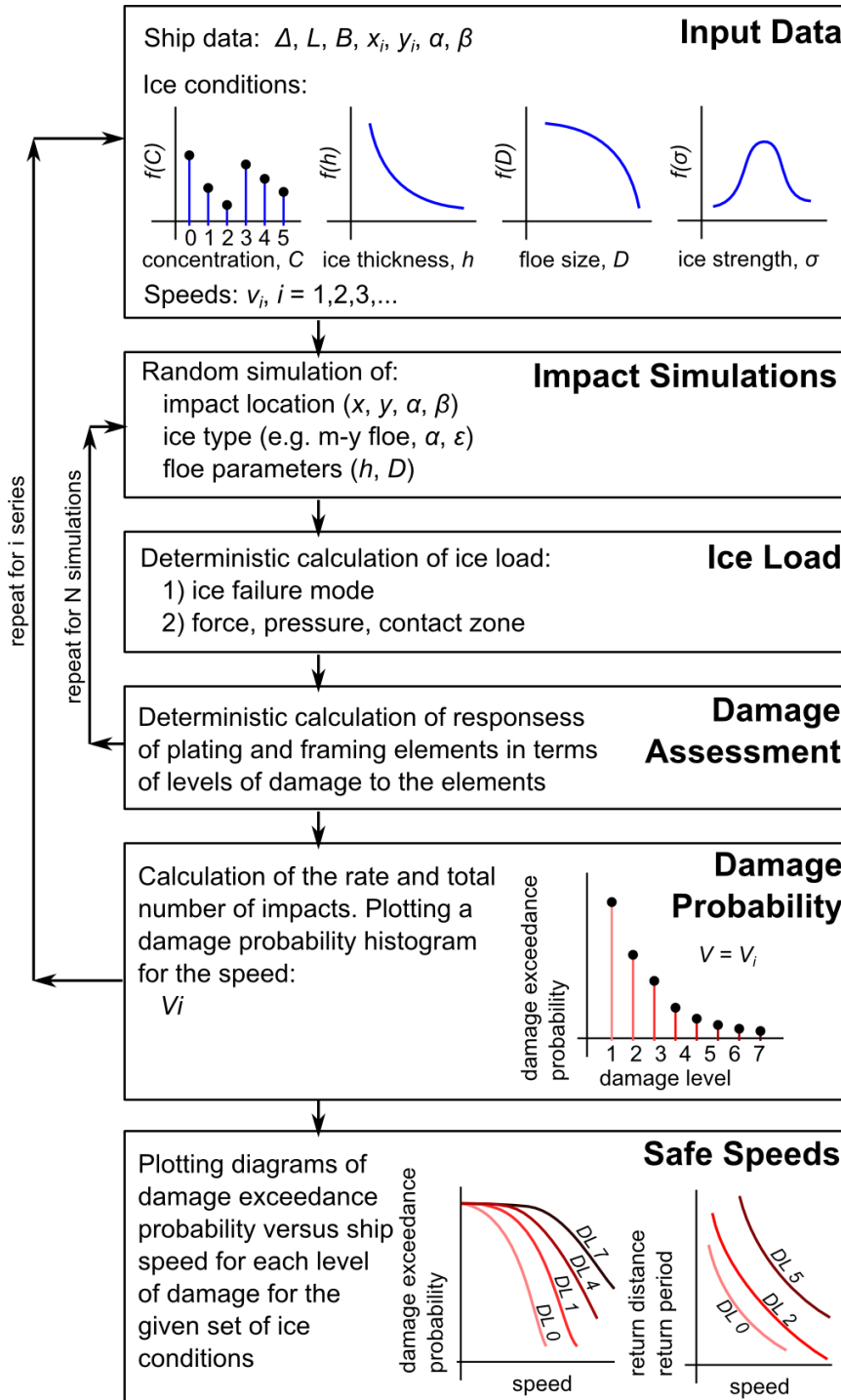


Figure 3-8: Probabilistic concept for safe speed in ice [from Tunik et al. (1990)]

3.3.3. Recent Approaches

The approaches discussed so far each consider the hydrodynamic model of ice-solid body impact combined with Popov collision mechanics. This model is generally considered as the standard Russian practice and has been employed for over 40 years. Recently, alternative models have been utilized, many of which are tied directly to the pressure-area relationship which underlies the technical background of the Polar UR, and is described in more detail later in this thesis.

Daley & Liu (2010) addressed ship ice loads in pack ice by modifying the Polar UR model to consider finite ice floes. Specifically, they explored the secondary impacts (i.e. reflected collisions) on the midbody following bow glancing events. Limiting speeds were established comparing the reflected load parameters with UR design values for sample PC7 ships (see Figure 3-9). This analysis demonstrated that secondary midbody collisions can be critical, especially for thick ice. While the structure was not directly analyzed, this study demonstrated the importance of considering off-design ship-ice interaction scenarios.

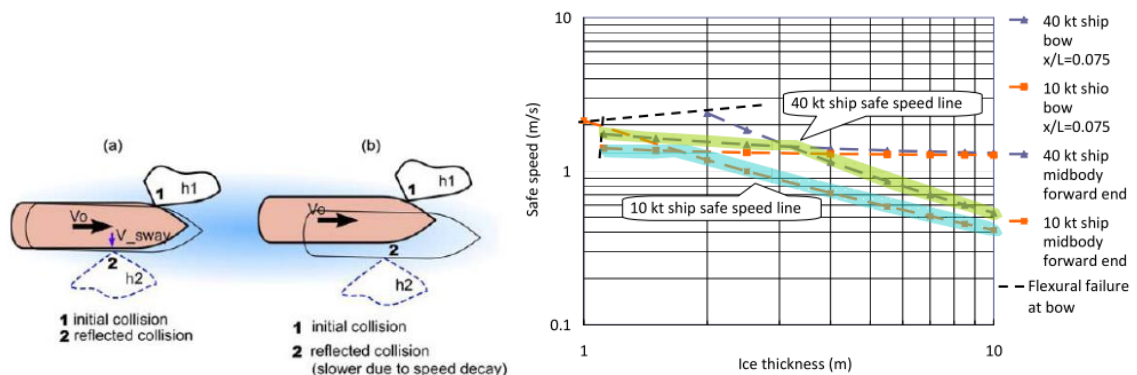


Figure 3-9: Reflected collision scenarios (left) and computed safe speed limits for PC7 ships (right) [from Daley & Liu (2010)]

Daley & Kim (2010) studied ice collision forces considering structural deformation assuming a linearized plastic component of the structural response. An additional component (structural indentation energy) was introduced to the energy balance in the mathematical model. To some degree, this approach circumvents the assumption of a rigid body. A regression analysis of grillages subjected to point loads using the nonlinear finite element analysis method was used to develop this plastic component. Limiting ship speeds were established against various masses of icebergs for different allowable deformation levels (see Figure 3-10). The inclusion of structural deformation into the impact model is a fairly novel concept. It was shown to play a moderate role in the ice load mechanics, in particular for lower ice class ships. Chapter 6 of this thesis builds on the methodology proposed by Daley & Kim (2010) to take into account structural indentation energy during the ice indentation process. The cases studies presented in Chapters 7 and 8 demonstrate the approach for different classes of ship.

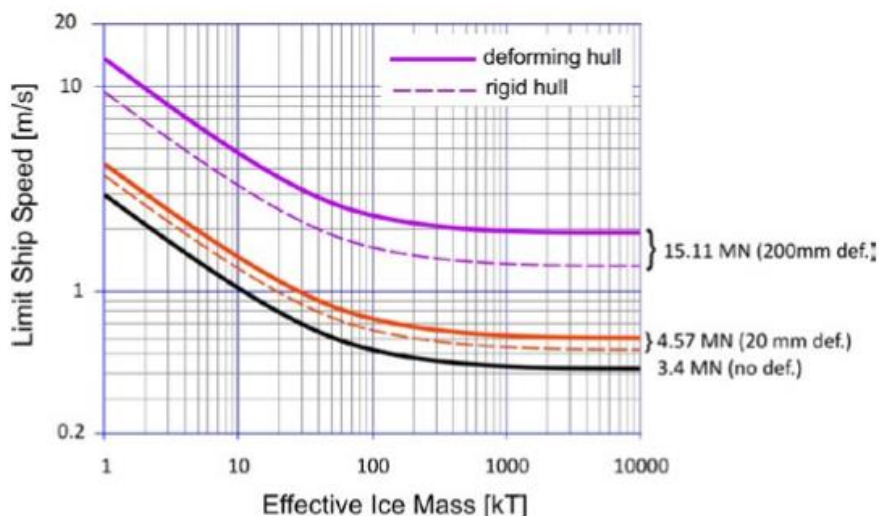


Figure 3-10: safe speed envelopes considering locally compliant structure [from Daley & Kim (2010)]

BMT Fleet Study on Safe Speeds in Ice

In a technical report by BMT Fleet Technology, Daley et al. (2011) examined the use of the IACS Polar Rules design ice load scenario for developing safe speed in ice curves for ships. One notable modification was an update to the flexural failure limit. The authors recognized the limitations of a static flexural limit in the Polar Rules and proposed an extension the model which included a horizontal force component, friction, and dynamic effects. The quasi-plastic structural response assumptions based on IACS UR limit states for plating and frame strength were applied to establish vessel speeds which resulted in the structure being loaded up to its design point.

PhD Thesis by Sazidy

In a PhD thesis by Sazidy (2014), the dynamic factors involved in the contact between a ship side and ice were studied in more detail, particularly relating to flexural ice failure. Sazidy initially explored the ice edge behavior using LS-Dyna, a commercially available explicit dynamic finite element program. The program was able to model the ice edge crushing and flexural response in a time-domain analysis that accounts for and can demonstrate dynamic effects. Figure 3-11 shows an example LS-Dyna simulation of a shoulder collision with an ice wedge on an elastic foundation.

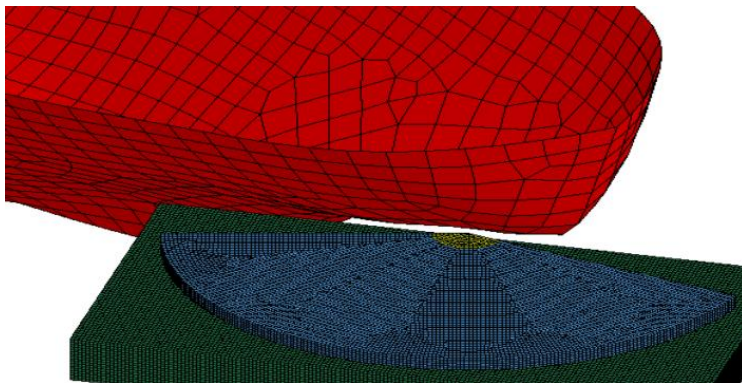


Figure 3-11: LS-Dyna model of shoulder collision with an ice edge on elastic foundation [Sazidy (2014)]

The numerical model was compared to several available analytical and semi-empirical mathematical models of ship-ice breaking, including models by Kashteljan, Lindqvist, Vartsa and Daley. A new empirical equation was formulated for a velocity-dependent flexural failure limit. The equation was cross-checked against data collected from full scale impact tests of a landing craft bow installed on the tug *RAUMA I*. The results of that comparison, plotted in Figure 3-12, show fairly good agreement. This model is used in the proposed technical methodology described later in this thesis.

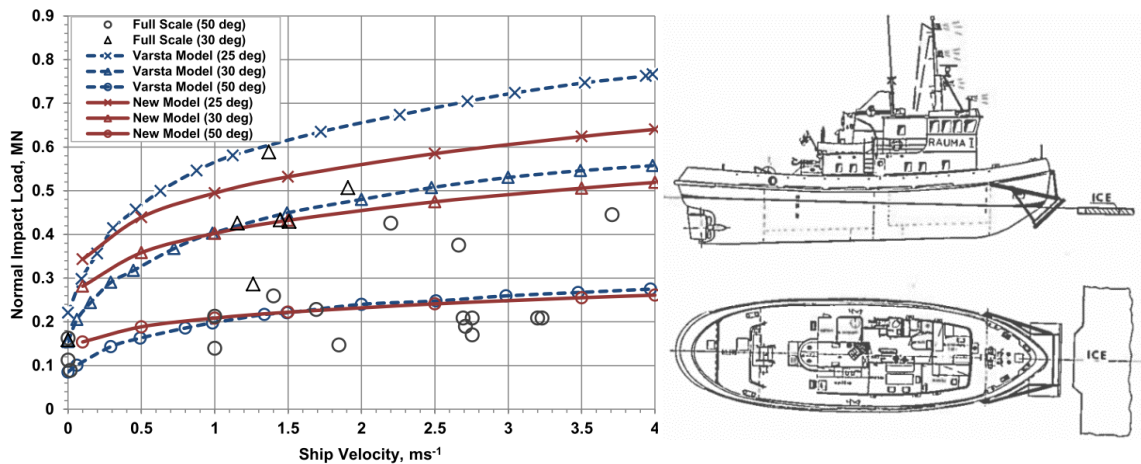


Figure 3-12: Cross-check of velocity dependant ice flexural failure model with full scale test data [from (Sazidy, 2014)]

Finnish/Swedish Submission to IMO

In a position paper submitted by Finland and Sweden to IMO during the development of the Polar Code, Kolari & Kurkela (2012) considered the case of a bow glancing collision with a spherical glacial ice mass. Their model solved a system of motion equations in the time domain estimating hydrodynamic effects by added mass terms, and adopted a pressure-area model for the treatment of ice crushing strength. The safety criterion used is the elastic response similar to that of the Russian Ice Passport for safe

speeds. Their model was applied for different framing scantlings on the commercial ship – *M/V EIRA*. Some sample results along with a depiction of the model are shown in Figure 3-13.

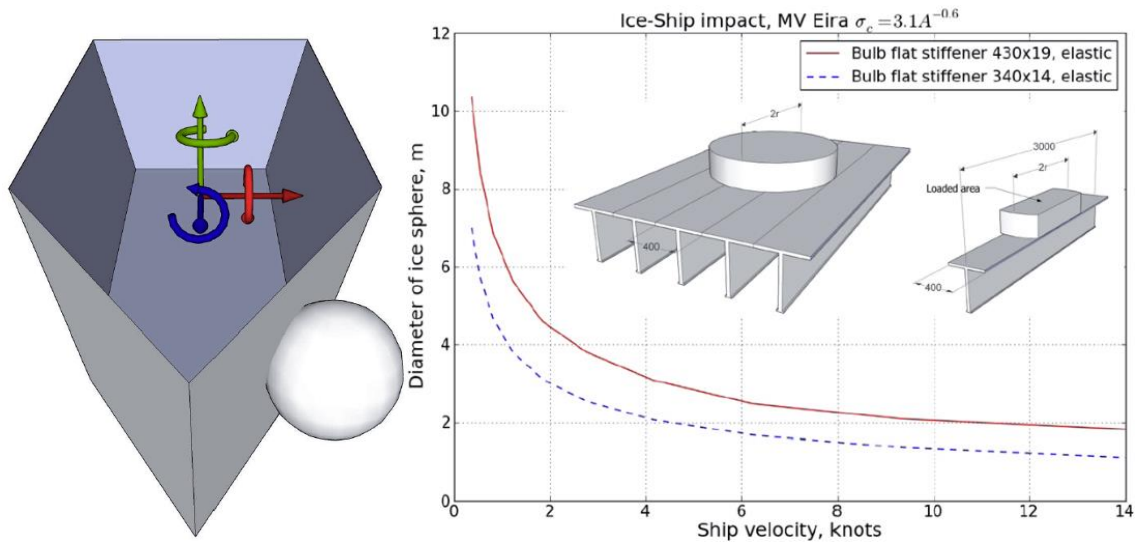


Figure 3-13: Safe speed assessment concept by Kolari & Kurkela (2012)

VARD Study for Transport Canada

VARD Marine with support from ABS carried out a project for Transport Canada in 2015 that explored how speed could be incorporated into current and future ice damage prevention/risk mitigation methods, including Transport Canada’s existing ice damage prevention system, the Arctic Ice Regime Shipping System (AIRSS). The objective of the project was improved safety and operability of shipping in the Arctic by applying technical analysis tools as input towards the further development and refinement of the AIRSS system (VARD, 2015). An ice load model, Direct Design for Polar Ships (DDePS), was used to explore the sensitivity of results to various parameters and assumptions including hull form, ice class, ship mass-to-ice mass ratios, and ice strength terms. This model is further explained in Chapter 0.

An example set of results which demonstrate the influence of ice strength and ice class on the technical safe speed curves for a 100,000 ton icebreaking ship are shown in Figure 3-14. Three sets of ice strength properties were used, and categorized as “weak”, “medium” and “strong”. The “strong” ice strength parameters correspond with the assumed parameters for “IACS PC 1” (i.e. multi-year ice), while the weak ice used the crushing strength for “IACS PC 7” and a lower flexural strength, typical of first-year sea ice. The superimposed design points represent the speed-thickness combination assumed in each Polar UR class factor. In this example the sensitivities to ice strength and the ship’s ice class are shown to be fairly significant.

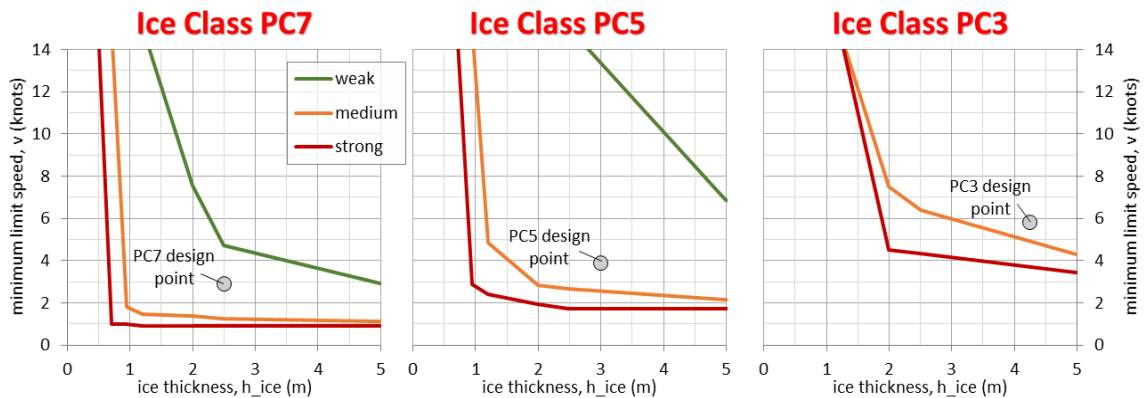


Figure 3-14: Example safe speed results demonstrating the sensitivities to ice strength and ice class [from VARD (2015)]

ABS Study on USCG WMSL Class Cutters

In 2015, ABS carried out an engineering evaluation of the USCG WMSL Class National Security Cutter’s structural capacity for operations in ice covered waters (ABS, 2015). Some results of the study were published in a technical paper by DeBord et al. (2015). State-of-the-art analytical and numerical methodologies of ship-ice interaction, collision mechanics, and structural response were exercised to develop estimates of the ship’s operational capabilities and limitations in various ice conditions and considering

different tolerance levels for structural damage. The work involved the advancement of key elements such as mechanics of “thin ice” and structural compliance which strongly influence the operational limits for this class of vessel. It was recognized that traditional ice-ship interaction models are based on several assumptions which are valid for heavy ice class hulls; structures are considered rigid and the ‘design’ ice is usually assumed to be thick and strong. However when analyzing lighter ship structures, attention must be given to aspects such as: structural indentation energy, variable floe sizes, rate effects on ice flexural failure modes, structural steel strain-rate sensitivities, dynamic moving ice load actions, and rupture.

The assessment included an extensive analysis of the bow structural arrangement using plastic limit state capacity equations and a nonlinear explicit finite element analysis procedure. Figure 3-15 is one example numerical simulation of the ice indentation process considering a deformable structural grillage. The results were used to obtain relationships between ice indentation, impact force, and structural deformation that could be used to estimate the relative energies expended into ice crushing and structural plastic damage.

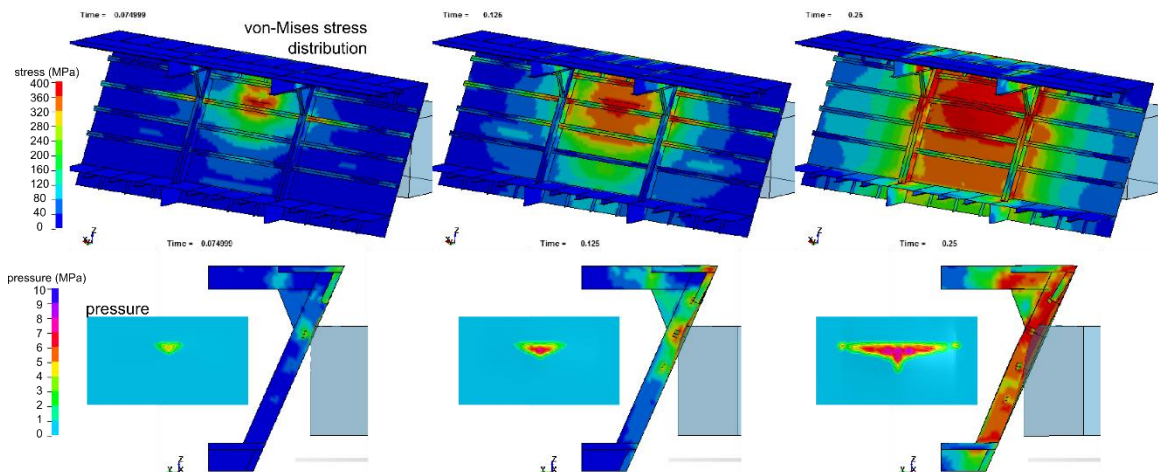


Figure 3-15: Numerical simulation considering deformable structure and ice [from (ABS, 2015)]

The above figure shows an ice edge crushing into the structure at a normal speed of 1.5 m/s. Cross-sectional views show the relative deformation of the structure and ice. Contour plots represent the von-Mises stress distributions in the plating and frames at different moments during the indentation process. The development of plastic regions are evident (shown in red) as the indentation progresses, even early in the simulation.

The results of the analysis were used to establish limiting conditions or ‘technical safe speeds’ for the ship in different ice regimes. Limit conditions were determined by comparing loading terms (force, pressure, line load, etc.) against different representations of capacity or strength, i.e. limit states. The loading terms were produced by a model of ship-ice interaction (*DDePS*) and the capacity was represented in several different ways; from a simple model of the notional elastic limit or plastic hinge formation to more complicated models that take into account detailed structural scantlings and large deformation response mechanisms (such as the model described above).

Figure 3-16 presents example results for the ship impacting 10 m diameter ice floes (often referred to as ‘cake ice’). Two different speed curves are specified. The more restrictive curve (blue) represents the plastic limit of the structure, where there is no observable damage. The red dashed curve utilized the results of the numerical analysis to estimate speeds that would plastically deform the structure up to 5 cm. The results suggest that operational speeds in cake ice of thicknesses greater than 25 cm (termed ‘grey ice’) would have to be kept very low (under 5 knots) if no plastic damage was tolerable. However, the results also provide insight to the potential consequences of operating more aggressively. In certain operational situations such as search and rescue or emergency

response, tolerance for relatively minor plastic damage can add considerably to the ability to move in marginal ice.

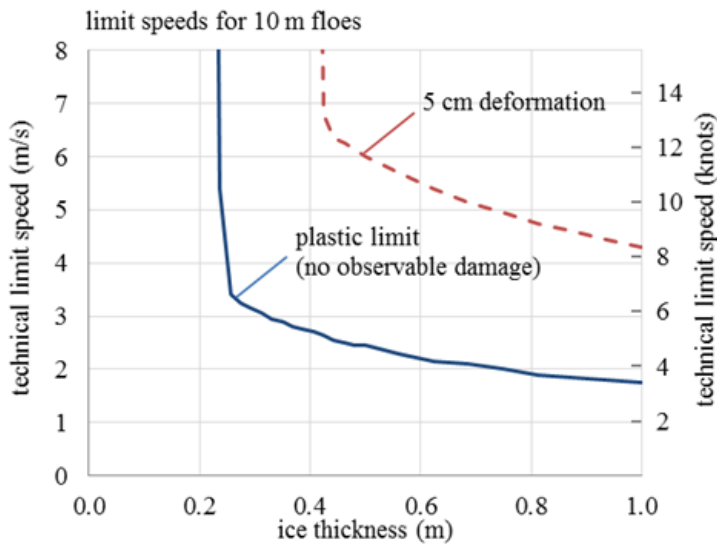


Figure 3-16: Technical safe speeds for the USCG WMSL Class cutter impacting ‘cake’ ice floes

DRDC Study on Ice Impact Capability of a Notional Destroyer

In a parallel effort to the USCG study described above, Daley (2015) exercised a similar methodology to estimate operational limitations for a non-ice strengthened notional destroyer in ice conditions. The ship is a concept warship and features a fine open water hull form and relatively light local structures as shown in Figure 3-17.

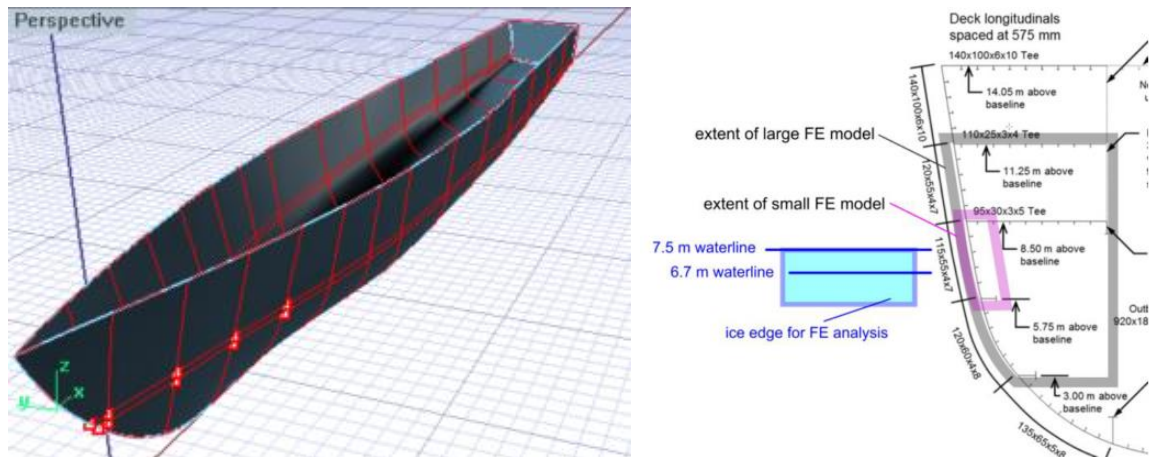


Figure 3-17: DRDC Notional Destroyer

DDePS calculations and numerical simulations of ice structure interaction were carried out to determine the effects of ice impacts for a variety of collisions cases. Example screenshots from the numerical simulations are presented in Figure 3-18. These were used to estimate the role of structural compliance in the ice crushing process. A variety of load cases were modeled numerically including framing, plating, web frame, and various moving load scenarios. This effort demonstrated a novel approach to model the structural response to ice loads.

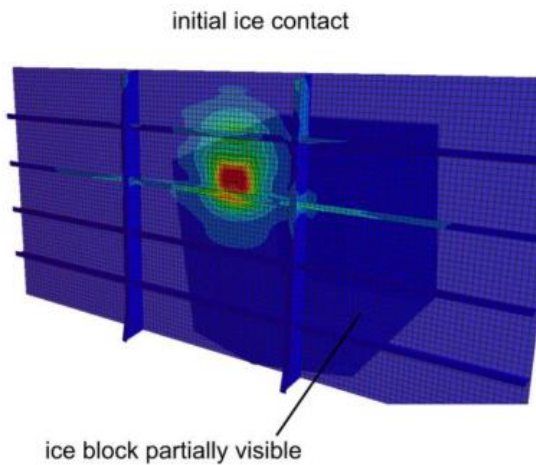


Figure 3-18: Numerical simulations of ice-structure interaction [from Daley (2015)]

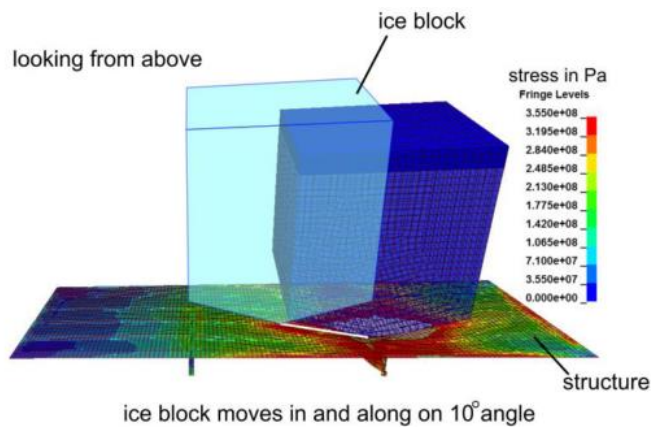


Figure 3-19: Numerical simulations of ice-structure interaction [from Daley (2015)]

An excerpt of the final results are plotted in Figure 3-20. Each curve corresponds to the ship speed that would bring the structure to permanent deformations up to 10cm. The study was used to demonstrate that this arrangement has structural plastic reserve and if employed cautiously, would allow the ship to impact moderate ice with a minor damage consequence.

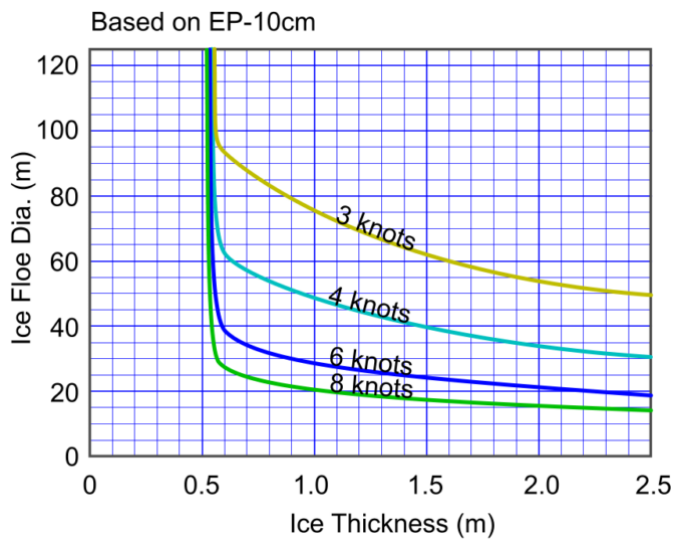


Figure 3-20: Limit speeds corresponding to 10cm permanent deformations [Daley (2015)]

4. Technical Methodology for Defining Safe Speeds in Ice

This Chapter outlines the detailed technical background of a proposed ship-specific analysis method that links a ship's actual structural capacity to ice loads that arise from different operational impact scenarios. Chapter 3 described several existing approaches which use varying ice load models and structural response criteria. The mathematical model derived here builds on these similar approaches. The methodology is principally comprised of four building blocks highlighted in Figure 4-1. First, an interaction scenario is identified and selected to form the core ice impact model. Next the mechanics of the ship-ice collision process are solved. This requires an implementation of ice strength models for both ice crushing and flexural failure modes. Finally, structural strength models are selected as limit conditions to determine technical limit speed curves.

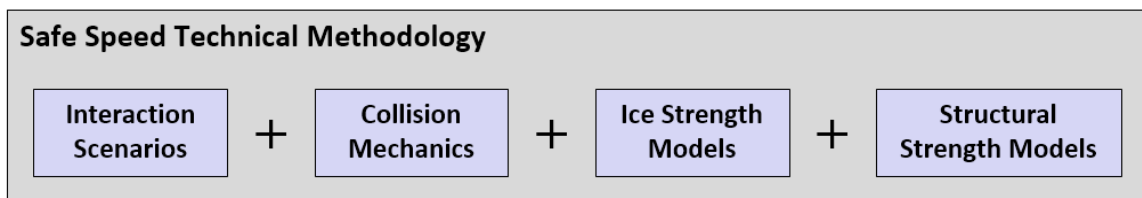


Figure 4-1: Building blocks of a safe speed technical methodology

The mathematical model is implemented into an updated version of the ice load software tool, *Direct Design for Polar Ship (DDePS)*, now called *DDePS_2a_Safe_Check* (latest version v3.4). This software tool allows a user to compute ice load parameters, explore damage estimates and develop technical limit speed envelope curves based on deterministic impact scenarios for a specific ship. It builds upon the original *DDePS Case 2a* (glancing impact with a wedge edge) by incorporating a number of technical elements and user features combined with various structural limit checks.

4.1. DDePS

Direct Design for Polar Ships (DDePS) is a Microsoft Excel® based spreadsheet tool capable of modeling a large set of ship-ice interaction scenarios. The impact models, described in several technical reports by BMT Fleet Technology and ABS (Kendrick & Daley, 2006a, 2006b, 2009; Daley & Liu, 2009) are based on the same overall methodology found in the IACS Polar Class Unified Requirements, but consider a wide range of scenarios, including infinite and finite ice floes. 25 total cases are available, each with as many as 25 user input variables. For the mathematical model described in this Chapter, *Case 2a* is the selected scenario. Figure 4-2 shows a list of the input variables that are used in a typical calculation and the output parameters that a user would obtain. A complete list of available *DDePS* interaction scenarios are provided in Figure 4-3.

Inputs			
Ship Particulars	Hull and Structural	Ice Parameters	Collision Conditions
<ul style="list-style-type: none"> • Length (L) • Beam (B) • Draft (T) • Block coefficient (C_B) • Displacement (M) • etc. 	<ul style="list-style-type: none"> • Impact locations • Hull angles • Plating and framing dimensions • Spacing (s) • Span (a) 	<ul style="list-style-type: none"> • Floe size • Thickness • Strength (flexural and crushing) • Edge angle • Failure models 	<ul style="list-style-type: none"> • Impact speeds (forward, sway, yaw, etc.) • Orientation • Impact location
Outputs			
Popov Collision Terms	Ice Load Parameters	Structural Checks	
<ul style="list-style-type: none"> • Directional cosines • Added mass terms • Gyration terms • Effective collision mass and energies • Impulse 	<ul style="list-style-type: none"> • Ice indentation • Normal force (F) • Pressure (p) • Load height (b) • Load width (w) • Line load (Q) 	<ul style="list-style-type: none"> • Elasto-plastic (onset of minor deformations) • Overload scenarios (large deformations) 	

Figure 4-2: Typical inputs and outputs for the mathematical model

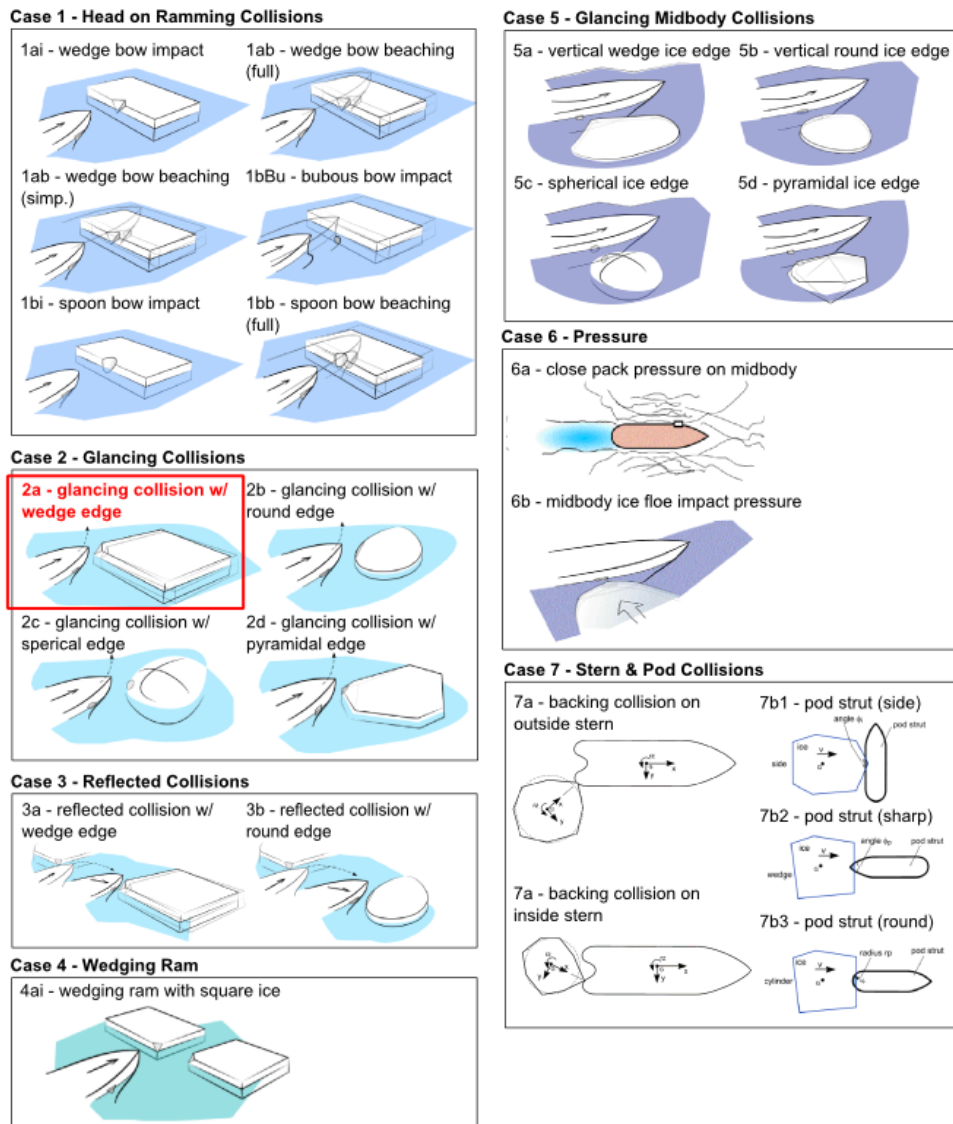


Figure 4-3: DDePS collision scenarios

4.2. Case 2a Interaction Scenario

For the purposes of evaluating technical safe speeds for ships in ice, *DDePS Case 2a* - glancing collision with a wedge-shaped ice edge on the bow shoulder - is a reasonable impact scenario to form the core mathematical model. A simplified version of the bow glancing scenario with the edge of a thick level ice sheet (original Case 2a), was selected for the IACS Polar Class Unified Requirements design ice load model (Daley, 2000). In

the rules, the ice is assumed infinitely large with strength and thickness terms fixed within Class Factors for each Polar Class notation. In the model presented here, ice can be treated as finite sized floes, allowing for investigation of pack ice speed limitations for ships. Figure 4-4 is a sketch of the assumed scenario adopted for the mathematical model.

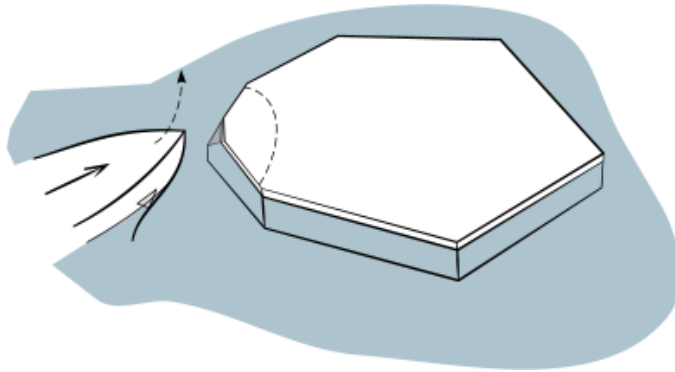


Figure 4-4: Ship-ice collision scenario

The total force during the impact event is limited by one of two limit conditions. When the ship impacts an ice feature, the force increases as the hull crushes into the ice. The ice indentation will cease if either the ship runs out of energy (in other words – relative normal speed between the ice and ship becomes zero) or the downward component of the force causes the ice to fail in flexure. The maximum structural impact force is determined either by a ‘momentum limit’ or by a ‘flexural failure limit’. Therefore, two models are required to determine the impact force: a crushing impact force model and a flexural force limit model. The following sections describe the detailed derivation of the ice impact model, ice crushing parameters, and flexural failure models.

4.3. Impact Model and Collision Mechanics

The mathematical model computes ice forces and ship responses for a glancing collision with an ice edge (*DDePS Case 2a*). Both finite sized and infinite floes (level ice

sheet) may be considered. The core method originates from Popov (1967), with an update by Daley (1999). Most earlier applications of the Popov model adopted the Kurdyumov-Khesin hydrodynamic ice crushing model to resolve the local contact pressure (Kurdyumov & Khesin, 1976a). The Khesin model is rate sensitive and can only be solved by numerical integration. The updated model by Daley uses a simple pressure-area relationship to resolve the local contact pressure and has a closed-form solution. The update makes it possible, and fairly simple, to implement the calculation in a spreadsheet. The model assumes that all motions are the result of an impulse along the normal to the shell at the collision point. Currently, no sliding friction, hull curvature, or buoyancy forces are considered in the collision mechanics solution. The only hydrodynamic effect considered is the added mass of the surrounding water. These assumptions are reasonable for single quick transient ship-ice impact situations.

The six motion equations for a general rigid body in 3D space can be converted into one motion equation along the normal of the contact surface;

$$F_n = M_e \cdot \ddot{\zeta}_n \quad (2)$$

Where,

ζ_n is the ice indentation from the initial contact point normal to the shell

$\ddot{\zeta}_n$ is net normal acceleration at the point of contact (i.e., the second time derivative of the ice indentation)

M_e is the effective mass of the ship-ice impact system.

$$M_e = \frac{1}{\frac{1}{M_{e_{ship}}} + \frac{1}{M_{e_{ice}}}} \quad (3)$$

$M_{e_{ship}}$ and $M_{e_{ice}}$ are the effective mass of the ship and ice respectively at the contact point.

These terms are obtained from equations (4) and (5). The full derivations, variable definitions and assumptions (with respect to added mass and mass radii of gyration terms) are provided in Appendix A.

$$M_{e_{ship}} = \frac{1}{\frac{l^2}{M_{sx}} + \frac{m^2}{M_{sy}} + \frac{n^2}{M_{sz}} + \frac{\lambda^2}{I_{sx}} + \frac{\mu^2}{I_{sy}} + \frac{v^2}{I_{sz}}} \quad (4)$$

$$M_{e_{ice}} = \frac{1}{\frac{li^2}{M_{ix}} + \frac{mi^2}{M_{iy}} + \frac{ni^2}{M_{iz}} + \frac{\lambda i^2}{I_{ix}} + \frac{\mu i^2}{I_{iy}} + \frac{v i^2}{I_{iz}}} \quad (5)$$

The various mass terms refer to the various degrees of freedom. For example, M_{sx} is the ship's mass plus added mass in surge, and I_{iy} is the mass moment of inertia of the ice floe in pitch. The ice floe is assumed to be oriented normal to the point of contact, somewhat simplifying the analysis, as shown in Figure 4-5. For the purposes of computing the mass and moments of inertia, the ice floe is idealized as a square with uniform thickness. The wedge shape at the impact point is simply used for the contact model.

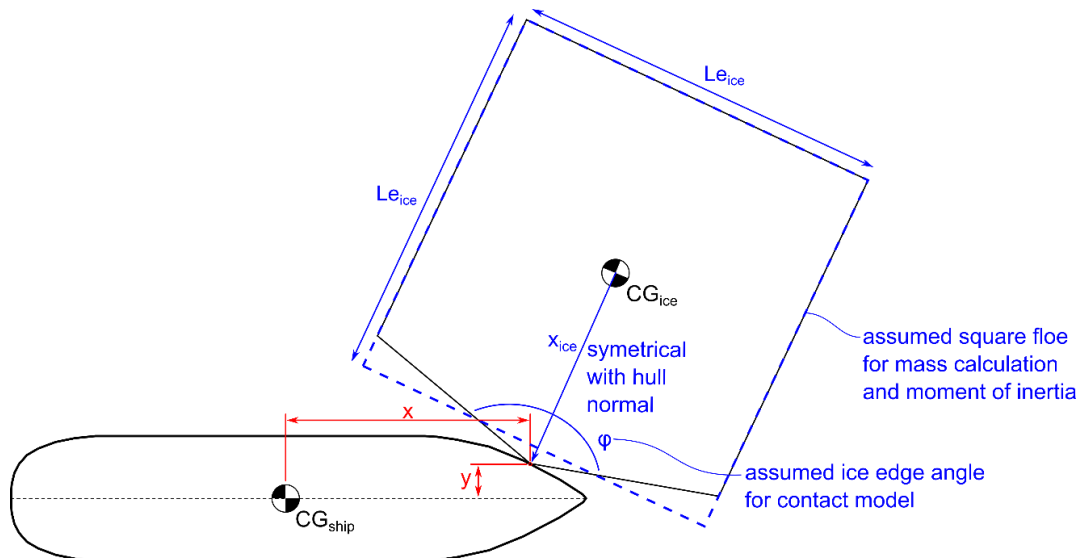


Figure 4-5: Diagram of ship-ice impact scenario for the mathematical model

The situation is reduced to one in which one body is initially moving (the impacting body - ship) and the other is at rest (the impacted body - ice). The solution is found by equating the available (effective) kinetic energy with the energy expended in ice crushing:

$$KE_e = IE_i \quad (6)$$

The left side of equation (6) - kinetic energy, KE_e - is calculated using the following equation.

$$KE_e = \frac{1}{2} M_e V_n^2 \quad (7)$$

The available kinetic energy is the difference between the initial kinetic energy of the impacting body and the total kinetic energy of both bodies at the point of maximum force. If the impacted body has finite mass it will gain kinetic energy. Only in the case of a direct (normal) collision involving one infinite (or very large) mass will the effective kinetic energy be the same as the total kinetic energy. In such a case all motion will cease at the time of maximum force. The right side of the equation - indentation energy, IE_i - is the integral of the normal indentation force F_n over the depth of crushing indentation ζ_n ;

$$IE_i = \int_0^{\zeta_c} F_n d\zeta_n \quad (8)$$

4.4. Ice Crushing Forces Considering Rigid Structures

The solution of the energy equations requires that force is described as a function of indentation. By using an ice ‘process’ pressure-area relationship, it is possible to derive a force-indentation relationship. This assumption means that ice force will depend only on indentation, and the maximum force occurs at the time of maximum indentation. The collision geometry is the ice-structure overlap geometry which describes the development

of nominal contact area, A . The average pressure P_{av} is related to the nominal contact area A as;

$$P_{av} = P_o A^{ex} \quad (9)$$

The above equation is a ‘process’ pressure area model. It describes the development of the average contact pressure (and its nominal contact area) throughout the ice indentation process. P_o is the average pressure at 1 m² and ex is a constant which defines the logarithmic slope of the pressure-area model. These terms are used to characterize the ice crushing strength and are determined empirically (see Chapter 5). Another form of a pressure-area relationship is a ‘spatial’ pressure-area model which describes the spatial variation of pressure distributed over a contact area at an instantaneous point in time. This type of model is not explicitly used in this methodology.

The ice force is related to the nominal contact area. The relationship between the indentation and nominal contact area can be found for each specific contact situation. For the case of a general ice wedge normal to the hull, as shown in Figure 4-6, the contact area can be expressed as;

$$A = \zeta_n^2 \left(\frac{\tan(\phi/2)}{\sin \beta' \cos^2 \beta'} \right) \quad (10)$$

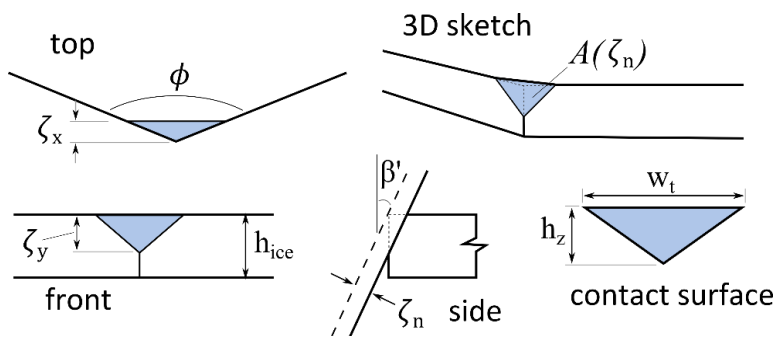


Figure 4-6: General wedge edge interaction geometry

The total normal force can then be expressed as;

$$F_n = P_{av} A = P_o A^{1+ex} \quad (11)$$

Combining equations (10) and (11), the impact force can be stated as;

$$F_n = P_o \zeta_n^{2+2ex} \left(\frac{\tan(\phi/2)}{\sin \beta' \cos^2 \beta'} \right)^{1+ex} \quad (12)$$

After grouping shape terms, the normal force is expressed as;

$$F_n = P_o f_a \zeta_n^{f_x-1} \quad (13)$$

Where the shape parameters, f_x and f_a , are as follows;

$$f_x = (3 + 2 ex) \quad (14)$$

$$f_a = \left(\frac{\tan(\phi/2)}{\sin(\beta') \cos^2(\beta')} \right)^{1+ex} \quad (15)$$

These parameters are only valid for the contact shape shown in Figure 4-6. The indentation energy can be obtained by integrating the force over the depth of normal indentation;

$$IE_i = \int_0^{\zeta_c} F_n d\delta_n = \frac{P_o}{3 + 2ex} \left(\frac{\tan(\phi/2)}{\sin \beta' \cos^2 \beta'} \right)^{1+ex} \zeta_n^{3+2ex} \quad (16)$$

Finally, the indentation energy can be stated as;

$$IE_i = \frac{P_o}{f_x} f_a \zeta_n^{f_x} \quad (17)$$

And by equating the ice indentation energy to the effective kinetic energy, the normal indentation ζ_n (i.e. ice indentation) can be solved;

$$\zeta_n = \left(\frac{KE_e \cdot f_x}{P_o \cdot f_a} \right)^{1/f_x} \quad (18)$$

The width and height of the nominal contact area can be represented as functions of ice indentation as shown in equations (19) and (20) and illustrated in Figure 4-6.

$$W_z = \frac{2 \zeta_n \tan(\phi/2)}{\cos(\beta')} \quad (19)$$

$$H_z = \frac{\zeta_n}{\sin(\beta') \cos(\beta')} \quad (20)$$

In *DDePS* and the Polar Rules design ice load model, a simple patch translation is preformed to convert the triangular load patch (caused by the geometric ship-ice overlap) to a rectangular load patch that is more applicable for structural analysis. The rectangular patch is then further reduced, maintaining a constant aspect ratio, to account for load concentration as ice edges spill off. This is illustrated in Figure 4-7 and dimensions for the final load patch width w and height b are derived in equations (21) through (24).

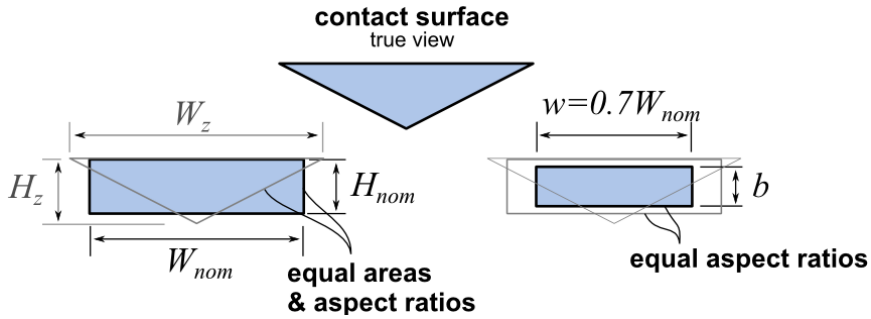


Figure 4-7: Translation and reduction of true contact surface to rectangular patch load

$$AR = W_z/H_z = W_{nom}/H_{nom} = 2 \tan(\phi/2) \sin(\beta') \quad (21)$$

$$W_{nom} = W_z/\sqrt{2} \quad (22)$$

$$w = 0.7 \cdot W_{nom} \quad (23)$$

$$b = w/AR \quad (24)$$

4.4.1. Modification for Steep Frame Angles

For interactions with thin ice at locations with steep frame angles (i.e. low β') the vertical component of the indentation depth may exceed the thickness of the ice sheet. This situation tends to arise when the crushing strength of the ice is weak and the frame angle

is not large enough to produce an effective downward force to break the ice in flexure. To account for through-thickness indentation during the contact process, a correction to the contact area is implemented into the mathematical model to treat the contact as a trapezoidal shape. The correction is sketched in Figure 4-8 and its algebraic derivation is provided in this section.

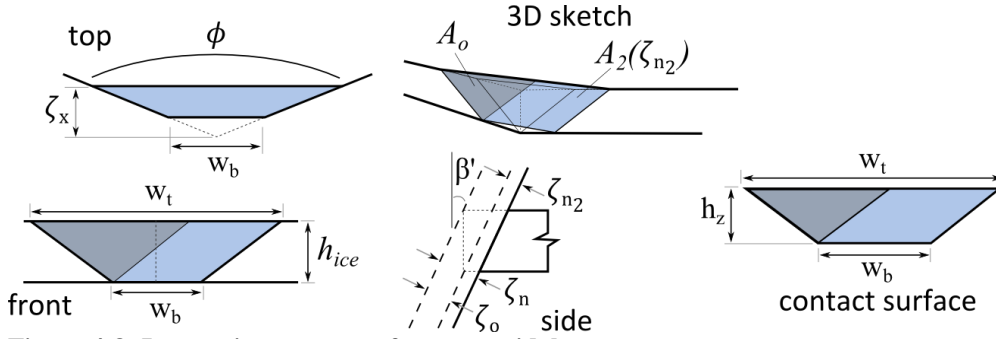


Figure 4-8: Interaction geometry for trapezoidal contact areas

The indentation depth for the maximum triangular contact area is taken as:

$$\zeta_o = h_{ice} \sin \beta' \quad (25)$$

Following equation (10), that contact area at ζ_o is simply:

$$A_o = \frac{\zeta_o^2 \tan(\phi/2)}{\sin \beta' \cos^2 \beta'} \quad (26)$$

And the indentation energy required to crush the ice to a depth of ζ_o is:

$$IE_o = \frac{P_o}{f_x} f_a \zeta_o^{f_x} \quad (27)$$

If the ship's available effective kinetic energy is greater than the indentation energy required to crush the ice to a depth of ζ_o an additional contact area, A_2 , is computed as a function of the continued indentation, ζ_{n2} .

$$A_2(\zeta_{n2}) = W_b \cdot H \quad (28)$$

Where,

$$H = \frac{h_{ice}}{\cos \beta'}, \quad W_b = \frac{2 \zeta_{n_2} \tan(\phi/2)}{\cos \beta'} \quad (29)$$

A_2 can be expressed and simplified as:

$$A_2(\zeta_{n_2}) = \frac{2 \zeta_{n_2} \tan\left(\frac{\phi}{2}\right) h_{ice}}{\cos^2 \beta'} = C_t \zeta_{n_2} \quad (30)$$

Where,

$$C_t = \frac{2 \tan\left(\frac{\phi}{2}\right) h_{ice}}{\cos^2 \beta'} \quad (31)$$

Therefore the total area of the trapezoidal contact area can be expressed as a function of the continued indentation beyond ζ_o .

$$A_{trap}(\zeta_{n_2}) = A_o + A_2(\zeta_{n_2}) = A_o + C_t \zeta_{n_2} \quad (32)$$

Recalling equation (11) and the assumed process pressure-area relationship, the normal force for a given indentation depth over the trapezoidal area is:

$$F_n = P_{av} A_{trap}(\zeta_{n_2}) = P_o (A_o + C_t \zeta_{n_2})^{1+ex} \quad (33)$$

The ice indentation energy in the trapezoidal domain, IE_{i2} , can be obtained by integrating the force from equation (33) over the depth of normal penetration beyond ζ_o .

$$\begin{aligned} IE_{i2} &= \int_0^{\zeta_{n_2}} F_n d\delta_n = \int_0^{\zeta_{n_2}} P_o (A_o + C_t \zeta_{n_2})^{1+ex} d\zeta_{n_2} \\ &= P_o \frac{(A_o + C_t \zeta_{n_2})^{2+ex}}{C_t (2+ex)} \Bigg|_0^{\zeta_{n_2}} \end{aligned} \quad (34)$$

This reduces to:

$$IE_{i2} = \frac{P_o}{C_t (2 + ex)} \left[(A_o + C_t \zeta_{n2})^{2+ex} - (A_o)^{2+ex} \right] \quad (35)$$

By equating the ice indentation energy, IE_{i2} , to the available effective kinetic energy, KE_{e2} , the normal indentation beyond ζ_o , is determined by equation (36). This algebraically solvable two-step solution is easily implemented into the DDePS spreadsheet tool.

$$\zeta_{n2} = \frac{\left(\frac{KE_{e2} C_t (2 + ex)}{P_o} + A_o^{2+ex} \right)^{\frac{1}{2+ex}} - A_o}{C_t} \quad (36)$$

Where,

$$KE_{e2} = KE_e - IE_o \quad (37)$$

Finally the total normal indentation depth is taken as:

$$\zeta_c = \zeta_{n2} + \zeta_o \quad (38)$$

The dimensions of the true (idealized) trapezoidal contact area can be represented as functions of ice indentations as shown in equations (39) through (41)

$$W_{zt} = \frac{2 \zeta_c \tan(\phi/2)}{\cos(\beta')} \quad (39)$$

$$W_{zb} = \frac{2 \zeta_{n2} \tan(\phi/2)}{\cos(\beta')} \quad (40)$$

$$H_z = \frac{h_{ice}}{\cos(\beta')} \quad (41)$$

Figure 4-9 shows the effect of this correction on nominal contact area and normal force for a sample scenario (thin ice, 75 cm thick with $\beta' = 10^\circ$). As the indentation increases, the assumption of triangular contact area becomes invalid. If the trapezoidal shape correction is considered, the area growth becomes linear instead of quadratic. This results in a slower buildup of force (i.e. softer collision). It should be noted that the ice

flexural failure and momentum limits are not shown on these plots. In some cases, the force limiting mechanisms (which depend on thickness, floe size, ice strength, hull form and ship speed) will govern and this correction becomes irrelevant.

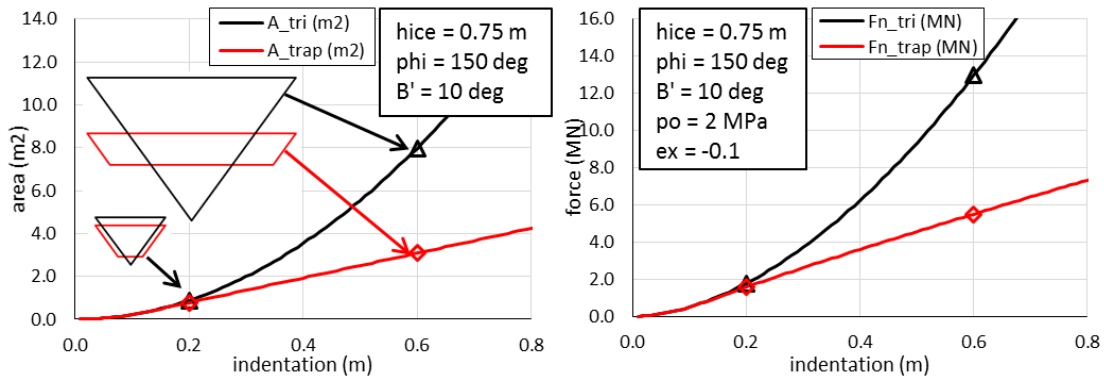


Figure 4-9: Contact area vs. indentation considering corrected trapezoidal contact shape

The patch shape is translated to a rectangle and reduced to account for load concentration and edge spalling while maintaining the same force. This process, similar to the triangular shape transformation describe earlier, is illustrated in Figure 4-10.

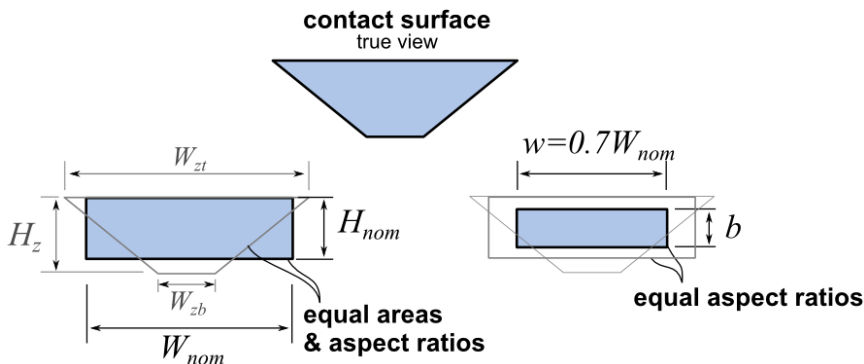


Figure 4-10: Translation and reduction of trapezoidal contact surface to rectangular patch load

The final load patch width w and height b are derived in equations (42) through (46).

$$AR = W_{zt}/H_z \quad (42)$$

$$A_z = \frac{1}{2}H_z(W_{zt} + W_{bt}) \quad (43)$$

$$W_{nom} = \sqrt{A_z \cdot AR} \quad (44)$$

$$w = 0.7 \cdot W_{nom} \quad (45)$$

$$b = w/AR \quad (46)$$

4.5. Ice Flexural Limit Model

In the IACS Polar Rules (2007) there is a simple quasi-static flexural limit force. The Polar Rules were formulated this way because they apply to the design cases considered in the rules, which is always very thick ice. In such cases the quasi-static assumptions are quite valid. The force normal to the ship's hull at the point of impact with the ice feature is limited to;

$$F_{n,UR} = \frac{1.2 \cdot \sigma_{flex} \cdot h_{ice}^2}{\sin(\beta')} \quad (47)$$

Where,

1.2 is a constant (assuming a wedge angle of 150°)

σ_{flex} is the flexural strength of the ice

h_{ice} is the ice thickness

β' is the angle measured from the vertical axis of the ship's hull at the point of impact (i.e. the normal frame angle)

Since the normal force is only a function of the flexural stress of the ice, we may say that the vertical force is simply:

$$F_v = 0.46 \cdot \sigma_{flex} \cdot h_{ice}^2 \cdot \phi \quad (48)$$

The Polar Rules flexural limit is not valid for cases of thinner ice and higher speeds. As a result, a new model is needed for the purposes of safe speed evaluations, especially for

light and non-ice class ships. The following section describes the development of a new velocity dependent ice flexural failure model.

4.5.1. Updated Flexural Failure Limit Model by Daley & Kendrick

For the more general cases of thinner ice and higher speeds, Daley and Kendrick (2011) first postulated an extension of the Polar Rules flexural force limit model to include horizontal stress, friction and dynamic effects. The authors considered the effect of

Horizontal Stress

Horizontal impact force causes compression stress in the ice feature. This compressive stress negates (or relieves) a portion of the tensile flexural stress in the top of the ice, thereby causing an apparent increase in the flexural capacity of the ice sheet. The horizontal stress σ_{comp} is given by:

$$\sigma_{comp} = F_h/A_{ice} \quad (49)$$

Where,

F_h is the horizontal force from both the normal and friction forces

A_{ice} is the cross sectional area of the ice feature

$A_{ice} = \phi l h_{ice}$ (see Figure 4-11)

ϕ is the ice edge angle

$l = 10h_{ice}$ is the length of the ice cusp (an assumption)

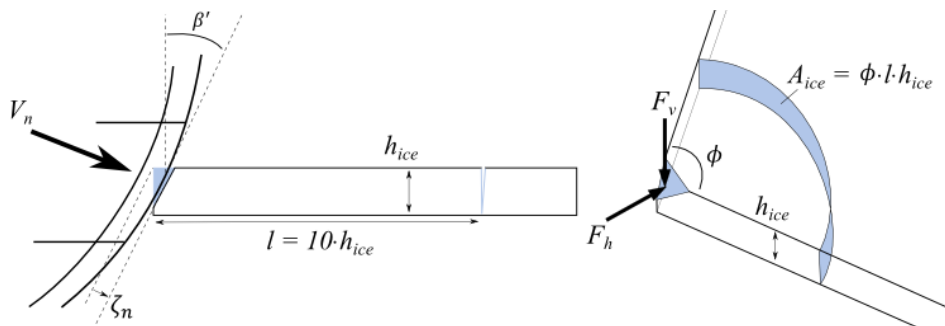


Figure 4-11: Geometry of flexural failure and ice cusp

Friction

Hull-ice friction is important because it affects the horizontal impact force, which influences the flexural force limit. Figure 4-12 shows that the horizontal component of both the normal and frictional forces are additive. The consideration of friction tends to increase the horizontal force (compressive stress) and decrease the vertical force (bending stress) in the ice during impact.

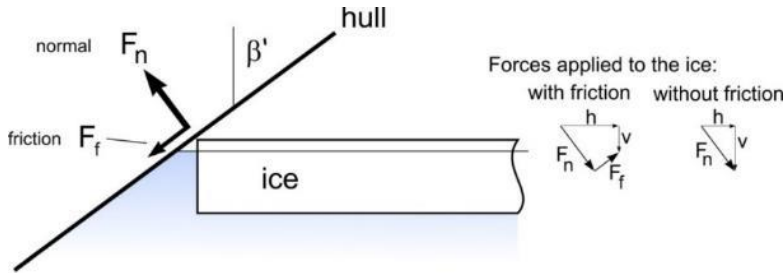


Figure 4-12: Hull-ice Contact showing Normal and Frictional Forces

When including friction, the horizontal force is;

$$F_h = F_n \cdot \cos(\beta') + \mu F_n \cdot \sin(\beta') \quad (50)$$

Where,

μ is the Coulomb friction factor

When including friction, the vertical force is;

$$F_v = F_n \cdot \sin(\beta') - \mu F_n \cdot \cos(\beta') \quad (51)$$

Design Normal Force

The total stress in the ice is given by:

$$\sigma_{total} = \sigma_{bend} - \sigma_{comp} \quad (52)$$

From F_v and F_h above we get:

$$\sigma_{total} = \frac{F_n \cdot (\sin(\beta') - \mu \cos(\beta'))}{C h_{ice}^2 \phi} - \frac{F_n \cdot (\cos(\beta') + \mu \sin(\beta'))}{10 h_{ice}^2 \phi} \quad (53)$$

Solving for the normal force, and substituting σ_{flex} for σ_{total} to get the design normal force:

$$F_n = \frac{C \cdot \sigma_{flex} \cdot h_{ice}^2 \cdot \phi}{[\sin(\beta') - \mu \cos(\beta')] - C/10 \cdot [\cos(\beta') + \mu \sin(\beta')]} \quad (54)$$

This design equation should be approximately equivalent to Polar Rules equation. Using a wedge angle of 150 degrees, a friction factor of 0.1 and β' of 45 degrees, the value of C needed to make the formula equivalent to the Polar Rules is 0.39. So the Formula for normal quasi-static force including friction effects becomes:

$$F_n = \frac{0.39 \cdot \sigma_{flex} \cdot h_{ice}^2 \cdot \phi}{[\sin(\beta') - \mu \cos(\beta')] - 0.039 \cdot [\cos(\beta') + \mu \sin(\beta')]} \quad (55)$$

Dynamic Effects

The final update by Daley and Kendrick (2011) was to include the dynamic support effects of water under the ice feature. While several authors (Colbourne, 1989; Valanto, 1996) have indicated a velocity dependence in the force required to break ice in bending, no analytical solutions were found to describe the phenomena. In response to the need for a practical analytical solution to this issue, a simple Froude scaling based method was developed. This method was offered as a starting point, with an understanding of the need for further improvement.

The dynamic effects of the water support arise from velocity dependent drag and acceleration dependent added mass; of which, the added mass effects are believed to dominate. Dynamic support effects are incorporated in the flexural force by scaling the design normal force (given above) with the ratio of Froude Numbers (raised to a power). A ‘quasi-static’ Froude Number is postulated, below which the “static” flexural case given above is used. For higher Froude numbers the flexural force is multiplied by a factor representing dynamic effects.

Previous experiments (Colbourne, 1989) suggest that the dynamic effects are related to Froude Number, a supposition that seems reasonable as Froude scaling will typically produce dynamic similitude. Further, Colbourne suggested that while the dynamic support increases with increasing Froude Number, the rate of change of this increase decreases with increasing Froude Number. Therefore, linear scaling based on some static case would not be appropriate. Considering this, the following approach was adopted:

$$F_{nd} = \frac{0.39 \cdot \sigma_{flex} \cdot h_{ice}^2 \cdot \phi \cdot Kd}{[\sin(\beta') - \mu \cos(\beta')] - 0.039 \cdot [\cos(\beta') + \mu \sin(\beta')]} \quad (56)$$

Where,

$$Kd = \left(\frac{FN}{FN_s} \right)^n \text{ or } 1 \quad \text{whichever is greatest} \quad (57)$$

F_n is the quasi-static normal force as given above

F_{nd} is the dynamic normal force

FN is the Froude Number for the dynamic case $FN = V_n / \sqrt{g \cdot h_{ice}}$

V_n is the normal speed of indentation $V_n = V_{ship} \sin(\alpha) \cos(\beta')$

g is acceleration due to gravity

h_{ice} is the ice thickness

$FN_s = V_{static} / \sqrt{g \cdot h_{ice}}$ is the Froude number for the static case (assume 0.1)

n is the scale factor modifying exponent (0.33 chosen here)

V_{static} is the maximum speed in the direction normal to the plane of impact with the ice feature at which the impact may be considered “static”. A static Froude number of 0.1 was chosen. This implies that the maximum speed at which an impact may be considered static, is dependent on ice thickness h_{ice} which is a reasonable assumption.

4.5.2. Updated Dynamic Effects based on work by Sazidy

Sazidy et al. (2014a; 2014b) studied the dynamic factors involved in the contact between a ship side and ice. Figure 4-13 illustrates the type of analysis that was used to study dynamic effects during flexural ice failure. The ice edge was modelled using LS-Dyna as a series of wedges supported by an elastic foundation as a proxy for water. The program was able to model the ice edge crushing and flexural response in a time-domain analysis that accounts for dynamic effects. A numerical approach was used to empirically arrive at equation (58), a new flexural failure model of vertical impact force for dynamic ice wedge breaking.

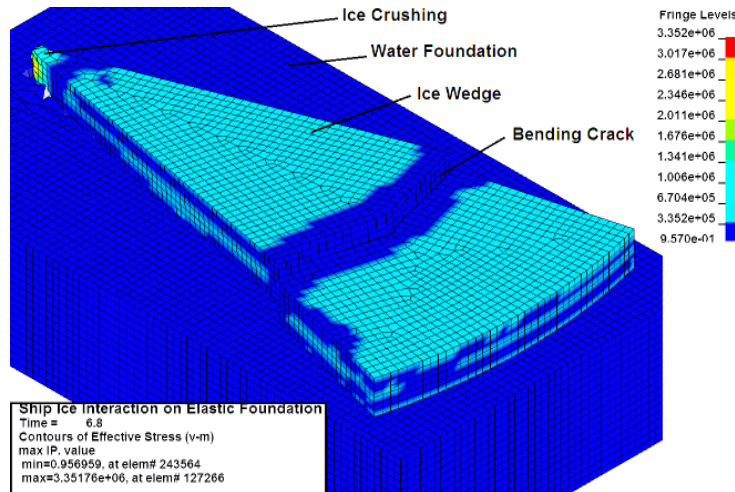


Figure 4-13: Simple ice wedge breaking pattern [Sazidy et al. (2014)]

$$F_{vd} = 0.29 n_w^{-0.3} \sigma_f h^2 \theta K_v \quad (58)$$

Where,

n_w is the number of wedges and

K_v is a dynamic factor defined as:

$$K_v = 1 + 2.57 \sin \alpha \cos \beta' (\theta/n_w)^{0.2} FN^{0.26} \quad (59)$$

The Froude Number (FN) is the same as defined in equation (57) and the normal impact force is expressed in the following form:

$$F_{nd} = \frac{F_{vd}}{\sin \beta'} \quad (60)$$

As described in section 3.3.3, Sazidy (2014) compared and calibrated his numerical analysis work to several available analytical and semi-empirical models. The equation for velocity dependent flexural failure was further cross-checked against full scale data with fairly good agreement. This analysis, however, did not originally take friction into account, although it did implicitly consider the horizontal stress. As a result, equation (56) and (60) are not directly comparable. The formulation can be adjusted to be compatible with equation (56) by making the following change.

$$F_{nd} = \frac{0.284 n_w^{-0.3} \sigma_f h^2 \theta K_v}{[\sin(\beta') - \mu \cos(\beta')] - 0.0284 \cdot [\cos(\beta') + \mu \sin(\beta')]} \quad (61)$$

The flexural ice failure models described in this section show an evolution from a simple static limit to complex dynamic limits. They are a function of many parameters. Figure 4-14 shows a simple comparison of the static (47) and dynamic (61) equations for a set of selected parameters (also listed in the figure). The mathematical model applied in the case studies in Chapters 7 and 8 utilize the dynamic model developed by Sazidy (2014) with the adjustment described in equation (61).

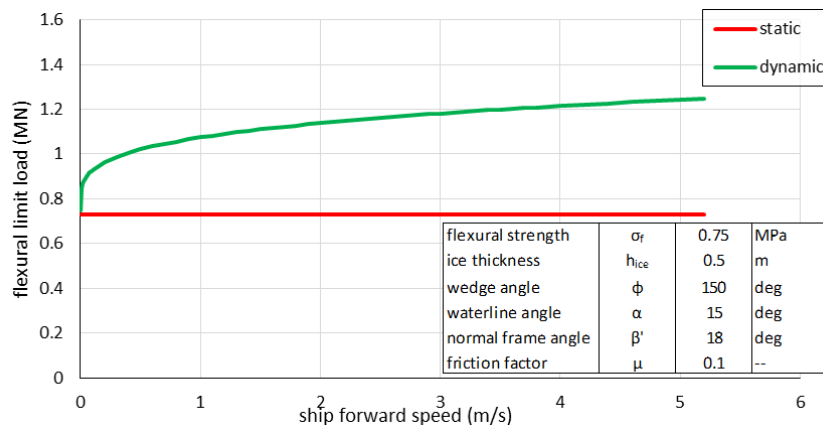


Figure 4-14: Comparison of static and dynamic flexural failure limits

4.6. Structural Limit States and Speed Check Algorithm

A variety of methods exist for establishing limiting conditions that can be used to determine technical safe speeds for ships in ice. In principle, each method compares a loading term against a representation of capacity or strength, i.e. a limit state. The loading term is produced by a mathematical model of ship-ice interaction, in this case DDePS following the derivations in the previous sections of this thesis. The model solves for ice load parameters as a function of many inputs describing an interaction scenario. The inputs are a combination of ship speed, impact location, ice thickness, floe size, and ice strength terms (flexural and crushing strength).

The capacity can be represented in several different ways; from complicated models that take into account detailed structural scantlings and response mechanisms, to simple criteria which anchor the limits on a notional design point. The selection of suitable limit states is a key area for debate with regard to safe speeds. *DDePS_2a_Safe_Check* offers three different criteria to assess structural capacity (i.e. limit states) against the applied ice load for a given scenario. Each of these methods are further described in the following sections.

1. Polar Class Design Limit Load Criteria
2. Direct Line Load Criteria
3. Large Deflection Criteria

4.6.1. Polar Class Design Limit Load Criteria

Perhaps the simplest representation of capacity, but perhaps more conservative, is the design ice load for a certain “reference” Polar ice class (if applicable). Instead of considering the structural capacity directly based on actual scantlings, limit speeds can be

established by comparing the loading terms against the design ice load of a selected Polar Class. This approach offers a surrogate to a detailed structural analysis but assumes the structure is built exactly to the design load (for the selected Polar Class) and the associated minimum requirements with no additional strengthening (i.e. no over design). In reality this is almost never the case. Due to practicalities of design, shipbuilding constraints, corrosion and abrasion allowances, etc. most designs inherently have some level of over design. For polar class ships (or ships with equivalent strengthening levels) the limit state can be expressed in terms of the design force for a certain “reference” polar ice class. Instead of considering the structural capacity directly, limits speeds are established when the loading term (Q_{load}) exceeds the design line load of a selected Polar Class (Q_{UR}).

$$v_{lim}(h) = v_i(Q_{load} > Q_{cap}) - \Delta v \quad (62)$$

Where,

$$Q_{cap} = Q_{UR} \quad (63)$$

In the algorithm, the load model is used to calculate the maximum design ice line load (from 4 bow locations) according to the specified Polar Class notation. The design point parameters for the specified polar class are assumed (infinite ice, V_{ship} , h_{ice} , P_o , and σ_f). The model is then reapplied with the user specified ice conditions and speed is incrementally increased until the limit condition is exceeded. A graphical representation of the process is shown in Figure 4-15.

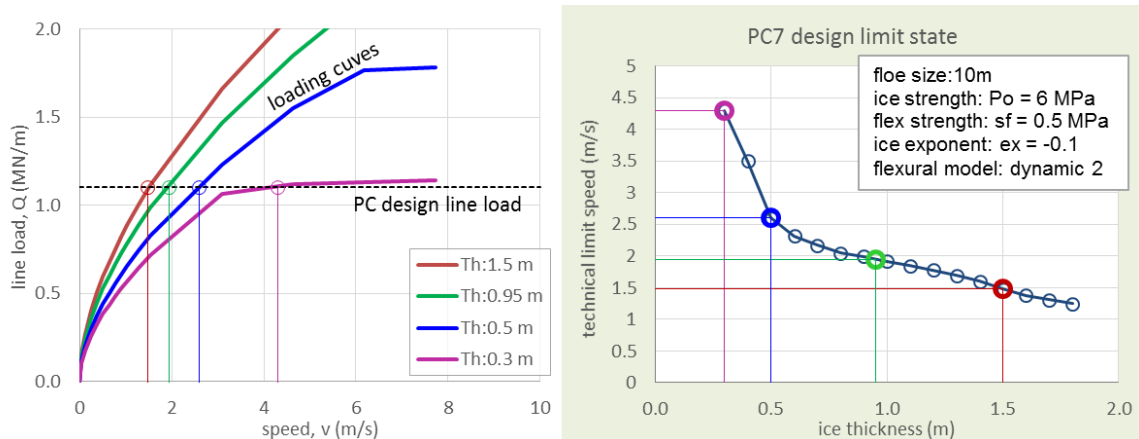


Figure 4-15: Description of PC design load criteria

4.6.2. Direct Line Load Criteria

Models which take into account the detailed structural scantlings can be applied to determine the direct capacity of the plating, a frame or grillage arrangement. For instance, the plastic limit state models which form the technical background behind in the IACS Polar Rules can be implemented as capacity equations for establishing technical safe speeds. This method was presented and applied in Dolny et. al (2013) and is implemented into *DDePS_2a_Safe_Check*. Limit speeds are established by incrementally increasing the speed until the loading term (Q_{load}) exceeds the structural capacity (Q_{cap}) for a given interaction scenario (speed, impact location, ice thickness or floe size, strength parameters, etc.). This limit condition is described by equation (64) and illustrated graphically in Figure 4-16.

$$v_{lim}(h) = v_i(Q_{load} > Q_{cap}) - \Delta v \quad (64)$$

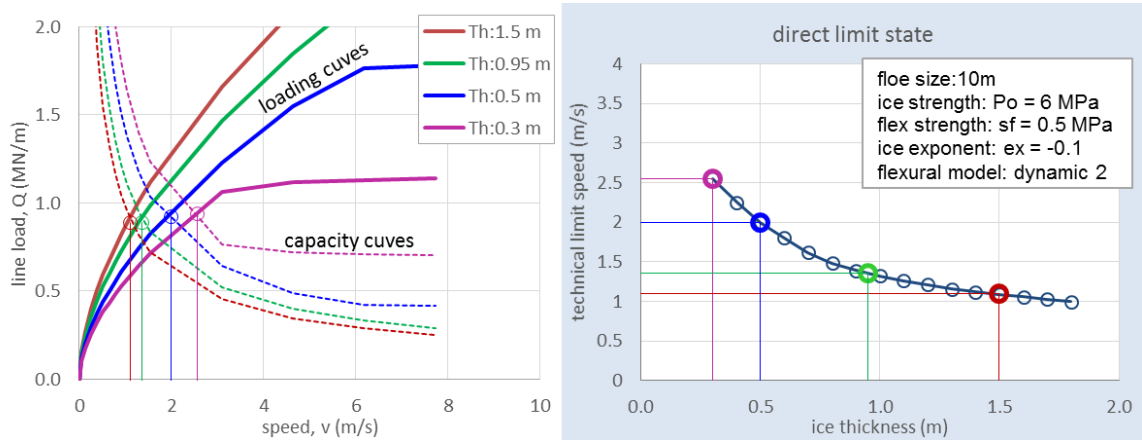


Figure 4-16: Description of direct limit load criteria

Q_{cap} is calculated from the equations (65) and (66), and is based on the technical background for the plastic structural limit states adopted by the IACS Polar Rules. These limit states define the point where denting begins to occur in a frame subjected to a patch load. Therefore, the speeds computed by this approach are set such that there will be no observable deformation of the hull. Several plastic limit mechanisms, expressed in terms of pressure and taking into account the actual structural dimensions, are considered. The capacity of a frame can be considered as the minimum of limit pressures for each mechanism.

$$p_{cap} = \min(p_1, p_2, \dots, p_n) \quad (65)$$

When combined with the ice load model, which requires the applied load height, the frame capacity can be expressed in terms of a line load capacity as shown in equation (66). Line load is used as the basis for comparison and establishing the technical safe speed limits because it is the closest parameter that relates to the load encountered by a single frame.

$$Q_{cap} = \frac{F_{cap}}{s} = p_{cap} \cdot b \quad (66)$$

The structural limit states adopted by the Polar Rules provide a set of analytical expressions for the capacity of primary stiffening members (Daley, 2002a, 2002b; Daley, Kendrick, & Appolonov, 2001; Kendrick & Daley, 2000). These models were derived on the basis of energy methods and make use of plastic limit analysis. They were validated against extensive numerical simulations and physical experiments. Conceptual sketches of the limit states are shown in Figure 4-17.

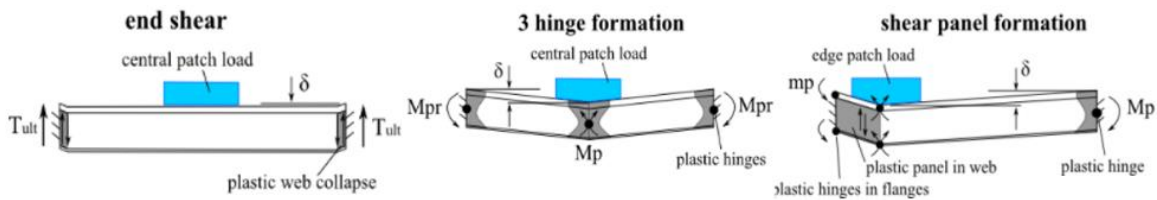


Figure 4-17: Structural limit states for frames subjected to lateral patch loads

The following sections present capacity equations, in terms of limit pressures, for transverse and longitudinal framing orientations. It should be understood that these notional “capacities” are in reality well below any ultimate strength due to strain hardening, membrane and many other effects. A robust structure can support 5-10 times the UR design load, as shown by extensive FE and experimental work (Daley & Hermanski, 2009; Kim et al., 2015; Manuel et al., 2013). A sketch of an ice load patch applied to transverse framing is provided in Figure 4-18.

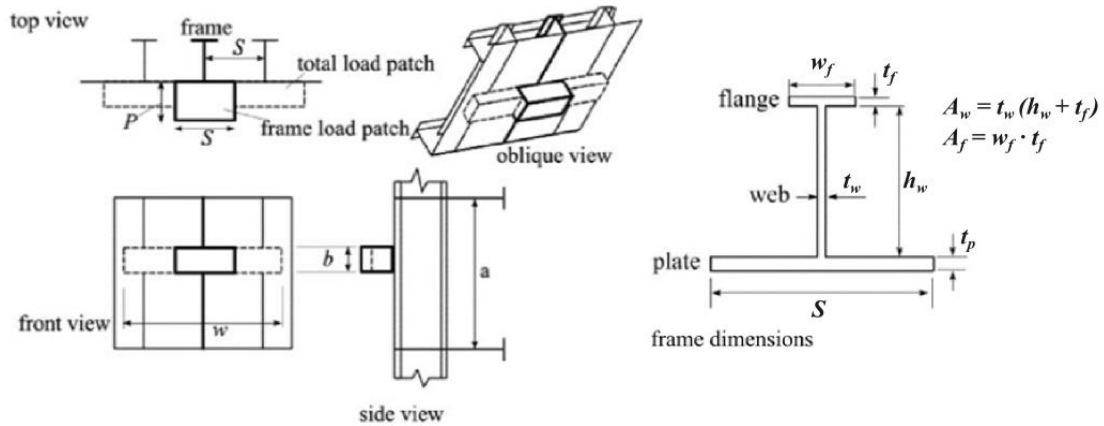


Figure 4-18: Sketch of ice load applied to transverse framing

Transverse framing

The limit state capacities used in the IACS Polar Rules are described below. The pure shear collapse limit in which a transverse frame will fail by shear at the supports due to a central load patch is shown in equation (67).

$$p_{lim, shear} = \frac{2 A_o \sigma_y}{b s \sqrt{3}} \quad (67)$$

Where,

A_s is the effective shear area of the frame [$A_s = (h_w + t_f) \cdot t_w$]

σ_y is the yield strength of the material

b is the load height

s is the frame spacing

Equations (68) through (70) consider pressure applied as a central load patch which causes the formation of three plastic hinges (one central and two end hinges) under bending. The frame is considered to have two fixed supports ($j = 2$). For case 1 (68), the total bending capacity is reduced based on a relatively simple quadratic shear-moment interaction.

$$p_{lim, c1} = \frac{1}{12 Z_{pns} + 1} \sigma_y Z_p \frac{4}{b s a \left(1 - \frac{b}{2a}\right)} \quad (68)$$

Where,

a is the frame span

Z_p is the effective plastic section modulus of the frame

$$Z_p = (t_f \cdot w_f) \cdot \left(\frac{t_f}{2} + h_w + \frac{t_p}{2} \right) + (t_w \cdot h_w) \cdot \left(\frac{h_w}{2} + \frac{t_p}{2} \right)$$

Z_{pns} is normalized plastic section modulus, squared, described in (69)

$$Z_{pns} = \left[\frac{Z_p}{A_o a \left(1 - \frac{b}{2a} \right)} \right]^2 \quad (69)$$

Case 2 (70) includes a modification in which the bending capacity is reduced only by the loss of web capacity.

$$p_{lim,c2} = \frac{[2 - kw + kw \sqrt{1 - 48 Z_{pns} (1 - kw)}]}{12 Z_{pns} kw^2 + 1} \sigma_y Z_p \frac{4}{b s a \left(1 - \frac{b}{2a} \right)} \quad (70)$$

Where,

kw is the ratio of web section modulus to the total plastic section modulus

$$[kw = Z_w / Z_p]$$

$$Z_w \text{ is the web section modulus } [Z_w = (t_w \cdot h_w) \cdot \left(\frac{h_w}{2} + \frac{t_p}{2} \right)]$$

A fourth limit state (71) considers the case of an off-center (end case) or asymmetric load in which plastic hinges form in the flanges along with a shear panel in the web near the load and a large plastic hinge at the far end.

$$p_{lim,asy} = \left[\frac{A_w}{\sqrt{3}} + \frac{Z_p}{l} f_z \right] \frac{\sigma_y}{b s \left(1 - \frac{b}{2a} \right)} \quad (71)$$

The capacity of the transverse frame can be considered as the minimum of the four limit states provided above.

$$p_{cap} = \min(p_{lim,c1}, p_{lim,c2}, p_{lim,asy}, p_{lim,shear}) \quad (72)$$

Longitudinal Framing

The longitudinal framing limit states are based on the same principles as the transverse cases however the relative orientation of the load patch is simply rotated. The pure shear collapse limit in which a longitudinal frame will fail by shear at the supports due to a central and symmetrical load patch is shown in equation (73).

$$p_{lim,shear} = \frac{2 A_o \sigma_y}{w_{1L} b_{1L} \sqrt{3}} \quad (73)$$

For longitudinal frames, the effective load patch height is taken as:

$$b_{1L} = \min(b, s) \quad (74)$$

The effective load patch width is taken as:

$$w_{1L} = \min(w, a) \quad (75)$$

Equation (76) considers a central and symmetrical load patches which causes the formation of three plastic hinges (one central and two end hinges) under bending.

$$p_{lim,c1} = \frac{1 + \frac{j}{2} \sqrt{3(j^2 - 4)} Z_{pnsL} + 1}{3 j^2 Z_{pnsL} + 1} \sigma_y Z_p \frac{4}{w_{1L} b_{1L} a \left(1 - \frac{w_{1L}}{2a}\right)} \quad (76)$$

Where,

j is the number of fixed supports (in this thesis j is always assumed to be 2, considering two fixed supports)

Z_{pnsL} is defined as:

$$Z_{pnsL} = \left[\frac{Z_p}{A_o a \left(1 - \frac{w_{1L}}{2a}\right)} \right]^2 \quad (77)$$

The capacity of the longitudinal frame can be considered as the minimum of the two limit states provided above.

$$p_{cap} = \min(p_{lim,c1}, p_{lim,shear}) \quad (78)$$

Before carrying out a safe speed assessment using the direct line load criteria, an FE model should be used to verify the limit state formulations described by equations (66) through (78) for various load patch sizes and orientations. Examples of verification efforts are presented in the case studies in Section 7 and 8.

4.6.3. Large Deflection Criteria

Numerical simulations (e.g. nonlinear finite element analysis) can be used to develop more complex structural response functions that consider, for example, the effects of structural deformation energy and limit conditions beyond the notional plastic capacity of a frame (e.g. large denting or collapse behavior). These methods require quite specific information on the scantlings and arrangements and a fairly in-depth analysis to derive the response functions. *DDePS_2a_Safe_Check* has an option to deal with large deflection limits states but the user must define additional parameters after a dedicated numerical analysis of the representative structural arrangement. This approach was previously developed and applied in several existing studies highlighted in Section 3.3.3. It is described in detail in Section 6 and demonstrated in case studies in Sections 7 and 8.

When the structural indentation energy model is included in the collision model, the amount of structural deformation ζ_s (plastic + elastic) can be calculated for a given interaction scenario. Limits speeds are established when the structural indentation at the

given load exceeds the allowable deformation level ζ_{s_allow} set by the user. This limit condition is described by equation (79) and illustrated graphically in Figure 4-19.

$$v_{lim_defl}(h) = v_i(\zeta_s > \zeta_{s_allow}) - \Delta v \quad (79)$$

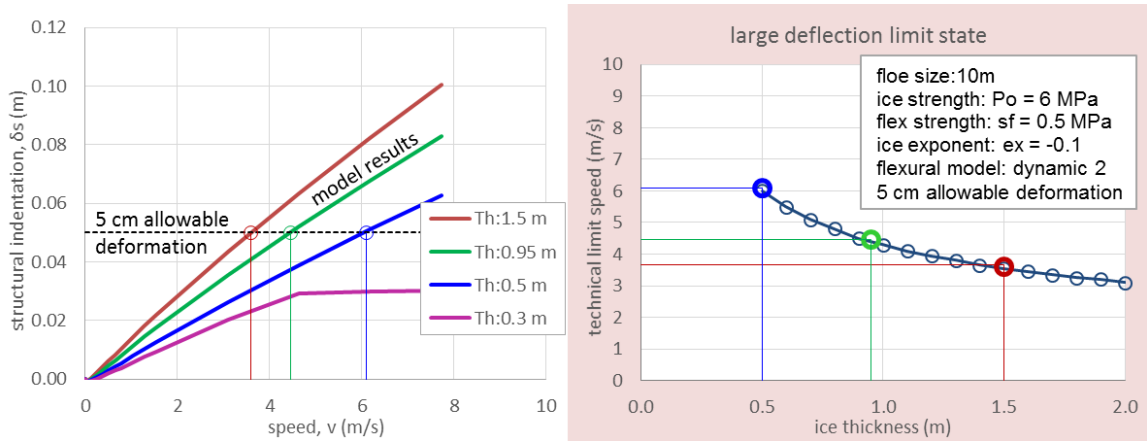


Figure 4-19: Description of large deflection criteria

5. Full Scale Data Comparison to the Ice Load Model

The validation of an analytical tool like DDePS presents an obvious challenge, especially for scenarios applicable to non-icebreaking hull forms. While conventional ice impact load data has been gathered from instrumented icebreakers and high ice class ships (i.e. icebreaking hull forms with strong local structures), no existing suitable validation data sets exist for light ice class or non-ice strengthened hulls in ice conditions. Furthermore, the majority of previous ice load measurement campaigns have generally targeted challenging ice conditions (i.e. thick first year ice, multi-year ice, high concentrations, etc.) to better understand the nature of extreme ice loads and the limits of vessel performance capabilities. Some notable examples of ice load measurement campaigns include:

- USCG Polar Sea (1980s)
- CCGS Louis St. Laurent (1990s)
- MS Kemira (1990s)
- KV Svalbard (2000s)
- Varandey Arctic Shuttle Tanker (2009+)

Modeling non-ice breaking hull forms in marginal ice conditions presents new challenges, some of which are addressed in this thesis. From an ice perspective, there are elements of ‘thin-ice’ mechanics that should be further considered including the edge flexural stiffness, floe transient added-mass effects during the collision process, and additional ice failure modes such as ice sheet buckling and floe splitting. From a structural perspective, the compliance of the local structure during the ice-interaction process acts as an energy sink and could be considered in the modeling approach. In the case of loads on icebreakers and

high ice class ships, the structure remains elastic and can be assumed rigid in an ice load analysis. Later chapters of this thesis present an approach to include the structural indentation energy as an energy sink in the ship-ice interaction model.

Unfortunately comprehensive validation data which cover all of these issues is not currently available and would be prohibitively expensive to obtain in the field. In this section, several attempts are made towards validation of the ice load model in *DDePS* using available field data. These offer a sanity check for the load levels produced by the model under reasonable assumptions. Data from the *USCG POLAR SEA* trials (1980s) and the Varandey Arctic Shuttle Tanker *TIMOFEY GUZHENKO* (2009) are presented here.

5.1. USCG POLAR SEA Data

During the 1980s, an extensive set of ice load measurements were made on the USCG Heavy Icebreaker *POLAR SEA*. Data was collected in a variety of sea areas, at different times of the year, and in various ice conditions. Table 5-1 includes a brief summary of all trials carried out. A strain gauge array installed over 10 bow frames formed an effective pressure sensing panel that was large enough to measure impact force events and both the temporal and spatial pressure variations over the instrumented area. The impact location are thus known quite accurately. Also the measured pressures can be used to estimate the ‘process pressure-area’ curves for the impacts, which is something the ice load model in *DDePS* requires when modeling ship-ice interaction.

Figure 5-1 shows a sketch of the instrumented bow frames and an extract from SSC Report 340 (Daley et al., 1990) which provides an indication of the hull angles. Figure 5-2 is a sketch of the *POLAR SEA* waterline shape, centerline profile, and bow sections which

have been used here to estimate the coordinates of the impacts. The SSC reports on the measurement program provide the impact angles, but not the precise coordinates, which is why this estimate has been made.

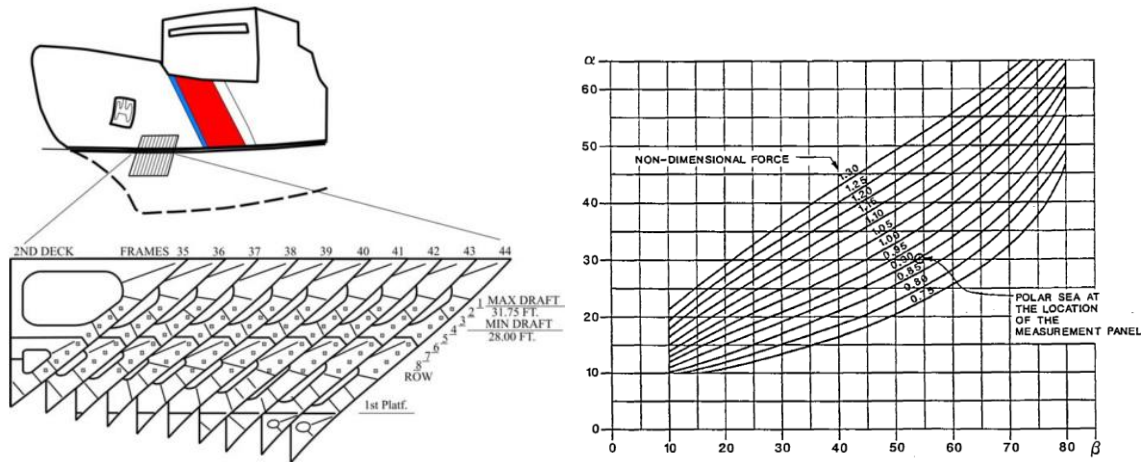


Figure 5-1: Sketch of ice load panel on *POLAR SEA* (left); Extract from SSC 340 Indicating Hull Angles (right)

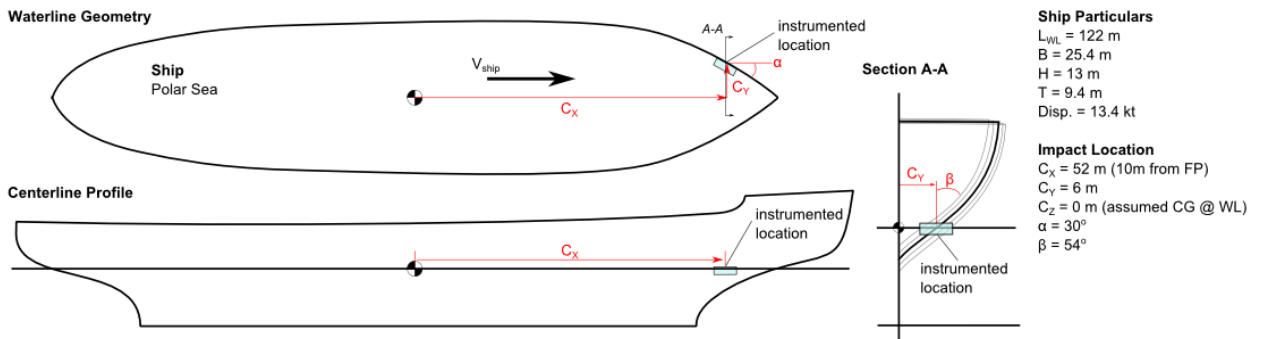


Figure 5-2: Sketch of USCG *POLAR SEA* and instrumented location

Ice impact data was collected in a variety of ice types and conditions. Two data sets are utilized here. Data collected from multi-year ice floe impacts in the Chuckchi Sea and Beaufort Sea are used as validation points for the crushing model in *DDePS*. Data collected from first-year pack ice transits in the Bering Sea are used as validation points of finite floe impacts and flexural limits. All assumptions made in the calculations are presented in the following sections.

Table 5-1: USCG POLAR SEA ice impact trials

Area	Dates	Ice Types	Impacts
Alaskan Beaufort	28 Sept - 16 October 1982	MY	167
South Bering	24-26 March 1983	FY	173
North Bering	27-28 March 1983	FY	243
South Chukchi	29 Mar - 2 Apr, 28 Apr - 2 May 1983	FY, MY	299
North Chukchi	3-27 April 1983	FY, MY	513
McMurdo Antarctica	9-13 Jan 1984	FY	309
Beaufort and Chukchi	18 Nov – 1 Dec 1984	FY, MY	337
Bering Sea Ice Edge	18-27 Apr 1986	FY	653

Notes:

FY - first-year ice

MY - multi-year ice

Bold - indicates trials data used in this report

5.1.1. USCG POLAR SEA Multi-year Floe Impacts

A series of *POLAR SEA* trials in the high Arctic were carried out in the North Chukchi Sea (April 1982) and the Beaufort Sea (October 1982). A plot of the measured force events against the ship's speed are shown in Figure 5-3. From an initial observation there is no clear and obvious relationship between force and speed in the data except for the upper force envelope in the slower speed ranges (1-5 knots) which generally indicates an increasing trend with speed. However the specific details of each event are not fully described in the data set. For example there is almost no recorded evidence of ice edge shape, thickness, strength, angle of impact etc. Each of these factors would influence the load magnitude. Furthermore, the captain would tend to operate more cautiously (i.e. slower) in severe ice conditions and perhaps more aggressively in lighter conditions. This human aspect of operations is not properly reflected in the data set and is difficult to interpret. Nevertheless the measured data can be utilized to help calibrate the *DDePS* ice load model.

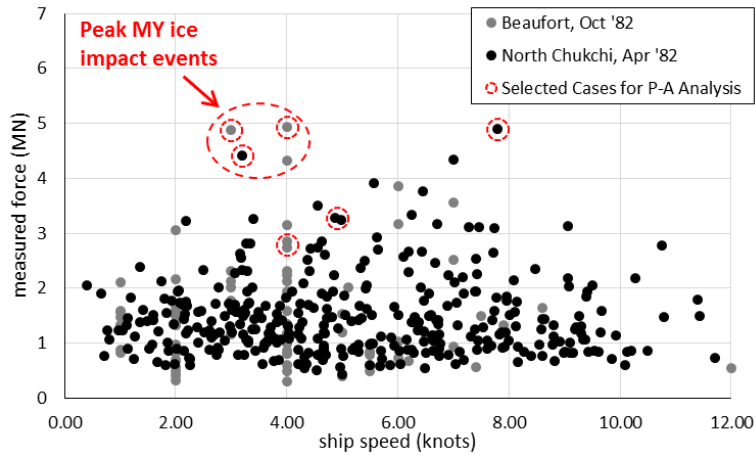


Figure 5-3: Summary of measured force events vs ship speed for *USCG POLAR SEA* Chukchi and Beaufort Sea trials

Six (6) events listed in Table 5-2 (also highlighted in the figure) are selected for further investigation. These represent peak force events from the Beaufort (Oct '82) and Chukchi (Apr '82) trials. The data will be used to extract process pressure-area relationships and compare with *DDePS* calculation results under several assumptions.

Table 5-2: Selected ice impact events

Event	Trial	File Name	Date	Time	Max Force (MN)	Speed (knots)	Event Description
beau1	Beaufort Sea 1982 Summer	R821014_113739	10/14/82	11:37:39	5.00	4.0	Backing and ramming into MY ice
beau2		R821012_170744	10/12/82	11:07:44	4.95	3.0	Running through MY and FY ice
beau3		R821014_114828	10/14/82	11:48:28	2.63	4.0	Backing and ramming into MY ice
chuk1	Chukchi Sea 1983 Winter	R830424_161159	4/24/83	16:11:59	4.89	7.8	Transit in MY ice
chuk2		R830420_130618	4/20/83	13:06:18	4.41	3.2	
chuk3		R830419_130556	4/19/83	13:05:56	3.28	4.9	

Figures 5-4 and 5-5 present a detailed look at one of the selected impact events (chuk3). The left side plot is the time history of total measured force on the impact panel, i.e. the sum of subpanel forces at each time step (sampling rate of 60 Hz). The right side plot is the process pressure-area relationship for the event. Each black marker represents the average pressure over the activated contact area at the respective time step. A pressure threshold of 0.2 MPa was applied to produce this process P-A curve. The red markers in each plot highlight size (6) selected instances while the force is rising. The pressure distributions for each instance are shown in Figure 5-5.

At the beginning of the event the contact area is small and located at the forward end of the panel. As the force rises, the activated contact area grows and the peak pressures tend to move aft (along the panel). The force-time history is not smooth and in this particular example the event takes approximately 2 seconds before reaching the peak force. The pressure distributions show areas of high and low pressure zones. The process pressure-area curve shows a slightly reducing average pressure as the area grows. Similar plots for the other selected events are provided in Appendix B.

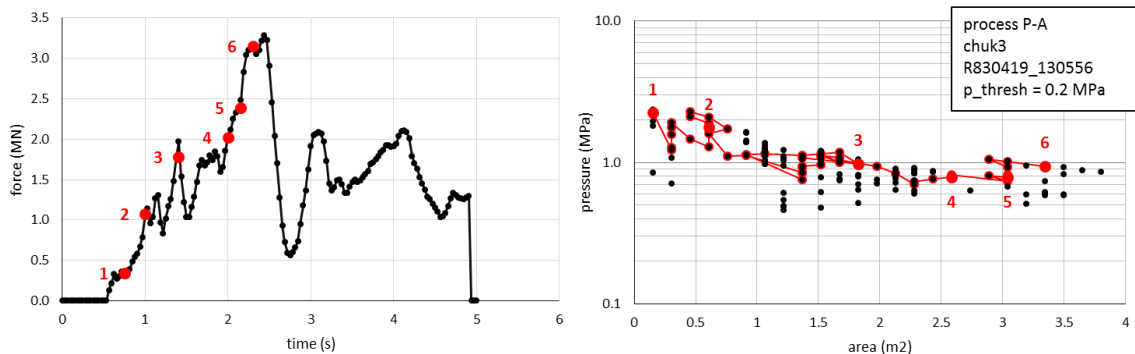


Figure 5-4: Force-time history and process P-A curve for selected *POLAR SEA* event (chuk3)

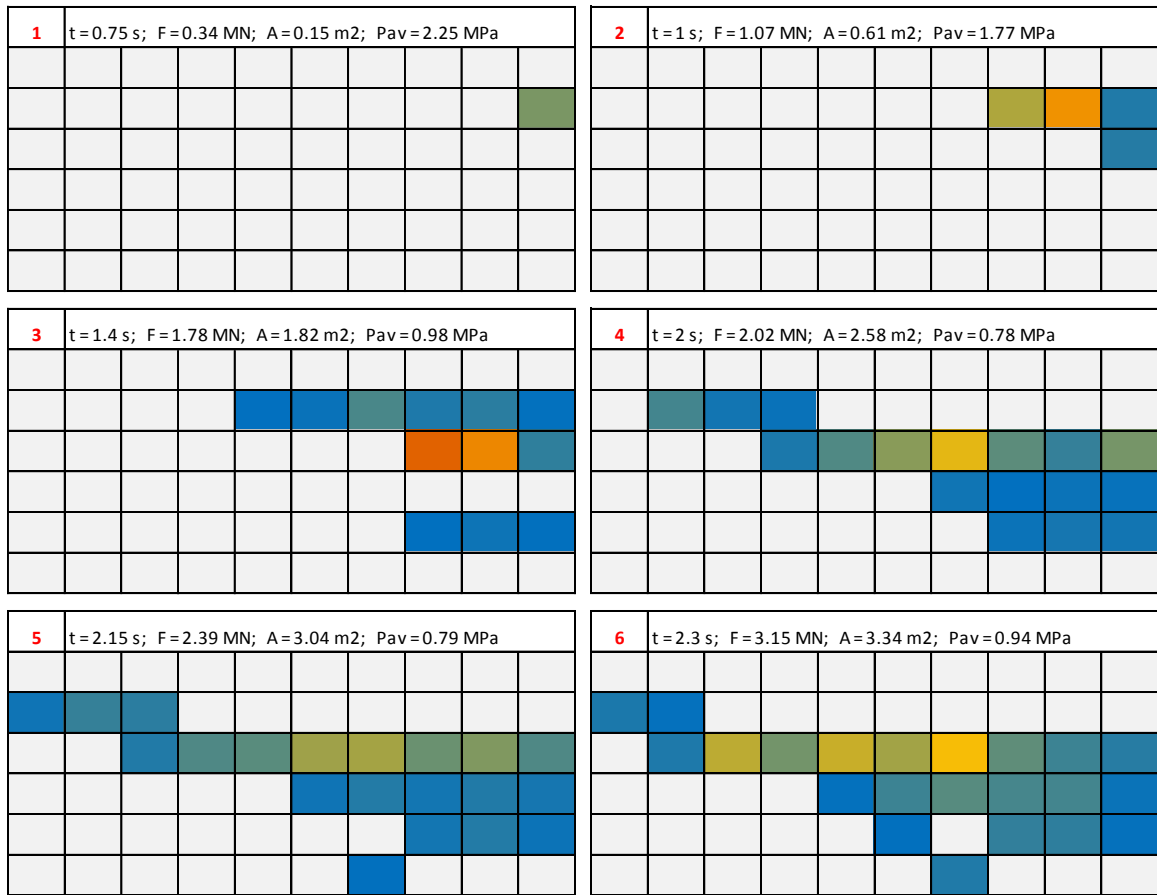


Figure 5-5: Pressure distributions (in MPa) at 6 instances for selected Polar Sea event (chuk3)

The process pressure-area curves for each of the six selected '82 and '83 Arctic events are plotted together in Figure 5-6. Some of the curves show rising pressures with contact area while others (e.g. chuk3) show declining trends. The nature of these curves depends on many factors. For example the subpanel areas are relatively large. If a single subpanel is activated during an event, its entire area is computed in the average pressure calculation; even if only part of the subpanel is exposed to ice pressure. This effectively increases the total measured area and reduces the average pressures. To accommodate for this, a pressure threshold of 0.2 MPa was applied for the area calculations in this plot. This,

unfortunately, is an artifact of most ice load instrumentation data, and influences the P-A data.

Also shown on Figure 5-6 are two pressure-area models which are used in *DDePS* to control the ice crushing strength. The green line ($P_o = 6 \text{ MPa}$, $ex = -0.1$) can be considered as an empirical (conservative) upper-bound envelope of the measured P-A data of the Polar Sea events analyzed here.

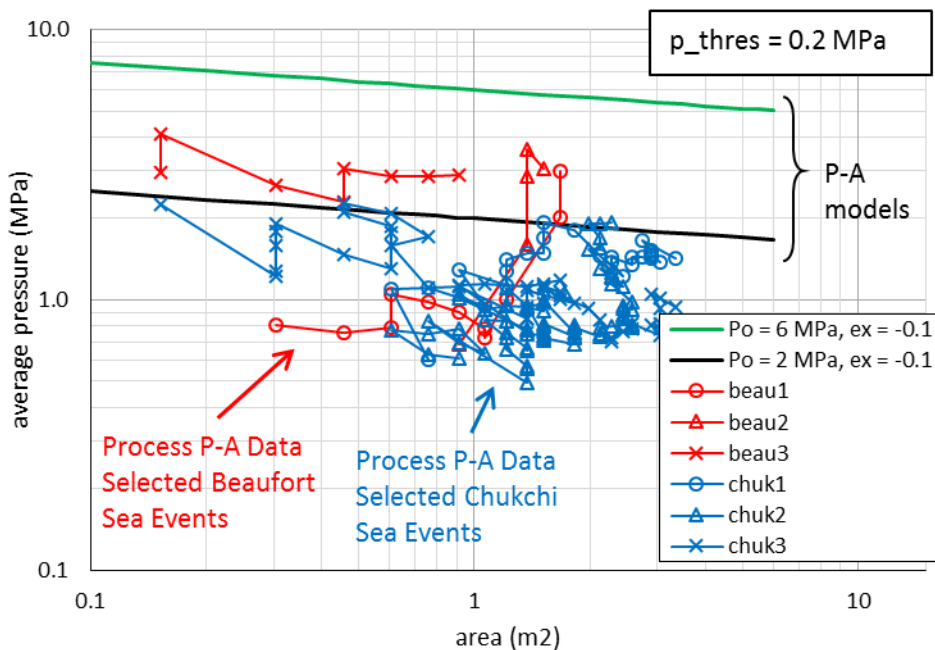


Figure 5-6: Process pressure-area data for selected Polar Sea events from Beaufort and Chukchi Seas

DDePS Calculations

In order to compare the measured data against *DDePS* calculations some assumptions are needed. Anecdotal evidence from several dedicated MY floe impacts suggest that the ice did not break in flexure, but only crushed. Furthermore, the ice floes were so large that they did not appear to move away after the impacts, indicating that they were far more massive than the ship. For this analysis, the peak ice MY impact force events highlighted in Figure 5-3 used to set up *DDePS* calculations under various assumptions.

Two (2) crushing strength cases are used to demonstrate sensitivities in *DDePS* load calculations (these are shown in Figure 5-6). Case A assumes a nominal crushing strength ($P_o = 2$ MPa) and a slightly decreasing trend ($ex = -0.1$) for average pressure as area increases. It is noted that this pressure-area curve is used for the design point IACS Polar Class PC5. Case B assumes a fairly conservative nominal crushing strength ($P_o = 6$ MPa) and a slightly decreasing trend ($ex = -0.1$) for pressure as area increases. It is noted that this pressure-area curve is used for the design point IACS Polar Class PC1.

The ice edge shape was not recorded during the trials, so several estimates will be used in the *DDePS* calculations including wedged and rounded shapes. The velocity was not precisely measured but the event logs included approximate speeds (3-4 knots). Speed is also varied in this case study to demonstrate its sensitivity to the loads. Based on the anecdotal evidence that the ice edge did not break in flexure and there was no movement after the impacts, it is reasonable to assume thick and massive ice floes. Under these assumptions, the scenarios illustrated in Figure 5-7 are computed in *DDePS*.

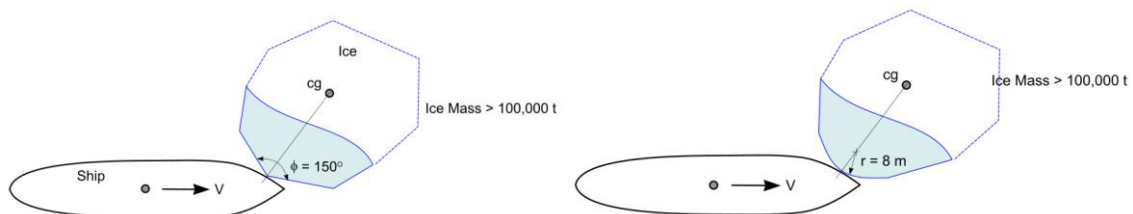


Figure 5-7: Assumed POLAR SEA MY ice impact scenarios

Force vs. speed results are shown in Figure 5-8 using *DDePS Case 2a* (150° wedge edge shape) for ice strength cases A (2 MPa) and B (6 MPa). The floe size was assumed to be 500 m and the ice thickness was varied between 2 – 5 m. The steep portion of the curves represent crushing dominated collisions, where there is not enough downward breaking

force to fail the ice in flexure. The horizontal portions represent the flexural failure limited conditions. The *POLAR SEA* data is superimposed on the plots.

For the selected peak MY ice events ($h_{ice} > 2$ m), *DDePS* predicts reasonable force levels that agree with the measured data. The flexural failure limits for thinner ice features ($h_{ice} \leq 2$ m) also generally bound the data for the higher speed events, which presumably were measured in thinner ice regimes. It is noted that 2 m is the nominally the upper bound thickness of first-year ice.

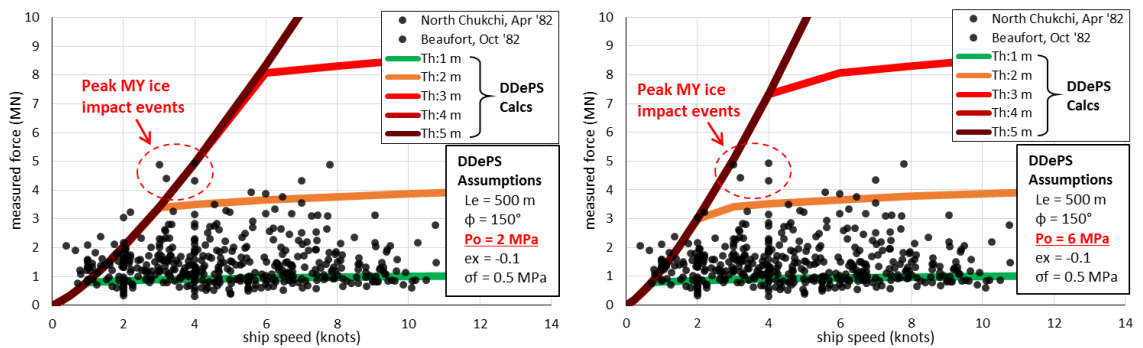


Figure 5-8: *DDePS* (wedge shape) calculation results – force vs. speed, *POLAR SEA* data superimposed

The results of the 5 m thick ice collisions are combined in Figure 5-9. These cases are crushing dominated with no flexural ice failure. As discussed above, anecdotal evidence from the ice trials suggest the ship speed was approximately 3-4 knots during the measured impacts and the resulting peak forces were on the order of 5 MN. The *DDePS* calculations show general agreement with these load levels when reasonable assumptions are made.

The Case B ice crushing model (high nominal crushing term, $P_o = 6$ MPa) produces slightly higher peak forces (6-7 MN). This demonstrates the sensitivity of crushing strength. Another example of sensitivity to ice edge angle (ϕ) is shown in Figure 5-9 (right). A smaller edge angle of 120° results in a slower build-up of force and lower peak force

values. The larger (i.e. blunt) ice edge angle (170°) produces a faster rise in force and higher peak loads. Nevertheless, load magnitudes at ~ 4 knots still show reasonable agreement with the full scale data.

Figure 5-10 is intended to demonstrate *DDePS* results considering a rounded ice edge (for local contact geometry) under similar assumptions. In the left-hand plot, the sensitivity of crushing strength considering an 8m edge radius is shown. The right-hand plot compares the calculation results for 4m and 6m edge radii. Again, the load magnitudes at ~ 4 knots show reasonable agreement with the full scale data.

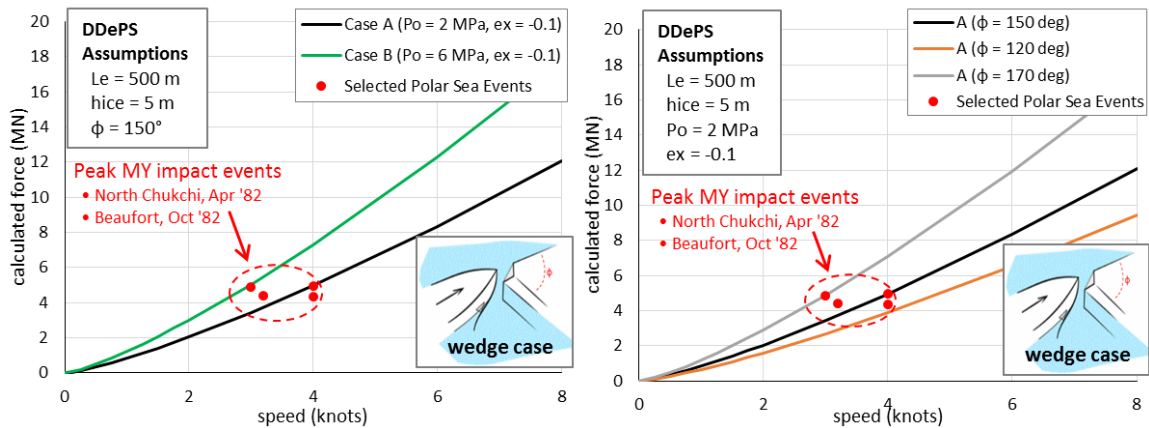


Figure 5-9: *DDePS* calculations results for wedge ice edge under various assumptions

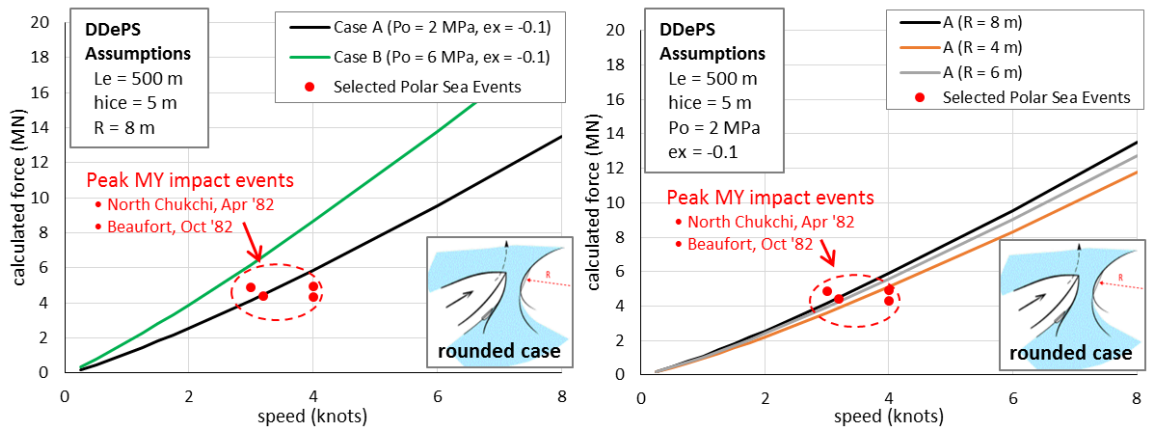


Figure 5-10: *DDePS* calculations results for rounded ice edge under various assumptions

5.1.2. USCG *POLAR SEA* Bering Sea Pack Ice Trials

In March 1986, ice trials of the *POLAR SEA* were carried out in Bering Sea pack ice conditions (see Figure 5-11). Over 650 impact measurements were collected over a 12 day period at speeds ranging from 0 – 16 knots. The event logs include some information about floe size and ice thickness that were likely estimated based on bridge observations and available ice charts. Floe diameters were reported in the range of 3 – 30 m and thicknesses ranged from 30cm – 2.5m.



Figure 5-11: USCG *POLAR SEA* in the Bering Sea [photo credit: USCG]

Figure 5-12 presents the force vs. speed data collected during the Bering Sea transits. Forces were measured up to 1.8 MN which is significantly lower than the multi-year ice impact loads. Again at slower speeds (up to ~6 knots), the upper force envelope increases with ship speed, however at higher speeds the force-speed relationship is not so

obvious. Table 5-3 lists three (3) of the peak events measured in the Bering Sea which have been selected for more in depth pressure-area analysis.

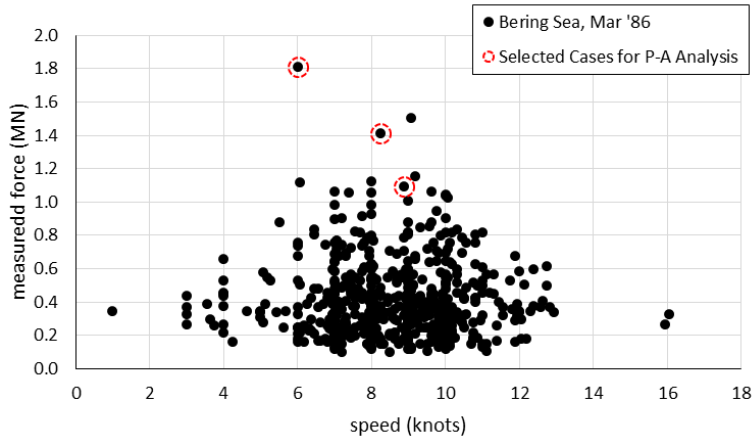


Figure 5-12: POLAR SEA Bering Sea Impact Data

Table 5-3: Selected POLAR SEA impact events in the Bering Sea

Event	Trial	Polar Sea Data File Name	Date	Time	Max Force (MN)	Rank (Force)	Speed (knots)
ber1	Bering Sea 1986 Winter Trials	R860317_210530	3/17/1986	21:05:30	1.81	1	6.0
ber2		R860320_175301	3/20/1986	17:53:01	1.41	3	8.3
ber3		R860323_174202	3/23/1986	17:42:02	1.10	7	8.9

For the peak event (ber1), the force- time history and process-pressure area data are presented in Figure 5-13 and the pressure distributions at several instances are shown in Figure 5-14. Similar to the example Chukchi Sea event described in section 5.1.1, the contact area increases as the force rises but the average pressure shows a slightly declining trend. There is also evidence of high and low pressure zones, however in this example the force rise is rather smooth and occurs over a shorter period (~0.5 s).

The process pressure-area curves for each of the three selected Bering Sea events are plotted together in Figure 5-15. Each of these curves show declining pressures as area

increases up to 1 m² followed by slightly increasing pressures . Two pressure-area models are also shown. The black line (P_o = 2 MPa, ex = -0.1) appears to be a reasonable empirical (conservative) upper-bound envelope of the measured Bering Sea P-A data.

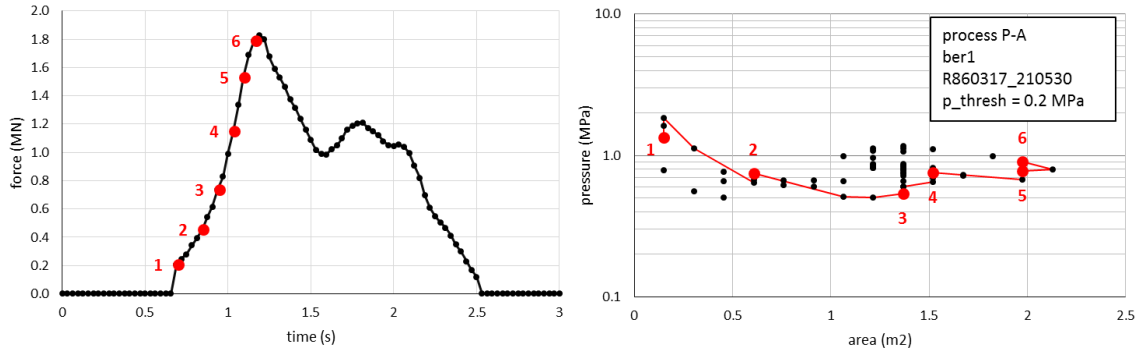


Figure 5-13: Force-time history and process P-A curve for selected Polar Sea event (ber1)

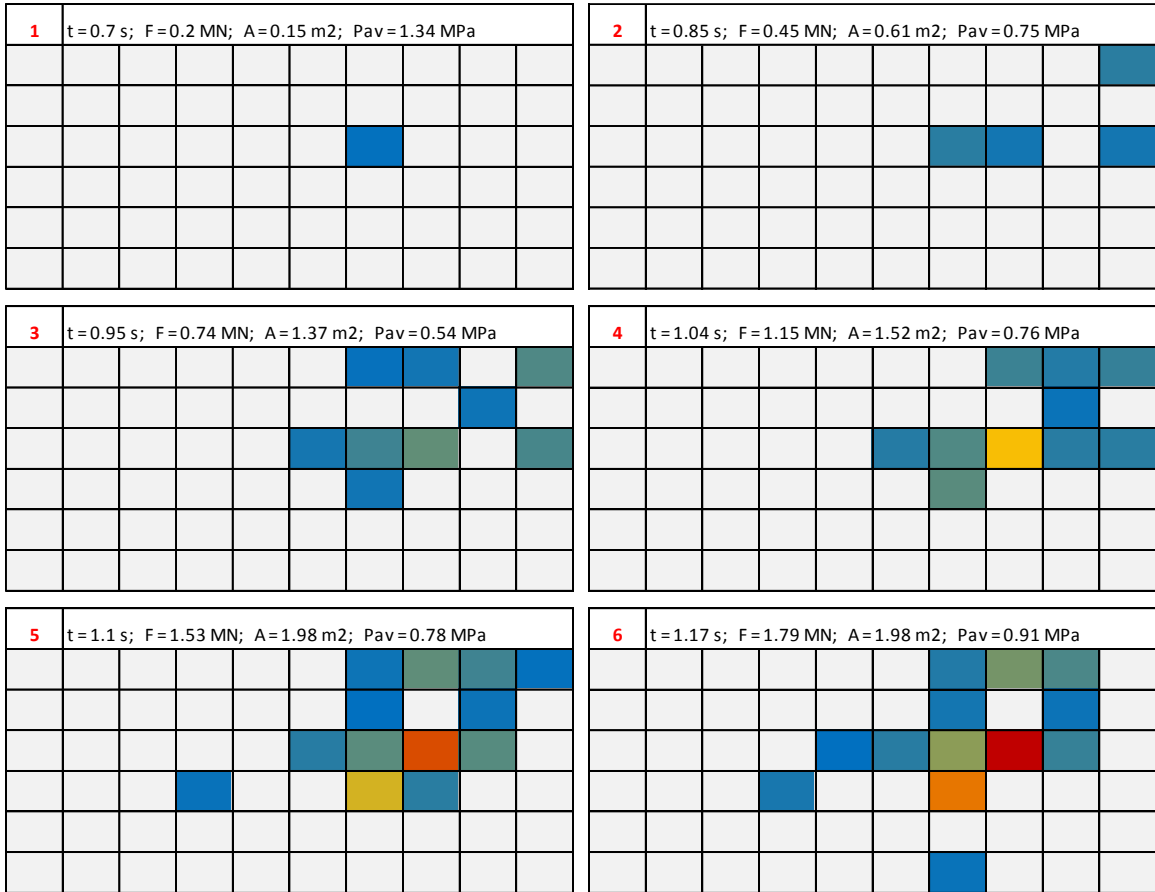


Figure 5-14: Pressure distributions (in MPa) at 6 instances for selected Polar Sea event (ber1)

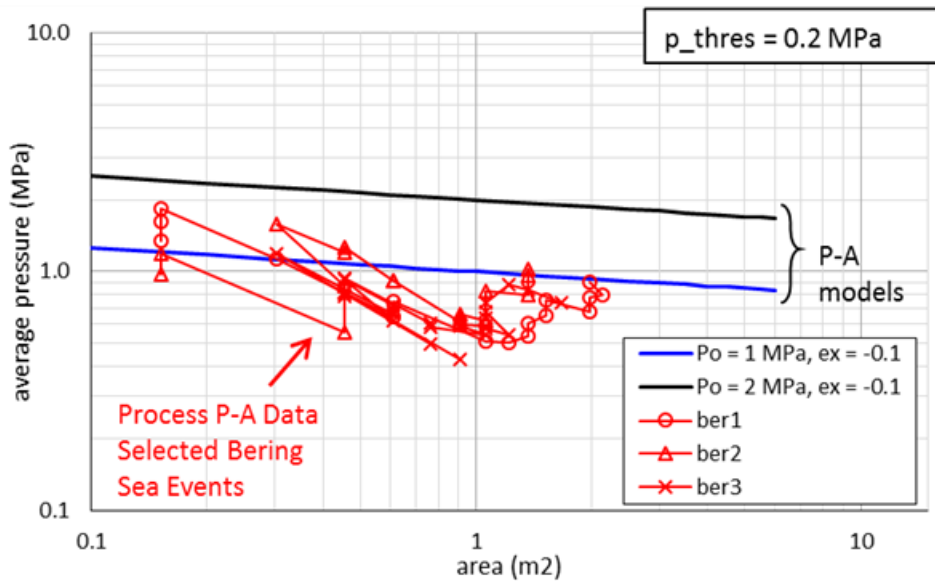


Figure 5-15: Process pressure-area data for selected *POLAR SEA* events from Bering Sea

DDePS Calculations

Figures 5-16 through 5-18 show the *POLAR SEA* pack ice trials data compared with *DDePS* calculations results for three different assumed floes sizes (35 m, 20 m, and 10 m) and a range of first-year ice thicknesses and ships speeds. A sketch of the assumed scenario is also included with each plot.

It is difficult to differentiate between the flexural & momentum limits in the measured data and there is some uncertainty in reliability of the ice descriptions for each event. Furthermore, *DDePS* assumes a specific ice wedge contact shape and a perfectly normal collision with the hull. No information about ice edge shape or collision orientation is available in the data. However, under very reasonable assumptions (e.g. ice strength terms, shape parameters, and collision scenario) the *DDePS* model produces reasonable results compared with the measured data. The model suggests smaller and thicker floes are governed by a momentum limit while larger and thinner floes are generally limited by flexural bending.

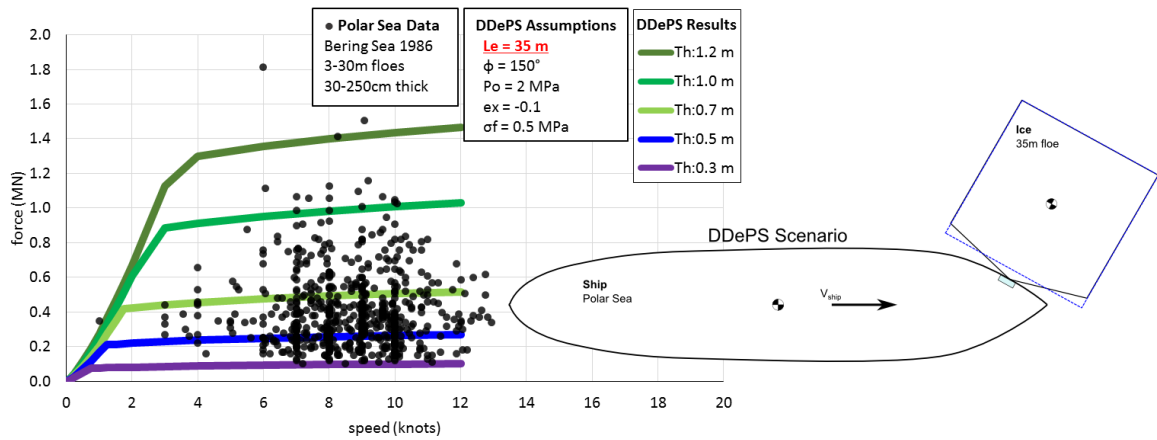


Figure 5-16: DDePS calculations results for pack ice impacts (35m ice floes)

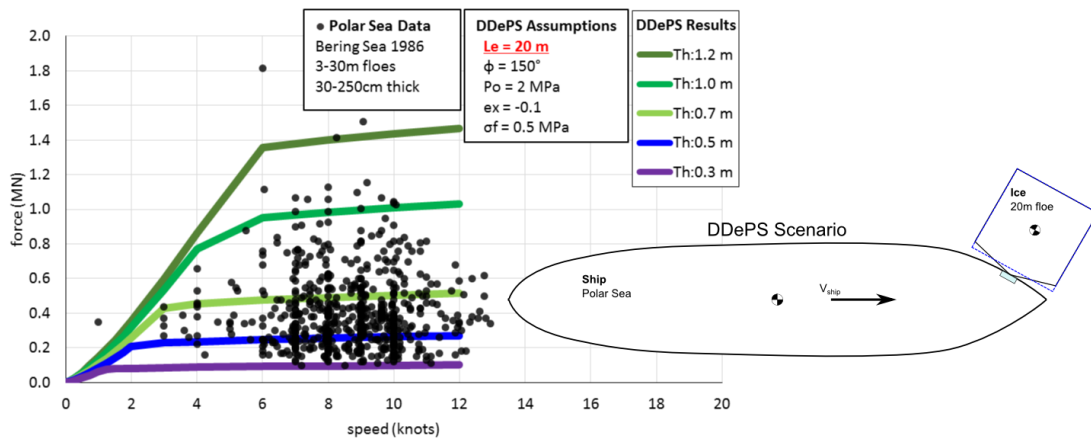


Figure 5-17: DDePS calculations results for pack ice impacts (20m ice floes)

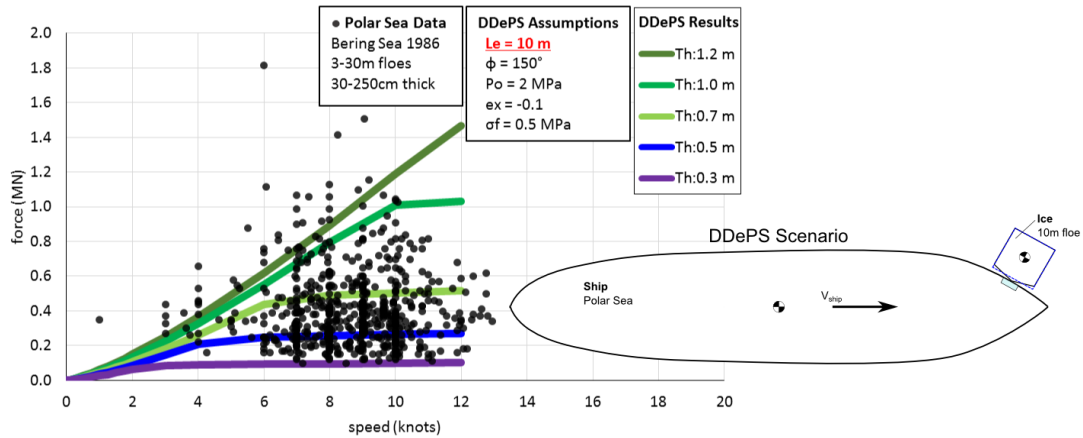


Figure 5-18: DDePS calculations results for pack ice impacts (10m ice floes)

5.2. Varandey Arctic Shuttle Tanker Ice Load Monitoring Program

M/T TIMOFEY GUZHENKO is a large icebreaking Arctic shuttle tanker built in 2009. The vessel transports crude oil year-round from an offshore loading terminal located in the Pechora Sea near the Varandey region, to the Port of Murmansk on the Barents Sea, and regularly encounters ice conditions in the winter months (see Figure 5-19). As part of Joint Development Project (JDP) between Samsung Heavy Industries (SHI), ConocoPhillips (COP) and American Bureau of Shipping (ABS), an ice load monitoring system (ILMS) is installed on the ship. The ILMS utilizes over 150 fiber-optic strain gauge arrays that effectively form pressure sensing panels on the bow and stern shoulders to measure and record ice loads. The ILMS processes the impact measurements in real time and also computes the resulting stresses at critical locations on the hull structure. Real-time feedback is presented to the ship's navigation officers as a visualization of the peak stress which is used as an aid to operational decision making. More detailed information about the background of the measurement system, descriptions of measured data, and pre/post-processing methods were discussed in Iyerusalimskiy et al., 2011, Yu et al., 2012 and Kim et al., 2016. Since commissioning in 2009, the ILMS has recorded almost 30,000 ice impact events at the bow.

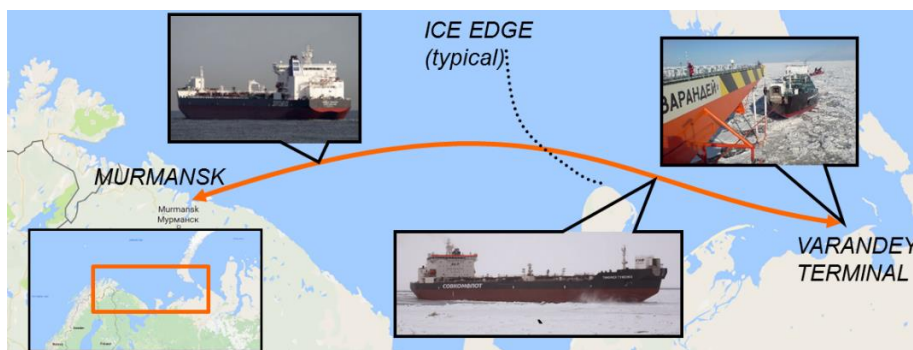


Figure 5-19: Main voyage route of the Varandey Tanker

A diagram of the ship indicating the location of instrumented bow panel is shown in Figure 5-20. The ship particulars and bow angles at this location are known precisely and will be used to set up DDePS calculations.

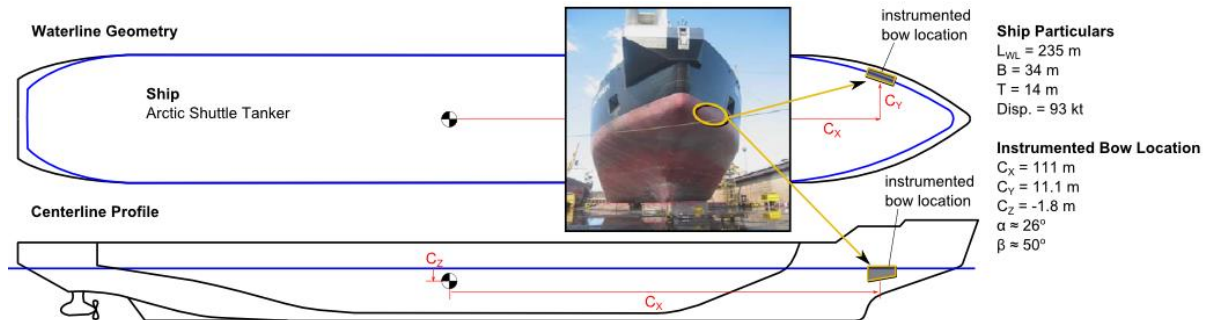


Figure 5-20: Sketch of Varandey Tanker indicating location of bow instrumented panel

Figure 5-21 plots the maximum measured force against ship speed for +2500 events recorded in 2009, the commissioning year of the ILSM. Three (3) of the peak events are highlighted in the figure and listed in Table 5-4. These events were recorded in early May and early June. As reported by Iyerusalimskiy et al. (2011) the worst ice conditions during winter 2009 were described as “ice pressure and high dynamics resulted in formation of very close pack predominantly of first-year thin and first-year medium ice, can be described as rafted ice, ridges, and rubble fields”.

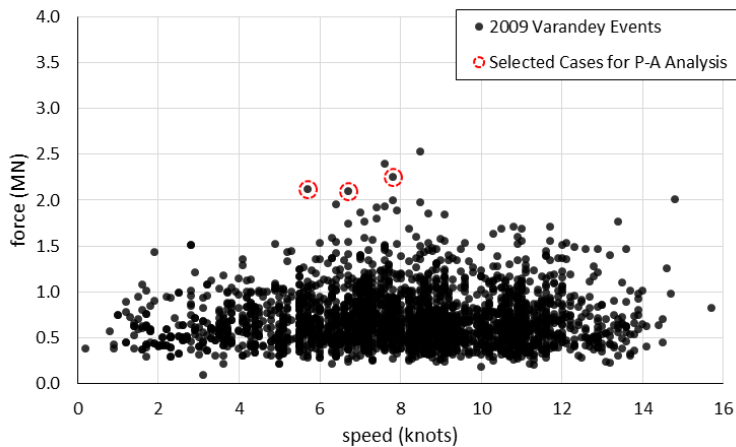


Figure 5-21: Varandey Tanker 2009 Impact Data

Table 5-4: Selected Varandey Tanker impact events

Event	Trial	Varandey Data File Name	Date	Time	Max Force (MN)	Speed (knots)
var1	Varandey 2009 V5W	B124603	6/8/2009	12:46:03	2.25	7.8
var2	Varandey 2009 V5W	B140328	6/8/2009	14:03:28	2.12	5.7
var3	Varandey 2009 V2W	B225052	5/8/2009	22:50:52	2.1	6.7

Figure 5-22 is one example event measured by the ILSM. The panel is comprised of 93 subpanels and pressures are recorded at 250 Hz. The left side plot is the time history of measured force and the right side plot is the process pressure-area relationship derived following the same procedure used in the *POLAR SEA* analysis. Visualizations of pressure distribution at six (6) instances during the event are shown Figure 5-23. Similar plots for the other selected events are provided in Appendix C.

In this example the nominal contact area starts small and grows as the force rises over about 0.5s. The load patch is more line-like compared with some of the *POLAR SEA* events but contact area becomes quite large ($\sim 3\text{-}4\text{ m}^2$). The process-pressure area curve shows slightly declining average pressures with nominal contact area. Figure 5-24 compares the process P-A curves for the three (3) selected peak events; each depicts as similar trend. Two pressure-area models are also shown. The black line ($P_o = 2\text{ MPa}$, $ex = -0.1$) appears to be a reasonable empirical upper-bound envelope of the measured data which was collected predominately in first-year ice conditions.

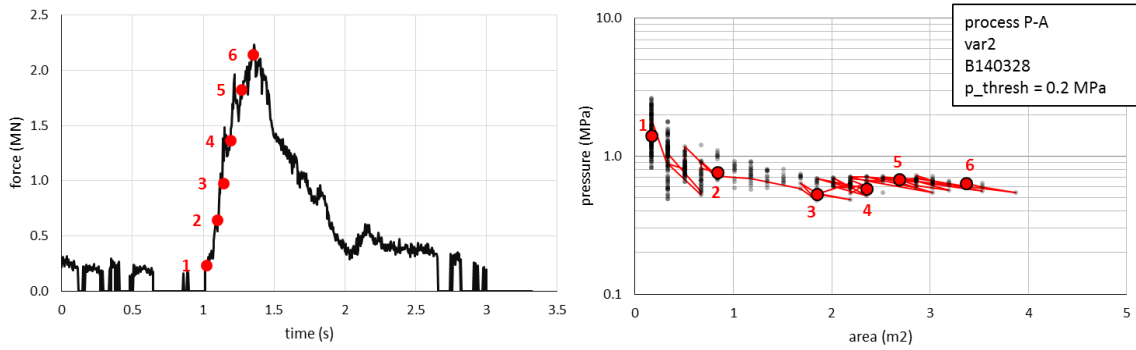


Figure 5-22: Force-time history and process P-A curve for selected Varandey Tanker event (var1)

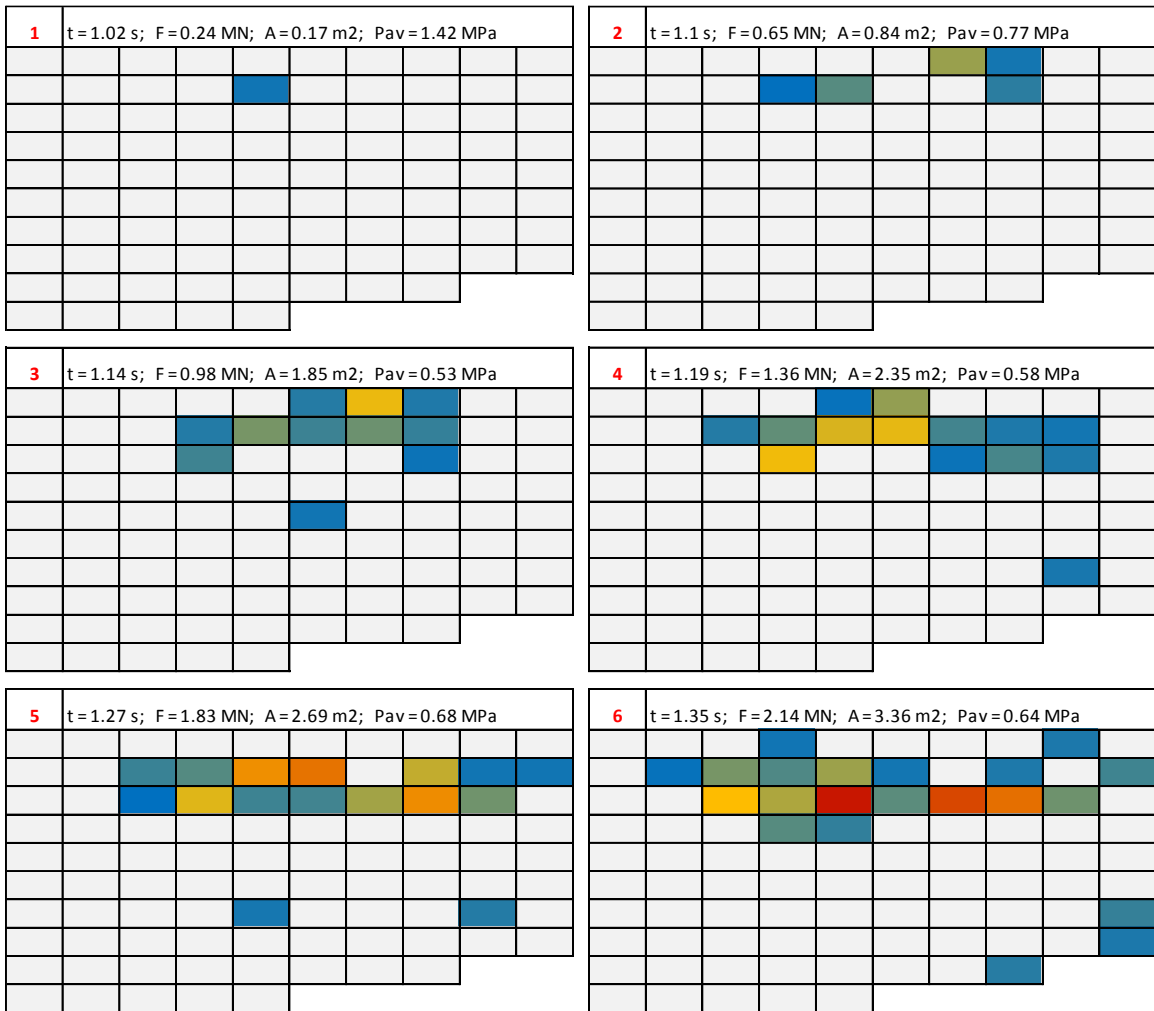


Figure 5-23: Pressure distributions (in MPa) at 6 instances for selected Varandey Tanker event (var2)

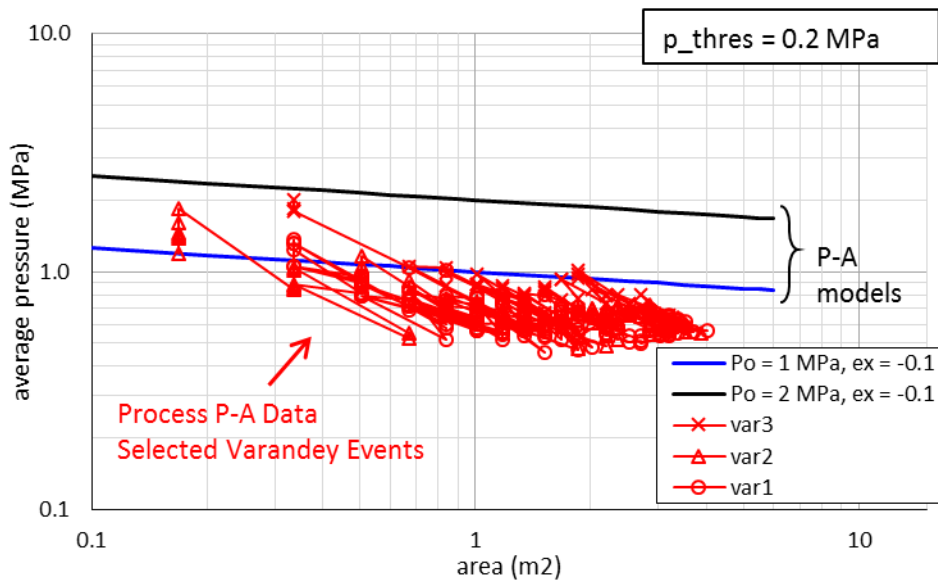


Figure 5-24: Process pressure-area data for selected Varandey Tanker events

DDePS Calculations

While the ice forces and pressure distributions are well recorded by the ILMS, there is very limited information about the actual ice conditions (other than general descriptions described above). The tanker is engaged in full time commercial operations, as opposed to dedicated ice trials, so there was a relatively low priority to collect detailed ice information. Some qualitative information can be inferred from local ice chart information and with reasonable assumptions, *DDePS* calculations can be setup to model typical loading events.

In *DDePS*, the ice floes are assumed to be infinitely large and ice thickness is varied up to 1.2m because the ship operates in predominately first-year level ice or pack ice conditions. During level ice breaking the dominating ice failure mode is flexural bending so two different ice flexural strengths, σ_f , are considered (0.5 MPa and 0.75 MPa) to demonstrate the sensitivity of this parameter. Figure 5-25 compares the measurement data with the *DDePS* calculation results under these assumptions. It is shown that the model

produces reasonable results within ‘order-of-magnitude’ agreement. In particular the calculated flexural limits appear to cover the upper limit of the measured forces.

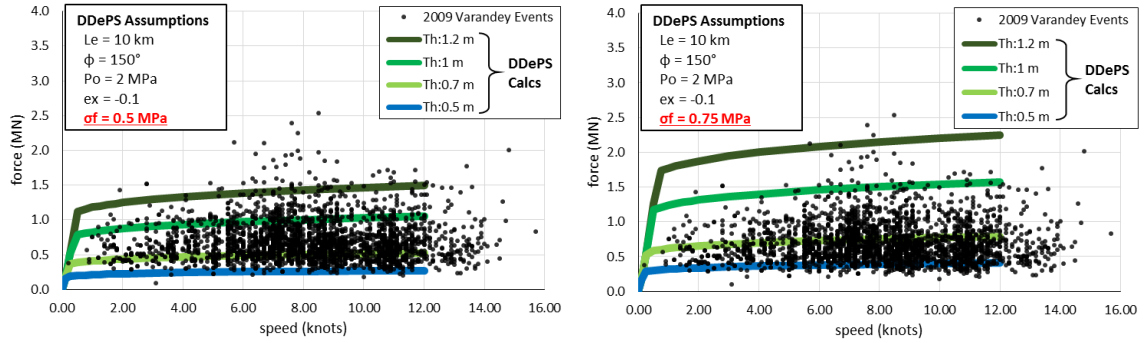


Figure 5-25: DDePS calculations results compared with Varandey Tanker data (2009 events)

6. Ice Crushing Forces Considering Deformable Structures

During a ship-ice interaction event, energy may be absorbed by deforming the structure elastically and plastically in addition to the energy expended into crushing the ice. Most standard models of ship-ice interaction (e.g. the ice load model described earlier in Section 4.4) assume the ship to be a perfectly rigid body. This assumption is in general valid for stiff structures (i.e. high ice class ships). However for non-ice classed (or even light-ice classed) ships, a substantial portion of the available kinetic energy KE_e can be expended into deforming the relatively compliant structure. This concept is generalized by the following energy balance equation where IE_i and IE_s are the ice and structural indentation energies respectively.

$$KE_e = IE_i + IE_s \quad (80)$$

For complex structural arrangements, no analytical equation exists to represent the combined structural and ice indentation processes. Daley & Kim (2010) approached this problem numerically by simplifying the ice load to a point load (highly localized force) and the plastic response of the structure was represented by a linear deformation function (81).

$$F_n = k_p \zeta_n + F_o \quad (81)$$

The concept, sketched in Figure 6-1, was implemented into a spreadsheet tool as a practical way to evaluate ice loads with the consideration of the ship's plastic deformation. Daley and Kim applied a 'design of experiments' (DOE) method to develop regressions models for the k_p and F_o terms. The models are functions of a range of input variables

which represent the structural parameters of a stiffened panel (frame spacing, span, dimensions, plate thickness, etc.). This is a very useful model that can easily be implemented into a spreadsheet tool however for large collisions that involve extensive damage and larger ice contact areas, the assumption of a point load is no longer valid.

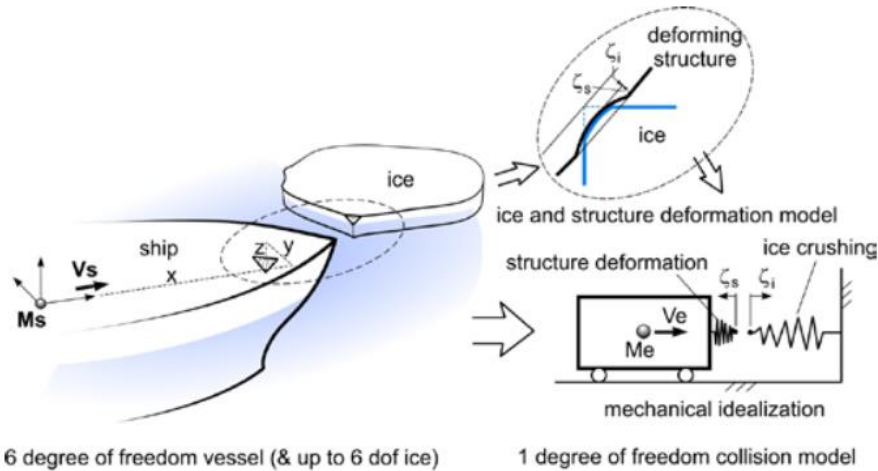


Figure 6-1: Concept sketch for compliant ship-ice collision model (from Daley & Kim, 2010)

In order to appropriately quantify the structural indentation energy, a more sophisticated approach has been developed which takes into account a more realistic developing load patch. Consider the idealized sketch in Figure 6-2. For a rigid structure indenting an ice edge, the ice edge crushes and the load patch develops as a growing triangular area (top). When the structure is deformable, local plastic and elastic deformations develop in the structure along with ice crushing. The changing structural shape alters the load distribution (i.e. patch shape) and the force development. This process can be expressed as a power function (82) where total contact force F_n is related to ‘total’ normal indentation ζ_n of the structure from its initial contact point.

$$F_n = C_s \zeta_n^{k_s} \quad (82)$$

The total normal indentation is simply the sum of the structural deformation and ice crushing indentation ($\zeta_n = \zeta_s + \zeta_c$). The specific power function coefficients, C_s and k_s , must be obtained from a numerical simulation analysis of a ship grillage impacting an ice edge. This section describes the setup and calibration of a numerical ice model and ship specific ice-structure interaction analyses are demonstrated in detail in the case studies in Chapters 7 and 8.

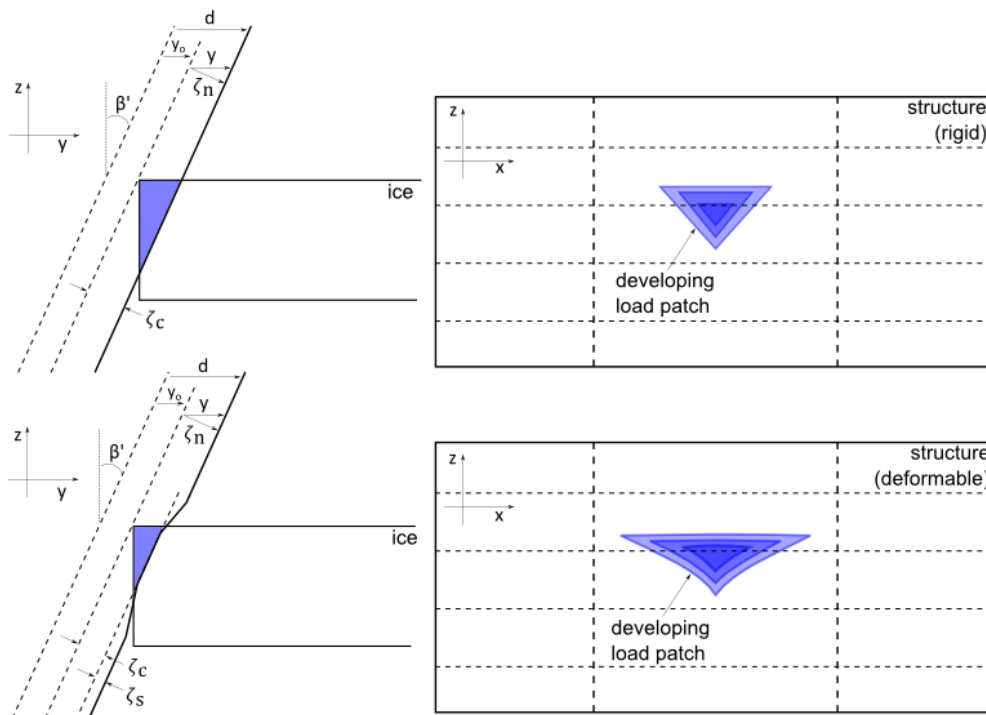


Figure 6-2: Sketch of interaction model for rigid (top) and deformable (bottom) structures

The sum of ice and structural indentation energies can be obtained by integrating the total force over the depth of ‘total’ normal indentation;

$$IE_i + IE_s = \int_0^{\zeta_n} F_n d\zeta_n \quad (83)$$

By equating the sum of the ice and structural indentation energies to the effective kinetic energy of a collision and integrating the force, one arrives at equation (84).

$$KE_e = \int_0^{\zeta_n} F_n d\zeta_n = \frac{C_s \zeta_n^{k_s+1}}{k_s + 1} \quad (84)$$

The ‘total’ normal indentation ζ_n can be solved for and expressed as equation (85). It can then be used to solve for the normal force by referring back to equation (82).

$$\zeta_n = \left(\frac{KE_e (k_s + 1)}{C_s} \right)^{\frac{1}{k_s+1}} \quad (85)$$

In order to resolve the structural indentation ζ_s portion of the total indentation, the results of numerical simulations are used to find a relationship with normal force. Later it is demonstrated that the force vs. structural indentation response can be simplified into two linearized portions, elastic and plastic:

$$\zeta_s = f(F_n) \quad (86)$$

Once the structural indentation is known, the ice indentation portion ζ_i is then simply the difference and is used to determine the size of the load patch.

$$\zeta_i = \zeta_n - \zeta_s \quad (87)$$

6.1. Numerical Simulations

Equations (82) and (87) describe power functions that are derived from the results of numerical simulations between ship structural grillage models interacting with a deformable ice material. The general purpose commercial finite element analysis code LS-Dyna was used to calibrate and conduct a series of simulation experiments. LS-Dyna is an explicit-dynamic commercial finite element analysis code capable of dealing with complex contact, nonlinear, transient, and dynamic problems. It can handle many simulation environments including, FEM, iCFD, ALE, SPH, EFG, X-FEM, DEM and others.

Several researchers have attempted to model ice crushing behavior numerically and recently LS-Dyna has been applied to an increasing number of ice problems. Gagnon & Derradji-Aouat (2006) first calibrated and applied LS-Dyna's *MAT_CRUSHABLE_FOAM* (*MAT_063*) material model to match ice impact parameters (peak force, impact duration, and pressure distribution) obtained from field trials of the Canadian Coast Guard Icebreaker TERRY FOX. Zong (2012) later applied the same 'crushable foam' ice model to simulate bow glancing collisions and calibrated the constitutive material parameters to produce process-pressure area relationships that match different IACS Polar Class P-A curves. Liu et. al (2012) modeled ice with an elasto-plastic material card which considers kinematic hardening *MAT_PLASTIC_KINEMATIC* (*MAT_003*) and compared peak impact forces and time histories against the Popov + P/A analytical model that is implemented in the IACS Polar Rules and described in section 4.2. Reasonable agreement was shown between the numerical and analytical models. The studies by ABS (2015) and Daley, (2015) described earlier in Section 3.3.3 also utilized numerical material models for ice in LS-Dyna following the same methodology described in this section.

Each of these researchers recognize that the numerical treatment of ice as an elasto-plastic continuum material in a finite element form introduces significant simplifications and ignores many of the complex ice failure mechanisms such as spalling, splitting, high internal spatial pressure zones, etc. Furthermore, results can be quite sensitive to factors such as contact geometries, contact algorithms, numerical parameters, and mesh size. Nevertheless it is possible to carefully employ these methods to achieve certain desired results.

Figure 6-3 illustrates the use of LS-Dyna analyses to obtain the coefficients C_s and k for a particular bow section of a non-ice strengthened naval combatant hull structure (case study from Section 8). The blue curve represents the force vs. indentation results from an LS-Dyna simulation considering a rigid plate crushing a 70cm ice edge (123° wedge angle). For a properly calibrated ice model, this curve will agree with the analytical model (dotted blue line) for the assumed pressure-area parameters. The red curves represents the force vs. total normal indentation (ice + structure) considering a deformable structure crushing the same ice model. A power function in the form of equation (82) can be fit to this curve as shown by the dotted red line.

The areas under either of these curves represents energy. Thus for any given available effective kinetic energy of a ship-ice collision scenario (arbitrarily highlighted in this plot), the maximum force can be determined. For this particular example of a weak non-ice strengthened structure, the force is reduced significantly (~30% lower) if the structural indentation energy is considered in the crushing process.

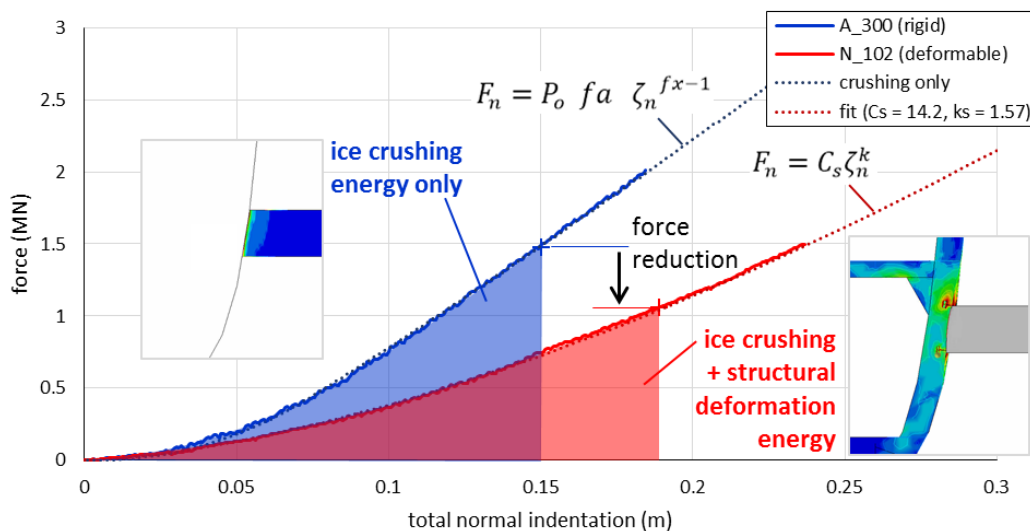


Figure 6-3: LS-Dyna analysis results for rigid and deformable structures crushing an ice edge

6.2. Calibration of the Numerical Ice Model

In order to carry out numerical simulations of a compliant structure interacting with a deformable ice model, the ice material model must first be developed and calibrated. Ice loads on ships depend on many factors and ice failure mechanisms. Ice-structure interaction is a complex phenomenon with many interrelated variables and significant uncertainty. Loads can be governed by local ice crushing, flexural bending, radial or circumferential cracking, friction, ice clearing, and even the dynamic response of the impacting structure; among many additional factors. The selection of an appropriate ice load model and calibration of its parameters to achieve desired strength characteristics is therefore a challenge. The calibration effort described in this section is focused on the crushing process of the ice. The ultimate objective is to produce target load levels (i.e. forces and contact areas) and pressure distributions that reasonably agree with empirical data.

First, we'll consider some available data. Figure 6-4 shows pressures measured in a lab setting during the STePS² project (Bruneau et al., 2013a; 2013b). Ice cones of various dimensions were grown in the lab and crushed against rigid indenters. Forces and contact areas were measured using a variety of techniques and pressures were determined. Contact pressures were measured in the 10 MPa range over areas up to 0.1 to 0.2 m². Ice pressures measured in the field show pressures on the order of a few MPa at ~ 0.5 to 1m². Several examples are discussed in Section 5 and compared with a few different nominal process-pressure area relationships. Design local pressures in the IACS polar rules range from a few MPa up to 6 MPa for the highest ice class and are typically applied over several square meters.

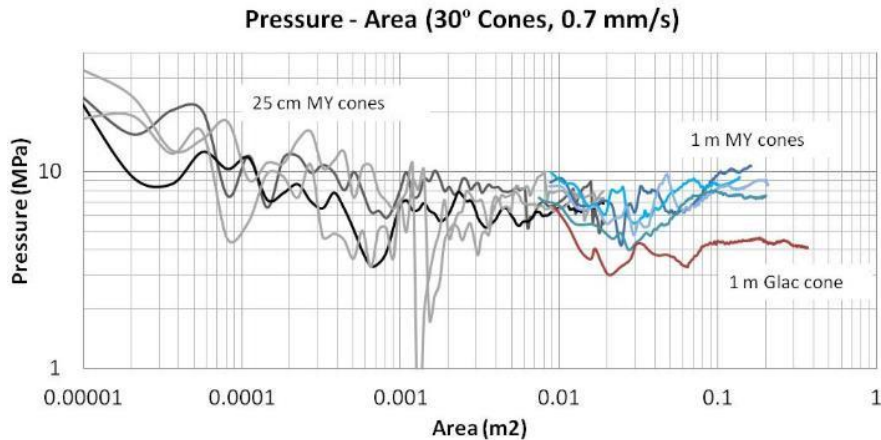


Figure 6-4: Measured pressures in STePS² lab tests (Bruneau et al., 2013a)

To develop an ice material model in LS-Dyna, a design of experiments (DOE) response surface methodology (RSM) approach was employed to systematically investigate the influence of elasto-plastic material parameters and geometric attributes on load magnitudes and pressure distributions during an ice-structure interaction process. Within the DOE umbrella of experimental design philosophies, the RSM employs mathematical and statistical methods to analyze the influence of various factors on a particular response (Montgomery, 2008). For complex and often highly nonlinear computer experiments, the RSM offers an attractive option to develop representative metamodels of the simulation results.

A sketch of the problem is provided in Figure 6-5 where a rigid shell indenter is used to crush a deformable ice model. The variable factors and their levels, fixed factors and responses are presented in Table 6-1 and an example constitutive model for the ice (elasto-plastic stress-strain curve) is plotted in Figure 6-6. The only variable factors for the ice model are the material yield strength σ_y and the ice thickness h_{ice} . This was a deliberate decision intended to simplify the analysis. The objective of this exercise was to develop

regressions for parameters of an elasto-plastic material model (proxy for ice) that will produce target process-pressure area curves, which are empirically defined, for a given set of geometric conditions. The result is a ‘constructed’ model, however it is well recognized that the elasto-plastic numerical treatment of ice crushing is highly idealized and does not capture many of the complex ice failure mechanisms that occur in reality.

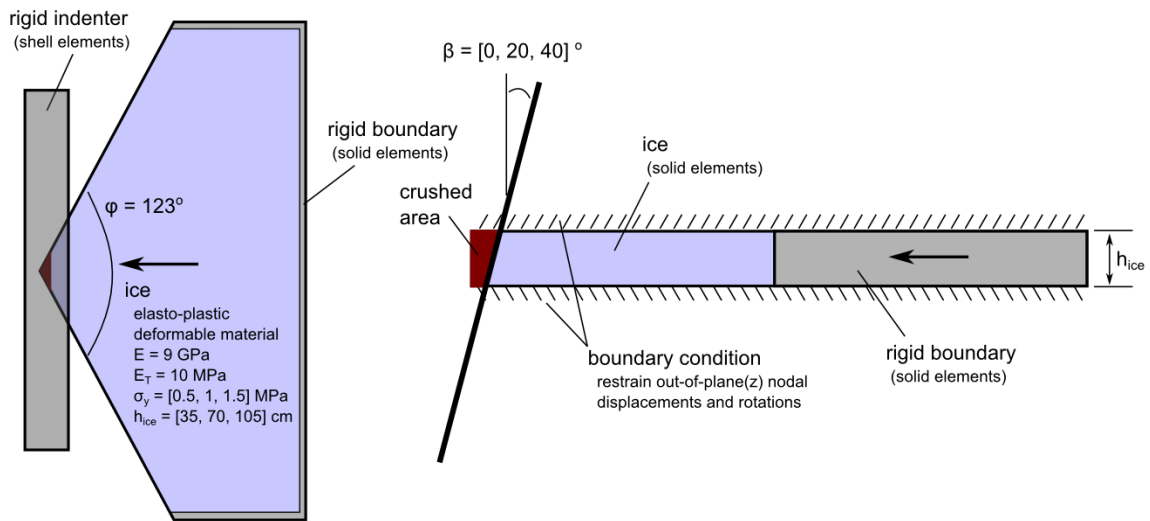


Figure 6-5: Sketch of DOE problem for ice calibration

Table 6-1: Factors and responses for ice calibration exercise

Factors	Description	Symbol	Units	Low	Medium	High
A	material yield strength	σ_y	MPa	0.5	1	1.5
B	ice thickness	h_{ice}	m	0.35	0.7	1.05
C	beta	β	°	0	20	40
fixed	ice wedge angle	Φ	°	123		
fixed	ice density	ρ_{ice}	kg/m ³	900		
fixed	ice modulus of elasticity	E_{ice}	GPa	9.0		
fixed	ice Poisson's ratio	ν_{ice}	--	0.3		
fixed	ice tangent modulus	E_t	MPa	10.0		
Responses	Description	Symbol	Units			
R1	nominal pressure at 1m ²	P_o	MPa			
R2	process P-A exponent	ex	--			

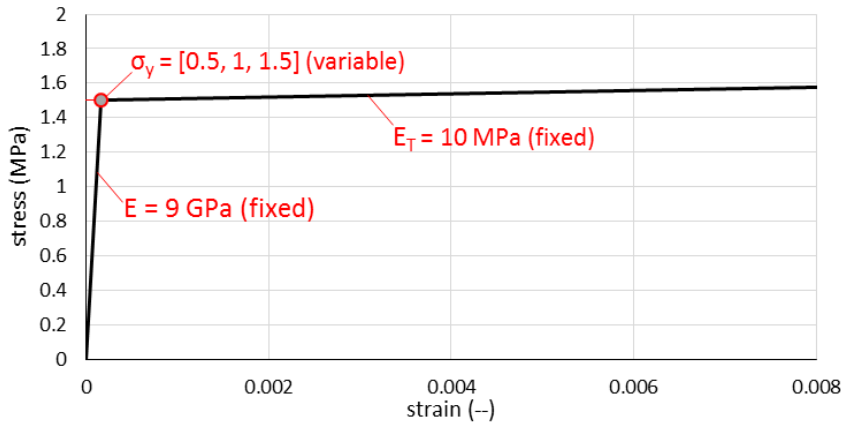


Figure 6-6: Stress-strain curve for elasto-plastic numerical ice material

The rigid indenter is a plate modeled with shell elements and rotated to variable beta β angles (0-40°). The ice is a 123° wedge, with variable thickness (35-105cm), modeled with solid elements and bounded on the back edges with a rigid support (also solid elements). Boundary conditions are imposed on the top and bottom of the ice edge to restrain out-of-plane displacements and rotations. The purpose of this restraint is to isolate the crushing problem and remove bending and bulging effects from the simulations. This is later shown to effectively concentrate contact pressures within the contact area.

In *DDePS* the nominal wedge angle ϕ is assumed to be 150°. However considering the patch size reduction to account for ice pressure concentration described in Section 4.4 (i.e. $w = 0.7 \cdot W_{nom}$), the effective pressure acting on the structure is actually increased and applied over a smaller contact area. It can be shown by rearranging the equations in Section 4.4 that an effective pressure-area model with $ex = -0.1$ and a new parameter P_{o_eff} can be derived as equation (88). Furthermore a reduced ice wedge angle can be determined following equation (89) to match the effective contact area. For a 150° nominal wedge

angle, the equivalent effective wedge is 123° and therefore used in the ice calibration simulations.

$$P_{o_eff} = \frac{P_o}{C_w^{2+2ex}} \quad (88)$$

$$\phi_{eff} = 2 \tan^{-1} \left(C_w^2 \tan \left(\frac{\phi}{2} \right) \right) \quad (89)$$

This is illustrated by Figure 6-7 for a nominal pressure-area model of $P_o = 3$ MPa, $ex = -0.1$ and a wedge angle $\phi = 150^\circ$ (black curve). Considering the patch area reduction (while maintaining constant force), the effective P-A acting on the structure is shown in by the red curve. Following equation (88) and a reduced wedge angle according to equation (89), an equivalent effective P-A relationship can be derived as $P_{o_eff} = 5.7$ MPa, $ex = -0.1$. The plot shows exact agreement with the effective P-A curve.

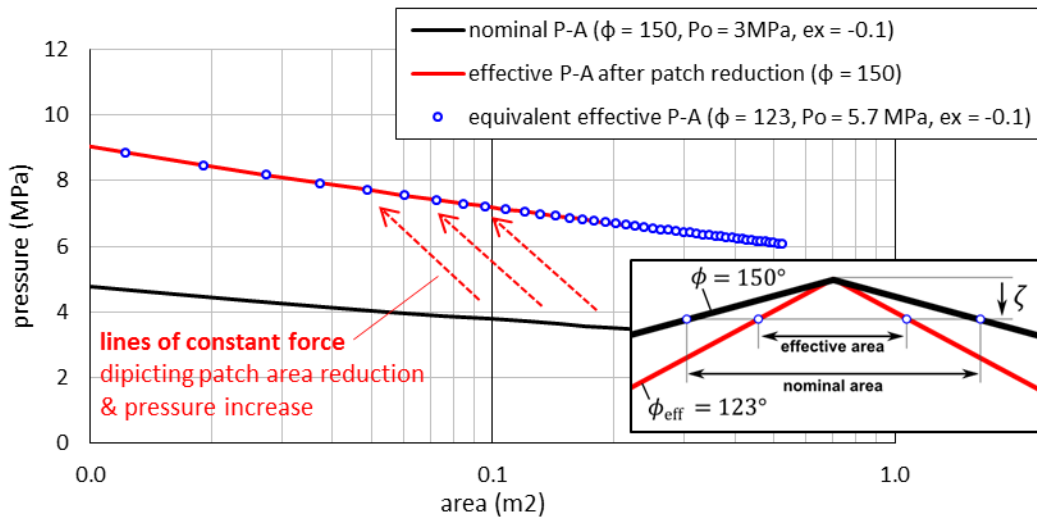


Figure 6-7: Diagram of patch size reduction and effective P-A relationship

Figure 6-8 is a snapshot of the simulation setup for an example ice calibration simulation (A_104). The solid elements for the ice are refined in the area of contact to a fine mesh (3-7cm edge length in the crushing zone). This mesh size was selected based on

the similar approximate mesh size of the structural models which are explained in the case studies. A 3.5cm mesh size was selected for the rigid plate. The final size of the ice model and mesh size selections were the result of a mesh convergence analysis and represent a balance between computational cost and numerical accuracy.

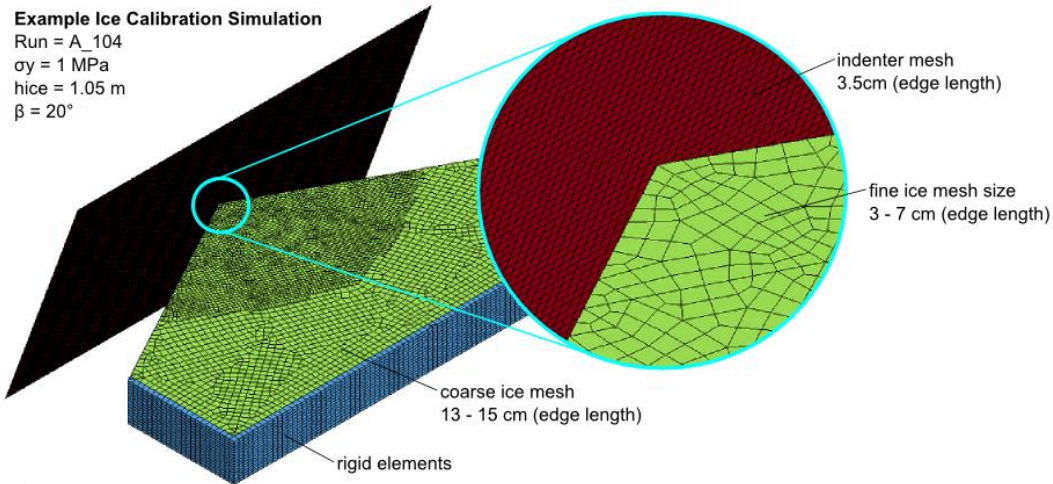


Figure 6-8: Numerical simulation setup for ice calibration simulation A_104

Figures 6-9 through Figure 6-14 present detailed results from two selected ice calibration simulation cases (A_104 and A_101 respectively). Plots are provided of the pressure distributions at 3 instances, force-time histories, area-time histories (nominal and measured), and the pressure-area results (nominal process + curve fit and measured process).

The nominal area, highlighted on the pressure distributions (white outline) and plotted on the area time histories (black), is computed following equation (32) as a function of the overlap geometry and indentation depth. This nominal area is also used in connection with the contact force to determine the nominal pressure-area relationship (black dots). For each simulation, the ‘computed’ pressure area terms (P_o and e_x) are determined by fitting a power function curve (blue) to the nominal process pressure-area data.

LS-Dyna's 'interface pressure' functionality was also used to obtain a measured contact area at each time step. The measured area is determined by the number of shell elements that are activated with a contact pressure at each time step. In almost all cases, this the measured area is larger than the nominal area. This is a result of the mesh size and contact model employed in LS-Dyna. While it is not used as part of the calibration it highlights concentrations of peak pressures inside the contact area, which are a desirable effect.

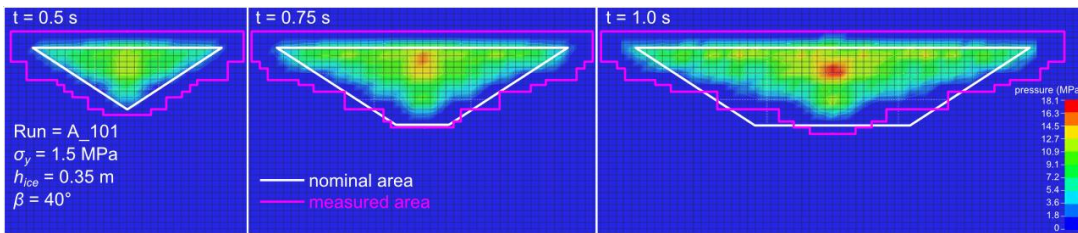


Figure 6-9: Interface pressures - ice calibration experiment A_101

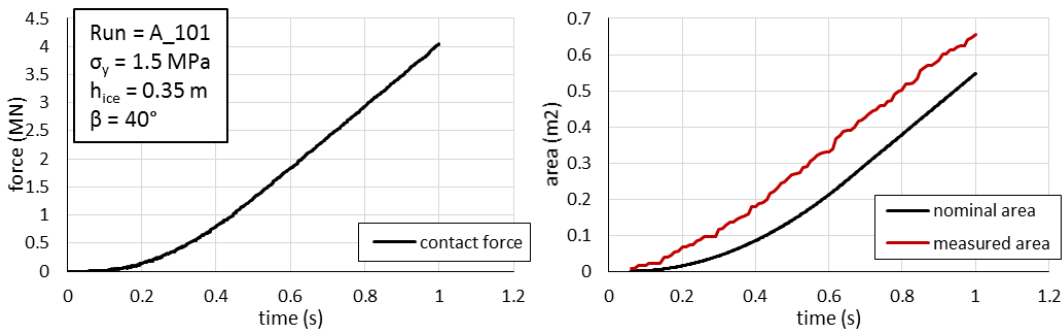


Figure 6-10: Time histories of force and contact area - ice calibration experiment A_101

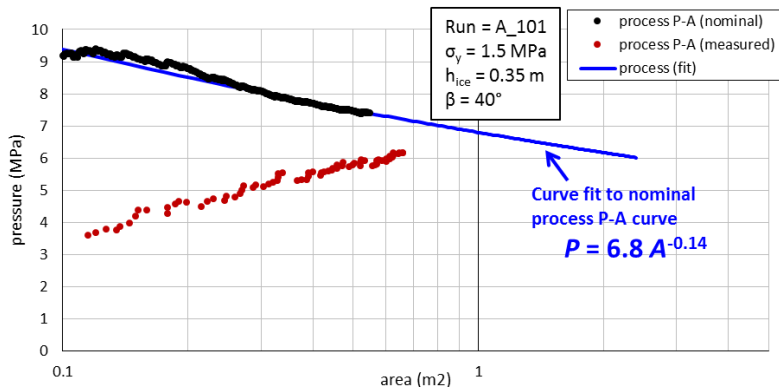


Figure 6-11: Process-pressure area curves - ice calibration experiment A_101

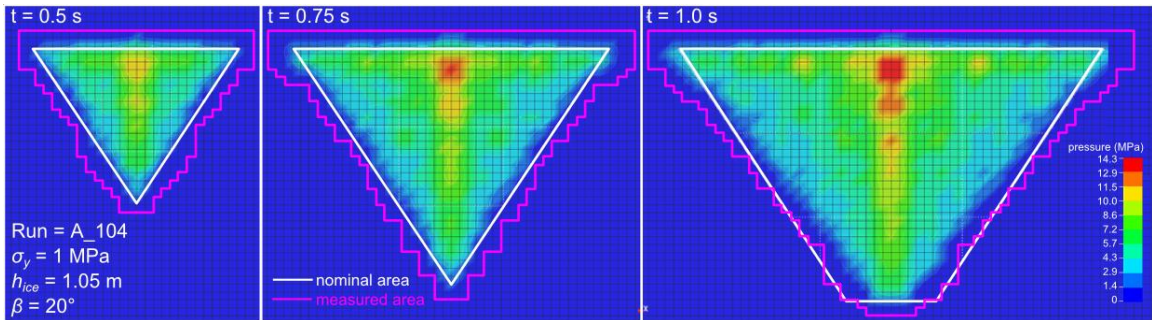


Figure 6-12: Interface pressures - ice calibration experiment A_104

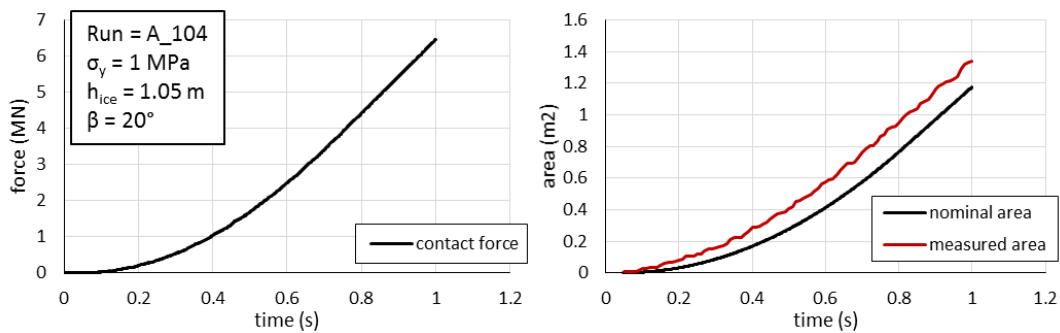


Figure 6-13: Time histories of force and contact area - ice calibration experiment A_104

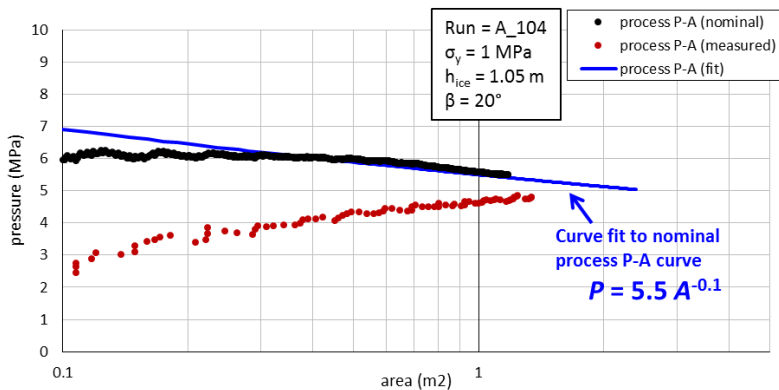


Figure 6-14: Process-pressure area curves - ice calibration experiment A_104

A summary of the initial ice calibration runs and their results are provided in Table 6-2. Randomization is not necessary when conducting computer experiments because there is no standard error. Thus, the results are sorted here in standard order. A total of 15 initial simulations were conducted and analyzed. For each run, the P-A terms (i.e. response

parameters P_o and ex) were obtained by fitting a curve to the nominal pressure-area relationship. These are listed in the table as “computed” responses. The range of P_o was 3.3 – 9.2 MPa and the range of ex was -0.2 to 0. These response levels suitably cover most target P-A model that are of interest for this study.

Table 6-2: Numerical ice calibration experiments and results – initial runs

Initial Runs							
run	σ_y (MPa)	h_{ice} (m)	β (°)	computed		predicted	
				P_o (MPa)	ex	P_o (MPa)	ex
A_101	1.5	0.35	40	6.8	-0.14	6.9	-0.1
A_102	0.5	0.7	20	3.5	-0.1	3.8	-0.1
A_103	0.5	1.05	0	3.3	0.0	3.1	0.0
A_104	1	1.05	20	5.5	-0.1	6.0	0.0
A_105	1.5	0.7	20	6.9	-0.09	7.2	-0.1
A_106	1	0.7	40	6.7	-0.07	6.1	-0.1
A_107	0.5	0.35	40	3.3	-0.2	3.3	-0.2
A_108	1	0.35	20	4.9	-0.05	5.0	-0.1
A_109	1.5	0.35	0	6.5	0.0	6.4	0.0
A_110	1.5	1.05	40	9.2	0.0	9.1	0.0
A_111	0.5	1.05	40	5.3	0.0	5.3	0.0
A_112	1	0.7	0	5.0	0.0	4.8	0.0
A_113	0.5	0.35	0	3.4	0.0	3.4	0.0
A_114	1.5	1.05	0	6.5	0.0	6.4	0.0
A_115	1	0.7	20	5.2	-0.1	5.5	-0.1

Stat-Ease, Inc.’s software package, Design Expert® Version 8.0.6, was used to determine the treatment combinations and analyze the results. Once the initial simulations were completed and the results were populated, regression calculations were conducted to check all polynomial models for each response. The effects for all model terms were calculated and statistical methods were used to compare each possible model (Stat-Ease, 2010). For both response parameters, two-factor interaction models were suggested and ultimately selected to develop metamodels. The metamodels for P_o and ex are shown in equations (90) and (91) respectively.

$$Po = 2.06 + 2.90\sigma_y - 0.56h_{ice} - 0.04\beta + 0.36\sigma_y h_{ice} + 0.01\sigma_y \beta + 0.08h_{ice}\beta \quad (90)$$

$$ex = -0.02 + 0.03\sigma_y + 0.004h_{ice} - 0.007\beta - 0.04\sigma_y h_{ice} + 0.0007\sigma_y \beta + 0.006h_{ice}\beta \quad (91)$$

In order to further verify the metamodels, an additional 12 simulations were run as verification experiments. These are necessary to test the metamodels for treatment combinations that were not tested in the original experiments. The three (3) variable factors were selected randomly for each verification run. Their results are presented in Table 6-3 and comparisons are made in Figure 6-15 between the metamodel predictions and the direct numerical simulation results. Po is predictable for a range of strength levels (3 – 9 MPa) and while not perfectly aligned with unity, the metamodel results corroborate quite well with the direct simulation results with some minimum acceptable variance. The exponent ex is less predictable but the values are within a reasonable range (-0.25 to 0).

Table 6-3: Numerical ice calibration experiments and results – verification runs

Verification Runs							
run	σ_y (MPa)	h_{ice} (m)	β (°)	computed		predicted	
				P_o (MPa)	ex	P_o (MPa)	ex
A_201	0.5	0.35	50	3.6	-0.25	3.3	-0.2
A_202	0.625	0.7	10	3.8	0.0	3.9	0.0
A_203	1.25	0.7	30	6.65	-0.08	6.7	-0.1
A_204	0.5	0.35	0	3.4	0.0	3.4	0.0
A_205	1.5	1.05	30	8.35	-0.03	8.4	0.0
A_206	1.5	0.35	10	6.5	-0.04	6.5	0.0
A_207	1.375	0.7	10	6.25	-0.03	6.4	0.0
A_208	0.875	0.35	20	4.5	-0.06	4.6	-0.1
A_209	1.5	1.05	40	9.3	-0.01	9.1	0.0
A_210	0.625	1.05	0	3.7	0.0	3.5	0.0
A_211	1.275	0.21	10	5.7	-0.04	5.7	0.0
A_212	1.2911	0.14	10	5.6	-0.04	5.7	0.0

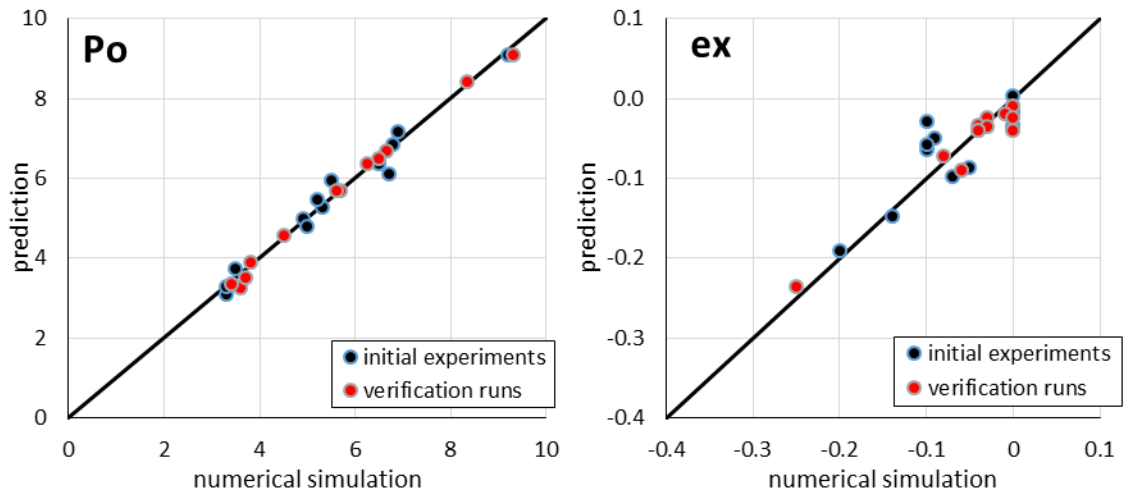


Figure 6-15: Regression predictions versus numerical simulation results for P_o and ex

Given an ice thickness h_{ice} , frame angle β , and target effective nominal pressure term P_o , equation (90) can be rearranged to find an appropriate ice yield strength σ_y for the numerical model. This is shown as equation (92)

$$\sigma_y = \frac{P_o - 2.06 + 0.56h_{ice} + 0.04\beta - 0.08h_{ice}\beta}{2.90 + 0.36h_{ice} + 0.01\beta} \quad (92)$$

7. Case Study – Ice Class PC5 Patrol Vessel

An example case study is presented in this chapter of the proposed safe speed methodology applied to a 5000 ton, Ice Class PC5 patrol vessel. First the hull form and a representative structural arrangement from the bow region are described. Next a finite element model of the representative structure is developed. The FE model is loaded using various patch loads (representing ice pressures) applied to different structural components in order to characterize the overload response and verify plastic limit states for the main frames. Once the limit states are verified, a safe speed assessment is carried out following the procedure established in Chapter 0. Several collision scenarios are used to demonstrate the mathematical model and results are presented for different assumption of nominal ice strength parameters. Finally the FE model is loaded with a deformable ice model to demonstrate the procedure in Chapter 6 taking into account the compliance of the structure.

7.1. Hull Form

The ship design in this case study is conceptual and developed by the author based on sample ships of similar hull forms and structural arrangements. Ice Class PC5 is a relatively light ice class within the IACS Unified Requirements for Polar Class Ships with a nominal ice description - “year-round operation in medium first-year ice which may include old ice inclusions” (IACS, 2011). Its strength level is higher than any of the Baltic Ice Classes or other first-year ice class notations. The ship features a moderate icebreaking hull form as shown in Figure 7-1. The lines are used to determine the hull angles and impact locations in the bow region for the ice load assessments. Table 7-1 shows the input deck for the mathematical model with all of the assumed ship particulars and hull data.

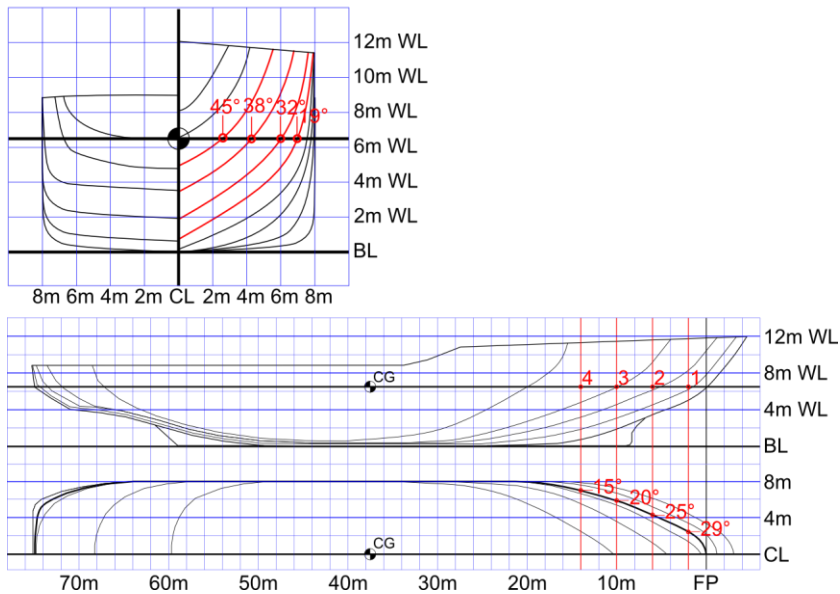


Figure 7-1: Lines plans showing bow hull angles for an Ice Class PC5 patrol vessel

Table 7-1: Main particulars and hull data for Ice Class PC5 patrol vessel

Main Particulars	Units	Symbol	Value			
ship type	--	ST	PV			
ice class	--	IC	PC5			
length overall	m	Loa	80.0			
length between perpendiculars	m	Lbp	75.0			
beam	m	B	16.0			
draft	m	T	6.5			
height (depth)	m	H	9.0			
block coef.	--	CB	0.625			
waterplane coef.	--	Cwp	0.895			
midship coef.	--	Cm	0.95			
displacement	tons	M	5000			
Hull Data	Units	Symbol	#1	#2	#3	#4
longitudinal distance from CG	m	x	35.5	31.5	27.5	23.5
transverse distance from CG	m	y	2.5	4.3	5.8	7.0
vertical distance from CG	m	z	0	0	0	0
waterline angle	deg	α	29	25	20	15
frame angle	deg	β	45	38	32	19

7.2. Hull Structural Design

A representative bow structural arrangement was developed and is sketched in Figure 7-2. The icebelt consists of T-section transverse frames spaced 610 mm apart and supported by primary decks. The scantlings of the framing and plating are indicated on the drawing and comply with minimum requirements of Ice Class PC5. The decks and bulkheads were also dimensioned along with stiffening arrangements according to typical ice belt designs. The figure highlights the extent of a finite element model that is described in the following section.

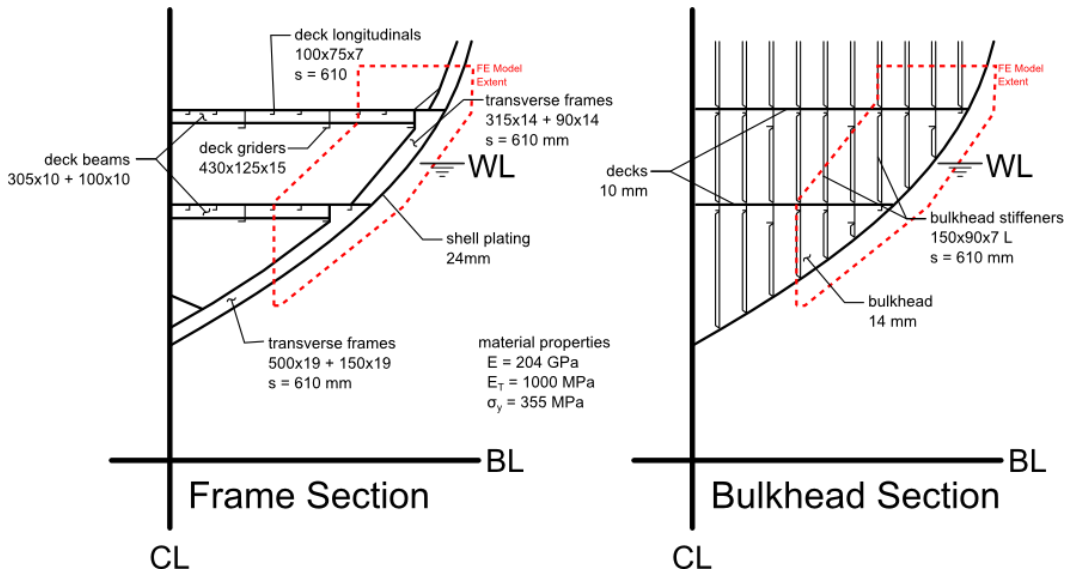


Figure 7-2: Representative structural arrangement for bow region of Ice Class PC5 patrol vessel

Table 7-2 lists the frame information is used in the analysis. It should be reiterated that this is a conceptual structural design developed to demonstrate the technical safe speed methodology. Actual structural details of a real ship are more sophisticated and dimensions/scantlings may differ from frame to frame. In this simplification, each of the neighboring frames are assumed to be identical and the finite element model was developed for one of the bow locations (between #3 and #4).

Table 7-2: Scantlings of typical frame of Ice Class PC5 patrol vessel

Offered Ice Frame Data	Units	Symbol	Value
frame orientation angle (to waterline)	deg	OA	90°
frame orientation type	--	FO	Transverse
frame attachment parameter	--	j	2
material yield strength	MPa	σ_y	355
main frame span	mm	a	2000
main frame spacing	mm	s	610
plate thickness	mm	t_p	24.0
web height	mm	h_w	315
web thickness	mm	t_w	14
flange width	mm	w_f	90
flange thickness	mm	t_f	14

7.3. Finite Element Model

A finite element model was developed based on the structural design presented above. The model, shown in Figure 7-3, is used for characterizing the response of the representative structure to various ice load scenarios and verifying the limit state equations described in Chapter 4.6. It is also used to investigate the effects of structural compliance during the ice-structure interaction process.

The finite element mesh for the hull plating, decks, bulkheads, frames, and all types of stiffening (including both webs and flanges) must be capable of capturing nonlinear material and geometric behavior. The Hughes-Liu shell element formulation offers a robust option in LS-Dyna® that explicitly considers element warping at a moderate computational expense (Quinton et al., 2016). Thus the entire structural mesh was modeled with HL shells. The longitudinal extent of the model (~4.5m) includes two transverse bulkheads (yellow) with 5 transverse icebelt frames (blue) that are supported by two

primary decks (green). The vertical extent of the model is ~6.5m. The boundary conditions include fixed nodes at the longitudinal and vertical extents, as well as the inboard extents of the bulkheads, decks, and deck beams. A mesh size of ~3-4 cm edge length was ultimately selected after a mesh convergence analysis. The mesh size and model extent were found to be sufficient to remove any mesh dependence on the load-deflection behavior. For the loading conditions considered in this study, these modeling assumptions were found to be appropriate.

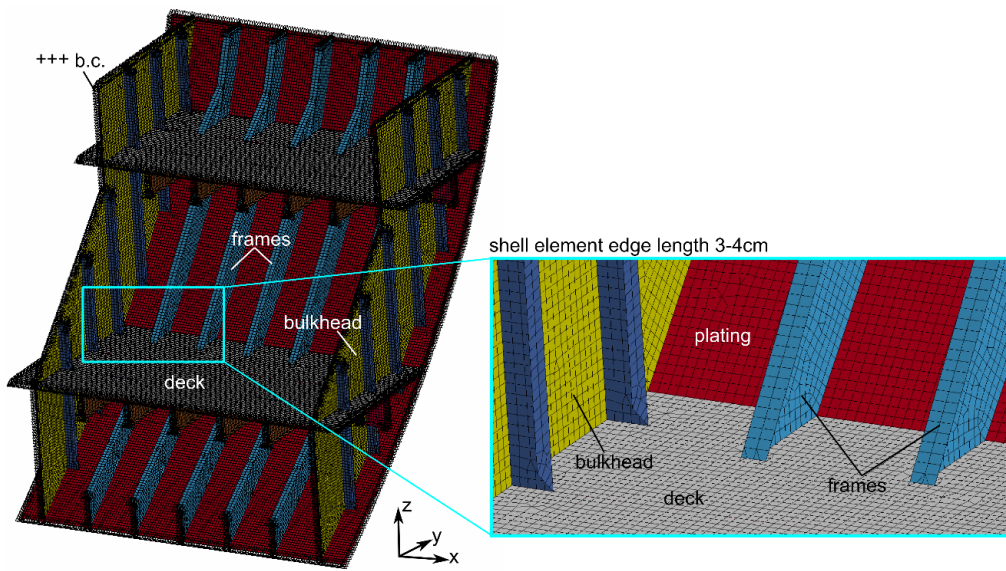


Figure 7-3: Finite element model of representative bow structure – Ice Class PC5 patrol vessel

The structure is assumed to be composed of high tensile steel with a nominal yield strength of 355 MPa, a typical material used for ice-strengthened ships. For the finite element analysis of the nonlinear response to ice loads, it is common to use bilinear plastic-kinematic hardening material model; which requires the selection of a tangent modulus that describes the strain-hardening behavior. Methods of selecting the tangent modulus differ. Preferred practice is to make a (successively refined) estimate of the range of strain experienced by highly deformed finite elements, and to choose a tangent modulus that best

predicts the strain in that range, while ensuring that stress is not over-predicted. The assumed material properties are provided in Table 7-3.

Table 7-3: Assumed material properties and bilinear plastic-kinematic model parameters

Material Properties			
Density	ρ	7,850	kg/m ³
Yield Strength	σ_y	355	MPa
Young's Modulus	E	204	GPa
Poisson's Ratio	ν	0.3	--
Tangent Modulus	E_T	1.0	GPa

7.4. Structural Response to Various Patch Loads

In order to characterize the overload response of the representative structure, a patch load analysis is carried out using the FE model via quasi-static nonlinear finite element simulations. Four load patches of different sizes and aspect ratios are applied at several locations on the structure, as shown in Table 7-4, and Figures 7-4 and 7-5. In each run, the force is gradually increased from 0 to approximately 10 MN (uniformly distributed over the load patch area).

The objective of these force-controlled simulations is to observe the overload capacity of the structure, well beyond the notional yield point of the material. In addition, the results are used to verify the Polar UR nominal frame limits for different load patch orientations. These limits can be considered notional capacities but in reality are well below any ultimate strength due to strain hardening, membrane and other effects. The results demonstrate it is reasonable to use the Polar UR frame criteria as a ‘safety point’ in an ice capability assessment.

Load cases include loads centered on a transverse frame, shell plating, and the bulkhead. The load patch sizes and aspect ratios were selected to show the different

response to concentrated local loads (A), longitudinally distributed loads (B & C), and vertically distributed loads (D).

Table 7-4: Patch load cases

run	description	load patch	force, F (MN)	pressure, P (MPa)	width, w (m)	height, b (m)
P_001	load cases centered on transverse frame	A	11.5	45.6	0.61	0.41
P_002		B	10.5	8.8	1.83	0.65
P_003		C	10.4	9.3	1.22	0.92
P_004		D	10.0	20.0	0.47	1.06
P_005	load cases centered on plating	A	11.5	45.6	0.61	0.41
P_006		B	10.5	8.8	1.83	0.65
P_007		C	10.4	9.3	1.22	0.92
P_008		D	10.0	20.0	0.47	1.06
P_009	load cases centered on bulkhead	A	11.5	45.6	0.61	0.41
P_010		B	10.5	8.8	1.83	0.65
P_011		C	10.4	9.3	1.22	0.92
P_012		D	10.0	20.0	0.47	1.06

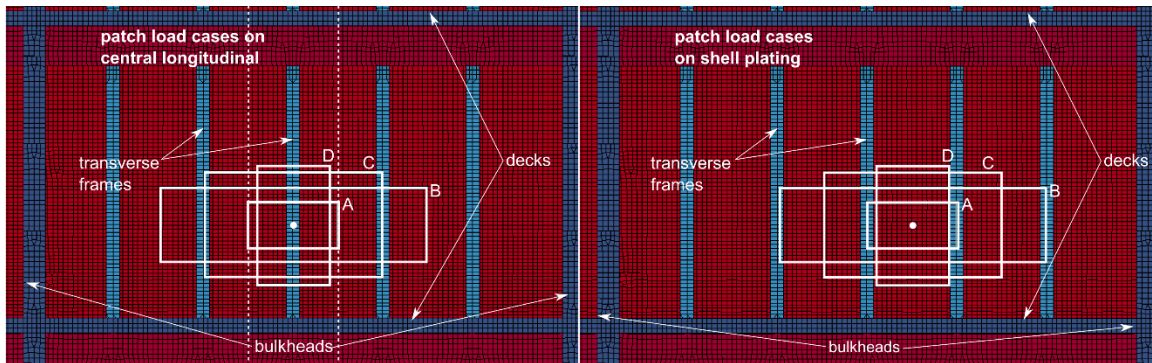


Figure 7-4: Load cases centered on transverse frame (left); Load cases centered on plating (right)

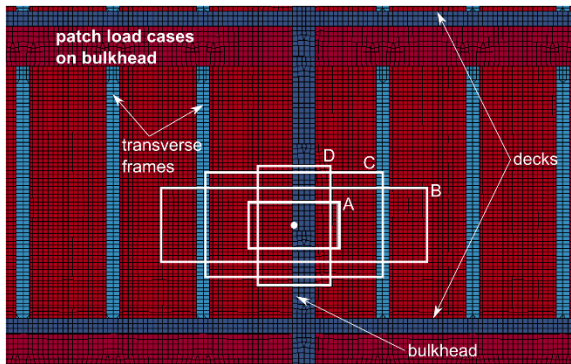


Figure 7-5: Load cases centered on bulkhead

The load vs. displacement curves (FEA results) for all of the patch load cases are shown in Figures 7-6 and 7-7. In these plots, the load is expressed as a line load $\left[Q = \frac{F}{w}\right]$ as it increases during the simulation, and displacement is the measured resultant displacement at the center of the load patch on the plating. For the frame load cases (black curves), the Polar UR nominal frame limits are also identified. While the frame response varies for each case, the limit state equations consistently predict a point prior to any major loss of frame stiffness. At these load levels, there is plasticity but the observable permanent deformation of the frame would be quite small.

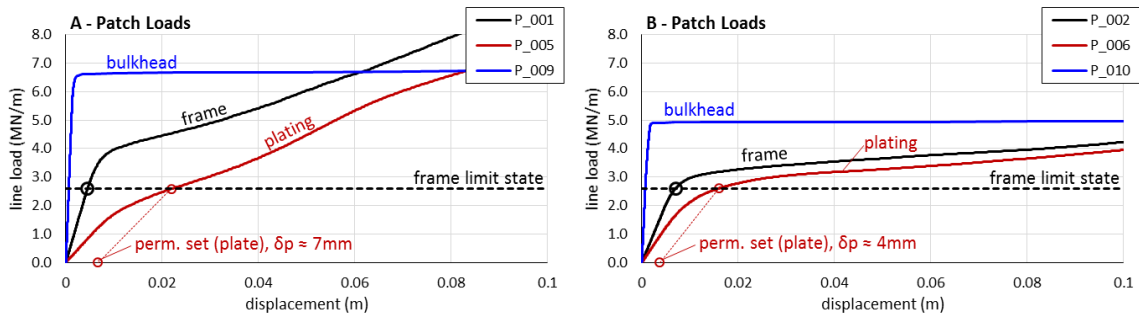


Figure 7-6: FEA results of structure response to various patch loads

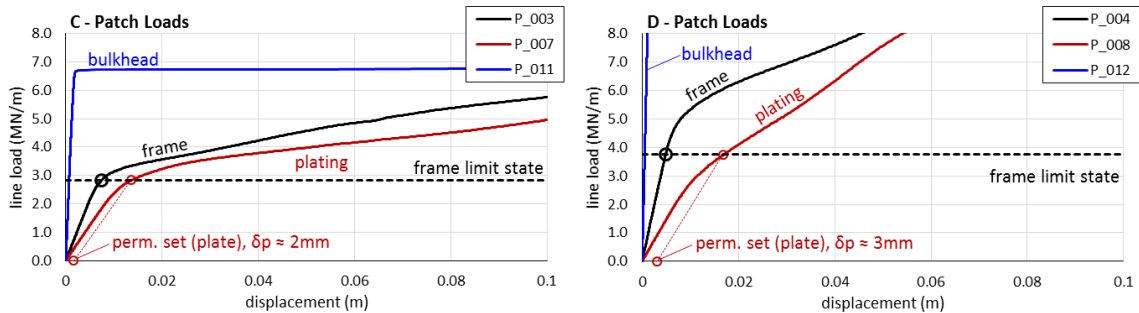


Figure 7-7: FEA results of structure response to various patch loads

For the same load patches centered on the plating, the response (red) can be quite different. At the frame limit loads, the plating exhibits some minor permanent deformation (indicated on the plots), but these are still relatively small compared to the thickness of the

plating. Two example von-Mises stress distribution plots are shown in Figure 7-8 for cases P_004 (patch D on frame) and P_008 (patch D on plating) at the frame limit load. Areas highlighted in red indicate where the stress has exceeded the material yield point (355 MPa).

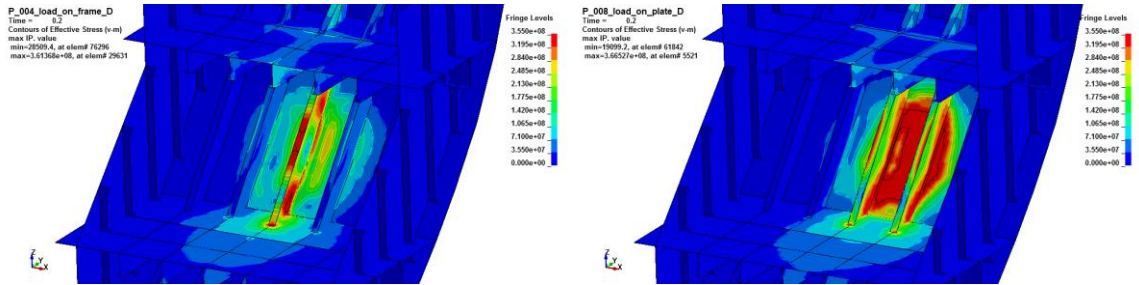


Figure 7-8: von-Mises stress distribution plots for cases P_004 (left) and P_008 (right) at the frame limit load

The bulkhead response to patch loads is substantially stiffer than the frames and plating. At the frame limits for each load case, the bulkhead remains elastic. However at higher load levels, the bulkhead web plating exhibits a rapid loss in capacity. This is caused by a post-yield instability of the bulkhead between supporting stiffeners. The contour plot in Figure 7-9 shows the stress distribution at the bulkhead collapse point in load case P_009. The transverse frames would reach their limit state at much lower load levels ($Q \approx 2 \sim 4$ MN/m, depending on the patch size), so it is not necessary to define a specific limit for these large members.

It should be noted that the frame limit state equations only consider an idealized single frame in isolation. In these analyses there is a load shedding effect to neighboring frames and other supporting members. Nevertheless, the equations predict quite reasonable load levels to set a safety point in a safe speed analysis.

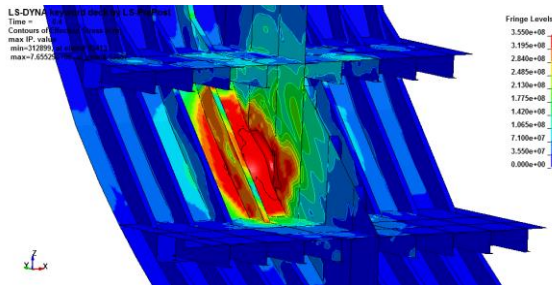


Figure 7-9: von-Mises stress distribution at point of web frame collapse – load case P_009

7.5. Safe Speed Assessment Considering Rigid Structure

An initial safe speed assessment of the patrol vessel is carried out using the mathematical model to calculate ice load parameters for a series of conditions and compare against the structural limit states. Floe size, ice thickness, and impact location are systematically varied. As described in Section 4.3 the ice floe is assumed oriented normal to the point of contact. For the purposes of computing the mass and moments of inertia, the floe is idealized as a square with uniform thickness. The wedge shape at the impact point is simply used for the contact model. At each realization of the model, the frame scantlings are checked against the load parameters. If the load (expressed as line load) exceeds the defined limit state for the transverse frame, a limit is established.

In an effort to demonstrate the procedure, several example outputs of the mathematical model are presented in the following sections. Figure 7-10 illustrates several impact scenarios that will be used for the safe speed assessment and identifies 4 example cases (i.e. individual realizations of the model). Figure 7-11 shows the line load vs. speed results for 10 m, 25 m, 50 m, and 100 m floes. Thickness is varied in each plot from 15 cm to 3 m. The example cases are also identified on the respective plots. As a general reference, recall from the previous section that the nominal frame limit loads are ~2-4 MN/m.

7.5.1. Example Outputs of the Mathematical Model

In an effort to confirm the results of the closed-form mathematical model, time history outputs for each example case are provided in Figures 7-12 through 7-15. The time histories are solved using a numerical integration scheme incrementing the normal velocity and position changes, starting from initial conditions. The algorithm calculates the ship's position (normal to collision) at each time step from the position and velocity at the previous time step.

The flexural failure modes are included to stop the integration scheme once a flexural limit is exceeded. In each example model output, the time histories of total force, patch dimensions (width and height), average pressure, and line load are provided. On the line load plots, the frame capacity is also shown (black line). The capacity is a function of the frame limit load divided by the effective load width which explains why the frame capacity reduces as the patch load becomes larger. For example F_d is the maximum force and p_d is the final pressure. These are the final values at the end of the integration scheme and are the same as the closed-form solution.

These four cases were selected in order to highlight different ice collision scenarios that produce loads which are close to the frame limit states (either slightly exceeding or below). They also represent different ice failure modes and limit conditions in the model (i.e. ice crushing/momentum limit or flexural bending limit).

Case 1 is a 6 knot impact with a 25m floe that is 3m thick. This impact is limited by momentum and there is no flexural limit in the ice. This scenario slightly exceeds the limit state of the frame.

Case 2 is 4 knot collision with a 50m floe that is 1 m thick. This scenario is also limited by momentum and the final line load is almost exactly at the frame limit state.

Case 3 is a higher speed collision (8 knots) with a large but relatively thin floe (100m x 50cm). The load is limited by a flexural failure in the ice, i.e. there is enough downward breaking force to break the ice in flexure for these thickness levels. The time history output for line load also shows the frame limit state is not exceeded.

Case 4 is a fast collision (10 knots) of a vast, thin floe (500m x 30cm). Again, the load is limited by a flexural failure in the ice and is below the frame limit state.

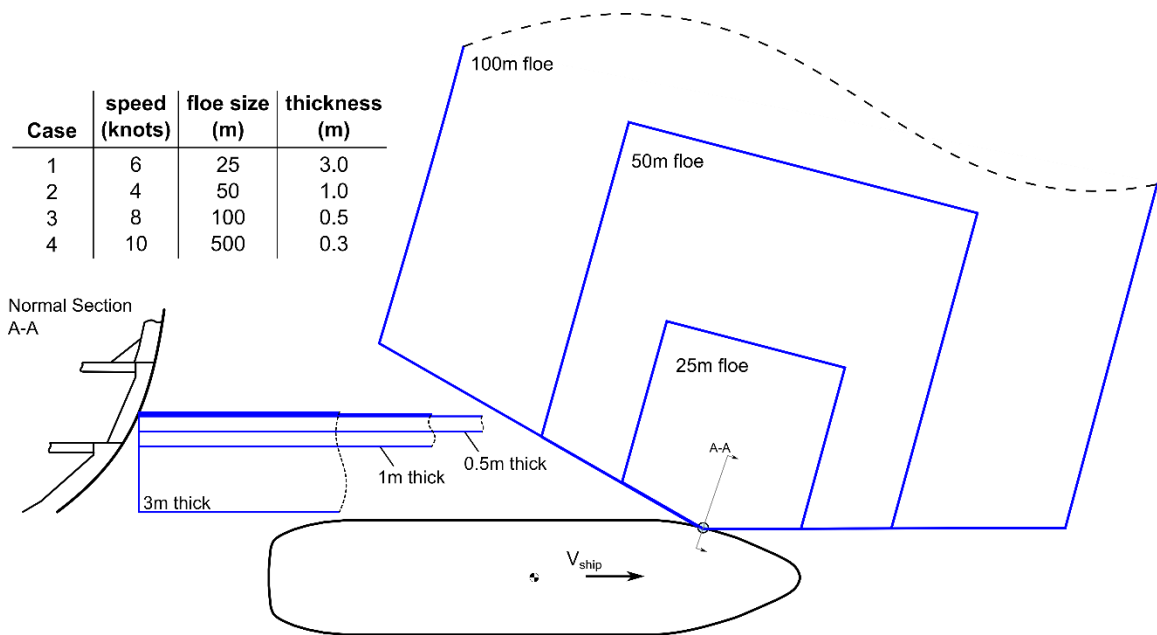


Figure 7-10: Sample DDePS calculation scenarios

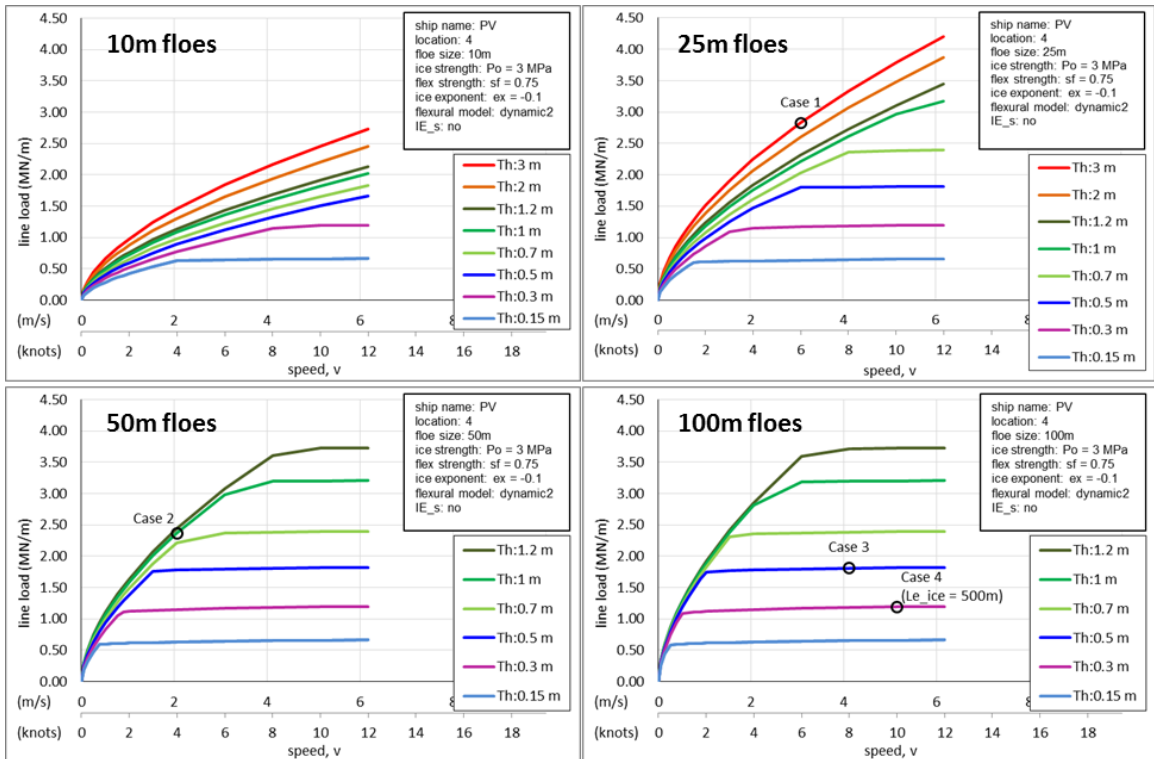


Figure 7-11: Load vs. speed results varying floe size and ice thickness (expressed in line load)

Case 1

$V_S = 6$ knots

$L_{ice} = 25$ m

$H_{ice} = 3.0$ m

$P_0 = 3$ MPa, $ex = -0.1$, $\sigma_f = 0.75$ MPa

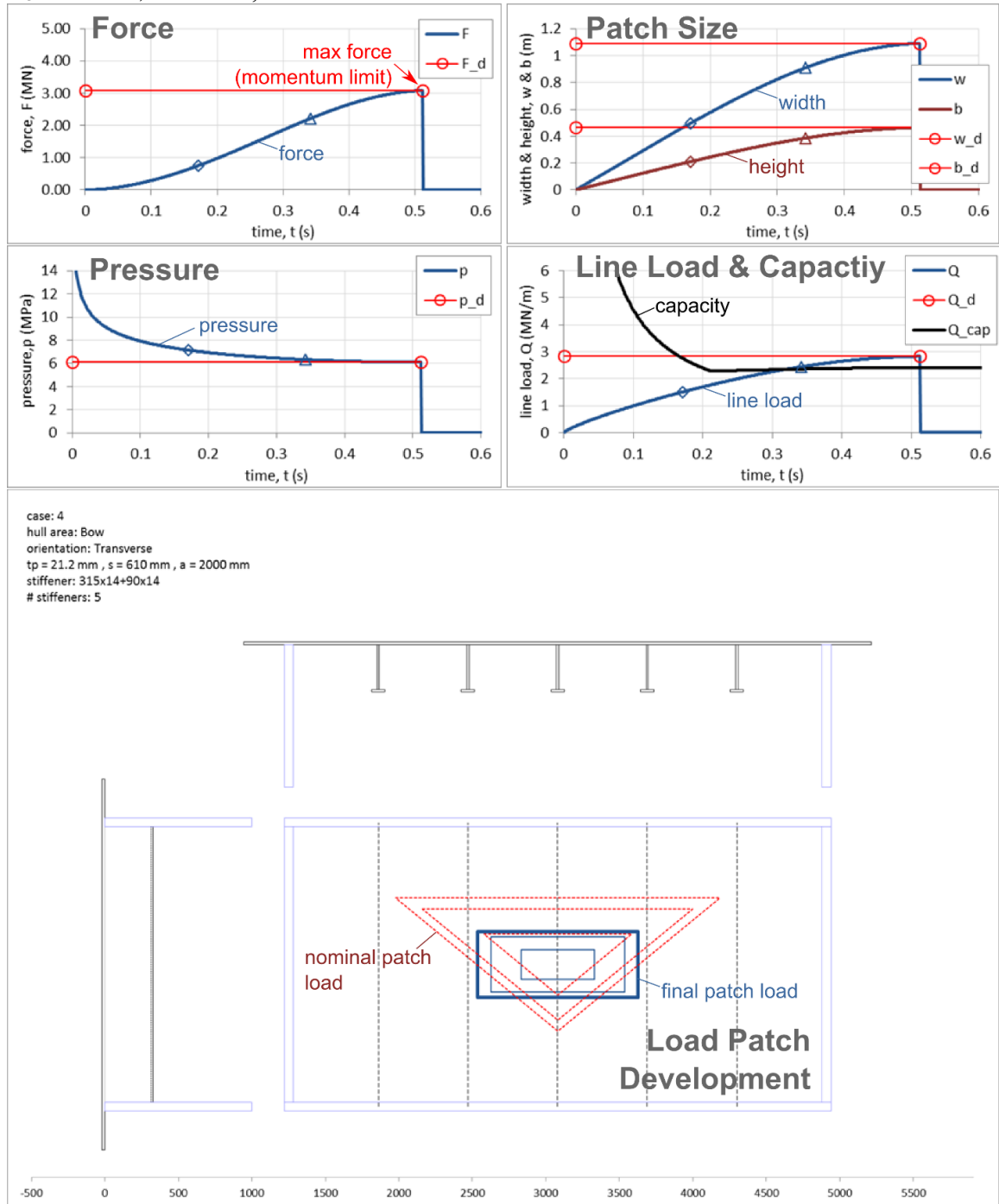


Figure 7-12: Case 1 – mathematical model outputs

Case 2

$L_{ice} = 50$ m

$H_{ice} = 1.0$ m

$V_S = 4$ knots

$P_0 = 3$ MPa, $ex = -0.1$, $\sigma_f = 0.75$ MPa

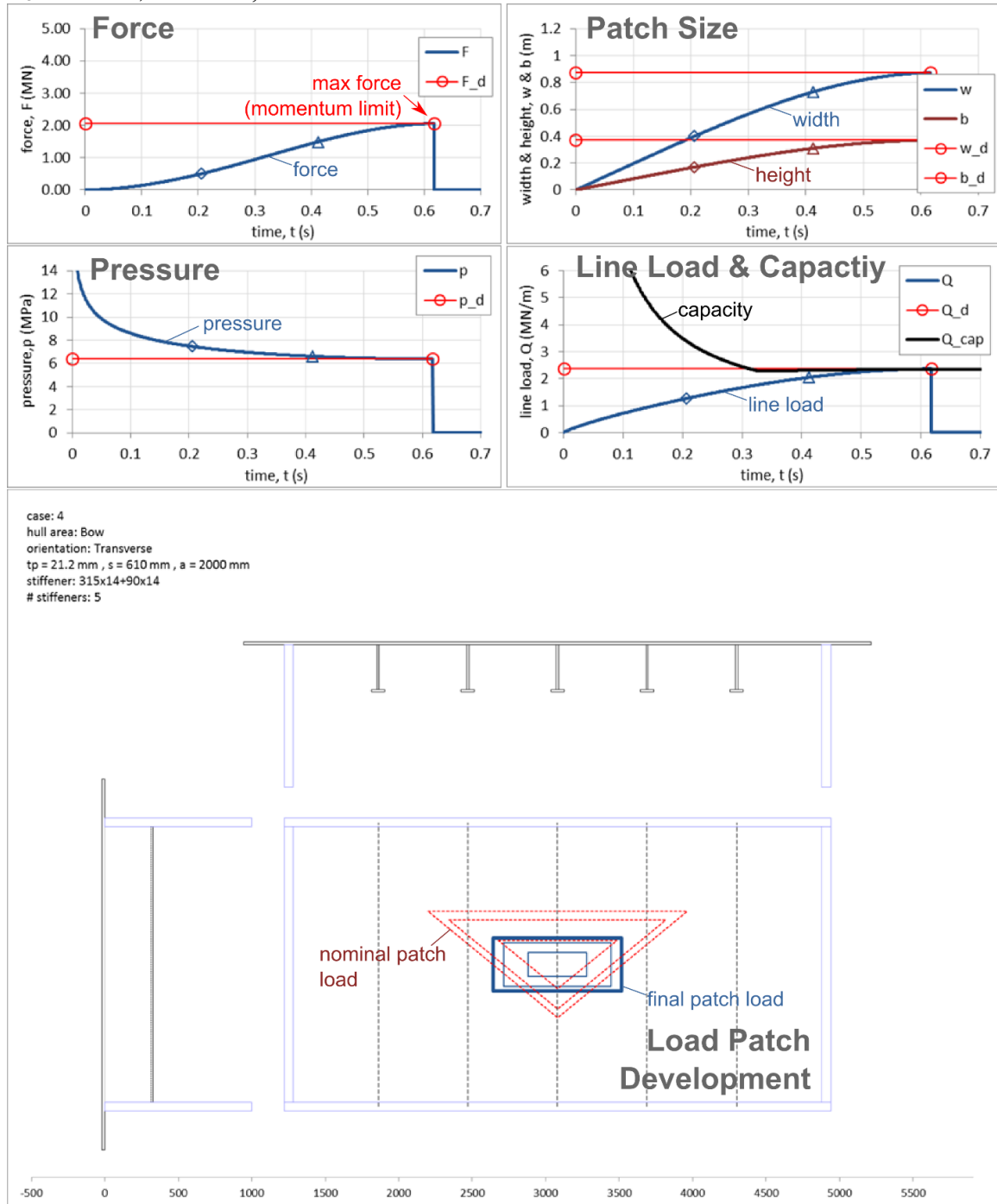


Figure 7-13: Case 2 - mathematical model outputs

Case 3

$L_{ice} = 100$ m

$H_{ice} = 0.5$ m

$V_S = 8$ knots

$P_0 = 3$ MPa, $ex = -0.1$, $\sigma_f = 0.75$ MPa

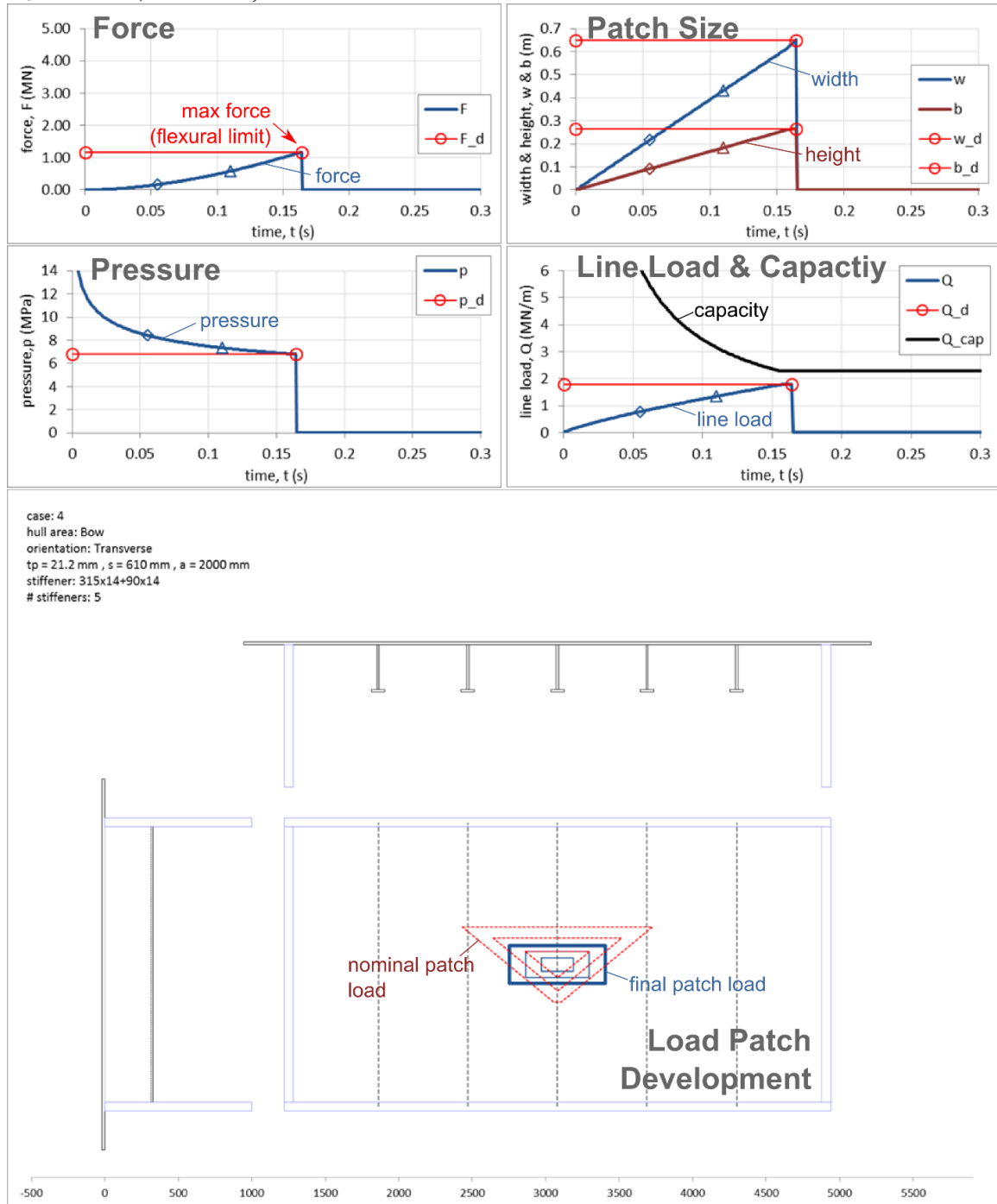


Figure 7-14: Case 3 - mathematical model outputs

Case 4

$L_{ice} = 500$ m

$H_{ice} = 0.3$ m

$V_S = 10$ knots

$P_0 = 3$ MPa, $ex = -0.1$, $\sigma_f = 0.75$ MPa

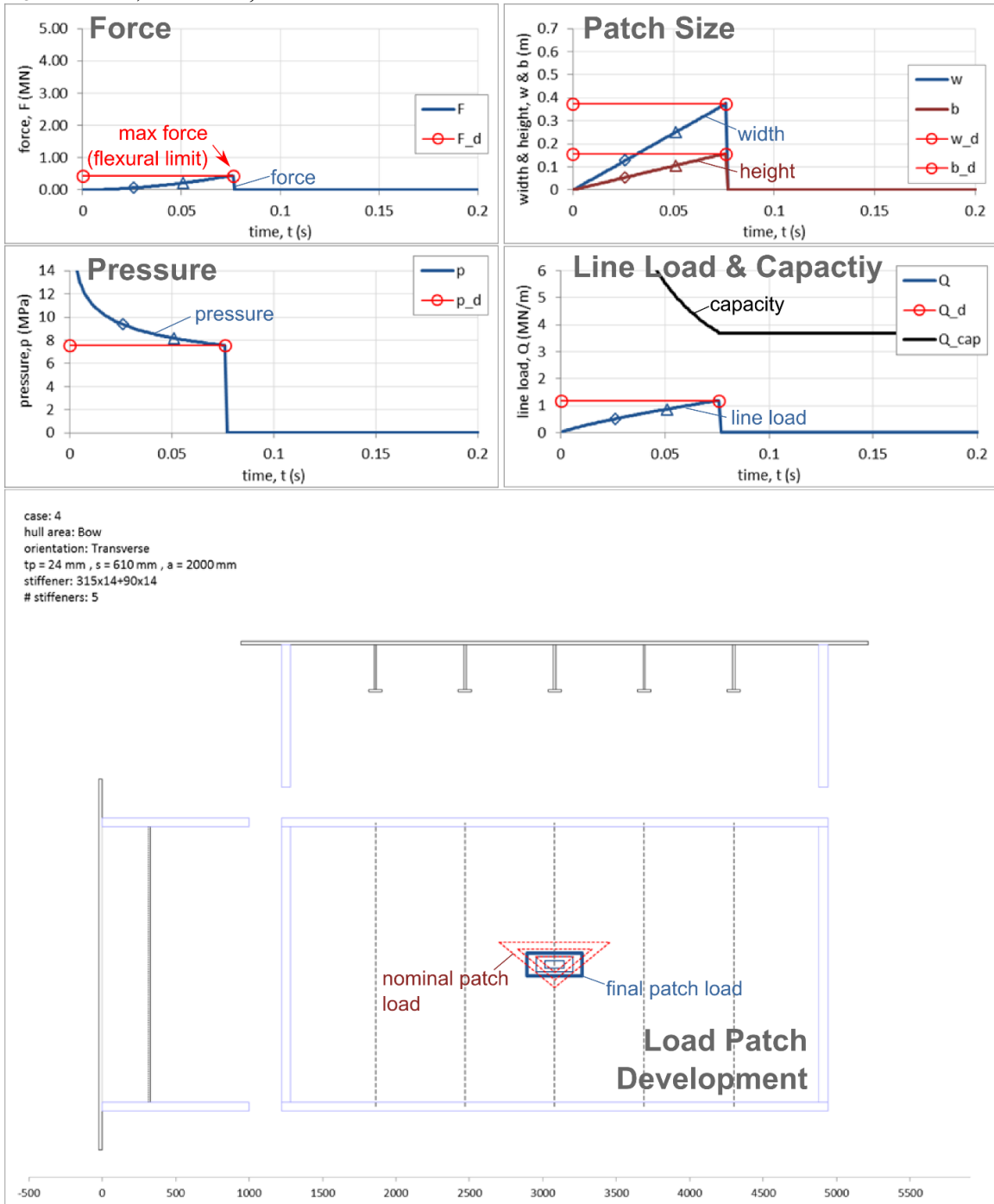


Figure 7-15: Case 4 - mathematical model outputs

7.5.2. Safe Speed Results

The mathematical model computes technical speed limits based on all combinations of ice parameters and several locations on the hull. The previous examples are just individual realizations of the model. Limits are established when the load exceeds the frame capacity. For the purposes of this study, line load (Q) is used as the basis for comparison and establishing the technical safe speed limits. Line load is the closest parameter that relates to the load encountered by a single frame. As previously described, the limit state is the formation of a 3 hinge plastic mechanism of a side shell frame under a patch load. This was shown to produce plasticity in the frame but without any major observable permanent dent size.

Figure 7-16 presents the technical safe speed results for the PC5 patrol vessel assuming the parameters in Table 7-5. In each plot, there are four curves representing different limits for different frame locations.

Table 7-5: Initial safe speed assessment parameters

Description	Units	Symbol	Value/Range
ice crushing strength	MPa	P_o	3.0 (ex = -0.1)
ice flexural strength	MPa	σ_f	0.75
floe size	m	L_{ice}	25 - 200
ice thickness	m	h_{ice}	0.15 – 3.0
ship speeds	knots	V_s	1 - 16
impact location	--	loc	1, 2, 3, 4 (see Figure 7-1)

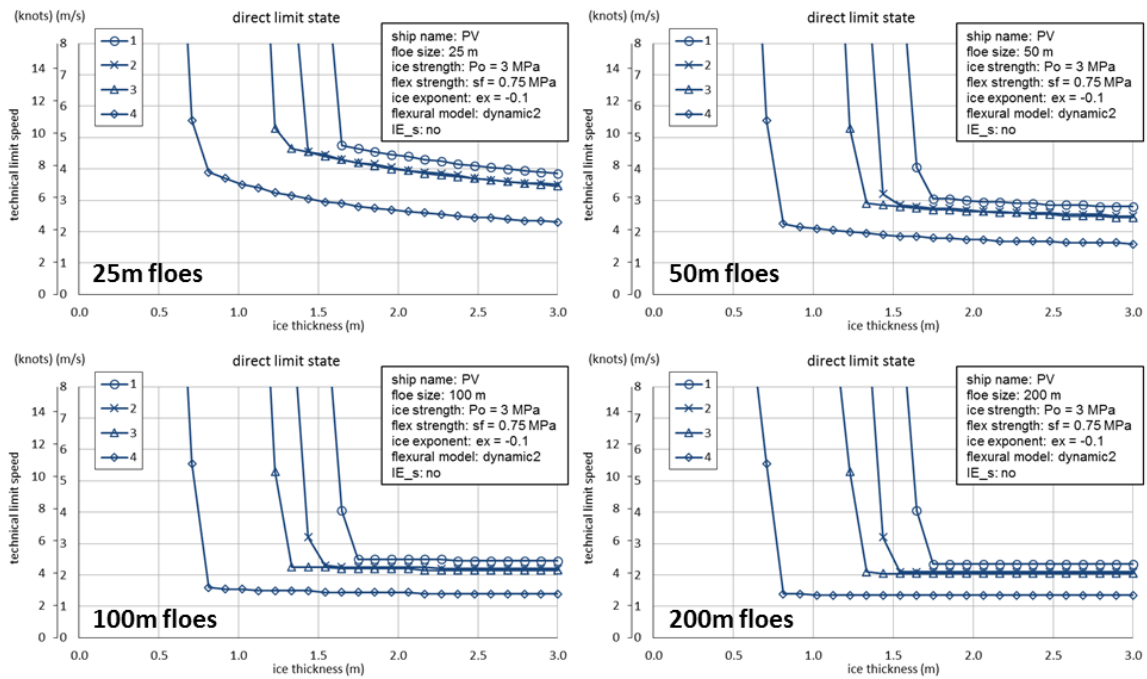


Figure 7-16: Technical safe speeds vs ice thickness for different floe sizes

Figure 7-17 is a summary plot of all the technical safe speed curves. For each impact scenario (combination of floe size and thickness), the minimum limit speed was taken of all the impact locations. The results suggest speed limitations for this ship at ice thicknesses greater than 0.5m. Below this thickness level, the flexural failure of the ice governs and the load magnitudes are lower than the frame limits. At approximately 0.75 m, the results suggest slow speed operations (< 5 knots) for floe sizes greater than 50m.

The nominal operational description for Ice Class PC5 is “year-round operation in medium first-year ice which may include old ice inclusions”. According to WMO nomenclature (referencing Table 2-1), the thickness range for medium first-year ice is 0.7-1.2 m. The outcome of this assessment is generally consistent with notional description of the ice class but offers additional information about the risks at different speeds for more combinations of conditions.

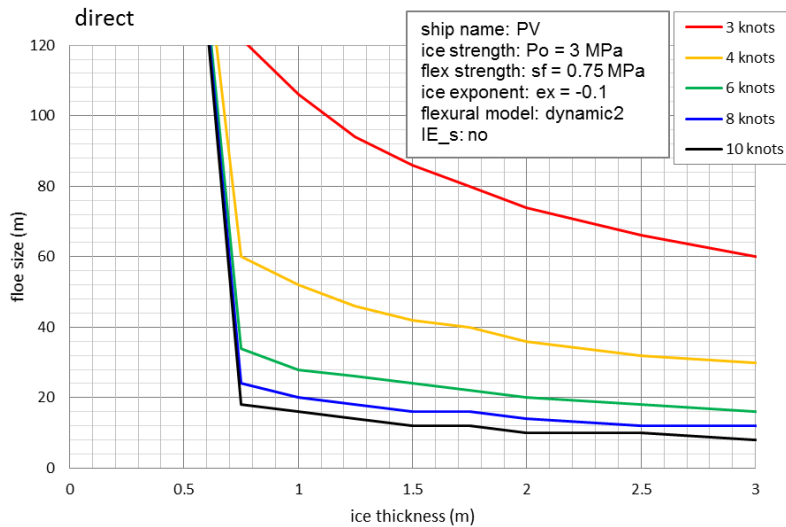


Figure 7-17: Summary plot of safe speed curves

Figure 7-18 demonstrates the influence of the ice strength terms (crushing, P_O and flexural, σ_f) on the safe speed calculation results. As indicated in the figure the crushing strength is the dominating ice failure mode in thicker ice regimes and the flexural limit dominates for thinner conditions. In this comparison the crushing strength is increased to 6 MPa, which is the assumed strength used in the design point for Ice Class PC1, and the flexural strength is increased to 1 MPa (used in the design point for Ice Class PC5).

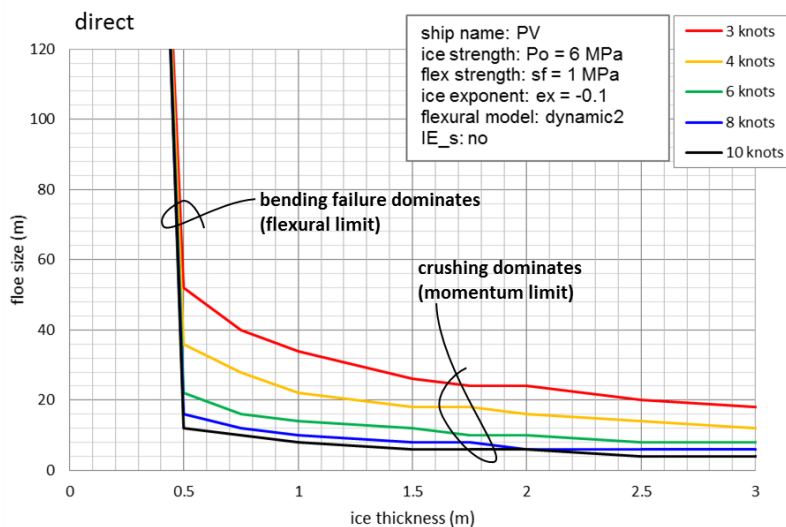


Figure 7-18: Summary plot of safe speed curves (stronger ice - $P_O = 6$ MPa, $\sigma_f = 1.0$ MPa)

7.6. Structural Response to Deformable Ice Model

The mathematical model used in the above safe speed assessment assumes the structure is rigid and all effective kinetic energy in a collision is expended into ice crushing. This section describes a numerical analysis of ice-structure interaction which takes into account the compliance of the structure during the indentation process. The analysis follows procedures presented in Chapter 6 and explores when the assumption of a rigid structure is no longer valid.

A series of numerical simulation between the Ice Class PC5 patrol vessel and deformable ice models of various thicknesses are listed in Table 7-6. The ice wedges all feature a 123° opening angle. The target strength for the ice model was based on effective process pressure area-model of $P_{o_eff} = 5.7$, $ex = -0.1$. This corresponds with a nominal P_o value of 3MPa which was used in the above safe speed assessment (which also assumed a 150° wedge angle and contact area reduction). Following the metamodel develop by the ice calibration exercise outlined in Section 6.2, the yield strength of the elasto-plastic ice model for each simulation runs is also listed in the table.

Table 7-6: Numerical simulations between Ice Class PC5 patrol vessel and deformable ice model

run	description	target P_{o_eff} (MPa)	target ex (--)	h_{ice} (m)	β (°)	$\sigma_{y_ice}^1$ (MPa)
P_101	load cases	5.7	-0.1	0.35	50	1.156
P_102	centered on	5.7	-0.1	0.7	50	0.803
P_103	transverse frame	5.7	-0.1	1.05	50	0.472
P_104	load cases	5.7	-0.1	0.35	50	1.156
P_105	centered on	5.7	-0.1	0.7	50	0.803
P_106	plating	5.7	-0.1	1.05	50	0.472
P_107	load cases	5.7	-0.1	0.35	50	1.156
P_108	centered on	5.7	-0.1	0.7	50	0.803
P_109	bulkhead	5.7	-0.1	1.05	50	0.472

Note: 1 – Determined based on metamodel, equation (92)

Screenshots of one numerical simulation (P_103) are shown in Figure 7-19. In this example a 1.05m thick ice edge is crushed against the central transverse frame. The figure highlights the development of applied pressure and von-Mises stress distribution of the hull structure. The pressure distributions exhibit areas of high and low pressures with a nominal contact area that grows as the simulation progresses. Hull stresses highlighted by a red fringe indicate areas of plasticity in the structure. Figure 7-20 plots the process pressure-area results of the applied pressure obtained from the numerical simulation. The average nominal pressure remains relatively constant and while there is minor divergence from the target P-A curve (5.7 MPa), the agreement is acceptable.

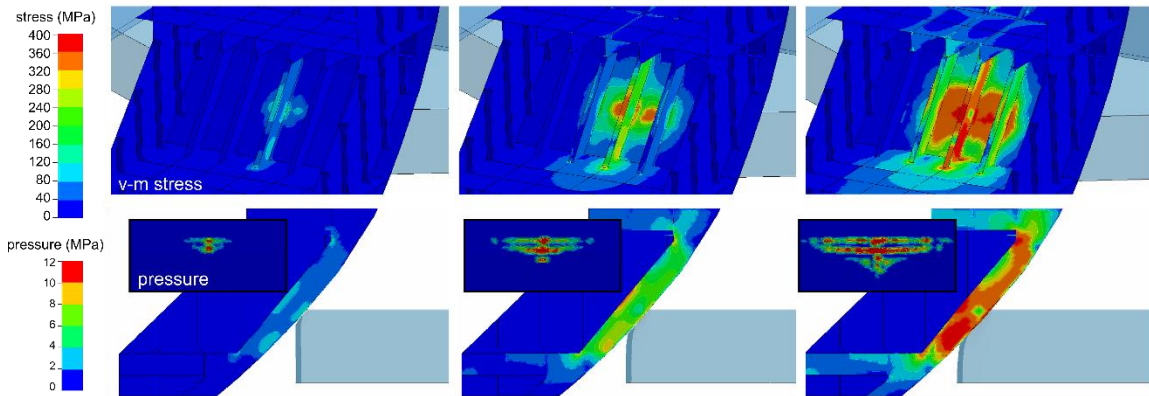


Figure 7-19: Numerical simulation – 1.05m ice edge centered on transverse frame (P_103)

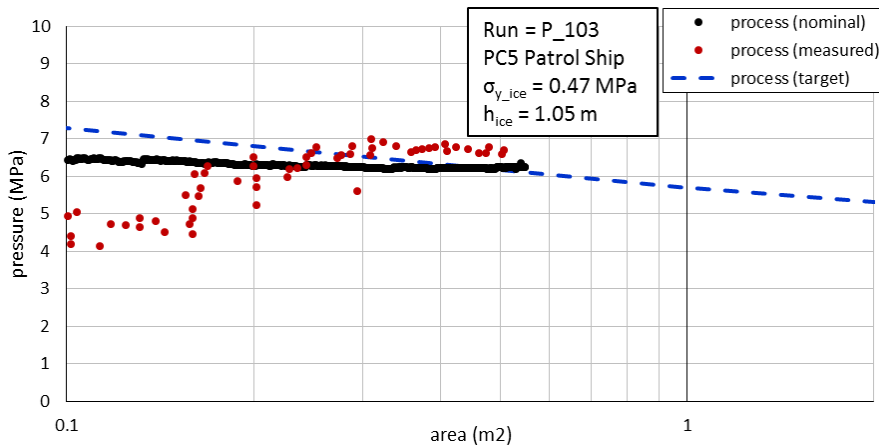


Figure 7-20: Pressure-area results – 1.05m ice edge centered on transverse frame (P_103)

From the simulation results, the structural deformation can be extracted and compared with the ice crushing component of total normal displacement. All three measurements are compared and plotted against total force in Figure 7-21. A power function curve fit (dotted red line) is also shown for the total normal displacement in the form of equation (82). Based on this plot, it appears the indentation process up to 3.5 MN is mostly dominated by ice crushing and the structural deformation component is negligible.

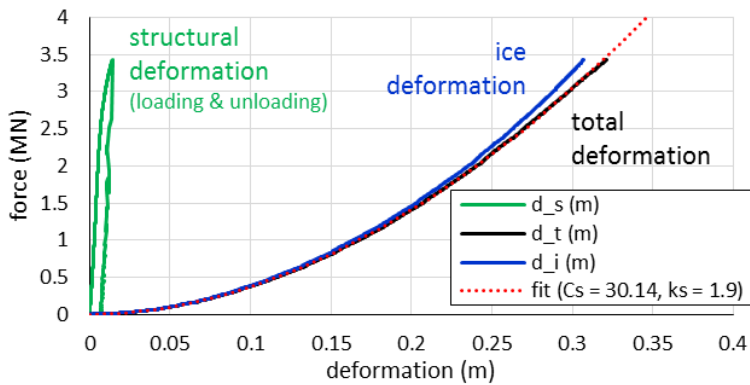


Figure 7-21: Force vs deformation results – 1.05m ice edge centered on transverse frame (P_103)

As a cross check to the patch load analysis described in Section 7.4, a plot of applied force versus structural deformation due to the indentation of the deformable ice model is shown in Figure 7-22 (green curve). The patch load analysis presented in Chapter 7.4 considered uniform pressures increasingly applied over constant areas. These load cases are also shown in the figure by the black curves. When the structure is loaded with the deformable ice model, the load patch size also increases as the force develops. This changes the response of the structure but is comparable for similar areas in the patch load analysis. The approximate patch load sizes are shown on the figure with the frame spacing as a

reference. The response to deformable ice (green) falls between cases C and D of the patch load analysis.

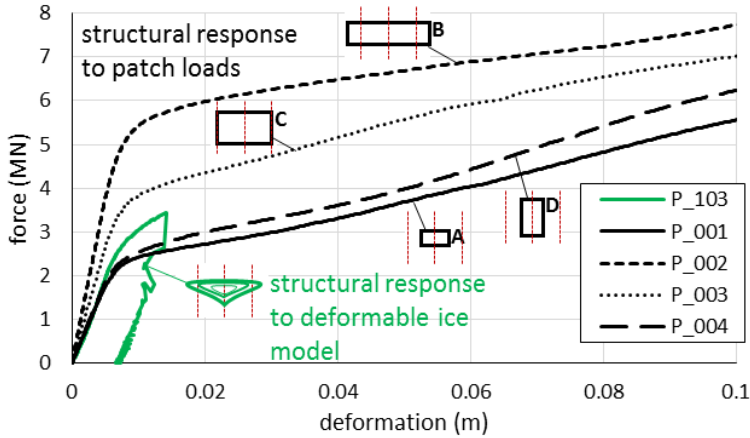


Figure 7-22: Force vs deformation comparison with patch load analysis

Additional load cases of the ice-structure interaction simulations are shown in Figure 7-23 where the ice is crushed into plate (P_106) and the bulkhead (P_109). A similar response to the frame load case is observed and thus it can be concluded that for this Ice Class PC5 vessel, structural compliance does not play a critical role in the ice structure interaction process. For higher load levels, i.e. extreme overload scenarios, one might consider higher stronger ice parameters or further indentation depths. While this is outside the scope of this thesis, the methods described in this section could certainly be applied.

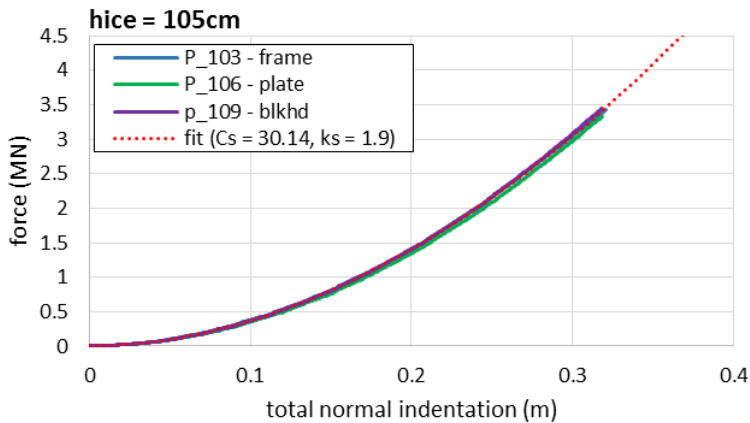


Figure 7-23: Force vs total normal deformation for additional load cases

8. Case Study – Non-ice Strengthened Naval Combatant

A second case study is presented in this chapter of a non-ice strengthened naval combatant. As described in Chapter 1, naval ships may be required to enter marginal ice zone conditions under various mission scenarios. While this particular ship type is not designed for ice operations, there is an interest to quantify its ice limitations and explore the structural risks of increasingly aggressive operations.

In a similar process as the previous case study, the first two sections of this chapter describe the hull form and a representative bow structural arrangement. A finite element model is then developed and used to characterize the overload response of different structural components and verify the plastic limit states for the side shell longitudinal stiffeners (i.e. frames). Once the limit states are verified, an initial safe speed assessment is carried out utilizing the mathematical model described in Chapter 0, assuming the structure is rigid. Several collision scenarios are used to demonstrate the mathematical model. The FE model is then loaded with a deformable ice model following the numerical analysis procedures presented in Chapter 6. Several numerical simulations are carried out to characterize the ice-structure interaction process taking into account the structural compliance, the results of which are finally used to re-evaluate the technical safe speeds of the ship while exploring the consequences of more aggressive operations (i.e. higher speeds) and a larger tolerance for structural deformations.

8.1. Hull Form

The ship design is conceptual and based on a typical frigate-sized naval combatant hull form. The bow is certainly not designed for ice operations and features relatively steep

(near vertical) frame angles. Compared to most ice class ships, the ship is extremely light. Figure 8-1 shows the lines plans and impact locations in the bow region that will be used in the ice load assessments. Table 8-1 lists the hull data (coordinates and hull angles) at four (4) locations in the bow which are used as inputs to the mathematical model.

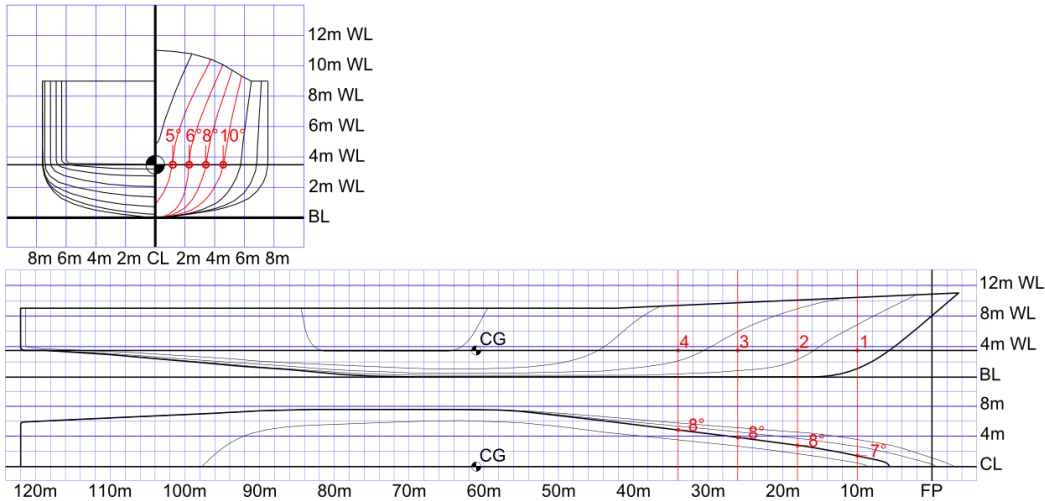


Figure 8-1: Naval combatant lines plans showing bow hull angles

Table 8-1: Main particulars and hull data for naval combatant

Main Particulars	Units	Symbol	Value			
ice class	--	IC	None			
length overall	m	Loa	130.0			
length between perpendiculars	m	Lbp	122.0			
beam	m	B	15.25			
draft	m	T	3.65			
height (depth)	m	H	9.0			
block coef.	--	CB	0.43			
waterplane coef.	--	Cwp	0.73			
midship coef.	--	Cm	0.79			
displacement	tons	M	3025			
Hull Data	Units	Symbol	#1	#2	#3	#4
longitudinal distance from CG	m	x	51	43	35	27
transverse distance from CG	m	y	1.44	2.78	3.86	4.89
vertical distance from CG	m	z	0	0	0	0
waterline angle	deg	α	7	8	8	8
frame angle	deg	β	5	6	8	10

8.2. Hull Structural Design

A representative bow structural arrangement was developed for the naval combatant. Sketches of several frame sections and other drawings are provided in Figures 8-2 and 8-3. The figures also indicate the extent of the finite element model that is used in the following sections. Near the waterline, the structure is comprised of side shell longitudinal stiffeners (i.e. frames), spaced 685 mm apart and supported by two transverse web frames. The span of the longitudinals are ~2m and the far ends are supported by stiffened bulkheads. The scantlings were verified against the minimum requirements of the *ABS Guide on International Naval Ships* (2016) for plating, framing, and decks. The structure is exceptionally light (e.g. $t_p = 9\text{mm}$, $t_w = 5\text{mm}$) relative to typical commercial structural standards and especially compared with ice class design. Table 8-2 lists the scantlings for the longitudinal stiffeners and transverse web frames developed for this case study.

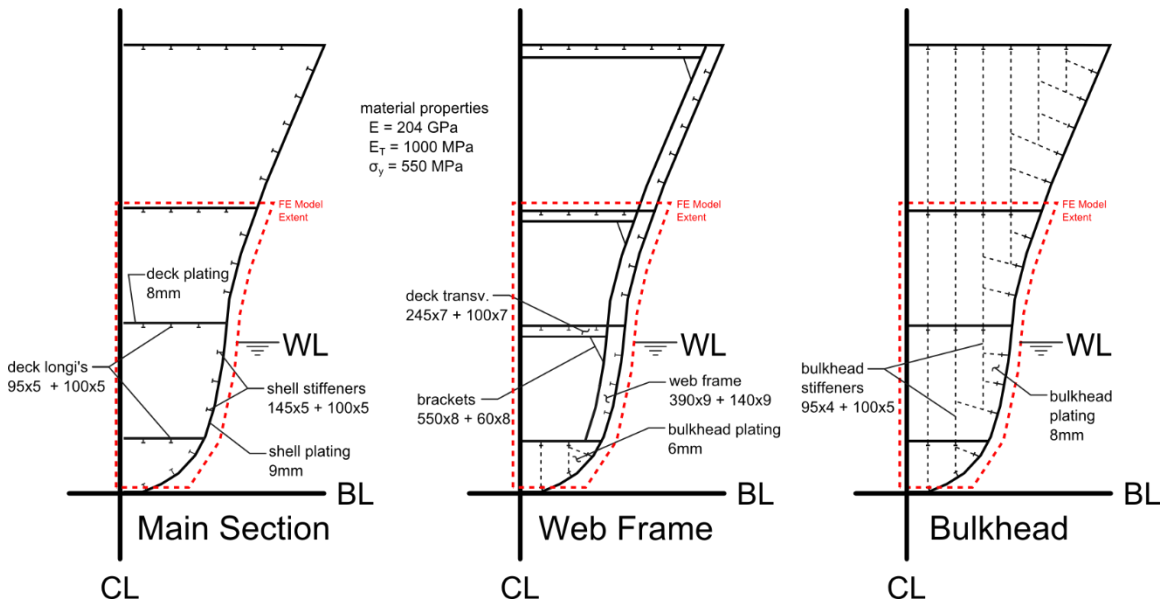


Figure 8-2: Naval combatant representative bow structural design – typical sections

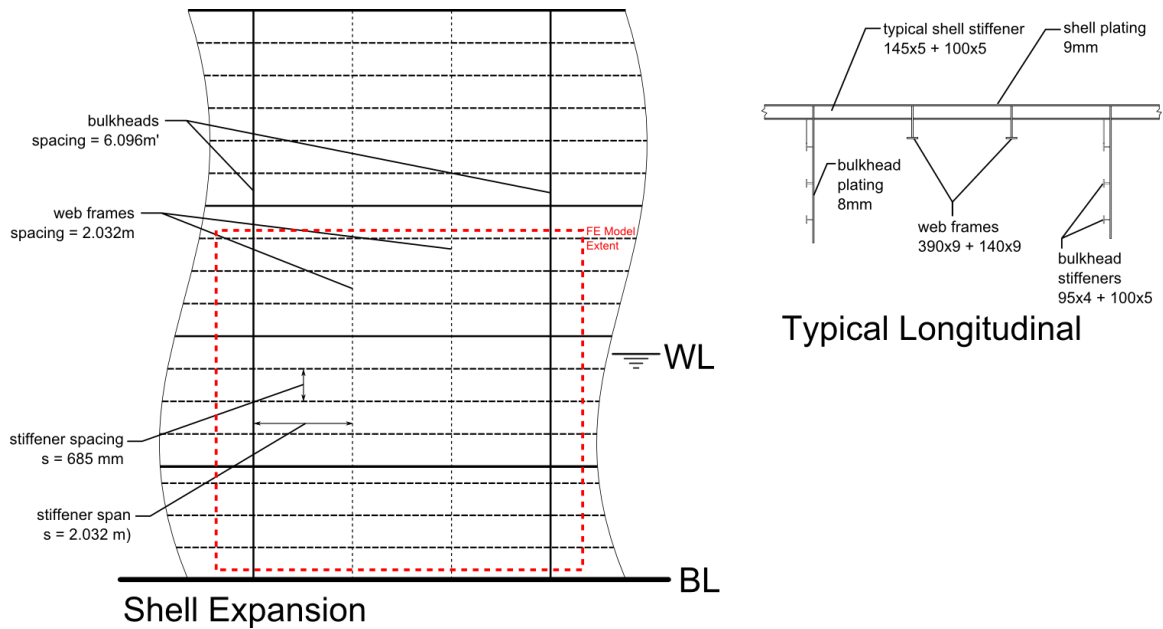


Figure 8-3: Naval combatant representative bow structural design – shell expansion and typical side shell longitudinal arrangement

Table 8-2: Scantlings of typical longitudinal and web frame for naval combatant

Description	Units	Symbol	Longitudinal	Web Frame
frame orientation angle	deg	OA	0°	90°
frame orientation type	--	FO	Longitudinal	Transverse
frame attachment parameter	--	j	2	2
material yield strength	MPa	σ_y	550	550
span	mm	a	2032	2500
spacing	mm	s	685	1000 ¹
plate thickness	mm	t_p	9	9
web height	mm	h_w	145	390
web thickness	mm	t_w	5	6
flange width	mm	w_f	100	140
flange thickness	mm	t_f	5	9

Note:

1 – effective web frame spacing used for scantling calculations

8.3. Finite Element Model

A finite element model was developed based on the representative structural design presented above. The model, shown in Figure 8-4, is used for characterizing the response of the representative structure to various ice load scenarios and verifying the limit state equations described in Chapter 4.6. It is also used to investigate the effects of structural compliance during the ice-structure interaction process.

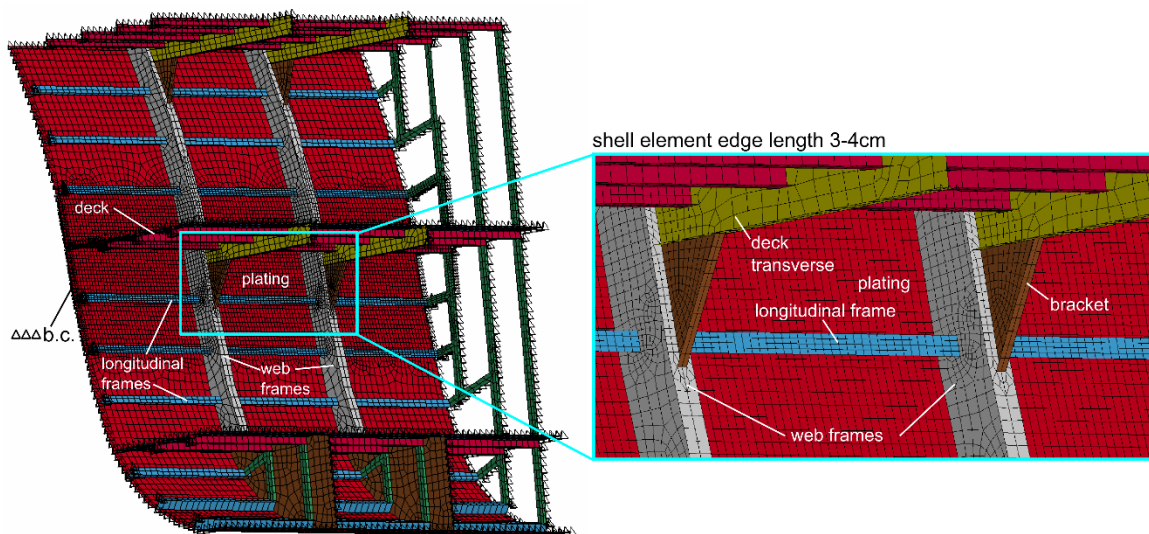


Figure 8-4: Finite element model of the representative bow structure for the naval combatant

The finite element mesh for the hull plating, decks, bulkheads, web frames, and all types of stiffening (including both webs and flanges) consists only of Hughes-Liu (HL) shell elements in order to effectively capture nonlinear material and geometric behavior.

A similar model extent was used in this case study. In the longitudinal direction, the model covers 3 spans (~6m total) of longitudinal stiffeners (blue) and includes two transverse web frames (grey). The web frames are attached to the deck transverses (yellow) via bracket connections. The vertical extent of the model is from the baseline to 3rd deck (~6.5m). The boundary conditions include fixed nodes at the longitudinal and vertical

extents, as well as the inboard extents of the decks and deck beams. A mesh size of ~3-4 cm edge length was ultimately selected after a mesh convergence analysis. This mesh size and model extent were found to be sufficient to remove any mesh dependence on the load-deflection behavior. For the loading conditions considered in this study, these modeling assumptions were found to be appropriate.

The entire structure is assumed to be composed of high-yield, high-tensile steel with a nominal yield strength of 550 MPa. A bilinear plastic-kinematic strain-hardening material model (i.e. hardening parameter = 0) with properties listed in Table 8-3 was applied. This has been shown to best represent the yield surface behavior under similar loading conditions to be applied to this model (Quinton, 2015).

Table 8-3: Material properties and bilinear plastic-kinematic model parameters

Material Properties			
Density	ρ	7,850	kg/m ³
Yield Strength	σ_y	550	MPa
Young's Modulus	E	204	GPa
Poisson's Ratio	ν	0.3	--
Tangent Modulus	E_T	1.0	GPa

8.4. Structural Response to Various Patch Loads

In order to characterize the overload response of the naval combatant representative structure, a series of patch loads were applied to the models via quasi-static nonlinear finite element simulations in the same manner as Section 7.4. Four load patches of different sizes and aspect ratios were applied at several locations on the structure for a total of 19 simulations listed in Table 8-4. Figures 8-5 and 8-6 illustrate the location of the load patches on various structural members. In each run, the force was gradually increased from 0 MN to approximately 1 MN (over the load patch area).

Table 8-4: Patch load cases

run	description	load patch	force, F (MN)	pressure, P (MPa)	width, w (m)	height, b (m)
N_001	central load cases on longitudinal	A	0.85	16.7	0.30	0.17
N_002		B	0.98	16.7	0.61	0.39
N_003		C	0.94	4.2	1.22	0.28
N_004		D	1.03	2.8	0.20	0.61
N_005	end load cases on longitudinal	A	0.85	8.3	0.30	0.17
N_006		B	0.98	16.7	0.61	0.39
N_007		D	1.03	4.2	0.20	0.61
N_008	central load cases on plate	A	1.24	8.3	0.30	0.24
N_009		B	0.93	16.7	0.61	0.37
N_010		C	0.83	4.2	1.22	0.24
N_011		D	1.05	2.8	0.20	0.62
N_012	central load cases on web frame	A	1.24	8.3	0.30	0.24
N_013		B	0.93	16.7	0.61	0.37
N_014		C	0.95	4.2	1.22	0.28
N_015		D	1.01	2.8	0.20	0.59
N_016	central load cases on bulkhead	A	0.99	8.3	0.30	0.19
N_017		B	0.99	16.7	0.61	0.39
N_018		C	0.99	4.2	1.22	0.29
N_019		D	1.03	2.8	0.20	0.61

The objective of these force-controlled simulations was to observe the overload capacity of the structure, well beyond the notional yield point of the material. In addition, the results are used to verify the Polar UR nominal frame limits described in Section 4.6 for different load patches. These limits can be considered notional “capacities” but in reality are well below any ultimate strength due to strain hardening, membrane and other effects. The results demonstrate it is reasonable to use the Polar UR frame criteria as a ‘safety point’ in an ice capability assessment.

Load cases included central loads on the longitudinal, end loads on the longitudinal, central loads on the plating, and loads on the web frame and bulkhead. The load patch sizes and aspect ratios were selected to show the different response to concentrated local loads

(A), longitudinally distributed loads (B & C), and vertically distributed loads (D). The load cases are not specific to any particular ice-hull interaction scenario but cover an approximate range of relevant contact areas for this ship.

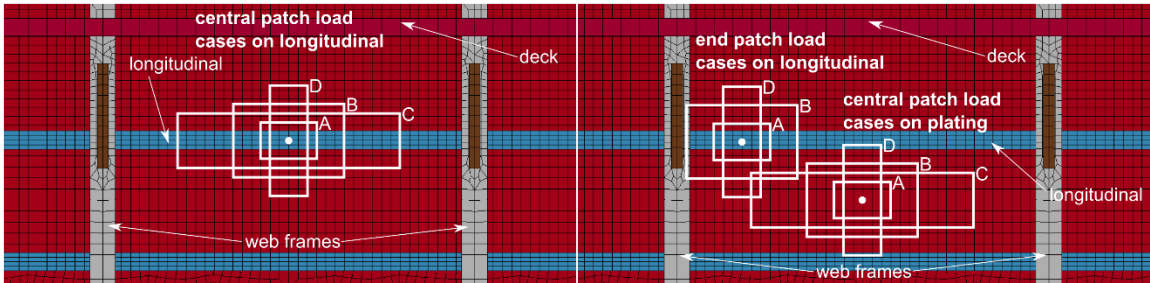


Figure 8-5: Central load cases on longitudinal (left); End load cases on longitudinal and load cases on plating (right)

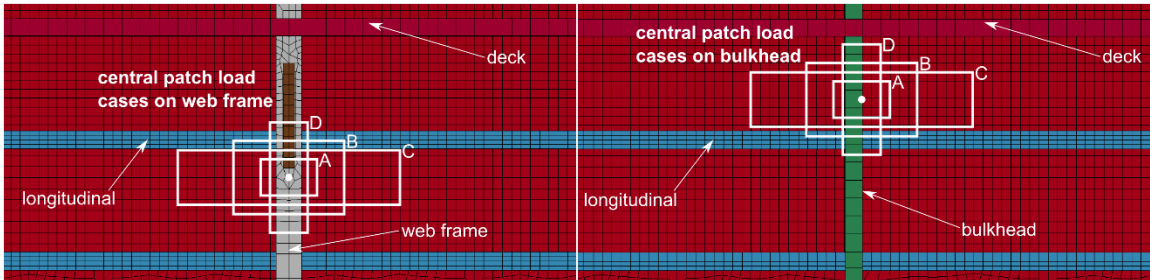


Figure 8-6: Load cases on web frame (left); Load cases on bulkhead (right)

The load vs. deflection curves (FEA results) for all of the patch load cases are shown in Figures 8-7 and Figure 8-8. Each plot corresponds to a different load patch size (A, B, C and D) and shows the structural response of various loaded components. For the longitudinal frame load cases (black curves), the Polar UR nominal frame limits are also identified. While the frame response varies for each case, the limit states consistently predict the onset of large deformations and a transition to loss of stiffness. At these load levels, there is plasticity but the observable permanent deformation of the frame would be quite small.

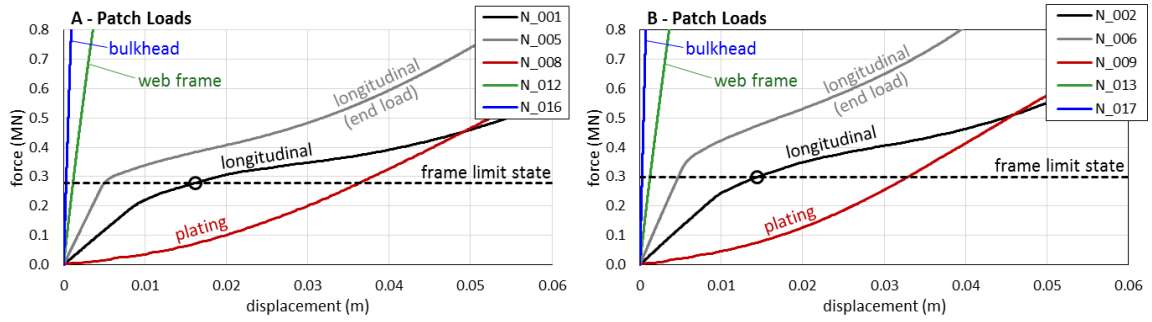


Figure 8-7: FEA results of structure response to various patch loads

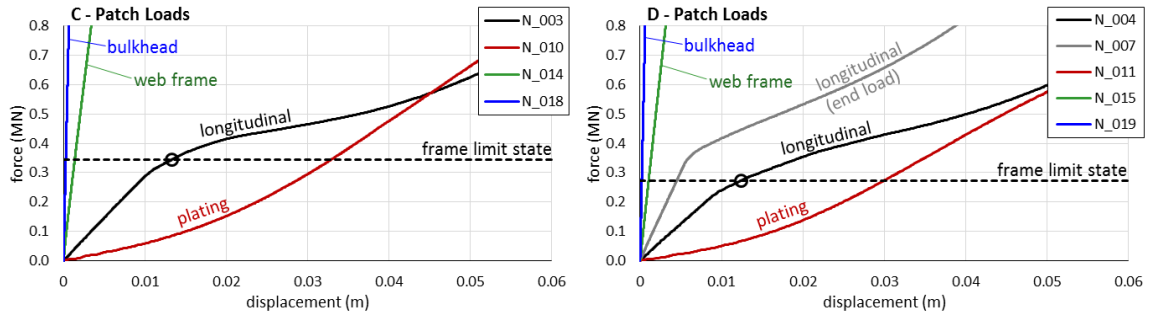


Figure 8-8: FEA results of structure response to various patch loads

When the load is applied to other structural members, the response exhibits a different behavior. The end load cases on the longitudinal frames generally show a stiffer response than the central cases. The plating for example, which is relatively thin, is dominated by a region of elastic membrane action followed by a plastic membrane response. At load levels corresponding to the respective frame limit (hashed black line), the response is predominantly elastic. Permanent deformations of the plating upon unloading from this point are negligible. Furthermore, the membrane action provides a much greater overload reserve for the plating compared with the longitudinal frames.

Example von-Mises stress distribution plots are shown in Figure 8-9 for cases N_001 (frame central load case A) and N_008 (plate central load case A) at the equivalent load level of the frame limit state. Areas highlighted in red indicate where the stress has exceeded the material yield point (550 MPa). It should be noted that the limit state

equations only consider an idealized single frame in isolation. In some of these analyses there is clearly a load shedding effect to neighboring frames and other supporting members. Nevertheless, the equations predict quite reasonable load levels to set a safety point.

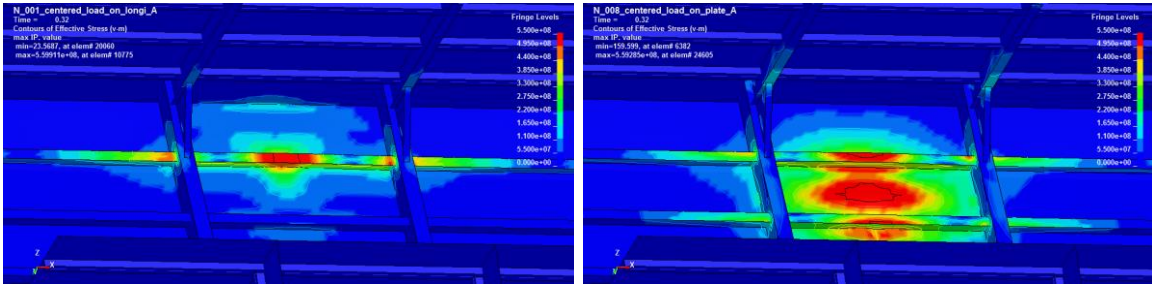


Figure 8-9: von-Mises stress distribution plots for cases N_001 (left) and N_008 (right) at the frame limit load

Figure 8-10 shows the response of the bulkhead and web frame load cases. For the most part the response of these large members remain elastic under the applied load cases. However for higher, concentrated loads (i.e. small concentration load patch on the web frame), the web frame and bulkhead exhibit a rapid loss in capacity. These plots show the stress distribution at the onset of this collapse. It is noted that the longitudinal frames would reach their limit state at a much lower load level ($\sim 0.2 - 0.4$ MN, depending on the patch size). Thus it is not necessary to define specific limits for these large members.

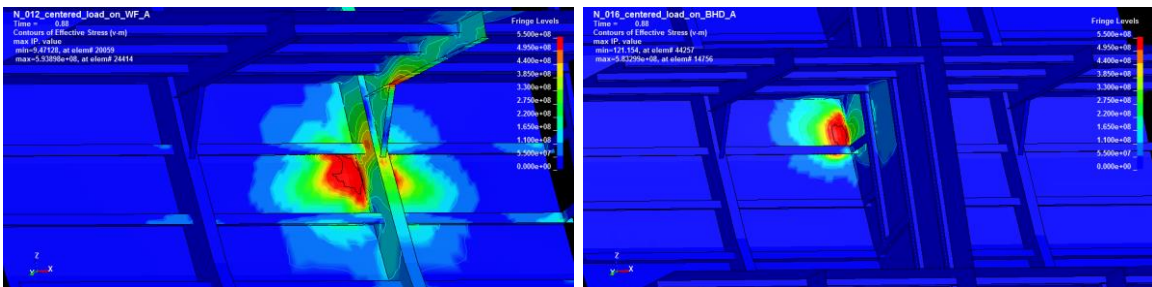


Figure 8-10: von-Mises stress distribution plots for cases N_012 (left) and N_016 (right) at web frame and bulkhead collapse points

8.5. Safe Speed Assessment Considering Rigid Structure

An initial safe speed assessment of the naval combatant is carried out using the mathematical model to calculate ice load parameters for a series of conditions and compare

against the structural limit states. Floe size, ice thickness, and impact location are systematically varied. As described in Section 4.3 the ice floe is assumed oriented normal to the point of contact. For the purposes of computing the mass and moments of inertia, the floe is idealized as a square with uniform thickness. The wedge shape at the impact point is simply used for the contact model. At each realization of the model, the frame scantlings are checked against the load parameters. If the load (expressed as line load) exceeds the defined limit state for the transverse frame, a limit is established.

In an effort to demonstrate the procedure, several example outputs of the mathematical model are presented in the following sub-section. Figure 8-11 is a sketch of several impact scenarios that will be used for the safe speed assessment and identifies 4 example cases (i.e. individual realizations of the model). Figure 8-12 shows the force vs. speed results for 10 m, 20 m, 50 m, and 100 m floes. Thickness is varied in each plot from 15 cm to 1.2 m. The example cases are also identified on the respective plots. As a general reference, recall from the previous section that the nominal limit loads of the longitudinals are ~0.2-0.4 MN.

8.5.1. Example Outputs of the Mathematical Model

In an effort to confirm the results of the closed-form mathematical model, time history outputs for each example case are provided in Figures 8-13 through 8-15. The time histories are solved using a numerical integration scheme incrementing the normal velocity and position changes, starting from initial conditions. The algorithm calculates the ship's position (normal to collision) at each time step from the position and velocity at the previous time step. In each example model output, the time histories of total force, patch

dimensions (width and height), average pressure, and line load are provided. On the line load plots, the frame capacity is also shown (black line). The capacity is a function of the frame limit load divided by the effective load width which explains why the frame capacity reduces as the patch load becomes larger. The subscript “_d” represents the final value for the respective parameter. For example F_d is the maximum force and p_d is the final pressure. These are the final values at the end of the integration scheme and are the same as the closed-form solution.

These three (3) cases were selected in order to highlight different ice collision scenarios that produce loads which are close to the frame limit states (either slightly exceeding or below). The flexural failure limit is never achieved in these cases because the frame angle is so close to the vertical ($\beta = 6^\circ$). The load is governed by ice crushing and a momentum limit.

Case 1 is a 5 knot impact with a 20m floe that is 30cm thick. The frame limit state is slightly exceeded.

Case 2 is 3 knot collision with a 50m floe that is 50cm thick. The frame limit state is significantly exceeded.

Case 3 is a very slow speed collision (2 knots) with a large but thin floe (100m x 15cm). Although the flexural limit of the ice is not exceeded the maximum ice load does not exceed the frame limit state.

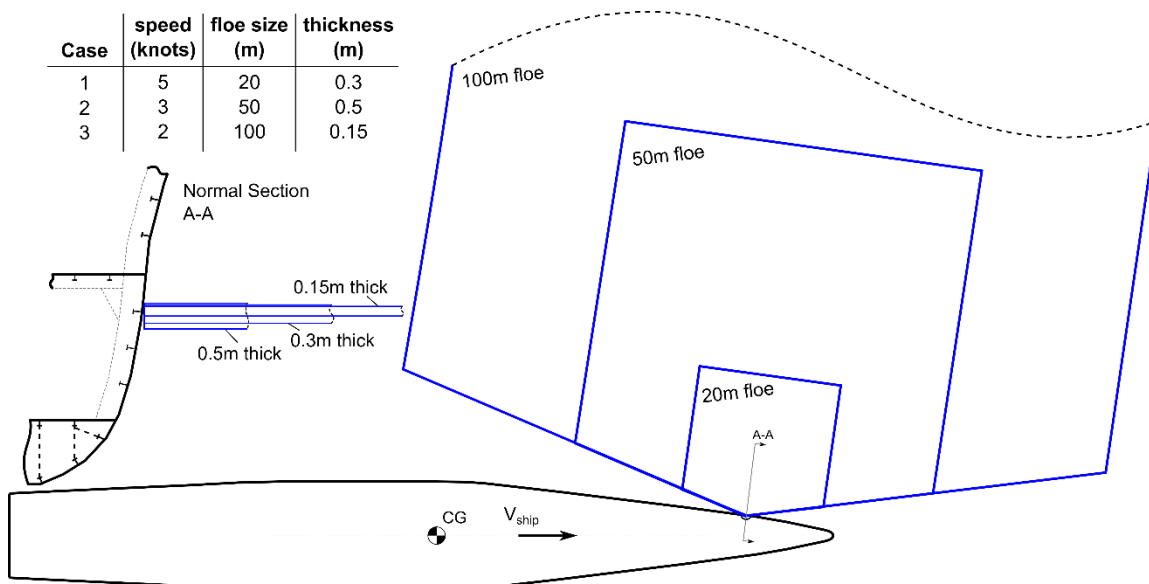


Figure 8-11: Impact scenarios for naval combatant safe speed assessment

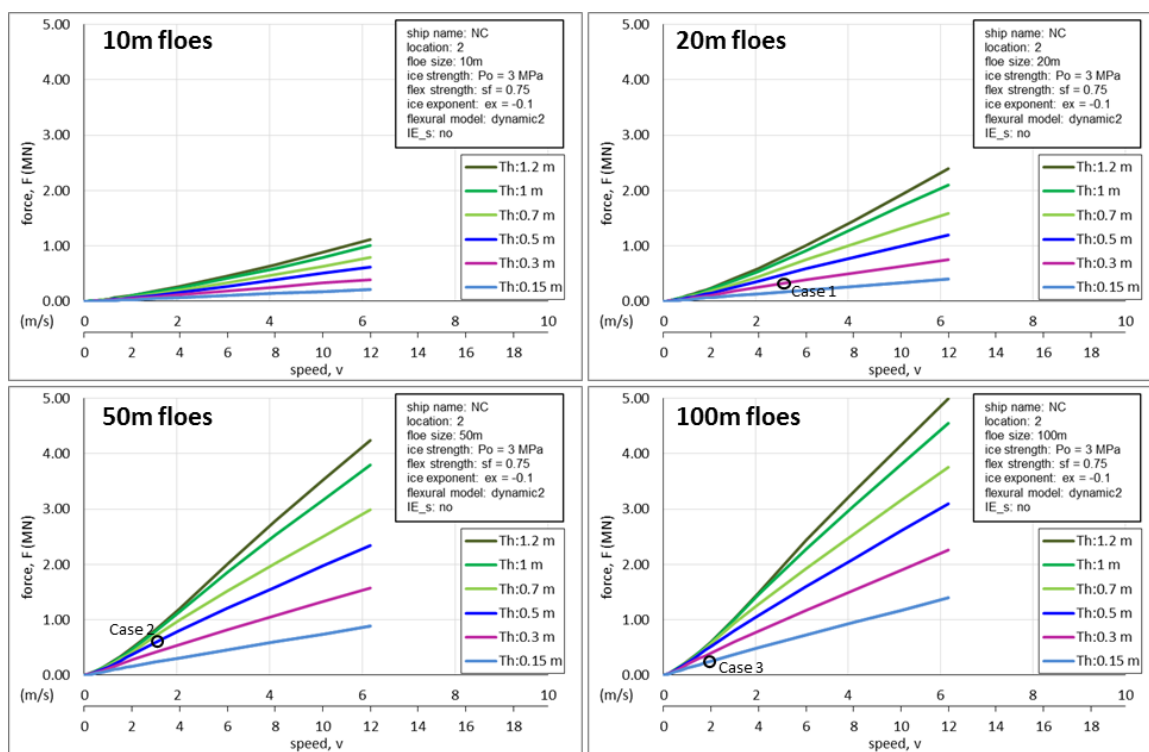


Figure 8-12: Force vs. speed results varying floe size and ice thickness

Case 1

$V_S = 5$ knots

$L_{ice} = 20$ m

$H_{ice} = 0.3$ m

$P_0 = 3$ MPa, $ex = -0.1$, $\sigma_f = 0.75$ MPa

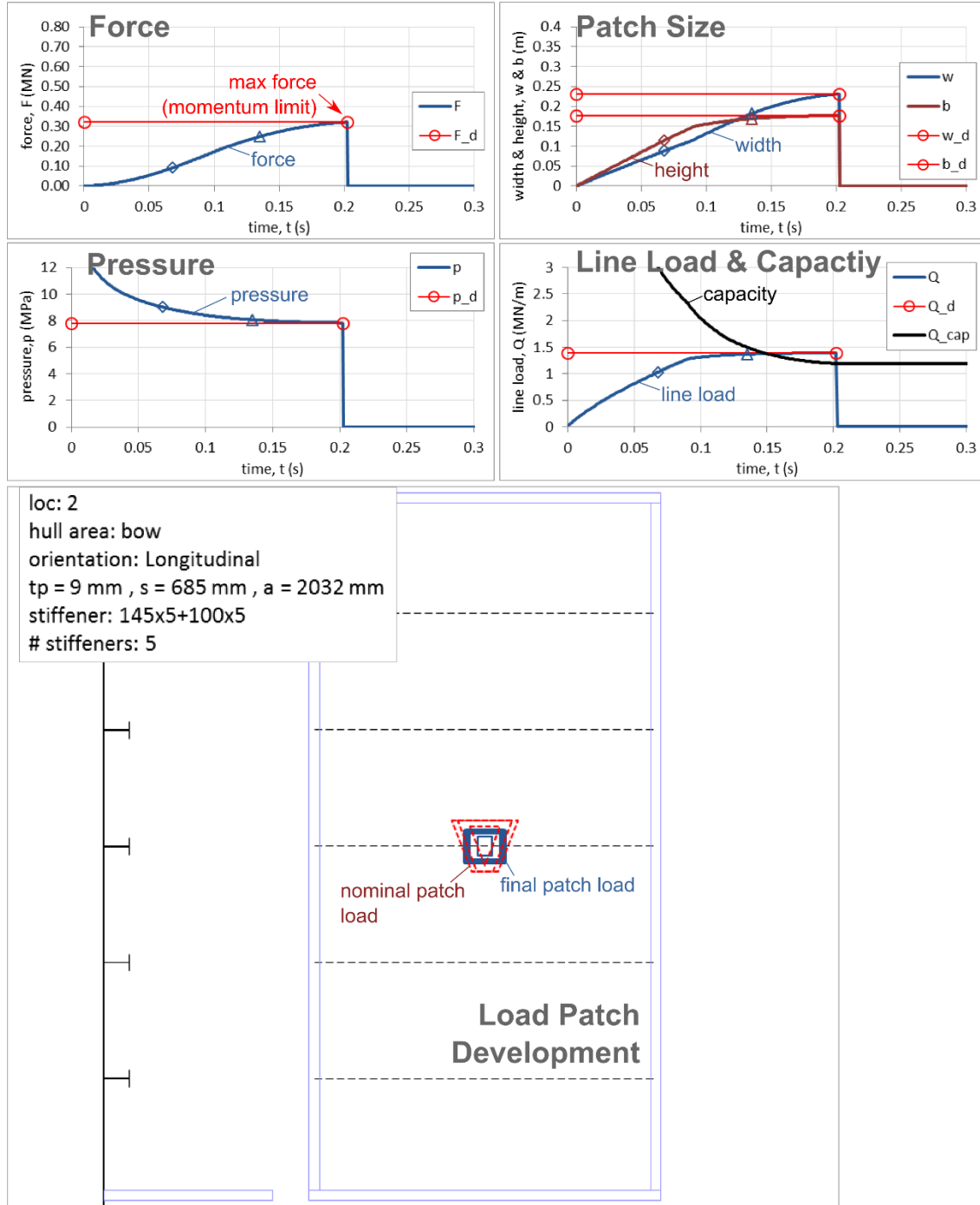


Figure 8-13: Case 1 - mathematical model outputs

Case 2

$V_S = 3$ knots

$L_{ice} = 50$ m

$H_{ice} = 0.5$ m

$P_0 = 3$ MPa, $ex = -0.1$, $\sigma_f = 0.75$ MPa

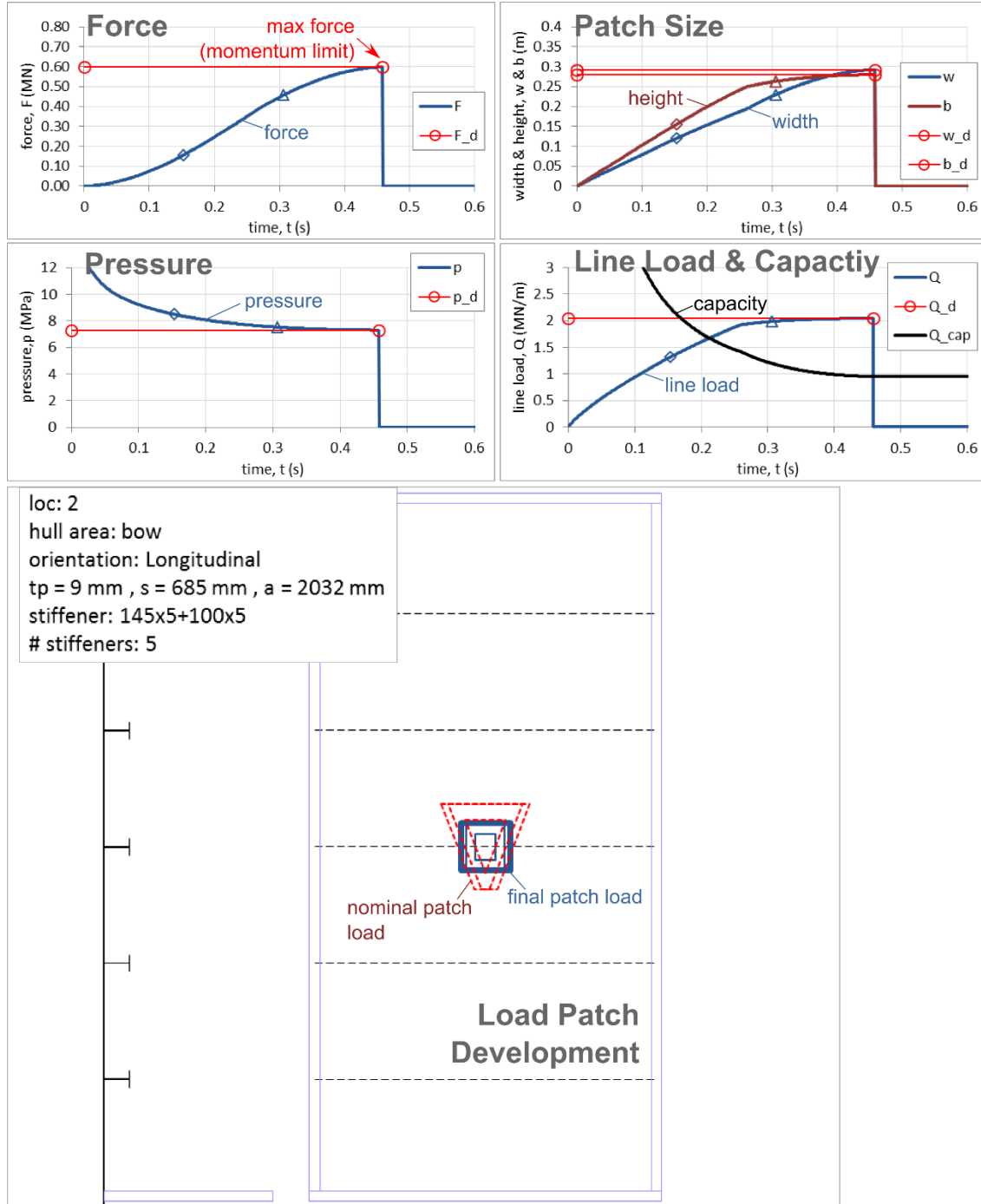


Figure 8-14: Case 2 - mathematical model outputs

Case 3

$V_S = 2$ knots

$L_{ice} = 100$ m

$H_{ice} = 0.15$ m

$P_0 = 3$ MPa, $ex = -0.1$, $\sigma_f = 0.75$ MPa

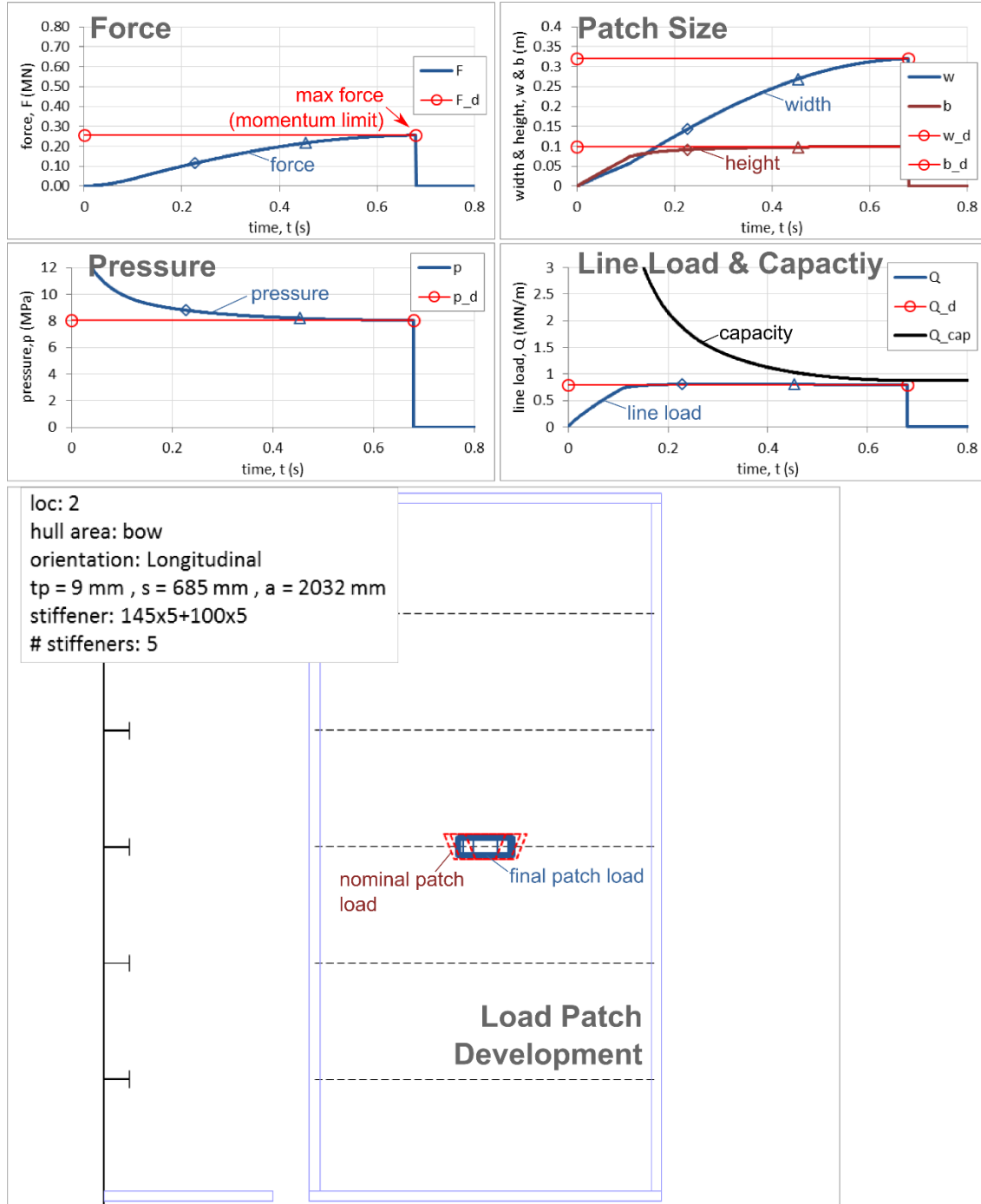


Figure 8-15: Case 3 - mathematical model outputs

8.5.2. Safe Speed Results

The mathematical model computes technical speed limits based on all combinations of ice parameters and several locations on the hull. The previous examples are just individual realizations of the model. Limits are established when the load exceeds the frame capacity. For the purposes of this study, line load (Q) is used as the basis for comparison and establishing the technical safe speed limits. Line load is the closest parameter that relates to the load encountered by a single frame. As previously described, the limit state is the formation of a 3 hinge plastic mechanism of a side shell frame under a patch load. This was shown to produce plasticity in the frame but without any major observable permanent dent size.

Figure 8-16 presents the technical safe speed results for the naval combatant assuming the parameters in Table 8-5. In each plot, there are four curves representing different limits for different frame locations.

Table 8-5: Safe speed assessment parameters

Description	Units	Symbol	Value/Range
ice crushing strength	MPa	P_o	3.0 (ex = -0.1)
ice flexural strength	MPa	σ_f	0.75
floe size	m	L_{ice}	10 - 100
ice thickness	m	h_{ice}	0.15 – 1.0
ship speeds	knots	V_s	1 - 10
impact location	--	loc	1, 2, 3, 4 (see Figure 8-1Figure 7-1)

Figure 8-17 is a summary plot of all the technical safe speed curves. For each impact scenario (combination of floe size and thickness), the minimum limit speed was taken of all the impact locations. The results, perhaps as expected for a non-ice strengthened ship, suggest that the ice capability is severely limited. Some operations could take place in very

light conditions. However, even when the ice is thin (<30 cm) and floe sizes are relatively small (<30m), speeds would be limited to ~3 knots. Operations in brush ice (generally considered <5m floe size) could be sustained if speeds are kept under ~5 knots.

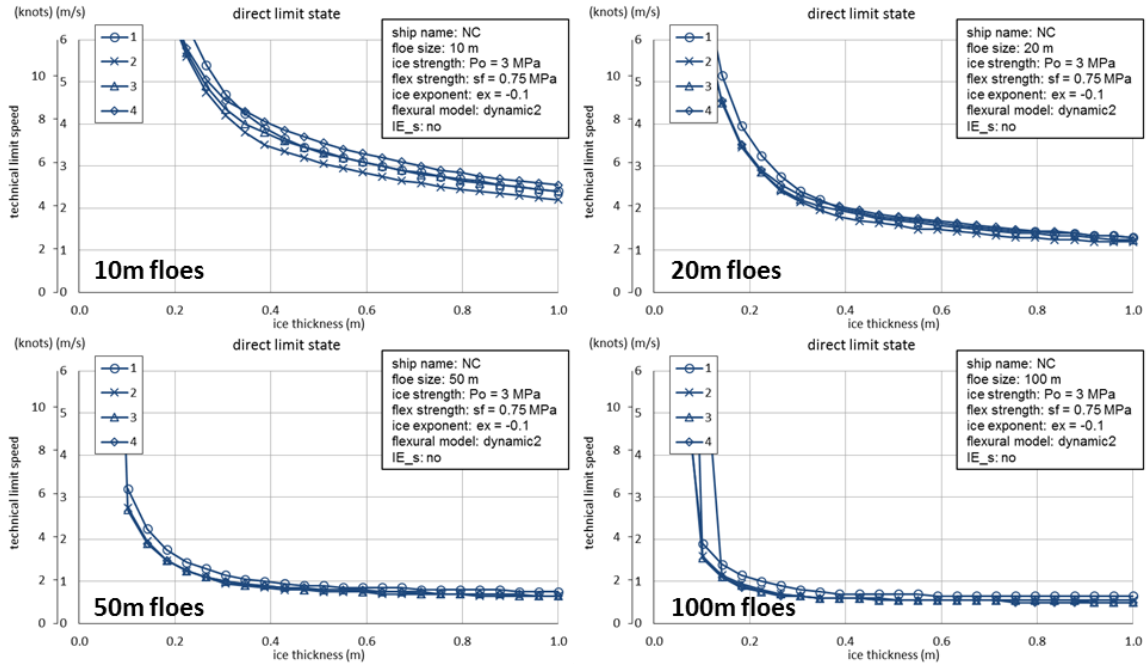


Figure 8-16: Technical safe speeds vs ice thickness for different floe sizes

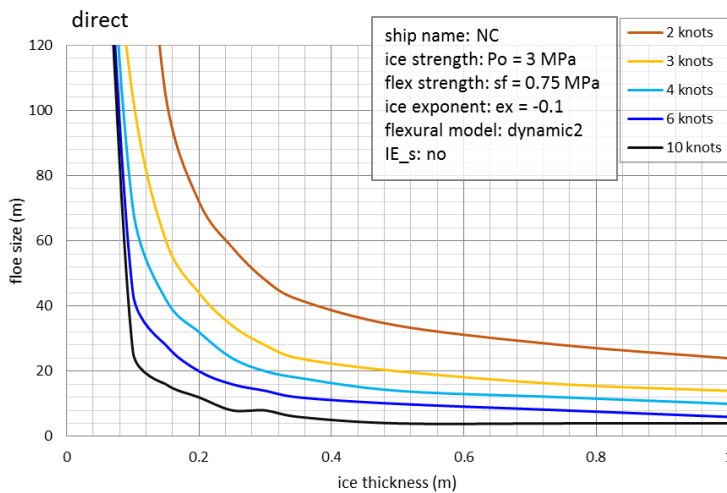


Figure 8-17: Summary plot of safe speed curves

Figure 8-18 demonstrates the influence of the ice crushing strength term (P_o) on the safe speed calculation results which was found to be the dominating ice failure mode for this hull form. Two limit speed curves (2 knots and 6 knots) are shown for $P_o = 2$ MPa (black) and $P_o = 6$ MPa (red).

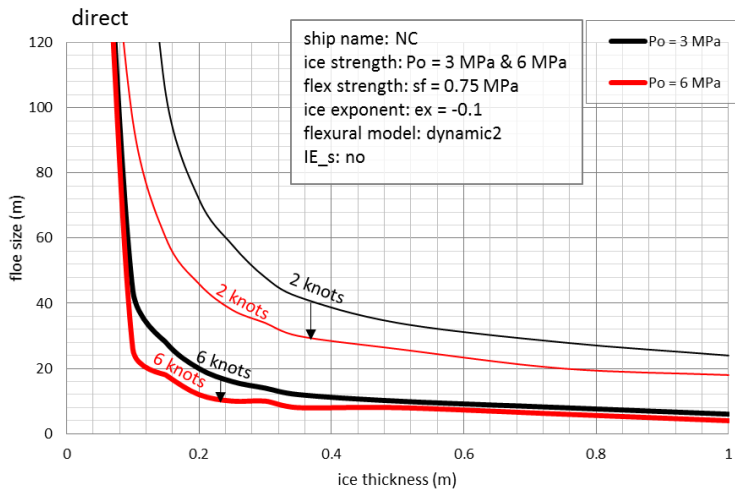


Figure 8-18: Influence of ice crushing strength to technical safe speed

8.6. Response of Compliant Structure to Deformable Ice Model

The mathematical model used in the above safe speed assessment assumes the structure is rigid and that all effective kinetic energy in a collision is expended into ice crushing. This section describes a numerical analysis of ice-structure interaction which takes into account the compliance of the structure during the indentation process. The analysis follows procedures presented in Chapter 6 and explores when the assumption of a rigid structure is no longer valid. Compared with the previous case study (Ice Class PC5 patrol vessel), this analysis suggests that the structural compliance of the non-ice strengthened naval combatant plays a critical role in the ice structure interaction process.

Table 8-6 lists a series of numerical simulation between the naval combatant representative structure and deformable ice models of various thicknesses.

Table 8-6: Numerical simulations between naval combatant ship and deformable ice model

run	description	target P_{o_eff} (MPa)	target ex (--)	h_{ice} (m)	β (°)	$\sigma_{y_ice}^1$ (MPa)
N_111	load cases centered on longitudinal frame	5.7	-0.1	0.14	6	1.281
N_110		5.7	-0.1	0.21	6	1.272
N_101		5.7	-0.1	0.35	6	1.255
N_102		5.7	-0.1	0.7	6	1.215
N_103		5.7	-0.1	1.05	6	1.179
N_104	load cases centered on plating	5.7	-0.1	0.35	6	1.255
N_105		5.7	-0.1	0.7	6	1.215
N_106		5.7	-0.1	1.05	6	1.179
N_107	load cases centered on web frame	5.7	-0.1	0.35	6	1.255
N_108		5.7	-0.1	0.7	6	1.215
N_109		5.7	-0.1	1.05	6	1.179

Note:

1 – Determined based on metamodel, equation (92)

The ice wedges all feature a 123° opening angle. The target strength for the ice model was based on effective process pressure area-model of $P_{o_eff} = 5.7$, $ex = -0.1$. This corresponds with a nominal P_o value of 3MPa which was used in the above safe speed assessment (which also assumed a 150° wedge angle and contact area reduction). Following the metamodel develop by the ice calibration exercise outlined in Section 6.2, the elasto-plastic ice model parameters (i.e. yield strength) are also listed in the table for each simulation run.

Screenshots of an example simulation (N_101) are shown in Figure 8-19. In this example, a 35cm thick ice edge is crushed against at the center of a longitudinal frame. The figure highlights the development of applied pressure and von-Mises stress distribution of the hull structure. The pressure distributions exhibit areas of high and low pressures with a

nominal contact area that grows as the simulation progresses. Hull stresses highlighted by a red fringe indicate areas of plasticity in the structure.

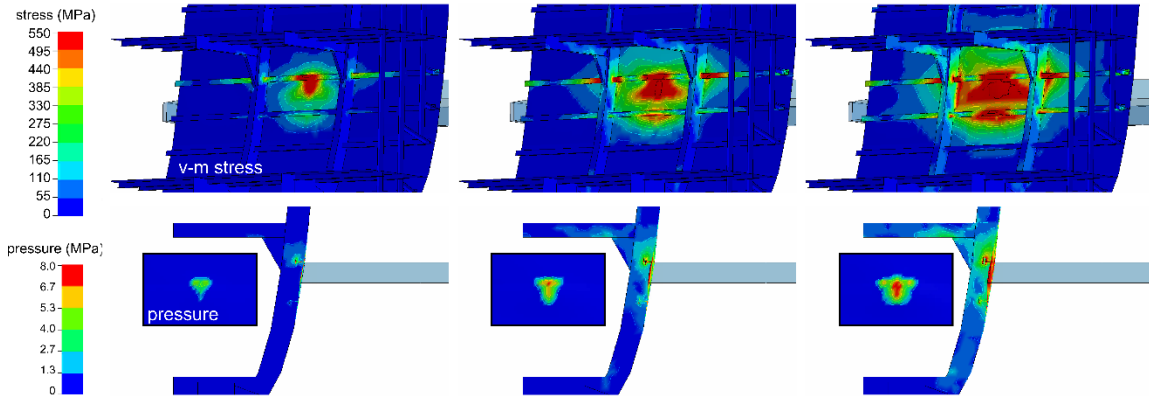


Figure 8-19: Numerical simulation – 35cm ice edge centered on longitudinal frame (N_101)

From the simulation results, the structural deformation can be extracted and compared with the ice crushing component of total normal displacement. All three measurements are compared and plotted against total force in Figure 8-20. A power function curve fit (dotted red line) is also shown for the total normal displacement in the form of equation (82). Based on this plot, the structural deformation appears to significantly influence the ice-structure interaction process from about 0.25 MN.

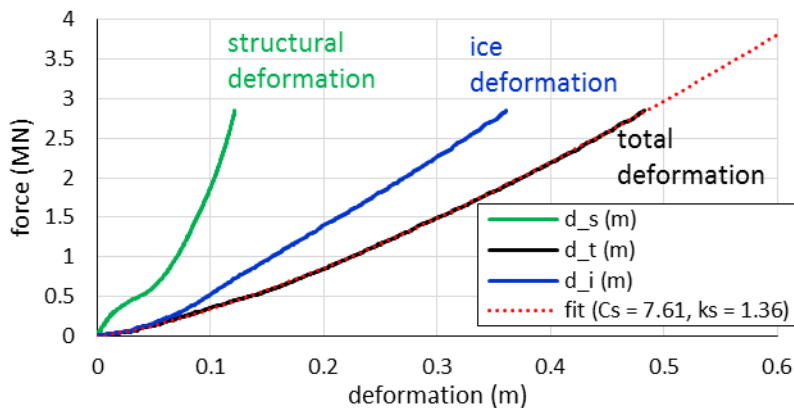


Figure 8-20: Force vs deformation results – 35cm ice edge centered on longitudinal frame (N_101)

Another simulation example is presented in Figure 8-21 where a 70cm ice wedge is crushed onto the web frame of the naval combatant structure. Figure 8-22 shows the force vs. deformation results and differentiates the structural and ice components. Similar to the results of the patch load analysis, the structure remains relatively stiff until a major collapse event of the web frame (~ 2 MN). The collapse point of the web frame is well above the nominal capacity of the longitudinal frame (~ 0.3 MN).

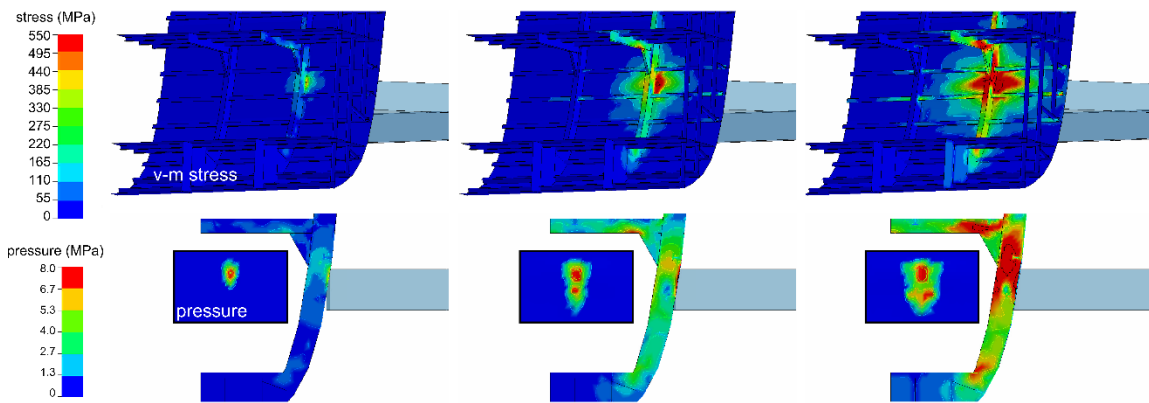


Figure 8-21: Numerical simulation – 70cm ice edge centered on web frame (N_108)

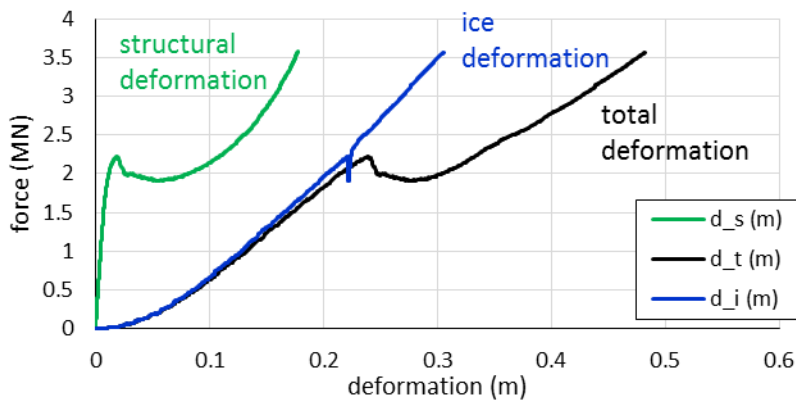


Figure 8-22: Force vs deformation results – 70cm ice edge centered on web frame (N_108)

Figure 8-23 presents a compilation of results for all of the numerical simulations of ice structure interaction considering deformable ice and the naval combatant. The top row of plots are force vs. total normal displacement for each ice thickness interval. The solid

curves represent the results of each load case and fitted power functions (red dotted line) are shown for the frame cases. They appear to also show reasonable agreement with the plate load cases. The bottom row of plots are force vs. structural deformation. Similar to the patch load analysis the structural response of the web frame load cases is considerably different than the frame and plate cases. The web frame exhibits a stiff, elastic response followed by a rapid collapse behavior which tends to occur at relatively high overload levels.

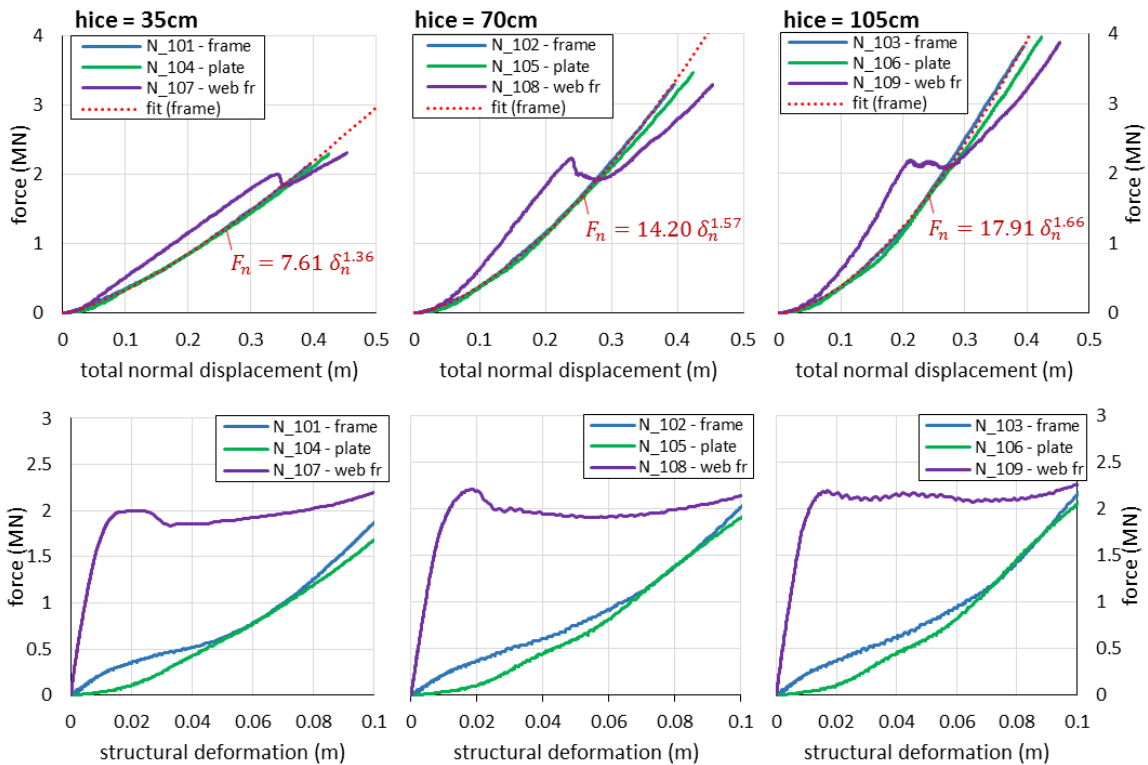


Figure 8-23: Numerical simulation results – force vs. total displacement (top), force vs. structural deformation (bottom)

Focusing on the frame load cases, Figure 8-24 compares the force vs. total normal displacement for five (5) different ice thicknesses, ranging from 14cm to 1.05m. Power

functions were fit to each curve (dotted red lines) in the form of equation (82). The terms C_s and k_s can then be expressed in terms of thickness.

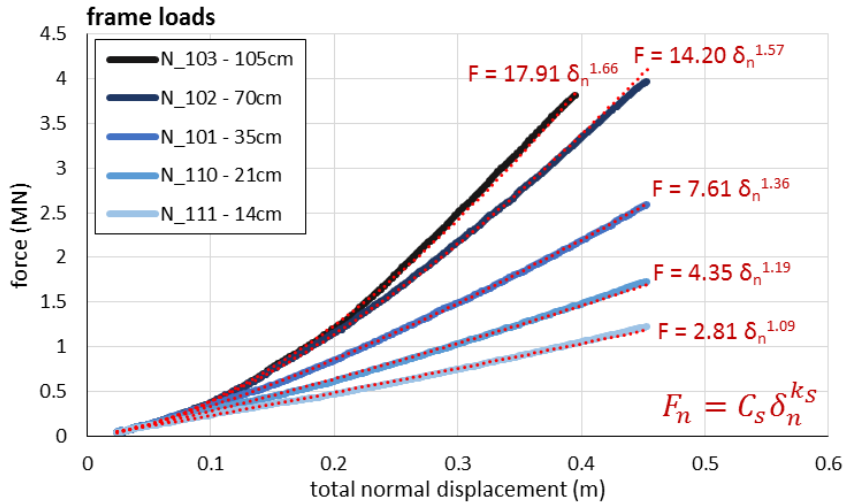


Figure 8-24: Force vs. total normal displacement for longitudinal frame load cases

Figure 8-25 shows the forces vs. structural deformation, a direct output of the numerical simulations, for each of the longitudinal frame load cases. Consider structural deformations less than 10 cm (a 5cm large deformation limit will be applied in the next section). Zooming into this portion of the plot, the load deflection curves exhibit an elastic portion followed by a plastic response. Both of these can be linearized within this range. The slope of the elastic portion (green line, $k_{el} = 22.87$ MN/m) appears to be the same for each of the simulations (i.e. independent of ice thickness). Also, the force level corresponding to the transition point between the elastic and plastic responses can be considered constant (for this structure, $F_{el} = 0.25$ MN). The slope of the plastic regime, however, varies a function of ice thickness (red line). This can be explained by the change in load pattern on the frame.

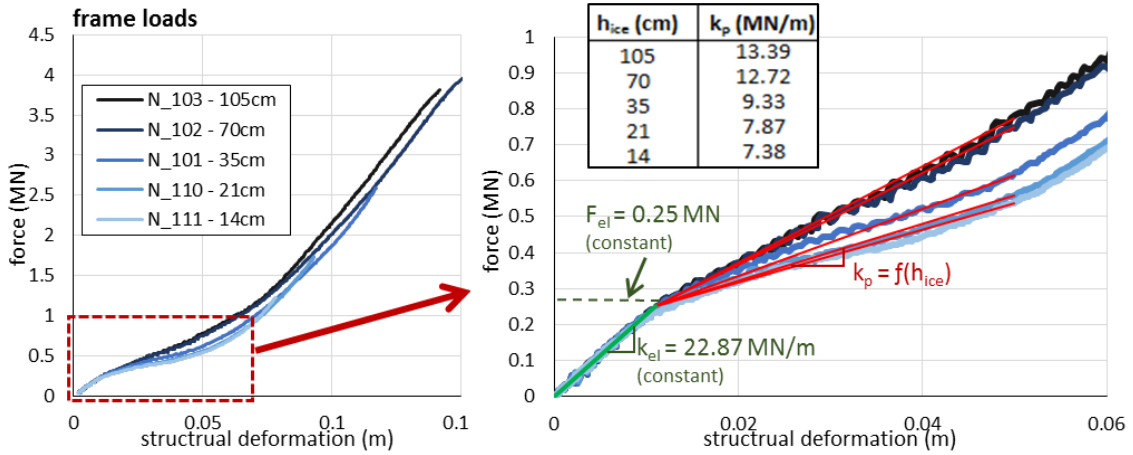


Figure 8-25: Force vs. structural deformation for longitudinal frame load cases

Figure 8-26 plots the parameters obtained from the numerical simulations as function of ice thickness. The left side plot includes both C_s and k_s terms which are used in the force vs. total normal displacement relationships. The right side plot shows the k_p term used to represent the plastic portion of the force vs. structural deformation relationship. All three terms can be expressed as linear functions of ice thickness/m with reasonable accuracy. These functions are implemented into *DDePS* following the procedure in Section 6.

$$C_s = 16.85h_{ice} + 1.12 \quad (93)$$

$$k_s = 0.61h_{ice} + 1.07 \quad (94)$$

$$k_p = 7.05h_{ice} + 6.68 \quad (95)$$

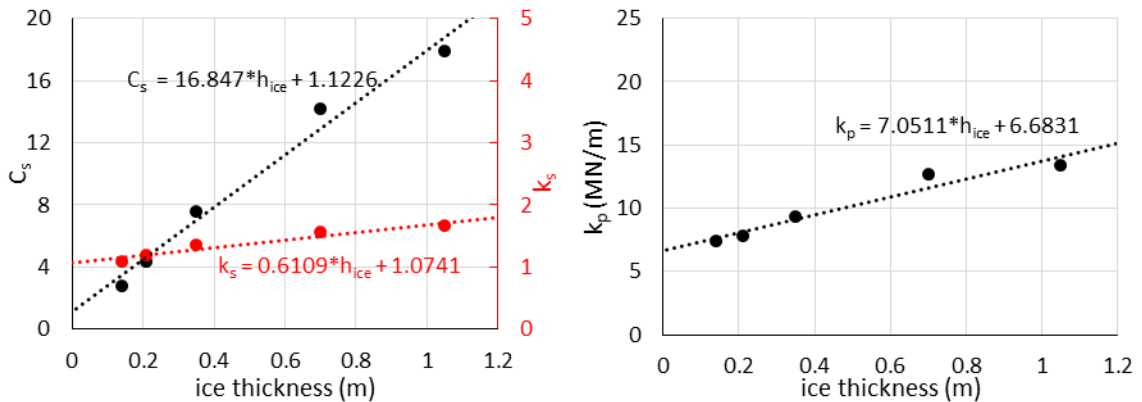


Figure 8-26: Parameters obtained from numerical simulations

8.6.1. Safe Speed Assessment Considering Deformable Structure

This final section presents a reanalysis of technical limit speeds for the naval combatant taking into account the compliance of the structure and considering different tolerance levels for structural damage. Comparisons are also made to the results of the ‘direct’ analysis discussed in the Section 8.5. In this analysis, energy absorbed by the structure due to elastic and plastic deformations is considered in the kinetic energy balance along with the ice crushing energy. The mathematical model follows the procedure outlined in Section 6 to resolve the ice load parameters. The parameters obtained from numerical simulations of ice-structure interaction are utilized in the model.

Figure 8-27 presents technical limit speeds for 20m (left) and 50m (right) floes considering three (3) limit conditions. The blue curves represent the speeds that bring the longitudinal frames to their plastic limit states (see Section 4.6). The solid blue line assumes the structure is rigid and the hashed line takes into account the structural compliance. This demonstrates the effect of structural energy absorption on the indentation process. The total normal force applied to the hull structure is reduced for the same available kinetic energy which effectively results in slightly higher speeds (1-2 knot increase) to bring the structure to same plastic limit.

The red curves represent the speeds that bring the structure to 5cm total deformation (including both elastic and plastic deformations). Limit speeds are established when the structural deformation calculated in the mathematical model exceeds the user defined value. The envelop curves (minimum speeds) are plotted in lieu of the curves for each

individual locations so that a clear comparison can be made between damage tolerance levels and the ‘direct’ analysis results.

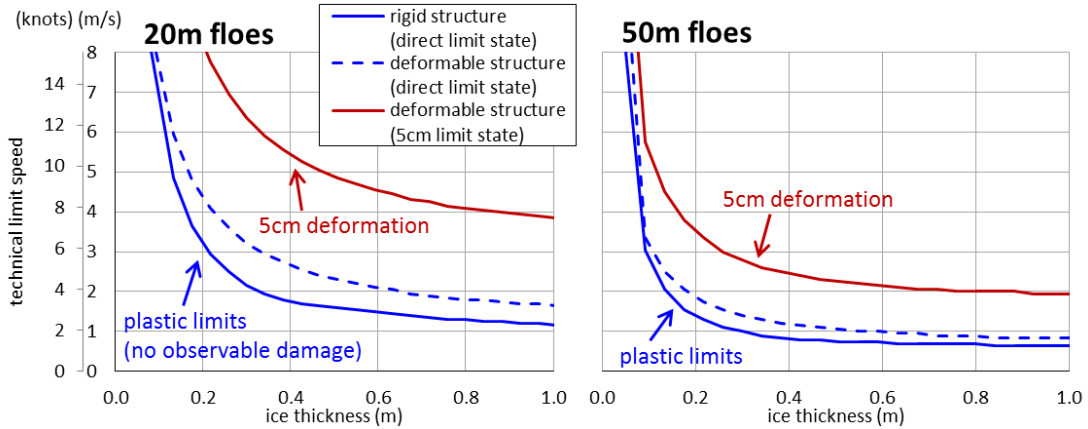


Figure 8-27: Technical limit speeds considering different damage tolerances

As a way to summarize the results into a more comprehensive form, Figure 8-28 has been produced. This plot presents the technical limit speeds that bring the structure to 5cm of total deflection for any combination of floe size and thickness. The resulting plastic deformations would be visible, but would permit considerably more aggressive impacts. Cautious impacts (speeds under 4 knots) could occur in first year ice up to 1 m thick, as long as floe sizes remain under about 40 - 50m.

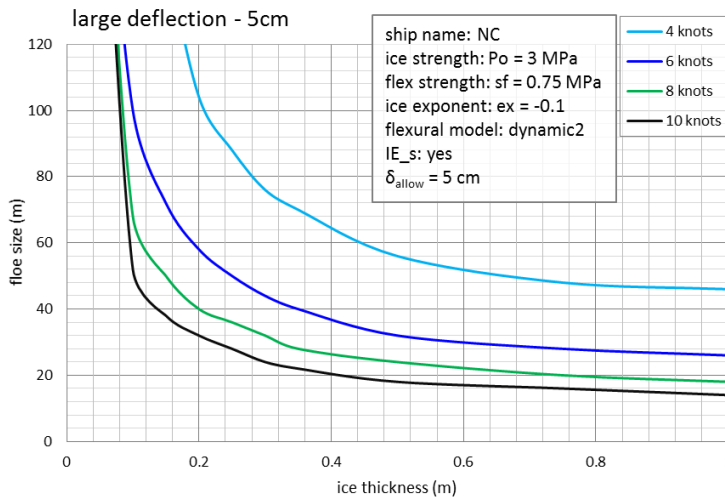


Figure 8-28: Summary plot of 5cm deflection limit speed curves vs. ice thickness and floe size

It is clear that the naval combatant has no practical ice capability in the normal meaning of the term. However, this study sheds insight on the structural consequences of operating in various types of first-year pack ice. In an emergency, a knowledgeable operator would be able to take the vessel through many forms of first year ice as long as they understood the situation and were prepared to have minor permanent deformations of the hull.

9. Conclusions and Recommendations for Future Work

With the potential for more marine traffic in the Arctic, the probability of incidents to occur may also increase. Commercial operators seeking to exploit opportunities in the region and government operators responsible for patrol or emergency assistance should have robust methods to understand the limitations of their assets and evaluate operational risk for various ice conditions. This applies to ships with ice strengthening and those without. Both of which may be deployed to ice infested areas for various mission scenarios. The technical methodology presented in this thesis relies on mechanics of ice-ship interaction and direct analysis of structural response as a rational approach to determining operational limitations in ice.

An overview of safe speeds in ice is first provided which outlines the key considerations for an evaluation of a ship's ice capability. A review of existing approaches for establishing operational limitations of ships in ice is also presented. This includes simplified risk-based control regimes as well as technical ship-specific deterministic approaches. A detailed technical methodology for determining safe speeds is proposed based on an assumed ice-ship interaction scenario, a mathematical model of ice collision mechanics, different ice failure modes including crushing and flexural bending failure, and structural response criteria. Data from available full scale measurements is used in an attempt to validate the model and calibrate the ice strength terms. An extension to the model is offered using a novel approach for ice-structure interaction which takes into account structural indentation energy during a collision event. This is shown to be particularly important for light and non-ice strengthened ships.

Finally, two case studies are presented as demonstrations of the proposed technical methodology. The first case study is of an Ice Class PC5 Patrol Vessel. The results are consistent with the nominal ice description for PC5 but offer additional information about the risks at different speeds with more combinations of ice conditions. The operational envelopes are useful in understanding a ship's structural capability in a variety of ice types.

The second case study is of a non-ice strengthened naval combatant. The results confirm the notion that this ship type has no practical capability to operate in ice unless conditions are extremely light (i.e. small and thin floes) and speeds are kept to a minimum. However, the analysis further highlights the consequences of operating more aggressively in various types of first year ice if minor amounts of structural deformation were tolerable.

It is reemphasized here that speeds presented in this report are termed "technical safe speeds" in order to clarify that the speeds are derived by a set of calculations for specific technical assumptions. An actual safe speed would need to take a variety of other factors into account, including various uncertainties, levels of training, field experience and organizational risk tolerance.

Throughout the course of this effort, a number of issues have come up that should be further studied to improve the technical approach and reduce uncertainties. Several assumptions have been made, most of which are believed to be conservative, but the results of the case studies help narrate a discussion of uncertainties in the modeling approach and highlight critical gaps for future development.

1) Develop a stronger link between ice crushing terms and actual ice properties

As described in section 2.4, there is a disconnect between the uniaxial ice crushing strength, which is most commonly reported from field measurements, and the process pressure-area relationship used to represent ice strength in the proposed technical methodology. The pressure-area approach is empirical and parameters are typically derived from full scale measurements of instrumented icebreakers. For this work, the crushing terms were drawn from a limited set of full scale measurements. Unfortunately little work has been done to draw a link between the two representations of crushing strength. A combination of dedicated laboratory experiments and a focused review of reported field testing programs and in-situ ice measurements could greatly improve this link.

2) Modeling moving loads and the resulting structural response

The model employed in this study is based on Popov collision mechanics, which assumes the collision process is quick and there is no sliding along the hull. Up to the limit states explored in this study (onset of plastic deformations and slightly beyond), this assumption is reasonable. However, for more severe limit states (e.g. larger deformation cases), moving load effects should be carefully considered. Quinton (2015) has demonstrated numerically and physically (experimental laboratory tests) the adverse effects of scoring action on a structure's ability to withstand a load, in particular when already subject to plastic damage.

3) Continued development of thin-ice mechanics

The assessments presented in this report make use of methods that do not account for the flexural elasticity of the ice edge as an energy absorption mechanism. For ships operating in thin ice conditions, the edge flexibility may have a significant effect on the

development of the ice force and pressure distributions on the hull structure. Especially in the case of large floe diameters, the impacts may be over-estimated. To better understand the mechanics of thin ice and ship interactions, a combination of physical and numerical approaches are suggested. Laboratory scale and perhaps full scale observations of ice edge bending, buckling and fracture at various loading rates would help towards the development of an updated physics-based mathematical model.

4) Maneuvering operations and the influence on load severity

The technical methodology currently only considers pure forward motion with impacts on the bow structure. Maneuvering through pack ice results in impacts with various degrees of lateral speed and at different positions along the hull. Maneuvering operations will affect the loads both positively and negatively. Further study of the navigation in pack ice is warranted. A new software technology called GPU Event Mechanics (GEM) has been used to explore natural variability in ice loads during different operational modes, including maneuvering (Daley et al., 2014; Daley et al., 2012). GEM is a novel modeling capability developed at Memorial University that makes use of the kind of formulations used in *DDePS*, but implements them in the context of a general vessel navigation simulation (Daley et al., 2014). GEM remains under continuous development and new features are regularly being incorporated into the model. Future work may apply the GEM software more extensively to further evaluate loads on ships from more natural operation conditions.

5) Consideration to full range natural ice conditions

This work focused on ships engaged in pack ice operations. Impacts were modeled as collisions with discrete ice floes and ship speed was used as the main parameter to explore structural risk. As described in Chapter 2, ice occurs in a variety of forms in nature. Ice

ridges for example, are formed by winds, currents, and tides that cause ice fields to converge under pressure. Ice ridges are not considered in this methodology but present a natural structural hazard to ships operating in ice covered waters, in particular consolidated ridges. Modeling ship interactions with ice ridge formations would require an alternative approach to the mathematical model that should take into account ice contact below the waterline and perhaps other operational aspects.

10. References

- ABS. (2015). *ABS Technical Report - USCG WMSL Class - Operational Capabilities and Limitations in Ice*. Houston, TX, USA.
- ABS. (2016a). *ABS Guide for Building and Classing International Naval Ships*. Houston, TX, USA: American Bureau of Shipping.
- ABS. (2016b). *ABS Rules for Building and Classing Steel Vessels*. Houston, TX, USA: American Bureau of Shipping.
- Belkin, M. (2016). Icebreaking assistance to major national Arctic hydrocarbon projects. *Arctic Shipping Forum*. Helsinki, Finland.
- Berthiaume, L. (2016). Canadian Coast Guard may be forced to lease icebreakers as aging fleet increasingly at risk of breakdowns. Retrieved November 18, 2016, from <http://news.nationalpost.com/news/canada/canadian-coast-guard-may-be-forced-to-lease-icebreakers-as-aging-fleet-increasingly-at-risk-of-breakdowns>
- Bird, K., Charpentier, R., Gautier, D., Houseknecht, D., Klett, T., Pitman, J., ... Wandrey, C. (2008). *Circum-Arctic resource appraisal: Estimates of undiscovered oil and gas north of the Arctic Circle. No.2008-3049*.
- Brown, C. (2016). Massive cruise ship brings new era of Arctic tourism to Cambridge Bay. Retrieved December 6, 2016, from <http://www.cbc.ca/news/canada/north/massive-cruise-ship-brings-new-era-of-arctic-tourism-to-cambridge-bay-1.3739491>
- Bruneau, S. E., Colbourne, B., Dragt, R., Dillenburg, A. K., Ritter, S., Pilling, M., & Sullivan, A. (2013). Laboratory Indentation Tests Simulating Ice-Structure Interactions Using Cone-Shaped Ice Samples and Steel Plates. *Port and Ocean Engineering under Arctic Conditions, POAC'13*. Espoo, Finland.
- Bruneau, S. E., Dillenburg, A. K., & Ritter, S. (2013). Ice Sample Production Techniques and Indentation Tests for Laboratory Experiments Simulating Ship Collisions with Ice. *International Offshore and Polar Engineering Conference, ISOPE'13* (Vol. 9, pp. 1268–1271). Anchorage, AK, USA.
- Canadian Coast Guard. (2012). *Ice Navigation in Canadian Waters*. Ottawa, ON, Canada: Icebreaking Program, Maritime Services, Canadian Coast Guard Fisheries and Oceans Canada.
- Colbourne, B. (1989). *A three component method of analyzing icebreaking resistance (IR-1989-07)*. St. John's, NL, Canada.
- Daley, C. (1999). Energy based ice collision forces. *Port and Ocean Engineering under Arctic Conditions, POAC'99*. Espoo, Finland.
- Daley, C. (2000). *IACS Unified Requirements for Polar Ships - Background Notes to Design Ice Loads*.
- Daley, C. (2002a). Application of plastic framing requirements for polar ships. *Marine Structures, 15*(6), 533–542. doi:10.1016/S0951-8339(02)00018-7
- Daley, C. (2002b). Derivation of plastic framing requirements for polar ships. *Marine Structures, 15*(6), 543–559. doi:10.1016/S0951-8339(02)00019-9
- Daley, C. (2004). *A Study on the Process-Spatial Link in Ice Pressure-Area Relationships (PERD/CHC Report 7-108)*.
- Daley, C. (2015). *Ice Impact Capability of DRDC Notional Destroyer*.

- Daley, C., Alawneh, S., Peters, D., & Colbourne, B. (2014). GPU-Event-Mechanics Evaluation of Ice Impact Load Statistics (OTC 24645). *Arctic Technology Conference, ATC'14*. Houston, TX, USA.
- Daley, C., Alawneh, S., Peters, D., Quinton, B., & Colbourne, B. (2012). GPU Modeling of Ship Operations in Pack Ice. *International Conference and Exhibition on Performance of Ships and Structures in Ice, IceTech'12*. Banff, AB, Canada.
- Daley, C., & Hermanski, G. (2009). *Investigation of Plastic Limit States for Design of Ship Hull Structures - Ship Frame Research Program - A Experimental Study of Ship Frames and Grillages Subjected to Patch Loads (Ship Structure Committee Report SSC-457)*. Washington, DC, USA.
- Daley, C., & Kendrick, A. (2011). *Safe Speeds in Ice (BMT Report 6931DFR.Rev00)*.
- Daley, C., Kendrick, A., & Appolonov, E. (2001). Plating and Framing Design in the Unified Requirements for Polar Class Ships. *Port and Ocean Engineering under Arctic Conditions, POAC'01*. Ottawa, ON, Canada.
- Daley, C., Kendrick, A., & Quinton, B. (2011). *Safe Speeds in Ice (errata)*.
- Daley, C., & Kim, H. (2010). Ice Collision Forces Considering Structural Deformation. *International Conference on Offshore Mechanics and Arctic Engineering, OMAE'10*. Shanghai, China.
- Daley, C., & Liu, J. J. (2009). *DDePS for Ship Ramming Infinite / Finite Ice*.
- Daley, C., & Liu, J. J. (2010). Assessment of Ship Ice Loads in Pack Ice. *International Conference and Exhibition on Performance of Ships and Structures in Ice, IceTech'10*. Anchorage, AK, USA.
- Daley, C., St. John, J. W., Brown, R., & Glen, I. (1990). *Ice Forces and Ship Response to Ice - Consolidation Report (SSC-340)*.
- DeBord, F., McAllister, T., Cleary, C., Dolny, J., & Kawamoto, R. (2015). Design considerations for operation of Coast Guard cutters and combatants in the Arctic. *SNAME World Maritime Technology Conference, WMTC'15*. Providence, RI, USA.
- Dlouhy, J. (2015). Shell leaves door open for future exploration in Alaska's Arctic. Retrieved December 6, 2016, from <https://www.adn.com/energy/article/shell-leaves-door-open-future-exploration-alaskas-arctic/2015/11/02/>
- Dolny, J., Yu, H., Daley, C., & Kendrick, A. (2013). Developing a Technical Methodology for the Evaluation of Safe Operating Speeds in Various Ice Conditions. *Port and Ocean Engineering under Arctic Conditions, POAC'13*. Espoo, Finland.
- Eason, C. (2015). FEDNAV vessel completes first Arctic voyage from Baffinland to Germany.
- Fetterer, F., Knowles, K., Meier, W., & Savoie, M. (2016). Sea Ice Index, Version 2 (updated daily). doi:10.7265/N5736NV7
- Finland, Sweden, Kolari, K., & Kurkela, J. (2012). DE 57/INF.3: Simulation of ship-ice interaction. *IMO Sub-Committee on Ship Design and Equipment, 57th Session, Agenda Item 11, Development of a Mandatory Polar Code*.
- Frederking, R. (1999). The local pressure-area relation in ship impact with ice. *Port and Ocean Engineering under Arctic Conditions, POAC'99* (pp. 687–696). Helsinki, Finland. doi:10.1039/B910216G
- Gagnon, R. E., & Derradji-Aouat, A. (2006). First Results of Numerical Simulations of

- Bergy Bit Collisions with the CCGS Terry Fox Icebreaker. *IAHR International Symposium on Ice, IAHR'06* (pp. 9–16). Sapporo, Japan.
- IACS. (2011). IACS Unified Requirements Concerning Polar Class. London, UK: International Association of Classification Societies.
- IACS, Canada, & Finland. (2014). MSC 94/INF.13: Technical background to POLARIS. *IMO Maritime Safety Committee, Agenda Item 3, Consideration and Adoption of Amendments to Mandatory Instruments*.
- IMO. (2015). *International Code for Ships Operating in Polar Waters (Polar Code - Environmental Part)*, IMO Resolution MEPC.264(68). Adopted 15 May 2015. London, UK.
- IMO. (2016). Guidance on Methodologies for Assessing Operational Capabilities and Limitations in Ice, IMO Circular MSC.1-CIRC.1519.
- Iyerusalimskiy, A., Choi, J., Park, G., Kim, Y., Yu, H., & John, J. S. (2011). The Interim Results of the Long-term Ice loads Monitoring on the Large Arctic Tanker. *Port and Ocean Engineering under Arctic Conditions, POAC'11*. Montreal, Canada.
- Kendrick, A., & Daley, C. (2000). *IACS Unified Requirements for Polar Ships - Background Notes to Derivation and Use of Formulations for Framing Design*.
- Kendrick, A., & Daley, C. (2006a). *Ice Interaction Scenarios and Load Modeling Approaches (BMT Report 6007A.DFR submitted to ABS)*.
- Kendrick, A., & Daley, C. (2006b). *Ice Loads for Structural and Vibration Analysis of Large Arctic LNG Carriers – Phase II (BMT Report 6055 DR submitted to ABS)*.
- Kendrick, A., & Daley, C. (2009). *DDPS for Stern Impacts with Ice (BMT Report 6512D.FR submitted to ABS and DSME)*.
- Kendrick, A., & Daley, C. (2011). Structural Challenges Faced by Arctic Ships (Ship Structure Committee Report SSC-461).
- Kim, H., Dolny, J., & Daley, C. (2015). An experimental study of the design and overload capacity of structural grillages subjected to ice loads. *Port and Ocean Engineering under Arctic Conditions, POAC'15* (Vol. 2015–Janua). Trondheim, Norway.
- Kim, H., Dolny, J., Quinton, B., Yu, H., & Peng, H. (2016). Characterization of Full Scale Operational Ice Pressures and Hull Response on a Large Arctic Tanker (OTC-27408). *Arctic Technology Conference, ATC'16*. St. John's, NL, Canada.
- Kurdyumov, V. A., & Kheisin, D. E. (1976a). Hydrodynamic Model of the Impact of a Solid on Ice (Translated). *Applied Mechanics*, 12(10), 103–109.
- Kurdyumov, V. A., & Kheisin, D. E. (1976b). Hydrodynamic Model of the Impact of Solid Body Impact Against Ice. *International Applied Mechanics*, 12(10), 1063–1068.
- Likhomanov, V. A., Timofeev, O. Y., Stepanov, I. V., Kashtelyan, V. I., Iltchuk, A., Krupina, N., & Klenov, A. (1997). *Scientific basis and methodology of the development of an ice passport*. St. Petersburg, Russia.
- Likhomanov, V. A., Timofeev, O. Y., Stepanov, I. V., Kashtelyan, V. I., & Tsoy, L. (1998). Ice Passport for Icebreaker Pierre Radisson and Passport's Concept: Further Development. *International Offshore and Polar Engineering Conference, ISOPE'98* (Vol. 2, pp. 566–571). Montreal, Canada.
- Liu, J. J., Daley, C., Yu, H., & Bond, J. (2012). Comparison of Analytical and Numerical Models of Glancing Ship-Ice Collisions. *International Conference and Exhibition on*

- Performance of Ships and Structures in Ice, IceTech'12*. Banff, AB, Canada.
- Maksutov, D. D., & Popov, Y. N. (1981). Development and Implementation of Ship Ice Certificates. *Second International Conference on Icebreaking & Related Technologies, IceTech'81*. Ottawa, ON, Canada.
- Manuel, M., Gudimelta, P. S. R., Daley, C., & Colbourne, B. (2013). Controlled Plastic Deformation of a Grillage Using Artificial Freshwater Ice at a Large Scale. *Port and Ocean Engineering under Arctic Conditions, POAC'13*. Espoo, Finland.
- Montgomery, D. C. (2008). *Design and Analysis of Experiments* (7th ed.). John Wiley & Sons, Inc.
- Popov, Y. N., Faddeyev, O. V, Kheysin, D. E., & Yalovlev, A. (1967). *Strength of ships sailing in ice* (FSTC-HT-23.). Leningrad: Sudostroenie Publishing House, U.S. Army Foreign Science and Technology Center (Translation).
- Popov, Y. N., Faddeyev, O. V, Kheysin, D. Y., & Yakovlev, A. A. (1967). *Strength of Ships Sailing In Ice (Translated), F3TC-HT-23-96-68* (Technical.). Leningrad, USSR: Sudostroyeniye Publishing House.
- Quinton, B. (2015). *Experimental and Numerical Investigation of Moving Loads on Hull Structures*. Memorial University of Newfoundland.
- Quinton, B., Daley, C. G., Gagnon, R. E., & Colbourne, D. B. (2016). Guidelines for the nonlinear finite element analysis of hull response to moving loads on ships and offshore structures. *Ships and Offshore Structures*, 5302(December), 1–6. doi:10.1080/17445302.2016.1261391
- Riska, K., & Kämäräinen, J. (2012). Comparison of Finnish-Swedish and IACS ice class rules. *RINA International Conference on Ice Class Ships* (pp. 43–62). London, UK.
- Rowlands, D. (2016). Teekay holds steel cutting ceremony for second ARC7 LNG carrier. Retrieved December 6, 2016, from <https://www.lngindustry.com/lng-shipping/29112016/teekay-holds-steel-cutting-ceremony-for-second-arc7-lng-carrier/>
- Sazidy, M. (2014). *Development of Velocity Dependent Ice Flexural Failure Model and Application to Safe Speed*. Memorial University of Newfoundland.
- Sazidy, M., Daley, C., & Colbourne, B. (2014). A Mathematical Model of Icebreaking for Safe Speed Assessment. *International Conference and Exhibition on Performance of Ships and Structures in Ice, IceTech'14* (pp. 1–8). Banff, AB, Canada.
- Sazidy, M., Daley, C., Colbourne, B., & Wang, J. (2014). Effect of Ship Speed on Level Ice Edge Breaking. *International Conference on Offshore Mechanics and Arctic Engineering, OMAE'14*. San Francisco, CA, USA.
- Timco, G. W., & Johnston, M. (2003). *Arctic Ice Regime Shipping System - Pictorial Guide (TP14044E)*.
- Timco, G. W., & Weeks, W. F. (2010). A review of the engineering properties of sea ice. *Cold Regions Science and Technology*, 60(2), 107–129. doi:10.1016/j.coldregions.2009.10.003
- Tunik, A. (2000). Safe Speeds of Navigation in Ice as Criteria of Operational Risk. *International Journal of Offshore and Polar Engineering*, 10(4).
- Tunik, A. L., Kheysin, D. E., & Kurdyumov, V. A. (1990). Probabilistic Concept of Safe Speeds for Arctic Shipping. *Ice Technology for Polar Operations: Proceedings of the*

- Second International Conference on Ice Technology* (pp. 295–306). Cambridge, United Kingdom.
- US Navy Task Force Climate Change. (2014). *US Navy Arctic Roadmap 2014–2030*. Washington, DC, USA.
- Valanto, P. (1996). On the transient response of a floating ice cover to an advancing ship. *International Conference on Offshore Mechanics and Arctic Engineering, OMAE'96* (pp. 24–40). Florence, Italy.
- VARD. (2015). *Safe Speed in Ice (305-000-01, Report for Transport Canada)*.
- WMO. (2014). *Sea Ice Nomenclature (WMO/OMM/BMO - No. 259)*.
- Yu, H., Iyerusalimskiy, A., Kim, Y., Industries, S. H., John, J. S., & Corporation, T. (2012). Hull Structural Performance Monitoring System for Ships Operating in Ice-Covered Waters (OTC 1368063). *Offshore Technology Conference, OTC'12*. Houston, TX, USA.
- Zong, R. (2012). *Finite Element Analysis of Ship-Ice Collision Using Ls-Dyna*. Memorial University of Newfoundland.

Appendix A - Description of Popov Terms

This appendix provides the technical derivations for the effective mass terms for the ship and ice that are used in *DDePS*. This approach was first developed by Popov et al. (1967).

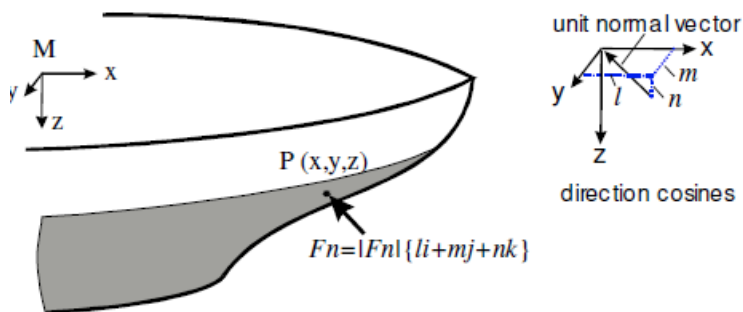
A.1 Popov Terms for Ship

A collision taking place at point 'P', will result in a normal force F_n . Point P will accelerate, and a component of the acceleration will be along the normal vector, with a magnitude $\ddot{\zeta}$. The collision can be modeled as if point P were a single mass (a 1 degree of freedom system) with an equivalent mass M_e of;

$$M_e = F_n / \ddot{\zeta} \quad (96)$$

The equivalent mass is a function of the inertial properties (mass, radii of gyration, hull angles and moment arms) of the ship. The equivalent mass is linearly proportional to the mass (displacement) of the vessel, and can be expressed simply by the following equation.

$$M_{e_{ship}} = \frac{M_{ship}}{C_o} = \frac{1}{\frac{l^2}{M_{sx}} + \frac{m^2}{M_{sy}} + \frac{n^2}{M_{sz}} + \frac{\lambda^2}{I_{sx}} + \frac{\mu^2}{I_{sy}} + \frac{\nu^2}{I_{sz}}} \quad (97)$$



The inertial properties of the vessel are as follows;

Hull angles at point P:

α : waterline angle

β : frame angle

β' : normal frame angle

γ : sheer angle

The various angles are related as follows:

$$\tan(\beta) = \tan(\alpha) \tan(\gamma) \quad (98)$$

$$\tan(\beta') = \tan(\beta) \cos(\alpha) \quad (99)$$

Based on these angles, the direction cosines l , m , and n are:

$$l = \sin(\alpha) \cos(\beta') \quad (100)$$

$$m = \cos(\alpha) \cos(\beta') \quad (101)$$

$$n = \sin(\beta') \quad (102)$$

and the moment arms are;

$$\lambda = ny - mz \quad (\text{roll moment arm}) \quad (103)$$

$$\mu = lz - nx \quad (\text{pitch moment arm}) \quad (104)$$

$$\eta = mx - ly \quad (\text{yaw moment arm}) \quad (105)$$

The added mass terms for the ship are represented by the following geometric relationships

(from Popov);

$$AM_x = 0 \quad (\text{added mass factor in surge}) \quad (106)$$

$$AM_y = 2 T/B \quad (\text{added mass factor in sway}) \quad (107)$$

$$AM_z = 2/3 (B C_{wp}^2)/(T(C_B(1 + C_{wp}))) \quad (\text{added mass factor in heave}) \quad (108)$$

$$AM_{roll} = 0.25 \quad (\text{added mass factor in roll}) \quad (109)$$

$$AM_{pit} = B(T/(3 - 2C_{wp})(3 - C_{wp})) \quad (\text{added mass factor in pitch}) \quad (110)$$

$$AM_{yaw} = 0.3 + 0.05 L/B \quad (\text{added mass factor in yaw}) \quad (111)$$

The mass radii of gyration (squared) are;

$$rx^2 = C_{wp}B^2/(11.4 C_m) + H^2/12 \quad (\text{roll}) \quad (112)$$

$$ry^2 = 0.07 C_{wp}L^2 \quad (\text{pitch}) \quad (113)$$

$$rz^2 = L^2/16 \quad (\text{yaw}) \quad (114)$$

The six force (moment) actions on the six degrees of freedom of the vessel's center of gravity are;

$$F_x = F_n l \quad (\text{force in surge}) \quad (115)$$

$$F_y = F_n m \quad (\text{force in sway}) \quad (116)$$

$$F_z = F_n n \quad (\text{force in heave}) \quad (117)$$

$$M_{rol} = F_n \lambda \quad (\text{moment in roll}) \quad (118)$$

$$M_{pit} = F_n \mu \quad (\text{moment in pitch}) \quad (119)$$

$$M_{yaw} = F_n \eta \quad (\text{moment in yaw}) \quad (120)$$

There are six accelerations at the center of gravity which are:

$$a_x = F_n l / (M(1 + AM_x)) \quad (\text{acceleration in surge}) \quad (121)$$

$$a_y = F_n m / (M(1 + AM_y)) \quad (\text{acceleration in sway}) \quad (122)$$

$$a_z = F_n n / (M(1 + AM_z)) \quad (\text{acceleration in heave}) \quad (123)$$

$$a_{rol} = F_n \lambda / (M r x^2 (1 + AM_{roll})) \quad (\text{acceleration in roll}) \quad (124)$$

$$a_{pit} = F_n \mu / (M r y^2 (1 + AM_{pit})) \quad (\text{acceleration in pitch}) \quad (125)$$

$$a_{yaw} = F_n \eta / (M r z^2 (1 + AM_{yaw})) \quad (\text{acceleration in yaw}) \quad (126)$$

Each of these accelerations contributes to the acceleration of the point of ice contact. The total acceleration at the point of contact can be expressed as;

$$\ddot{\zeta} = F_n C_o / M_{ship} \quad (127)$$

where;

$$C_o = \frac{l^2}{1+AM_x} + \frac{m^2}{1+AM_y} + \frac{n^2}{1+AM_z} + \frac{\lambda^2}{rx^2(1+AM_{roll})} + \frac{\mu^2}{ry^2(1+AM_{pit})} + \frac{\eta^2}{rz^2(1+AM_{yaw})} \quad (128)$$

The collision applies an impulse I_e to the vessel at the point of contact. The changes in velocity at the center of gravity are;

$$dV_x = I_e l / (M(1 + AM_x)) \quad (\text{velocity change in surge}) \quad (129)$$

$$dV_y = I_e m / (M(1 + AM_y)) \quad (\text{velocity change in sway}) \quad (130)$$

$$dV_z = I_e n / (M(1 + AM_z)) \quad (\text{velocity change in heave}) \quad (131)$$

$$dV_{rol} = I_e \lambda / (M \cdot rx^2 (1 + AM_{roll})) \quad (\text{velocity change in roll}) \quad (132)$$

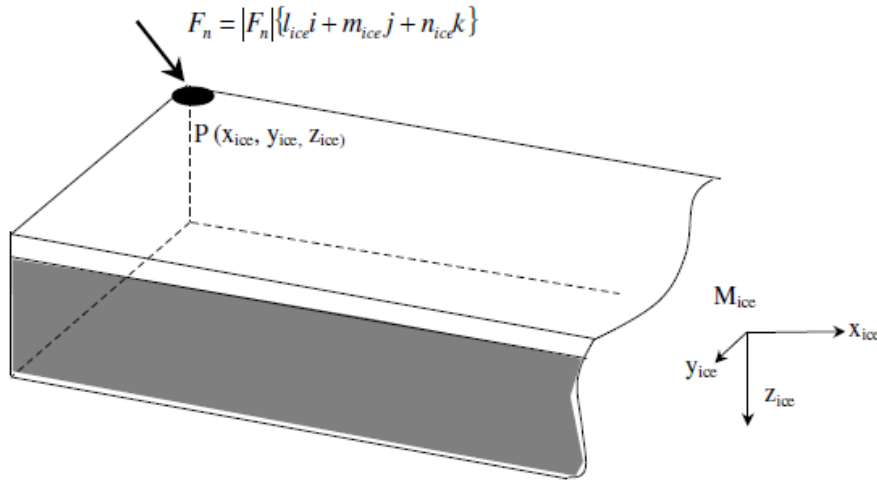
$$dV_{pit} = I_e \mu / (M \cdot ry^2 (1 + AM_{pit})) \quad (\text{velocity change in pitch}) \quad (133)$$

$$dV_{yaw} = I_e \eta / (M \cdot rz^2 (1 + AM_{yaw})) \quad (\text{velocity change in yaw}) \quad (134)$$

A.2 Popov Terms for Ice

In the Popov model, the ice floe is regarded as a special ship with similar dimensional definitions. The formulations for the ship added mass terms depend on empirical formulas based on the ship experimental data. In this report, the added mass terms for the ice are selected based on expected reasonable values for ice floes. In the future, more rational derivations of ice added mass terms may be developed. The ice floe equivalent mass can be expressed as:

$$M_{e_{ice}} = \frac{1}{\frac{l^2}{M_{ix}} + \frac{m^2}{M_{iy}} + \frac{n^2}{M_{iz}} + \frac{\lambda^2}{I_{ix}} + \frac{\mu^2}{I_{iy}} + \frac{\nu^2}{I_{iz}}} \quad (135)$$



For the ice block the direction cosines l , m , and n are:

$$l_{ice} = -\cos(\beta') \quad (136)$$

$$m_{ice} = 0 \quad (137)$$

$$n_{ice} = -\sin(\beta') \quad (138)$$

and the moment arms are;

$$\lambda_{ice} = n_{ice}y_{ice} - m_{ice}z_{ice} \quad (\text{roll moment arm}) \quad (139)$$

$$\mu_{ice} = l_{ice}z_{ice} - n_{ice}x_{ice} \quad (\text{pitch moment arm}) \quad (140)$$

$$\eta_{ice} = m_{ice}x_{ice} - l_{ice}y_{ice} \quad (\text{yaw moment arm}) \quad (141)$$

The added mass terms for the ice are assumed as follows;

$$AM_{x_{ice}} = 0.05 \quad (\text{added mass factor in surge}) \quad (142)$$

$$AM_{y_{ice}} = 0.05 \quad (\text{added mass factor in sway}) \quad (143)$$

$$AM_{z_{ice}} = 1.0 \quad (\text{added mass factor in heave}) \quad (144)$$

$$AM_{roll_{ice}} = 1.0 \quad (\text{added mass factor in roll}) \quad (145)$$

$$AM_{pit_{ice}} = 1.0 \quad (\text{added mass factor in pitch}) \quad (146)$$

$$AM_{yaw_{ice}} = 0.05 \quad (\text{added mass factor in yaw}) \quad (147)$$

The mass radii of gyration (squared) are;

$$rx_{ice}^2 = L^2/12 \quad (\text{roll}) \quad (148)$$

$$ry_{ice}^2 = L^2/12 \quad (\text{pitch}) \quad (149)$$

$$rz_{ice}^2 = L^2/9 \quad (\text{yaw}) \quad (150)$$

The six force (moment) actions on the six degrees of freedom of the vessel's center of gravity are;

$$F_{x_{ice}} = F_n l_{ice} \quad (\text{force in surge}) \quad (151)$$

$$F_{y_{ice}} = F_n m_{ice} \quad (\text{force in sway}) \quad (152)$$

$$F_{z_{ice}} = F_n n_{ice} \quad (\text{force in heave}) \quad (153)$$

$$M_{rol_{ice}} = F_n \lambda_{ice} \quad (\text{moment in roll}) \quad (154)$$

$$M_{pit_{ice}} = F_n \mu_{ice} \quad (\text{moment in pitch}) \quad (155)$$

$$M_{yaw_{ice}} = F_n \eta_{ice} \quad (\text{moment in yaw}) \quad (156)$$

There are six accelerations at the center of gravity are:

$$a_{x_{ice}} = F_n l / (M(1 + AM_x)) \quad (\text{acceleration in surge}) \quad (157)$$

$$a_{y_{ice}} = F_n m / (M_{ice}(1 + AM_y)) \quad (\text{acceleration in sway}) \quad (158)$$

$$a_{z_{ice}} = F_n n / (M_{ice}(1 + AM_z)) \quad (\text{acceleration in heave}) \quad (159)$$

$$a_{rol_{ice}} = F_n \lambda_{ice} / (M_{ice} r x_{ice}^2 (1 + AM_{roll_{ice}})) \quad (\text{acceleration in roll}) \quad (160)$$

$$a_{pit_{ice}} = F_n \mu_{ice} / (M_{ice} r y_{ice}^2 (1 + AM_{pit_{ice}})) \quad (\text{acceleration in pitch}) \quad (161)$$

$$a_{yaw_{ice}} = F_n \eta_{ice} / (M_{ice} r z_{ice}^2 (1 + AM_{yaw_{ice}})) \quad (\text{acceleration in yaw}) \quad (162)$$

Each of these accelerations contributes to the acceleration of the point of ice contact. The total acceleration at the point of contact can be expressed as;

$$\ddot{\zeta}_{ice} = F_n C_{o_{ice}} / M_{ice} \quad (163)$$

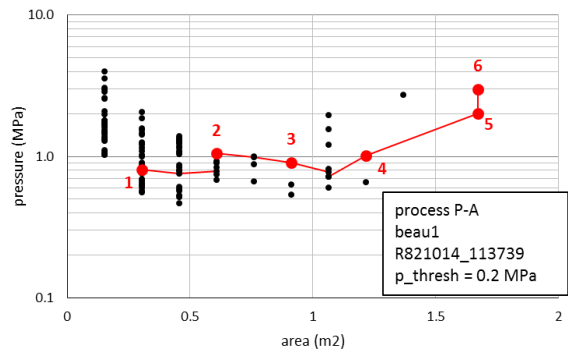
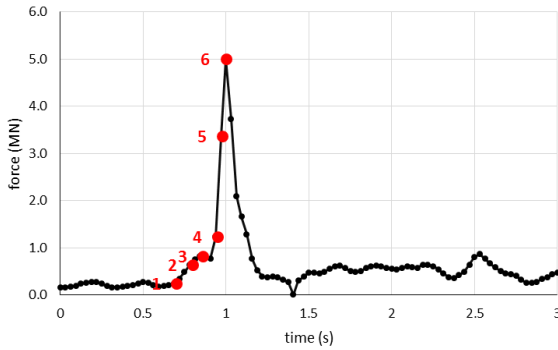
where;

$$C_o = \frac{l_{ice}^2}{1+AM_x} + \frac{m_{ice}^2}{1+AM_y} + \frac{n_{ice}^2}{1+AM_z} + \frac{\lambda_{ice}^2}{r x_{ice}^2 (1+AM_{roll})} + \frac{\mu_{ice}^2}{r y_{ice}^2 (1+AM_{pit})} + \frac{\eta_{ice}^2}{r z_{ice}^2 (1+AM_{yaw})} \quad (164)$$

Appendix B – Polar Sea Full Scale Data Cases

B.1 Beaufort Sea – Case 1

Event	Trial	Event File Name	Date	Time	Max Force (MN)	Speed (knots)
beau1	Beaufort Sea 1982 Summer	R821014_113739	10/14/1982	11:37:39	5.003	4.00



1	t=0.7 s; F=0.25 MN; A=0.3 m2; Pav=0.81 MPa									
0.00	0.03	0.03	0.00	0.04	0.01	0.00	0.01	0.01	0.01	
0.00	0.02	0.00	0.03	0.03	0.01	0.00	0.03	0.00	0.01	
0.01	0.01	0.01	0.02	0.00	0.00	0.03	0.01	0.00	0.03	
0.00	0.00	0.00	0.01	0.02	0.00	0.00	0.00	0.00	0.05	
0.00	0.10	0.00	0.00	0.00	0.01	0.04	0.59	0.00	0.03	
0.03	0.03	0.08	0.00	0.00	0.21	0.00	0.03	0.00	0.01	

2	t=0.8 s; F=0.64 MN; A=0.61 m2; Pav=1.05 MPa									
0.00	0.01	0.03	0.00	0.04	0.01	0.00	0.02	0.01	0.02	
0.01	0.01	0.00	0.04	0.01	0.01	0.01	0.03	0.00	0.00	
0.01	0.01	0.00	0.02	0.00	0.01	0.04	0.00	0.01	0.02	
0.00	0.00	0.01	0.03	0.10	0.00	0.00	0.00	0.00	0.14	
0.00	1.22	0.00	0.00	0.01	0.00	0.59	1.14	0.00	0.07	
0.10	0.06	0.06	0.00	0.00	0.22	0.00	0.01	0.04	0.00	

3	t=0.86 s; F=0.82 MN; A=0.91 m2; Pav=0.9 MPa									
0.00	0.01	0.03	0.00	0.04	0.01	0.00	0.02	0.01	0.02	
0.01	0.01	0.00	0.04	0.01	0.01	0.01	0.03	0.00	0.00	
0.01	0.00	0.00	0.03	0.00	0.01	0.03	0.00	0.00	0.00	
0.00	0.00	0.03	0.08	0.23	0.19	0.00	0.00	0.00	0.28	
0.00	2.24	0.00	0.00	0.18	0.06	0.74	0.52	0.00	0.09	
0.10	0.05	0.00	0.00	0.00	0.22	0.00	0.05	0.01	0.01	

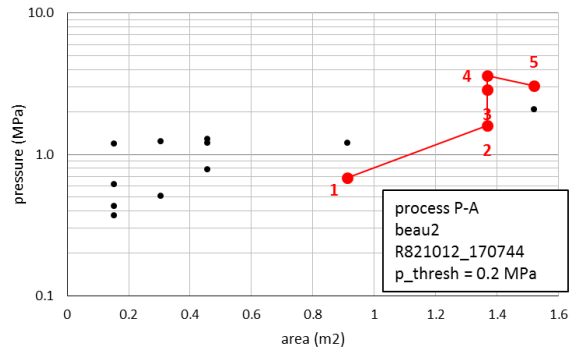
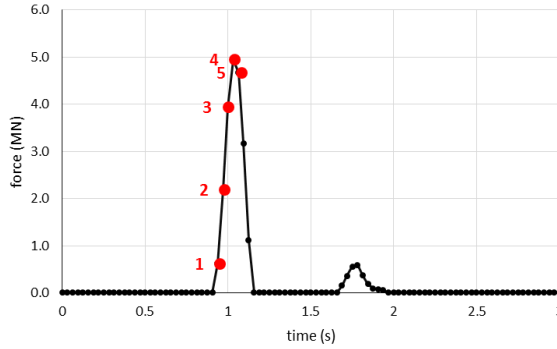
4	t=0.95 s; F=1.23 MN; A=1.22 m2; Pav=1.01 MPa									
0.00	0.02	0.03	0.00	0.03	0.01	0.00	0.05	0.01	0.02	
0.01	0.01	0.00	0.02	0.03	0.01	0.00	0.04	0.00	0.02	
0.00	0.01	0.01	0.01	0.00	0.02	0.06	0.00	0.00	0.00	
0.00	0.00	0.00	0.09	0.15	0.38	0.00	0.27	1.21	0.42	
0.06	0.89	0.05	0.14	3.10	0.00	0.22	0.00	0.00	0.10	
0.17	0.08	0.06	0.00	0.00	0.21	0.00	0.01	0.00	0.01	

5	t=0.98 s; F=3.38 MN; A=1.67 m2; Pav=2.02 MPa									
0.00	0.00	0.02	0.00	0.01	0.01	0.00	0.10	0.00	0.00	
0.00	0.00	0.18	0.00	0.00	0.00	0.00	0.01	0.00	0.03	
0.00	0.00	0.00	0.00	0.00	0.01	0.01	0.00	0.00	0.00	
0.00	0.00	0.00	0.01	0.10	0.05	0.00	1.28	5.10	0.54	
0.20	0.43	0.00	1.77	9.55	0.00	0.67	0.00	0.01	0.50	
0.91	0.14	0.29	0.00	0.00	0.28	0.00	0.00	0.00	0.00	

6	t=1 s; F=5 MN; A=1.67 m2; Pav=2.99 MPa									
0.00	0.00	0.01	0.00	0.01	0.00	0.01	0.13	0.00	0.00	
0.00	0.00	0.17	0.00	0.00	0.00	0.00	0.00	0.00	0.00	
0.00	0.00	0.00	0.00	0.00	0.00	0.00	0.00	0.00	0.00	
0.00	0.00	0.00	0.00	0.10	0.01	0.00	2.70	8.98	0.61	
0.13	0.55	0.00	4.00	11.15	0.01	1.14	0.00	0.00	1.30	
1.14	0.10	0.42	0.00	0.00	0.24	0.00	0.00	0.00	0.00	

B.2 Beaufort Sea – Case 2

Event	Trial	Event File Name	Date	Time	Max Force (MN)	Speed (knots)
beau2	Beaufort Sea 1982 Summer	R821012_170744	10/12/1982	11:07:44	4.954	3.00



1	t=0.95 s; F=0.62 MN; A=0.91 m2; Pav=0.68 MPa									
0.00	0.00	0.00	0.03	0.00	0.00	0.00	0.00	0.00	0.00	0.00
0.00	0.00	0.00	0.07	0.00	0.00	0.00	0.00	0.00	0.00	0.00
0.00	0.75	1.08	0.00	0.00	0.00	0.06	0.24	1.17	0.32	0.00
0.00	0.00	0.01	0.00	0.38	0.00	0.00	0.00	0.00	0.00	0.00
0.00	0.00	0.00	0.00	0.00	0.00	0.00	0.00	0.00	0.00	0.00
0.00	0.00	0.00	0.00	0.00	0.00	0.00	0.00	0.00	0.00	0.00

2	t=0.98 s; F=2.2 MN; A=1.37 m2; Pav=1.61 MPa									
0.00	0.00	0.00	0.03	0.00	0.00	0.00	0.00	0.00	0.00	0.00
0.00	0.00	0.00	0.13	0.00	0.00	0.00	0.00	0.03	0.00	0.00
0.00	1.23	2.73	2.09	0.37	0.00	0.00	0.38	2.48	3.78	0.00
0.00	0.05	0.01	0.00	0.88	0.25	0.00	0.00	0.00	0.00	0.00
0.00	0.00	0.00	0.00	0.00	0.00	0.00	0.00	0.00	0.00	0.00
0.00	0.00	0.00	0.00	0.00	0.00	0.00	0.00	0.00	0.00	0.00

3	t=1 s; F=3.94 MN; A=1.37 m2; Pav=2.88 MPa									
0.00	0.00	0.00	0.04	0.00	0.00	0.00	0.00	0.00	0.00	0.00
0.00	0.00	0.00	0.17	0.00	0.00	0.00	0.00	0.03	0.00	0.00
4.17	2.39	1.59	1.25	0.00	0.00	3.23	4.32	6.03	0.00	0.00
0.00	0.13	0.00	0.00	1.85	0.75	0.00	0.00	0.00	0.00	0.00
0.00	0.00	0.00	0.00	0.00	0.00	0.00	0.00	0.00	0.00	0.00
0.00	0.00	0.00	0.00	0.00	0.00	0.00	0.00	0.00	0.00	0.00

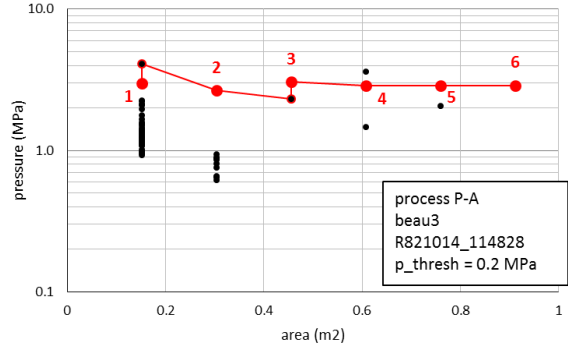
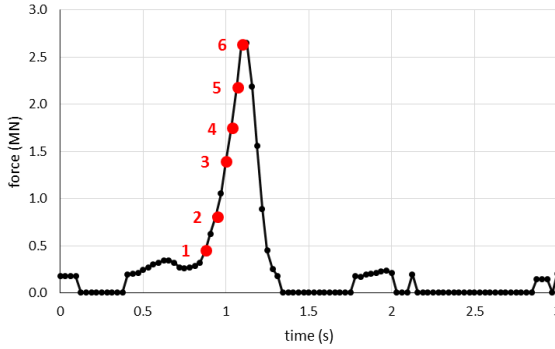
4	t=1.04 s; F=4.95 MN; A=1.37 m2; Pav=3.62 MPa									
0.00	0.00	0.00	0.06	0.00	0.00	0.00	0.00	0.00	0.00	0.00
0.00	0.00	0.00	0.20	0.00	0.00	0.00	0.00	0.04	0.00	0.00
5.08	3.18	1.57	1.76	0.00	0.00	4.76	4.61	7.26	0.00	0.00
0.00	0.14	0.00	0.00	2.84	1.09	0.00	0.00	0.00	0.00	0.00
0.00	0.00	0.00	0.00	0.00	0.00	0.00	0.00	0.00	0.00	0.00
0.00	0.00	0.00	0.00	0.00	0.00	0.00	0.00	0.00	0.00	0.00

5	t=1.08 s; F=4.67 MN; A=1.52 m2; Pav=3.07 MPa									
0.00	0.00	0.00	0.06	0.00	0.00	0.00	0.00	0.00	0.00	0.00
0.00	0.00	0.00	0.27	0.00	0.00	0.00	0.08	0.07	0.00	0.00
5.63	4.31	2.14	1.97	0.00	0.00	3.24	3.38	6.89	0.15	0.00
0.00	0.03	0.00	0.00	0.91	1.61	0.00	0.00	0.00	0.00	0.00
0.00	0.00	0.00	0.00	0.00	0.00	0.00	0.00	0.00	0.00	0.00
0.00	0.00	0.00	0.00	0.00	0.00	0.00	0.00	0.00	0.00	0.00

6	#####									
0.00	0.00	0.00	0.02	0.00	0.00	0.00	0.00	0.00	0.00	0.00
0.00	0.00	0.00	0.04	0.00	0.00	0.00	0.00	0.00	0.00	0.00
0.00	0.00	0.00	0.00	0.00	0.00	0.00	0.00	0.00	0.00	0.00
0.00	0.00	0.00	0.00	0.00	0.00	0.00	0.00	0.00	0.00	0.00
0.00	0.00	0.00	0.00	0.00	0.00	0.00	0.00	0.00	0.00	0.00
0.00	0.00	0.00	0.00	0.00	0.00	0.00	0.00	0.00	0.00	0.00

B.3 Beaufort Sea – Case 3

Event	Trial	Event File Name	Date	Time	Max Force (MN)	Speed (knots)
beau3	Beaufort Sea 1982 Summer	R821014_114828	10/14/1982	11:48:28	2.633	4.00



1	t=0.88 s; F=0.45 MN; A=0.15 m2; Pav=2.98 MPa									
0.00	0.05	0.00	0.00	0.04	0.04	0.01	0.00	1.65	0.00	
0.06	0.01	0.00	0.06	0.14	0.08	0.00	0.06	0.00	0.00	
0.03	0.02	0.01	0.03	0.00	0.01	0.03	0.03	0.01	0.02	
0.00	0.00	0.00	0.03	0.01	0.00	0.00	0.15	0.10	0.02	
0.00	0.01	0.00	0.03	0.00	0.03	0.00	0.00	0.00	0.00	
0.01	0.00	0.00	0.00	0.00	0.16	0.00	0.02	0.00	0.03	

2	t=0.95 s; F=0.81 MN; A=0.3 m2; Pav=2.65 MPa									
0.00	0.14	0.06	0.00	0.08	0.04	0.10	0.00	3.56	0.00	
0.10	0.00	0.00	0.09	0.08	0.21	0.00	0.08	0.00	0.00	
0.05	0.03	0.00	0.03	0.00	0.01	0.03	0.01	0.00	0.02	
0.00	0.00	0.00	0.01	0.01	0.00	0.00	0.14	0.08	0.03	
0.00	0.01	0.00	0.07	0.00	0.03	0.00	0.00	0.00	0.00	
0.00	0.00	0.00	0.00	0.00	0.16	0.00	0.02	0.00	0.03	

3	t=1 s; F=1.39 MN; A=0.46 m2; Pav=3.05 MPa									
0.00	0.12	1.19	0.00	0.16	0.02	0.20	0.00	5.94	0.00	
0.13	0.00	0.00	0.11	0.00	0.41	0.00	0.12	0.00	0.03	
0.05	0.00	0.01	0.02	0.00	0.02	0.03	0.00	0.00	0.03	
0.00	0.00	0.00	0.01	0.00	0.00	0.00	0.18	0.09	0.03	
0.00	0.00	0.00	0.07	0.00	0.02	0.00	0.00	0.00	0.00	
0.00	0.00	0.00	0.00	0.00	0.16	0.00	0.02	0.00	0.01	

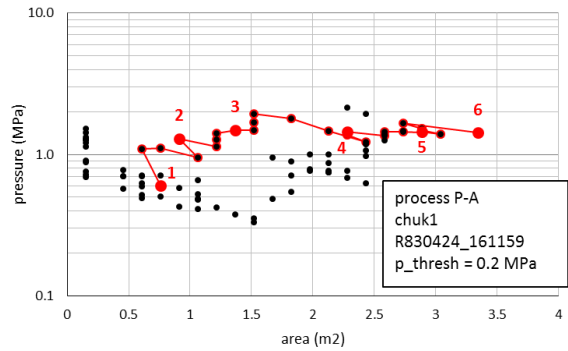
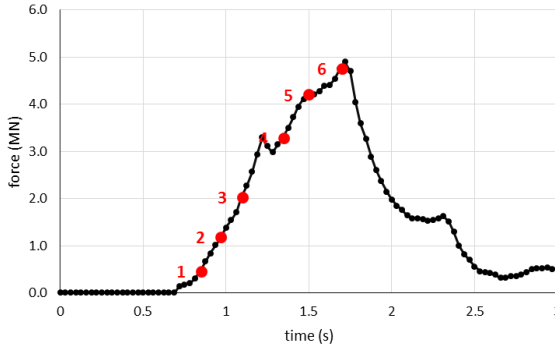
4	t=1.04 s; F=1.75 MN; A=0.61 m2; Pav=2.87 MPa									
0.00	0.00	2.70	0.00	0.23	0.01	0.18	0.00	6.60	0.00	
0.14	0.01	0.00	0.12	0.00	0.56	0.00	0.15	0.00	0.04	
0.04	0.00	0.00	0.02	0.00	0.02	0.03	0.00	0.00	0.01	
0.00	0.00	0.00	0.00	0.01	0.00	0.00	0.19	0.09	0.03	
0.00	0.00	0.00	0.07	0.00	0.01	0.00	0.00	0.00	0.00	
0.01	0.00	0.00	0.00	0.00	0.17	0.00	0.02	0.00	0.02	

5	t=1.07 s; F=2.18 MN; A=0.76 m2; Pav=2.87 MPa									
0.00	0.00	4.72	0.00	0.32	0.00	0.13	0.00	6.90	0.36	
0.08	0.05	0.00	0.13	0.00	0.70	0.00	0.18	0.00	0.05	
0.03	0.00	0.00	0.03	0.00	0.03	0.03	0.00	0.00	0.00	
0.00	0.00	0.00	0.00	0.00	0.00	0.00	0.18	0.09	0.03	
0.00	0.00	0.00	0.07	0.00	0.01	0.00	0.00	0.00	0.00	
0.00	0.00	0.00	0.00	0.00	0.17	0.00	0.02	0.00	0.02	

6	t=1.1 s; F=2.63 MN; A=0.91 m2; Pav=2.89 MPa									
0.00	0.00	6.95	0.00	0.43	0.00	0.09	0.00	6.58	0.92	
0.03	0.11	0.00	0.12	0.21	0.67	0.00	0.18	0.00	0.03	
0.20	0.17	0.00	0.01	0.00	0.06	0.01	0.00	0.00	0.00	
0.00	0.00	0.00	0.00	0.00	0.00	0.00	0.18	0.06	0.01	
0.00	0.00	0.00	0.06	0.00	0.01	0.00	0.00	0.00	0.00	
0.01	0.00	0.00	0.00	0.00	0.18	0.00	0.02	0.00	0.02	

B.4 Chukchi Sea – Case 1

Event	Trial	Event File Name	Date	Time	Max Force (MN)	Speed (knots)
chuk1	Chuckchi Sea 1983 Winter	R830424_161159	4/24/1983	16:11:59	4.892	7.80



1	t=0.85 s; F=0.46 MN; A=0.76 m2; Pav=0.6 MPa									
0.00	0.01	0.00	0.00	0.00	0.00	0.00	0.00	0.00	0.00	0.00
0.00	0.00	0.00	0.00	0.00	0.00	0.00	0.00	0.00	0.00	0.00
0.00	0.00	0.00	0.00	0.01	0.00	0.06	0.24	0.00	0.00	0.00
0.00	0.00	0.00	0.01	0.02	0.06	0.00	0.00	0.70	1.11	0.00
0.00	0.01	0.00	0.00	0.00	0.00	0.00	0.06	0.28	0.34	0.00
0.01	0.00	0.00	0.09	0.00	0.00	0.00	0.00	0.00	0.00	0.00

2	t=0.97 s; F=1.18 MN; A=0.91 m2; Pav=1.3 MPa									
0.08	0.00	0.00	0.00	0.00	0.00	0.00	0.00	0.00	0.00	0.00
0.00	0.01	0.00	0.00	0.00	0.00	0.00	0.00	0.00	0.00	0.00
0.00	0.01	0.01	0.00	0.00	0.05	0.19	0.00	0.00	0.00	0.00
0.01	0.00	0.00	0.01	0.03	0.00	0.06	0.51	1.16	1.67	0.00
0.01	0.03	0.00	0.01	0.00	0.00	0.04	0.81	1.50	1.35	0.00
0.00	0.01	0.06	0.00	0.00	0.00	0.14	0.00	0.00	0.00	0.00

3	t=1.1 s; F=2.03 MN; A=1.37 m2; Pav=1.48 MPa									
0.00	0.00	0.00	0.00	0.00	0.00	0.00	0.00	0.00	0.00	0.00
0.00	0.00	0.00	0.00	0.00	0.00	0.00	0.00	0.00	0.00	0.00
0.00	0.01	0.00	0.00	0.17	0.00	0.08	0.00	0.00	0.00	0.00
0.00	0.00	0.00	0.00	0.08	0.10	0.24	0.74	0.32	1.32	0.00
0.00	0.03	0.01	0.00	0.00	0.14	0.83	2.00	4.36	2.28	0.00
0.05	0.00	0.00	0.00	0.00	0.00	0.60	0.00	0.00	0.00	0.00

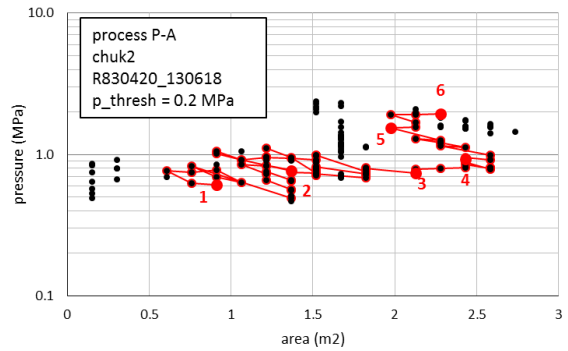
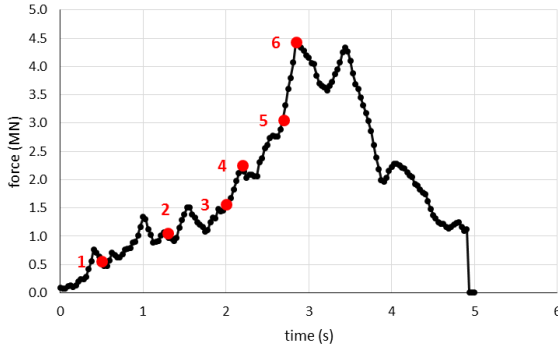
4	t=1.35 s; F=3.29 MN; A=2.28 m2; Pav=1.44 MPa									
0.00	0.00	0.00	0.00	0.00	0.00	0.00	0.00	0.00	0.00	0.00
0.00	0.00	0.00	0.00	0.00	0.00	0.00	0.00	0.00	0.00	0.00
0.00	0.01	0.01	0.00	0.00	0.00	0.14	0.00	0.00	0.00	0.49
0.00	0.00	0.02	0.17	0.23	0.49	0.46	1.05	1.23	0.02	0.00
0.02	0.00	0.00	0.18	1.63	1.70	1.04	4.43	1.05	0.19	0.00
0.00	0.00	0.00	0.50	0.49	1.34	4.72	0.00	0.00	0.00	0.00

5	t=1.5 s; F=4.2 MN; A=2.89 m2; Pav=1.46 MPa									
0.00	0.00	0.00	0.00	0.00	0.00	0.00	0.00	0.00	0.00	0.00
0.00	0.00	0.00	0.00	0.00	0.00	0.00	0.07	0.00	0.00	0.00
0.00	0.04	0.01	0.00	0.12	0.00	0.08	0.00	0.30	0.28	0.00
0.00	0.02	0.17	0.37	0.38	0.16	0.52	0.70	0.51	0.18	0.00
0.00	0.00	0.69	0.65	0.99	5.14	2.23	0.64	0.12	0.24	0.00
0.00	0.01	1.84	3.36	2.88	2.63	2.21	0.00	0.12	0.00	0.00

6	t=1.7 s; F=4.76 MN; A=3.34 m2; Pav=1.42 MPa									
0.00	0.00	0.00	0.00	0.00	0.00	0.00	0.00	0.00	0.00	0.00
0.00	0.00	0.00	0.00	0.00	0.00	0.00	0.01	0.00	0.00	0.00
0.00	0.08	0.00	0.03	0.10	0.00	0.04	0.00	0.00	0.00	0.00
0.00	0.47	0.49	0.24	0.36	0.50	0.37	0.79	0.49	0.30	0.00
0.22	0.00	0.00	0.62	3.27	1.65	0.12	0.40	1.03	0.21	0.00
1.06	4.66	6.83	6.12	0.52	0.24	0.08	0.00	0.00	0.00	0.00

B.5 Chukchi Sea – Case 2

Event	Trial	Event File Name	Date	Time	Max Force (MN)	Speed (knots)
chuk2	Chuckchi Sea 1983 Winter	R830420_130618	4/20/1983	13:06:18	4.414	3.20



1	t = 0.5 s; F = 0.56 MN; A = 0.91 m ² ; Pav = 0.61 MPa									
0.00	0.00	0.00	0.00	0.00	0.00	0.00	0.00	0.00	0.00	0.00
0.00	0.00	0.03	0.00	0.00	0.00	0.00	0.00	0.00	0.00	0.00
0.00	0.00	0.00	0.00	0.03	0.00	0.00	0.38	0.52	0.71	0.00
0.00	0.33	0.30	0.15	0.01	0.00	0.00	0.07	0.20	0.07	0.00
0.03	0.14	0.00	0.00	0.08	0.09	0.00	0.05	0.01	0.04	0.00
0.00	0.00	0.02	0.00	0.07	0.24	0.08	0.00	0.00	0.00	0.00

2	t = 1.3 s; F = 1.06 MN; A = 1.37 m ² ; Pav = 0.77 MPa									
0.08	0.00	0.00	0.00	0.00	0.00	0.00	0.00	0.00	0.00	0.00
0.00	0.00	0.00	0.01	0.00	0.00	0.00	0.00	0.00	0.00	0.00
0.00	0.10	0.00	0.00	0.08	0.30	0.42	0.27	0.00	0.52	0.00
0.20	0.12	0.00	0.00	0.00	0.11	0.37	0.74	2.29	0.82	0.00
0.00	0.00	0.00	0.00	0.00	0.00	0.00	0.21	0.07	0.00	0.00
0.00	0.11	0.07	0.00	0.00	0.00	0.08	0.00	0.00	0.00	0.00

3	t = 2 s; F = 1.57 MN; A = 2.13 m ² ; Pav = 0.74 MPa									
0.00	0.00	0.00	0.00	0.00	0.00	0.00	0.00	0.00	0.00	0.00
0.00	0.00	0.00	0.00	0.00	0.00	0.00	0.04	0.00	0.00	0.00
0.00	0.04	0.00	0.00	0.00	0.00	0.00	0.00	0.00	0.00	0.00
0.00	0.06	0.50	0.94	1.79	1.63	0.48	0.63	0.58	0.88	0.00
0.00	0.00	0.00	0.14	0.28	0.72	0.59	0.22	0.45	0.08	0.00
0.00	0.01	0.00	0.01	0.00	0.03	0.21	0.00	0.00	0.00	0.00

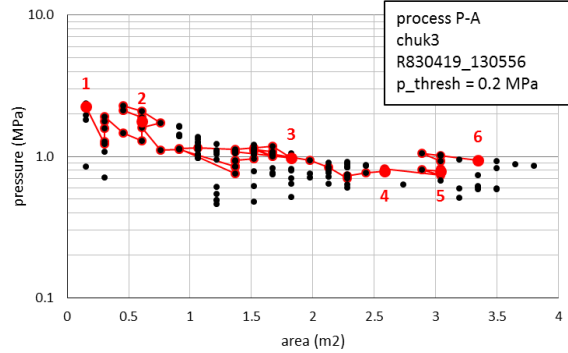
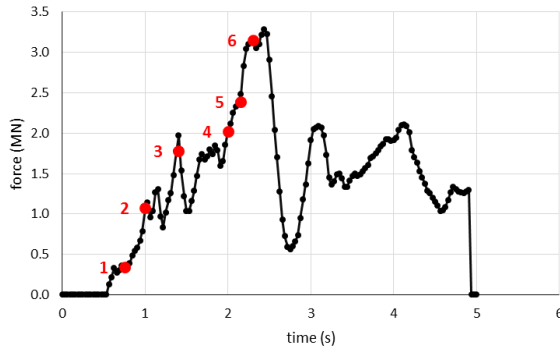
4	t = 2.2 s; F = 2.26 MN; A = 2.43 m ² ; Pav = 0.93 MPa									
0.00	0.00	0.00	0.00	0.00	0.00	0.00	0.00	0.00	0.00	0.00
0.00	0.00	0.03	0.00	0.00	0.00	0.00	0.01	0.00	0.00	0.00
0.00	0.01	0.00	0.00	0.00	0.00	0.00	0.00	0.00	0.00	0.00
0.00	0.58	2.70	0.84	1.01	1.37	0.36	0.67	0.51	0.68	0.00
0.00	0.00	0.03	1.29	0.78	0.79	1.06	0.46	1.14	0.41	0.00
0.00	0.04	0.02	0.00	0.00	0.00	0.08	0.00	0.00	0.00	0.00

5	t = 2.7 s; F = 3.05 MN; A = 1.98 m ² ; Pav = 1.54 MPa									
0.00	0.00	0.00	0.00	0.00	0.00	0.00	0.00	0.00	0.00	0.00
0.00	0.00	0.00	0.00	0.00	0.00	0.00	0.00	0.00	0.00	0.00
0.00	0.07	0.01	0.02	0.03	0.00	0.06	0.00	0.00	0.00	0.00
0.18	0.11	0.00	0.06	0.12	0.28	0.01	0.11	0.00	0.11	0.00
0.00	1.13	3.36	2.34	1.99	2.92	0.91	1.43	1.50	0.82	0.00
0.00	0.00	0.44	1.08	0.00	0.00	0.97	0.00	0.00	0.00	0.00

6	t = 2.85 s; F = 4.43 MN; A = 2.28 m ² ; Pav = 1.94 MPa									
0.00	0.00	0.00	0.00	0.00	0.00	0.00	0.00	0.00	0.00	0.00
0.00	0.00	0.00	0.00	0.00	0.00	0.00	0.00	0.00	0.00	0.00
0.00	0.21	0.08	0.13	0.05	0.00	0.04	0.00	0.06	0.00	0.00
0.17	0.00	0.00	0.11	0.00	0.22	0.00	0.00	0.00	0.00	0.00
0.00	2.78	6.59	1.73	3.20	2.63	0.82	2.03	1.79	1.48	0.00
0.00	0.65	1.41	1.70	0.00	0.11	1.14	0.00	0.00	0.00	0.00

B.6 Chukchi Sea – Case 3

Event	Trial	Event File Name	Date	Time	Max Force (MN)	Speed (knots)
chuk3	Chuckchi Sea 1983 Winter	R830419_130556	4/19/1983	13:05:56	3.278	4.90



1	t=0.75 s; F=0.34 MN; A=0.15 m2; Pav=2.25 MPa									
0.14	0.00	0.04	0.02	0.00	0.00	0.00	0.00	0.08	0.06	
0.00	0.03	0.02	0.00	0.01	0.00	0.00	0.00	0.11	1.38	
0.05	0.00	0.03	0.03	0.00	0.00	0.01	0.03	0.00	0.00	
0.01	0.03	0.00	0.00	0.00	0.00	0.00	0.00	0.01	0.06	
0.03	0.01	0.00	0.00	0.00	0.00	0.00	0.00	0.00	0.01	
0.00	0.01	0.00	0.00	0.00	0.00	0.00	0.06	0.00	0.00	

2	t=1 s; F=1.07 MN; A=0.61 m2; Pav=1.77 MPa									
0.09	0.00	0.05	0.00	0.00	0.00	0.00	0.00	0.00	0.00	0.00
0.00	0.01	0.00	0.00	0.00	0.00	0.00	0.00	1.88	3.25	0.52
0.05	0.00	0.04	0.03	0.00	0.00	0.04	0.00	0.00	0.00	0.56
0.00	0.06	0.00	0.00	0.00	0.00	0.00	0.08	0.17	0.00	
0.02	0.00	0.00	0.00	0.00	0.00	0.00	0.00	0.09	0.12	
0.00	0.00	0.00	0.00	0.00	0.00	0.00	0.01	0.00	0.00	

3	t=1.4 s; F=1.78 MN; A=1.82 m2; Pav=0.98 MPa									
0.00	0.00	0.01	0.00	0.00	0.00	0.00	0.01	0.00	0.00	
0.01	0.00	0.00	0.00	0.22	0.29	0.91	0.49	0.61	0.23	
0.04	0.00	0.04	0.00	0.00	0.00	0.00	3.86	3.39	0.66	
0.00	0.06	0.00	0.00	0.00	0.00	0.06	0.00	0.00	0.00	
0.01	0.01	0.00	0.00	0.00	0.00	0.00	0.21	0.33	0.23	
0.00	0.00	0.00	0.00	0.00	0.00	0.02	0.00	0.00	0.00	

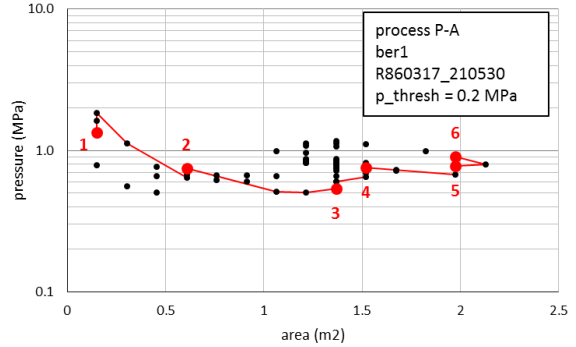
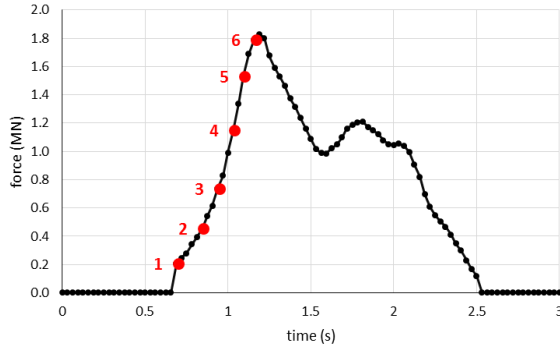
4	t=2 s; F=2.02 MN; A=2.58 m2; Pav=0.78 MPa									
0.00	0.00	0.00	0.00	0.00	0.00	0.00	0.00	0.00	0.00	0.00
0.00	0.85	0.38	0.29	0.15	0.00	0.00	0.00	0.00	0.00	0.00
0.06	0.00	0.09	0.47	0.98	1.52	2.40	1.09	0.71	1.34	
0.00	0.11	0.00	0.00	0.00	0.05	0.36	0.22	0.31	0.27	
0.00	0.01	0.00	0.03	0.08	0.00	0.14	0.31	0.41	0.38	
0.03	0.00	0.03	0.00	0.00	0.04	0.15	0.00	0.06	0.00	

5	t=2.15 s; F=2.39 MN; A=3.04 m2; Pav=0.79 MPa									
0.00	0.00	0.00	0.00	0.00	0.00	0.00	0.00	0.00	0.00	
0.34	0.72	0.62	0.06	0.00	0.00	0.00	0.00	0.00	0.00	
0.06	0.00	0.52	0.97	1.06	1.73	1.79	1.23	1.43	0.97	
0.00	0.07	0.00	0.00	0.00	0.34	0.54	0.39	0.52	0.41	
0.01	0.02	0.00	0.03	0.08	0.04	0.19	0.39	0.54	0.32	
0.00	0.00	0.03	0.01	0.00	0.07	0.23	0.00	0.00	0.00	

6	t=2.3 s; F=3.15 MN; A=3.34 m2; Pav=0.94 MPa									
0.00	0.00	0.06	0.01	0.00	0.00	0.00	0.00	0.00	0.00	0.00
0.47	0.25	0.00	0.00	0.00	0.00	0.00	0.00	0.00	0.00	0.00
0.00	0.49	2.01	1.31	2.13	1.77	2.58	1.12	0.79	0.58	
0.00	0.05	0.00	0.00	0.24	0.79	1.04	0.88	0.85	0.30	
0.01	0.03	0.00	0.01	0.19	0.23	0.18	0.68	0.65	0.26	
0.00	0.00	0.04	0.06	0.01	0.17	0.51	0.00	0.00	0.00	

B.7 Bering Sea – Case 1

Event	Trial	Event File Name	Date	Time	Max Force (MN)	Speed (knots)
ber1	Bering Sea 1986 Winter	R860317_210530	3/17/1986	21:05:30	1.813	6.00



1	t=0.7 s; F=0.2 MN; A=0.15 m2; Pav=1.34 MPa									
0.03	0.00	0.03	0.00	0.03	0.00	0.08	0.14	0.06	0.00	
0.00	0.00	0.02	0.03	0.00	0.00	0.00	0.01	0.10	0.05	
0.00	0.02	0.03	0.01	0.01	0.05	0.22	0.14	0.00	0.02	
0.01	0.01	0.00	0.03	0.00	0.00	0.01	0.00	0.01	0.06	
0.00	0.00	0.00	0.01	0.00	0.01	0.00	0.02	0.00	0.01	
0.00	0.00	0.00	0.00	0.01	0.03	0.03	0.00	0.00	0.00	

2	t=0.85 s; F=0.45 MN; A=0.61 m2; Pav=0.75 MPa									
0.03	0.00	0.03	0.00	0.03	0.01	0.19	0.18	0.03	0.44	
0.00	0.00	0.02	0.00	0.00	0.00	0.00	0.02	0.06	0.16	
0.02	0.01	0.04	0.01	0.00	0.20	0.43	0.31	0.00	0.32	
0.01	0.01	0.00	0.03	0.00	0.00	0.14	0.00	0.06	0.00	
0.00	0.00	0.02	0.00	0.00	0.01	0.00	0.03	0.00	0.03	
0.00	0.00	0.00	0.00	0.02	0.03	0.04	0.01	0.00	0.01	

3	t=0.95 s; F=0.74 MN; A=1.37 m2; Pav=0.54 MPa									
0.03	0.00	0.03	0.00	0.00	0.05	0.23	0.30	0.12	0.65	
0.00	0.00	0.00	0.01	0.00	0.00	0.01	0.00	0.28	0.05	
0.00	0.02	0.05	0.00	0.03	0.32	0.55	0.75	0.00	0.61	
0.01	0.01	0.00	0.08	0.00	0.00	0.30	0.00	0.05	0.00	
0.00	0.00	0.02	0.00	0.01	0.02	0.00	0.01	0.00	0.01	
0.00	0.00	0.00	0.02	0.01	0.04	0.07	0.03	0.03	0.02	

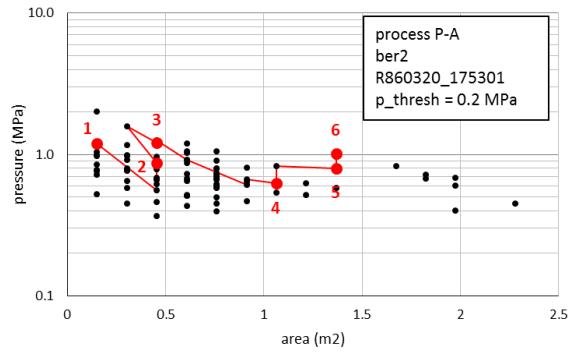
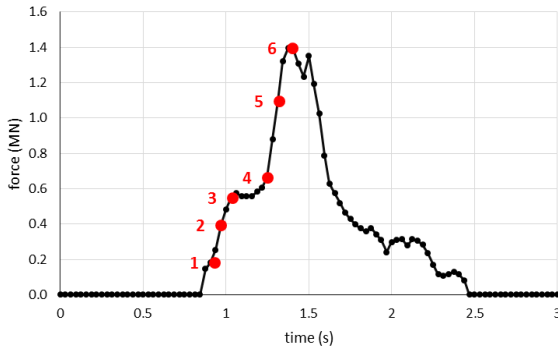
4	t=1.04 s; F=1.15 MN; A=1.52 m2; Pav=0.76 MPa									
0.03	0.00	0.03	0.00	0.02	0.06	0.19	0.54	0.40	0.50	
0.00	0.01	0.00	0.03	0.00	0.00	0.07	0.00	0.26	0.06	
0.00	0.01	0.05	0.00	0.17	0.41	0.66	1.61	0.43	0.43	
0.01	0.05	0.00	0.20	0.00	0.00	0.70	0.18	0.00	0.00	
0.00	0.00	0.03	0.00	0.03	0.06	0.00	0.00	0.00	0.00	
0.00	0.00	0.00	0.02	0.03	0.04	0.11	0.08	0.05	0.00	

5	t=1.1 s; F=1.53 MN; A=1.98 m2; Pav=0.78 MPa									
0.02	0.01	0.01	0.00	0.03	0.06	0.28	0.74	0.56	0.23	
0.00	0.01	0.00	0.06	0.00	0.00	0.21	0.00	0.27	0.00	
0.00	0.02	0.05	0.00	0.19	0.42	0.71	2.52	0.69	0.15	
0.00	0.09	0.00	0.25	0.00	0.00	1.39	0.43	0.00	0.06	
0.00	0.00	0.05	0.00	0.06	0.07	0.00	0.00	0.00	0.00	
0.00	0.00	0.00	0.01	0.03	0.06	0.17	0.12	0.08	0.00	

6	t=1.17 s; F=1.79 MN; A=1.98 m2; Pav=0.91 MPa									
0.02	0.01	0.04	0.00	0.06	0.03	0.39	0.86	0.63	0.00	
0.00	0.01	0.02	0.05	0.00	0.00	0.32	0.00	0.27	0.01	
0.00	0.02	0.04	0.03	0.21	0.43	0.99	3.08	0.51	0.00	
0.00	0.09	0.00	0.34	0.00	0.00	2.20	0.14	0.01	0.08	
0.00	0.00	0.06	0.00	0.07	0.13	0.00	0.04	0.01	0.00	
0.00	0.00	0.00	0.01	0.03	0.10	0.26	0.13	0.07	0.00	

B.8 Bering Sea – Case 2

Event	Trial	Event File Name	Date	Time	Max Force (MN)	Speed (knots)
ber2	Bering Sea 1986 Winter	R860320_175301	3/20/1986	17:53:01	1.415	8.25



1	t=0.93 s; F=0.18 MN; A=0.15 m2; Pav=1.19 MPa									
0.01	0.01	0.01	0.03	0.00	0.00	0.00	0.00	0.01	0.01	
0.00	0.01	0.00	0.00	0.00	0.00	0.00	0.08	0.40	0.00	
0.02	0.03	0.09	0.01	0.03	0.00	0.00	0.00	0.00	0.03	
0.01	0.06	0.00	0.01	0.00	0.01	0.01	0.00	0.01	0.00	
0.01	0.01	0.02	0.00	0.03	0.00	0.00	0.00	0.01	0.13	
0.03	0.00	0.03	0.02	0.02	0.00	0.00	0.00	0.00	0.00	

2	t=0.97 s; F=0.4 MN; A=0.46 m2; Pav=0.87 MPa									
0.01	0.01	0.01	0.03	0.01	0.00	0.03	0.00	0.02	0.01	
0.00	0.00	0.01	0.00	0.00	0.00	0.00	1.03	0.45	0.00	
0.02	0.07	0.04	0.00	0.03	0.00	0.03	0.00	0.00	0.05	
0.01	0.04	0.14	0.02	0.01	0.01	0.01	0.00	0.04	0.00	
0.01	0.01	0.00	0.00	0.02	0.00	0.00	0.00	0.03	0.24	
0.03	0.00	0.03	0.02	0.02	0.00	0.00	0.00	0.03	0.01	0.00

3	t=1.04 s; F=0.55 MN; A=0.46 m2; Pav=1.21 MPa									
0.01	0.01	0.03	0.03	0.01	0.00	0.13	0.02	0.08	0.00	
0.01	0.00	0.04	0.00	0.00	0.00	0.56	1.37	0.17	0.00	
0.02	0.06	0.01	0.00	0.03	0.02	0.00	0.00	0.06	0.02	
0.05	0.01	0.12	0.03	0.00	0.01	0.01	0.00	0.04	0.01	
0.01	0.04	0.00	0.02	0.02	0.00	0.00	0.00	0.32	0.08	
0.02	0.00	0.03	0.01	0.04	0.01	0.02	0.03	0.00	0.00	

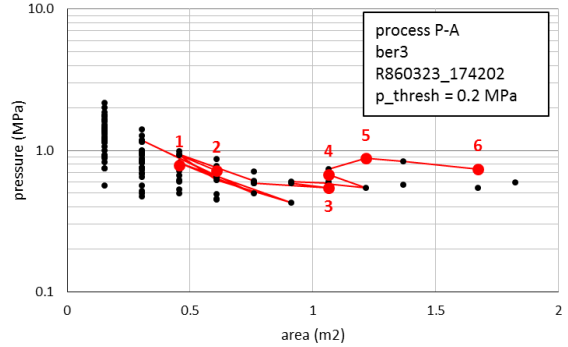
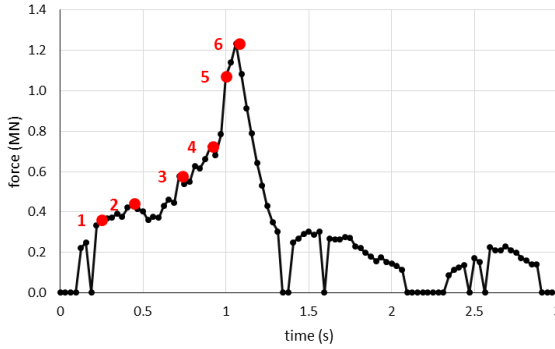
4	t=1.25 s; F=0.67 MN; A=1.06 m2; Pav=0.63 MPa									
0.01	0.01	0.00	0.00	0.32	0.74	0.23	0.14	0.14	0.02	
0.00	0.00	0.00	0.00	0.25	0.41	0.56	0.39	0.08	0.00	
0.02	0.03	0.00	0.02	0.08	0.08	0.00	0.01	0.03	0.05	
0.00	0.01	0.00	0.06	0.00	0.00	0.05	0.00	0.06	0.01	
0.01	0.04	0.03	0.01	0.01	0.06	0.04	0.01	0.06	0.02	
0.03	0.00	0.03	0.03	0.05	0.08	0.07	0.01	0.00	0.00	

5	t=1.32 s; F=1.1 MN; A=1.37 m2; Pav=0.8 MPa									
0.01	0.01	0.00	0.44	1.34	0.94	0.76	0.20	0.21	0.01	
0.00	0.00	0.00	0.25	0.09	0.37	0.46	0.20	0.06	0.00	
0.03	0.03	0.04	0.09	0.24	0.17	0.09	0.10	0.05	0.02	
0.00	0.06	0.00	0.06	0.00	0.00	0.08	0.03	0.06	0.04	
0.04	0.03	0.03	0.00	0.05	0.00	0.00	0.03	0.05	0.03	
0.02	0.00	0.03	0.06	0.11	0.10	0.06	0.02	0.01	0.00	

6	t=1.4 s; F=1.39 MN; A=1.37 m2; Pav=1.02 MPa									
0.01	0.00	0.01	1.55	1.05	1.81	0.88	0.29	0.35	0.10	
0.00	0.00	0.08	0.00	0.00	0.00	0.14	0.09	0.06	0.03	
0.03	0.01	0.11	0.35	0.35	0.37	0.20	0.12	0.08	0.06	
0.00	0.09	0.00	0.00	0.00	0.00	0.11	0.02	0.06	0.02	
0.03	0.02	0.03	0.00	0.05	0.01	0.00	0.05	0.06	0.01	
0.02	0.00	0.06	0.10	0.12	0.10	0.06	0.03	0.03	0.01	

B.9 Bering Sea – Case 3

Event	Trial	Event File Name	Date	Time	Max Force (MN)	Speed (knots)
ber3	Bering Sea 1986 Winter	R860323_174202	3/23/1986	17:42:02	1.096	8.88



1	t=0.25 s; F=0.36 MN; A=0.46 m2; Pav=0.79 MPa									
0.01	0.01	0.01	0.00	0.00	0.00	0.00	0.34	0.26	0.06	
0.01	0.00	0.03	0.00	0.08	0.00	0.00	0.02	0.12	0.01	
0.00	0.03	0.01	0.01	0.00	0.00	0.00	0.21	0.20	0.02	
0.06	0.02	0.02	0.15	0.00	0.00	0.03	0.03	0.13	0.01	
0.11	0.00	0.10	0.14	0.00	0.00	0.00	0.02	0.00	0.00	
0.01	0.00	0.02	0.00	0.01	0.00	0.01	0.03	0.03	0.00	

2	t=0.45 s; F=0.44 MN; A=0.61 m2; Pav=0.72 MPa									
0.00	0.01	0.00	0.15	0.00	0.28	0.66	0.05	0.04	0.00	
0.00	0.01	0.03	0.00	0.08	0.00	0.00	0.01	0.00	0.00	
0.01	0.00	0.03	0.03	0.00	0.28	0.57	0.08	0.00	0.00	
0.02	0.01	0.01	0.02	0.00	0.00	0.01	0.03	0.03	0.00	
0.01	0.17	0.03	0.00	0.01	0.03	0.00	0.02	0.00	0.00	
0.03	0.00	0.03	0.00	0.00	0.03	0.05	0.01	0.00	0.01	

3	t=0.74 s; F=0.58 MN; A=1.06 m2; Pav=0.54 MPa									
0.01	0.00	0.28	0.13	0.00	0.03	0.03	0.00	0.01	0.03	
0.00	0.06	0.00	0.00	0.00	0.00	0.33	0.79	0.26	0.00	
0.06	0.06	0.28	0.50	0.28	0.08	0.00	0.00	0.00	0.05	
0.03	0.12	0.00	0.10	0.00	0.00	0.03	0.00	0.01	0.02	
0.02	0.00	0.00	0.00	0.01	0.03	0.00	0.00	0.00	0.01	
0.00	0.00	0.03	0.00	0.02	0.01	0.02	0.01	0.01	0.01	

4	t=0.92 s; F=0.72 MN; A=1.06 m2; Pav=0.68 MPa									
0.11	0.03	0.00	0.17	0.00	0.04	0.00	0.00	0.03	0.03	
0.00	0.00	0.00	0.15	0.64	0.79	0.64	0.44	0.19	0.00	
0.38	0.23	0.02	0.01	0.00	0.00	0.00	0.00	0.02	0.08	
0.03	0.00	0.10	0.01	0.00	0.00	0.02	0.00	0.27	0.19	
0.00	0.00	0.00	0.00	0.01	0.00	0.00	0.01	0.00	0.05	
0.01	0.00	0.00	0.00	0.01	0.02	0.01	0.00	0.01	0.00	

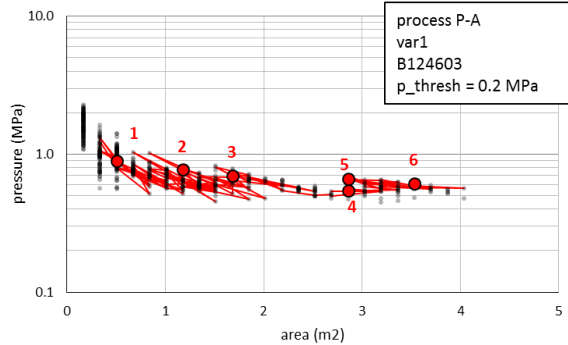
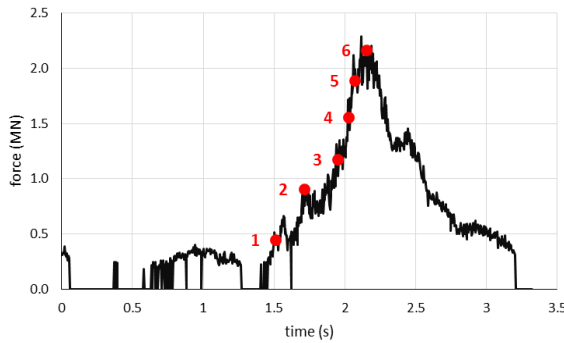
5	t=1 s; F=1.07 MN; A=1.22 m2; Pav=0.88 MPa									
0.00	0.01	0.09	0.06	0.06	0.06	0.05	0.00	0.08	0.02	
0.01	0.00	0.43	1.12	0.57	0.64	0.86	1.48	0.34	0.00	
0.01	0.07	0.03	0.00	0.00	0.00	0.00	0.00	0.03	0.01	
0.03	0.08	0.00	0.03	0.00	0.00	0.01	0.10	0.45	0.00	
0.01	0.00	0.00	0.00	0.01	0.02	0.00	0.11	0.04	0.00	
0.00	0.00	0.02	0.01	0.01	0.03	0.02	0.03	0.02	0.00	

6	t=1.08 s; F=1.23 MN; A=1.67 m2; Pav=0.74 MPa									
0.00	0.01	0.06	0.15	0.10	0.18	0.28	0.11	0.15	0.02	
0.00	0.14	0.37	0.94	0.68	0.63	0.94	1.33	0.59	0.32	
0.02	0.03	0.05	0.00	0.00	0.00	0.00	0.00	0.00	0.00	
0.01	0.05	0.00	0.03	0.00	0.00	0.03	0.15	0.23	0.00	
0.01	0.00	0.00	0.00	0.02	0.02	0.00	0.23	0.03	0.00	
0.00	0.00	0.01	0.01	0.03	0.03	0.05	0.03	0.04	0.00	

Appendix C Varandey Tanker Full Scale Data Cases

C.1 Varandey – Case 1

Event	Trial	Event File Name	Date	Time	Max Force (MN)	Speed (knots)
var1	Varandey 2009 V5W	B124603	6/8/2009	12:46:03	2.250	7.80



1	t=1.51 s; F=0.45 MN; A=0.5 m2; Pav=0.89 MPa									
0.06	0.00	0.00	0.00	0.00	0.03	0.11	0.33	0.00	0.07	
0.02	0.03	0.02	0.00	0.02	0.00	0.14	0.34	0.04	0.04	
0.04	0.05	0.00	0.00	0.01	0.02	0.12	0.29	0.07	0.00	
0.00	0.01	0.00	0.00	0.00	0.02	0.00	0.00	0.09	0.01	
0.01	0.04	0.00	0.00	0.00	0.02	0.00	0.00	0.00	0.03	
0.00	0.00	0.00	0.00	0.00	0.00	0.00	0.01	0.00	0.00	
0.00	0.02	0.00	0.00	0.02	0.00	0.00	0.01	0.00	0.00	
0.00	0.00	0.01	0.02	0.00	0.05	0.02	0.00	0.00	0.00	
0.00	0.00	0.02	0.01	0.10	0.08	0.00	0.01			
0.00	0.00	0.00	0.13	0.03						

2	t=1.71 s; F=0.91 MN; A=1.18 m2; Pav=0.77 MPa									
0.03	0.02	0.02	0.00	0.01	0.19	0.41	0.36	0.11	0.08	
0.00	0.00	0.00	0.00	0.00	0.44	0.52	0.33	0.12	0.09	
0.00	0.00	0.00	0.01	0.00	0.07	0.37	0.33	0.15	0.03	
0.02	0.00	0.00	0.00	0.00	0.05	0.04	0.10	0.07	0.11	
0.00	0.00	0.00	0.00	0.00	0.00	0.00	0.08	0.03	0.05	
0.03	0.00	0.00	0.00	0.00	0.02	0.06	0.09	0.04	0.05	
0.00	0.05	0.00	0.00	0.04	0.02	0.00	0.07	0.01	0.03	
0.00	0.00	0.01	0.00	0.00	0.00	0.00	0.00	0.03	0.11	
0.00	0.00	0.04	0.03	0.00	0.04	0.00	0.08			
0.05	0.02	0.09	0.14	0.04						

3	t=1.95 s; F=1.18 MN; A=1.68 m2; Pav=0.7 MPa									
0.02	0.00	0.09	0.18	0.25	0.13	0.35	0.28	0.09	0.04	
0.03	0.00	0.16	0.15	0.44	0.25	0.75	0.42	0.18	0.05	
0.00	0.04	0.00	0.10	0.10	0.00	0.33	0.28	0.07	0.05	
0.03	0.00	0.00	0.05	0.07	0.06	0.03	0.02	0.08	0.10	
0.00	0.03	0.00	0.08	0.04	0.00	0.07	0.00	0.02	0.00	
0.00	0.03	0.00	0.00	0.03	0.00	0.01	0.05	0.05	0.08	
0.03	0.03	0.00	0.03	0.03	0.00	0.00	0.12	0.04	0.06	
0.00	0.03	0.03	0.00	0.00	0.00	0.01	0.00	0.19	0.09	
0.00	0.04	0.00	0.00	0.00	0.00	0.00	0.08			
0.03	0.03	0.01	0.01	0.00						

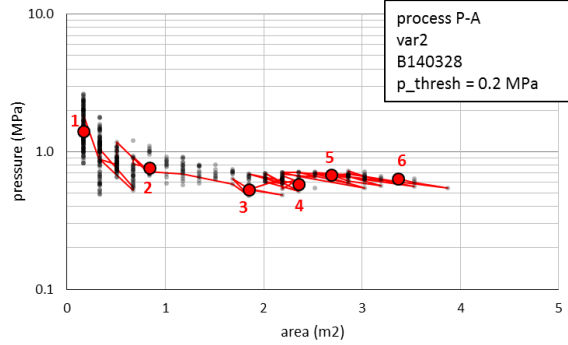
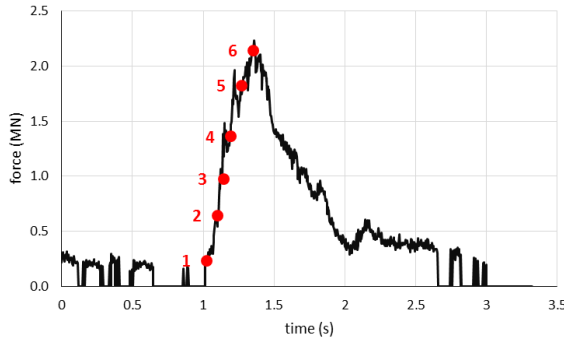
4	t=2.025 s; F=1.56 MN; A=2.86 m2; Pav=0.54 MPa									
0.00	0.10	0.05	0.24	0.24	0.00	0.27	0.21	0.05	0.35	
0.00	0.15	0.30	0.29	0.82	0.39	0.59	0.55	0.44	0.21	
0.00	0.02	0.00	0.12	0.12	0.00	0.34	0.38	0.27	0.09	
0.03	0.00	0.06	0.05	0.07	0.01	0.02	0.09	0.17	0.16	
0.01	0.04	0.08	0.00	0.09	0.00	0.06	0.00	0.11	0.06	
0.00	0.01	0.02	0.01	0.08	0.00	0.00	0.09	0.12	0.06	
0.02	0.03	0.03	0.00	0.02	0.00	0.00	0.17	0.01	0.05	
0.00	0.06	0.00	0.00	0.02	0.00	0.01	0.00	0.09	0.05	
0.00	0.00	0.05	0.00	0.04	0.00	0.00	0.45			
0.04	0.02	0.03	0.00	0.02						

5	t=2.07 s; F=1.89 MN; A=2.86 m2; Pav=0.66 MPa									
0.01	0.18	0.15	0.33	0.03	0.13	0.28	0.41	0.04	0.46	
0.00	0.50	0.34	0.39	0.40	0.20	0.53	0.75	0.43	0.45	
0.00	0.00	0.00	0.19	0.07	0.00	0.63	0.66	0.48	0.11	
0.00	0.03	0.00	0.09	0.05	0.00	0.04	0.13	0.17	0.24	
0.00	0.02	0.03	0.01	0.05	0.00	0.05	0.05	0.00	0.10	
0.00	0.04	0.09	0.07	0.04	0.00	0.00	0.12	0.12	0.11	
0.00	0.02	0.00	0.00	0.01	0.00	0.06	0.12	0.00	0.06	
0.02	0.00	0.00	0.00	0.00	0.01	0.05	0.00	0.14	0.04	
0.00	0.01	0.02	0.00	0.00	0.01	0.02	0.79			
0.08	0.00	0.00	0.01	0.00						

6	t=2.15 s; F=2.17 MN; A=3.53 m2; Pav=0.61 MPa									
0.05	0.06	0.19	0.34	0.05	0.00	0.19	0.36	0.04	0.46	
0.38	0.33	0.75	0.42	0.28	0.21	0.29	0.92	0.43	0.86	
0.00	0.00	0.05	0.17	0.01	0.04	0.40	0.91	0.71	0.11	
0.00	0.08	0.03	0.08	0.07	0.00	0.04	0.15	0.33	0.27	
0.00	0.04	0.09	0.05	0.00	0.00	0.00	0.00	0.10	0.15	
0.00	0.10	0.00	0.15	0.00	0.00	0.07	0.14	0.19	0.12	
0.05	0.00	0.00	0.00	0.02	0.01	0.07	0.17	0.00	0.00	
0.02	0.00	0.01	0.02	0.00	0.04	0.35	0.00	0.00	0.04	
0.01	0.02	0.00	0.03	0.01	0.03	0.42	0.30			
0.00	0.00	0.04	0.00	0.00						

C.2 Varandey – Case 2

Event	Trial	Event File Name	Date	Time	Max Force (MN)	Speed (knots)
var2	Varandey 2009 V5W	B140328	6/8/2009	14:03:28	2.120	5.70



1	t=1.02 s; F=0.24 MN; A=0.17 m2; Pav=1.42 MPa								
0.01	0.04	0.00	0.10	0.08	0.00	0.07	0.05	0.00	0.00
0.03	0.01	0.01	0.07	0.24	0.00	0.00	0.00	0.00	0.00
0.00	0.06	0.03	0.00	0.05	0.00	0.00	0.04	0.00	0.00
0.00	0.00	0.03	0.05	0.03	0.00	0.02	0.00	0.00	0.00
0.00	0.00	0.01	0.00	0.03	0.09	0.00	0.02	0.00	0.00
0.00	0.00	0.00	0.01	0.00	0.01	0.00	0.00	0.00	0.05
0.03	0.00	0.00	0.00	0.00	0.03	0.00	0.02	0.00	0.00
0.00	0.00	0.00	0.01	0.00	0.00	0.00	0.00	0.00	0.00
0.00	0.00	0.00	0.00	0.00	0.03	0.00	0.00	0.00	0.00
0.06	0.00	0.00	0.00	0.00	0.00	0.00	0.00	0.00	0.00

2	t=1.1 s; F=0.65 MN; A=0.84 m2; Pav=0.77 MPa								
0.00	0.09	0.00	0.08	0.07	0.02	0.56	0.25	0.02	0.09
0.02	0.00	0.05	0.21	0.40	0.00	0.06	0.30	0.18	0.06
0.00	0.00	0.00	0.15	0.00	0.00	0.03	0.15	0.07	0.05
0.00	0.00	0.00	0.02	0.00	0.01	0.04	0.01	0.07	0.03
0.00	0.00	0.00	0.00	0.00	0.16	0.04	0.00	0.03	0.02
0.02	0.00	0.09	0.00	0.00	0.03	0.00	0.04	0.05	0.08
0.01	0.00	0.00	0.00	0.00	0.00	0.00	0.00	0.00	0.00
0.00	0.00	0.00	0.00	0.00	0.00	0.00	0.01	0.04	0.02
0.07	0.00	0.00	0.00	0.00	0.01	0.00	0.02	0.00	0.00
0.02	0.00	0.00	0.00	0.00	0.00	0.00	0.00	0.00	0.00

3	t=1.14 s; F=0.98 MN; A=1.85 m2; Pav=0.53 MPa								
0.00	0.00	0.00	0.14	0.08	0.29	0.75	0.27	0.00	0.01
0.03	0.00	0.05	0.28	0.48	0.34	0.45	0.32	0.15	0.06
0.02	0.00	0.00	0.35	0.00	0.00	0.18	0.23	0.07	0.00
0.00	0.00	0.00	0.05	0.08	0.04	0.05	0.07	0.06	0.02
0.00	0.00	0.00	0.00	0.00	0.24	0.04	0.00	0.01	0.00
0.03	0.00	0.00	0.00	0.00	0.07	0.02	0.06	0.10	0.06
0.02	0.00	0.00	0.00	0.00	0.01	0.00	0.00	0.08	0.00
0.00	0.00	0.01	0.00	0.00	0.00	0.05	0.00	0.00	0.00
0.00	0.02	0.00	0.00	0.05	0.02	0.01	0.00	0.00	0.00
0.00	0.00	0.00	0.00	0.00	0.00	0.00	0.00	0.00	0.00

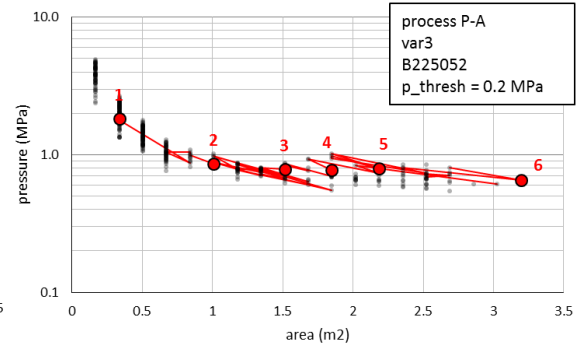
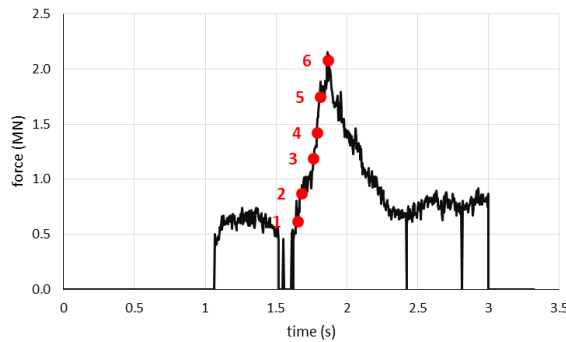
4	t=1.19 s; F=1.36 MN; A=2.35 m2; Pav=0.58 MPa								
0.01	0.00	0.00	0.13	0.22	0.54	0.14	0.15	0.02	0.14
0.03	0.00	0.28	0.43	0.70	0.74	0.35	0.27	0.25	0.11
0.09	0.00	0.08	0.76	0.00	0.00	0.23	0.37	0.27	0.06
0.01	0.00	0.06	0.11	0.13	0.03	0.07	0.08	0.06	0.06
0.01	0.00	0.00	0.00	0.00	0.19	0.04	0.00	0.00	0.06
0.00	0.00	0.03	0.00	0.00	0.04	0.01	0.08	0.07	0.07
0.00	0.00	0.00	0.00	0.07	0.00	0.00	0.02	0.26	0.00
0.00	0.00	0.00	0.00	0.00	0.00	0.05	0.00	0.03	0.02
0.00	0.00	0.00	0.00	0.00	0.07	0.01	0.00	0.00	0.00
0.01	0.00	0.00	0.00	0.00	0.00	0.00	0.00	0.00	0.00

5	t=1.27 s; F=1.83 MN; A=2.69 m2; Pav=0.68 MPa								
0.06	0.00	0.00	0.19	0.17	0.00	0.03	0.12	0.06	0.18
0.06	0.04	0.33	0.40	0.95	1.03	0.09	0.65	0.24	0.24
0.02	0.00	0.20	0.72	0.34	0.35	0.58	0.95	0.46	0.06
0.00	0.00	0.04	0.10	0.13	0.00	0.03	0.13	0.17	0.18
0.05	0.00	0.00	0.00	0.01	0.00	0.00	0.00	0.06	0.09
0.00	0.00	0.00	0.00	0.00	0.00	0.05	0.13	0.09	0.11
0.00	0.00	0.00	0.00	0.25	0.01	0.00	0.10	0.28	0.08
0.00	0.00	0.00	0.00	0.05	0.00	0.00	0.04	0.01	0.06
0.00	0.00	0.00	0.00	0.00	0.01	0.02	0.07	0.00	0.00
0.00	0.00	0.03	0.00	0.00	0.00	0.00	0.00	0.00	0.00

6	t=1.35 s; F=2.14 MN; A=3.36 m2; Pav=0.64 MPa								
0.00	0.00	0.00	0.24	0.00	0.00	0.05	0.11	0.27	0.14
0.03	0.22	0.48	0.38	0.56	0.25	0.16	0.27	0.19	0.35
0.01	0.03	0.81	0.60	1.32	0.41	1.17	1.05	0.46	0.07
0.00	0.00	0.06	0.40	0.32	0.00	0.04	0.14	0.17	0.17
0.02	0.00	0.00	0.06	0.06	0.00	0.00	0.00	0.03	0.06
0.00	0.00	0.04	0.00	0.01	0.00	0.04	0.19	0.08	0.09
0.00	0.00	0.00	0.00	0.15	0.00	0.00	0.11	0.05	0.32
0.00	0.01	0.00	0.02	0.00	0.00	0.00	0.08	0.00	0.27
0.00	0.02	0.00	0.00	0.00	0.02	0.00	0.29	0.00	0.00
0.00	0.00	0.06	0.00	0.00	0.00	0.00	0.00	0.00	0.00

C.3 Varandey – Case 3

Event	Trial	Event File Name	Date	Time	Max Force (MN)	Speed (knots)
var3	Varandey 2009 V2W	B225052	5/8/2009	22:50:52	2.100	6.70



1	t=1.65 s; F=0.62 MN; A=0.34 m2; Pav=1.83 MPa								
0.00	0.09	0.05	0.01	0.09	0.00	0.00	0.13	0.01	0.12
0.01	0.00	0.00	0.00	0.01	0.00	0.00	0.15	0.32	0.10
0.00	0.00	0.01	0.04	0.04	0.00	0.02	0.10	0.33	0.05
0.00	0.02	0.02	0.00	0.00	0.00	0.06	0.07	0.09	0.09
0.01	0.08	0.06	0.00	0.00	0.00	0.00	0.02	0.04	0.07
0.03	0.13	0.06	0.04	0.06	0.00	0.03	0.02	0.03	0.07
0.05	0.14	0.07	0.03	0.00	0.00	0.05	0.08	0.04	0.01
0.02	0.04	0.00	0.00	0.01	0.00	0.00	0.00	0.07	0.01
0.00	0.02	0.02	0.06	0.00	0.00	0.04	0.03		
0.03	0.00	0.00	0.03	0.01					

2	t=1.68 s; F=0.87 MN; A=1.01 m2; Pav=0.86 MPa								
0.00	0.03	0.02	0.01	0.01	0.00	0.23	0.32	0.02	0.15
0.01	0.05	0.01	0.06	0.05	0.01	0.15	0.32	0.32	0.14
0.01	0.01	0.02	0.00	0.00	0.00	0.19	0.27	0.35	0.07
0.00	0.04	0.02	0.02	0.00	0.00	0.07	0.11	0.11	0.13
0.04	0.05	0.00	0.05	0.00	0.00	0.00	0.01	0.04	0.08
0.04	0.13	0.05	0.03	0.06	0.00	0.06	0.10	0.04	0.05
0.04	0.14	0.06	0.00	0.04	0.00	0.02	0.09	0.04	0.04
0.05	0.02	0.02	0.00	0.01	0.00	0.01	0.02	0.07	0.02
0.00	0.05	0.03	0.00	0.01	0.00	0.07	0.11		
0.03	0.00	0.01	0.00	0.01					

3	t=1.7645 s; F=1.19 MN; A=1.51 m2; Pav=0.79 MPa								
0.03	0.00	0.08	0.37	0.22	0.00	0.15	0.17	0.04	0.16
0.00	0.00	0.03	0.29	0.49	0.50	0.24	0.13	0.18	0.14
0.01	0.00	0.00	0.17	0.00	0.00	0.30	0.42	0.48	0.10
0.03	0.04	0.00	0.12	0.07	0.00	0.04	0.16	0.16	0.14
0.02	0.06	0.02	0.02	0.00	0.00	0.00	0.00	0.07	0.16
0.00	0.10	0.07	0.06	0.00	0.00	0.03	0.13	0.07	0.06
0.04	0.05	0.05	0.00	0.04	0.00	0.00	0.13	0.02	0.03
0.04	0.03	0.00	0.01	0.01	0.00	0.00	0.04	0.03	0.04
0.00	0.05	0.01	0.03	0.00	0.01	0.03	0.05		
0.00	0.00	0.00	0.00	0.00					

4	t=1.79 s; F=1.43 MN; A=1.85 m2; Pav=0.77 MPa								
0.00	0.07	0.39	0.47	0.21	0.00	0.08	0.14	0.07	0.13
0.00	0.03	0.34	0.45	0.48	0.52	0.22	0.06	0.16	0.14
0.00	0.01	0.06	0.10	0.09	0.02	0.31	0.99	0.40	0.11
0.02	0.01	0.08	0.08	0.05	0.00	0.07	0.13	0.15	0.17
0.06	0.07	0.04	0.02	0.00	0.00	0.00	0.00	0.00	0.11
0.03	0.05	0.05	0.06	0.01	0.00	0.05	0.16	0.07	0.09
0.07	0.07	0.02	0.05	0.06	0.00	0.00	0.07	0.04	0.05
0.00	0.04	0.02	0.00	0.02	0.00	0.00	0.00	0.03	0.07
0.00	0.07	0.02	0.04	0.00	0.00	0.01	0.07		
0.01	0.00	0.02	0.01	0.00					

5	t=1.81 s; F=1.75 MN; A=2.19 m2; Pav=0.8 MPa								
0.00	0.28	0.50	0.55	0.15	0.00	0.11	0.15	0.03	0.16
0.00	0.22	0.57	0.55	0.59	0.66	0.21	0.01	0.18	0.16
0.00	0.00	0.08	0.26	0.12	0.18	0.61	1.14	0.26	0.09
0.02	0.07	0.03	0.17	0.03	0.00	0.05	0.15	0.18	0.18
0.01	0.07	0.01	0.02	0.00	0.00	0.00	0.00	0.07	0.11
0.03	0.11	0.01	0.06	0.03	0.00	0.05	0.16	0.10	0.08
0.02	0.10	0.04	0.02	0.07	0.00	0.03	0.08	0.00	0.04
0.05	0.00	0.00	0.01	0.00	0.00	0.01	0.00	0.04	0.03
0.00	0.02	0.03	0.02	0.00	0.00	0.01	0.07		
0.00	0.02	0.07	0.00	0.03					

6	t=1.864 s; F=2.08 MN; A=3.2 m2; Pav=0.65 MPa								
0.23	0.38	0.14	0.21	0.06	0.00	0.09	0.21	0.05	0.19
0.03	0.44	0.45	0.34	0.42	0.61	0.00	0.00	0.22	0.16
0.00	0.06	0.00	0.42	0.73	0.41	1.66	1.42	0.15	0.10
0.01	0.01	0.03	0.07	0.10	0.00	0.13	0.27	0.25	0.22
0.00	0.05	0.00	0.00	0.04	0.00	0.00	0.00	0.06	0.17
0.04	0.09	0.03	0.04	0.00	0.00	0.07	0.31	0.07	0.11
0.04	0.06	0.06	0.00	0.07	0.00	0.00	0.14	0.02	0.08
0.01	0.04	0.00	0.03	0.00	0.00	0.00	0.02	0.04	0.05
0.00	0.05	0.07	0.00	0.00	0.00	0.07	0.08		
0.02	0.00	0.03	0.04	0.00					

Appendix D – LS-Dyna K-files

Numerical simulations were conducted throughout the course of this work using the commercial software package – LS-Dyna®. This appendix provides screenshots of sample LS-Dyna k-files that were used to perform each type of simulation. Three different types were carried out.

- 1) Ice Calibration Simulations (referenced in section 6.2)
- 2) Patch Load Analysis Simulation (referenced in sections 7.4 and 8.4)
- 3) Ice-structure Interaction Analysis Simulations (sections 7.6 and 8.6)

Each simulation utilized several k-files. The main simulations file names are prefixed with the label “**sim_**” followed by a unique number. Complete lists of simulations are referenced in the respective sections of this thesis. Additional k-files are appended to each main simulation file using the ***INCLUDE** card. These generally include a control file, finite element mesh files, material files, and part files. It is noted that all lists of nodes and elements are abbreviated, denoted by “.”. The red text provides comments to further explain the organizational structure of the k-files.

D.1 Ice Calibration Simulations

ice calibration
simulations
page (1/3)

sim_A_101.k — *main simulation file*

```
*KEYWORD
*TITLE
A_101_ice_calibration
*PARAMETERS
$control parameters
In_asc,1000
In_bin,25
In_inf,100
Rte,1.0
Rssf,0.9
$simulation parameters
Ioutnid1,203922
Rpen_y,-0.5
Rsigy,1.5e6
*PARAMETER_EXPRESSION
Rasc_dt,&te/n_asc
Rbin_dt,&te/n_bin
Rinf_dt,&te/n_inf
*INCLUDE
../01_control/control_rig.k
../02_structure/plate_40.k
../03_ice/ice_350_123.k
../03_ice/mat_ice_ep.k
*END
```

n_asc, n_bin, n_inf = number of outputs for ASCII, binary and interface force databases
te = total simulation time [s]
tssf = maximum stable timestep scale factor
outnid1 = output node for measuring ice displacement
pen_y = total ice displacement depth (y-direction) [m]
sigy = ice material yield strength [Pa]
expressions to set sampling rates for ASCII (*asc_dt*), binary (*bin_dt*) and interface force (*inf_dt*) databases
additional k-files to include in simulation

plate_40.k — *FE mesh for rigid indenter (e.g. 40deg beta angle)*

```
*SET_NODE_LIST
$# sid da1 da2 da3 da4 solver
1 0.000 0.000 0.000 0.000MECH
$# nid1 nid2 nid3 nid4 nid5 nid6 nid7 nid8
1 2 3 4 5 6 7 8
9 10 11 12 13 14 15 16
*ELEMENT_SHELL
$# eid pid n1 n2 n3 n4 n5 n6 n7 n8
1 1 1 2 174 173 0 0 0 0
2 1 2 3 175 174 0 0 0 0
3 1 3 4 176 175 0 0 0 0
*NODE
$# nid x y z tc rc
1 5.000000 1.920061 2.330273 0 0
2 5.000000 1.897506 2.303394 0 0
3 5.000000 1.874953 2.276516 0 0
```

set_node_list for plate boundary condition (fixed support, id:1)
shell elements
nodes

ice_350_123.k — *FE mesh for ice wedge (e.g. 35cm thick, 123 deg phi angle)*

```
*SET_NODE_LIST
$# sid da1 da2 da3 da4 solver
2 0.000 0.000 0.000 0.000MECH
$# nid1 nid2 nid3 nid4 nid5 nid6 nid7 nid8
205245 205246 205247 205248 205257 205258 205275 205276
205277 205278 205295 205296 205297 205298 205317 205318
*ELEMENT_SOLID
$# eid pid n1 n2 n3 n4 n5 n6 n7 n8
200000 200 201854 200261 202032 202036 205229 205230 205231 205232
200001 200 205229 205230 205231 205232 205233 205234 205235 205236
200002 200 205233 205234 205235 205236 205237 205238 205239 205240
*NODE
$# nid x y z tc rc
200000 -0.758101 1.181865 0.000 0 0
200001 -1.911819e-005 1.700599 0.000 0 0
200002 -1.763552e-005 1.141582 0.000 0 0
```

set_node_list for ice boundary condition (position control, id:2)
solid elements
nodes

mat_ice_ep.k — *material for deformable ice model (e.g. 35cm thick, 123 deg phi angle)*

```
$material for deformable ice
*MAT_PLASTIC_KINEMATIC
$ MID RHO E PR SIGY ETAN BETA
200 900.0 9e9 0.330 6sigy1 10e6 0.000
$ src sxp fs vp
0.000 0.000 0.000 0.000
```

material card
mat_plastic_kinematic for ice material model (id:200)

control_rig.k — control card for ice calibration simulations

ice calibration
simulations
page (2/3)

```

=====
$execution controls
=====
*CONTROL_MPP_IO_NODUMP
*CONTROL_TERMINATION
$  endtim  endcyc  dtmin  endeng  endmas
   &te      0      0.000  0.000  0.000
*CONTROL_TIMESTEP
$  dtinit  tssfacc  isdo  tslimit  dt2ms  lctm  erode  msist
   0.000  0.000  0  0.000  0.000  0  0  0
$  dt2msf  dt2ms1c  imsc1
   0.000  0  0
*CONTROL_ENERGY
$  hgen  rven  slnten  rylen
   2  2  2  2
*CONTROL_ACCURACY
$$  osu  inn  pidosu
   0  2  0
=====
$output controls
=====
*DATABASE_GLSTAT
$  dt  binary  lcur  ioopt
   &asc_dt  0  0
*DATABASE_MATSUM
$  dt  binary  lcur  ioopt
   &asc_dt  0  0
*DATABASE_RCFORC
$  dt  binary  lcur  ioopt
   &asc_dt  0  0
*DATABASE_BINARY_D3PLOT
$  dt  lcdt  beam  npltc  psetid
   &bin_dt  0  0  0  0
$  ioopt
   0
*DATABASE_BINARY_INTFOR
$  dt  lcdt  beam  npltc  psetid
   &inf_dt  0  0  0  0
*DATABASE_EXTENT_INTFOR
$  NGLBV  NVELO  NPRESU  NSHEAR  NFORC  NGAPC  NFAIL  IEVERF
   -1  -1  1  -1  -1  -1  0  0
*DATABASE_NODOUT
$  dt  binary  lcur  ioopt
   &asc_dt  0  0
*DATABASE_HISTORY_NODE
$  id1  id2  id3  id4 ...
   &outnid1
=====
$material for rigid indenter and ice support
=====
*MAT_RIGID
$  MID  RHO  E  PR  N  COUPLE  M  ALIAS
   1  7850.0  200E9  0.30000  0  0  0  0
$  CMO  CON1  CON2
   0.000  0.000  0.000
$  A1  A2  A3  V1  V2  V3
   0.000  0.000  0.000  0.000  0.000  0.000
=====
$contacts
=====
*CONTACT_AUTOMATIC_SINGLE_SURFACE
$$  ssid  msid  sstyp  mstyp  sboxid  mboxid  spr  mpr
   0  0  0  0  0  0  1  1
$  fs  fd  dc  vc  vdc  penchk  bt  dt
   0  0  0  0  0  0  0  1.0E20
$  sfs  sfm  sst  mst  sfst  sfmt  fsf  vsf
   1  1  0  0  1  1  1  1
$  soft  sofscl  lcidab  maxpar  sbopt  depth  bsort  frcfrq
   2  0.1  0  1.025  2  2  0  1
*CONTACT_FORCE_TRANSDUCER_PENALTY_ID
$  cid  title
   3
$  ssid  msid  sstyp  mstyp  sboxid  mboxid  spr  mpr
   1  0  3  0  0  0  1  0
$  fs  fd  dc  vc  vdc  penchk  bt  dt
   0.000  0.000  0.000  0.000  0.000  0  0.0001.0000E+20
$  sfs  sfm  sst  mst  sfst  sfmt  fsf  vsf
   1.000000  1.000000  0.000  0.000  1.000000  1.000000  1.000000  1.000000

```

execution controls

output controls

material card
mat_rigid for indenter and
ice support base material
models (id:1)

contact cards
automatic_single_surface
for ice-plate contact
force_transducer_penalty
for measuring contact
pressures

control_rig.k (cont')

ice calibration
simulations
page (3/3)

```

=====
$parts and sections
=====
*PART
H200 - Ice
$  pid  secid  mid  eosid  hgid  grav  adpopt  tmid
  200   200   200    0     0     0     0     0
*SET_PART_LIST
$#  sid  da1  da2  da3  da4  solver
  200   0     0     0     0     0     MECH
$#  pid1  pid2  pid3  pid4  pid5  pid6  pid7  pid8
  200    0     0     0     0     0     0     0
*SECTION_SOLID
$  secid  elform  aet
  200     1     0
*PART
H201 - Ice Base
$  pid  secid  mid  eosid  hgid  grav  adpopt  tmid
  201   201    1     0     0     0     0     0
*SET_PART_LIST
$#  sid  da1  da2  da3  da4  solver
  201   0     0     0     0     0     MECH
$#  pid1  pid2  pid3  pid4  pid5  pid6  pid7  pid8
  201    0     0     0     0     0     0     0
*SECTION_SOLID
$  secid  elform  aet
  201     1     0
*PART
1 - Plate
$  pid  secid  mid  eosid  hgid  grav  adpopt  tmid
  1     1     1     0     0     0     0     0
*SECTION_SHELL
$  secid  elform  shrf  nip  propt  qr/irid  icomp  setyp
  1     2     1.0000  5.0  0.0  0.0     0
$  t1  t2  t3  t4  nloc  marea
  0.01 0.01 0.01 0.01 0.0
=====
$boundary conditions and ice position control
=====
*BOUNDARY_PRESCRIBED_MOTION_RIGID
$  sid  dof  vad  lcid  sf  vid  death  birth
  201  1  2  6  1.0
  201  2  2  7  1.0
  201  3  2  6  1.0
  201  5  2  6  1.0
  201  6  2  6  1.0
  201  7  2  6  1.0
*BOUNDARY_SPC_SET
$#  nsid  cid  dofz  dofry  dofyz
  1     0     1     1     1
*BOUNDARY_SPC_SET
$#  nsid  cid  dofz  dofry  dofyz
  2     0     0     0     1
*DEFINE_CURVE
$  lcid  sidr  sfa  sfo  offa  offo  dattyp
  6
$  a1  o1
  0.000  0
  &te  0
  1000.0  0
*DEFINE_CURVE
$  lcid  sidr  sfa  sfo  offa  offo  dattyp
  7
$  a1  o1
  0.000  0
  &te  &pen_y
  1000.0  &pen_y

```

parts and sections

section_solid for deformable
ice model (id:200) and ice
support base (id:201)

section_shell for rigid plate
indenter (id:1)

boundary conditions and ice
position control

D.2 Patch Load Analysis Simulation

sim_N_001.k — *main simulation file*

```

*KEYWORD
*TITLE
N_001_centered_load_on_longi_A
*PARAMETERS
$load parameters
RF,0.5E6
Rw,0.3
Rh,0.2
Rdp,2.0
$load box
Rxcen,1.016
Rycen,2.2574
Rzcen,-0.4557
Ipltpid,1
$output nodes
Ioutnid1,2363
Ioutnid2,29164
Ioutnid3,2361
Ioutnid4,24577
$control parameters
In_asc,1000
In_bin,25
Rt1,0.5
Rte,1.0
Rtssf,0.9
$material properties
Rsigy,550E6
Rey,204E9
Ret,1000E6
RSRC,0.0
RSRF,0.0
$shell thicknesses
Rt_1,0.009
Rt_2,0.005
Rt_3,0.009
Rt_4,0.007
Rt_5,0.008
Rt_6,0.005
Rt_7,0.008
Rt_8,0.005
$shell element parameters
Rshrf,0.83333333
Ielform,1
*PARAMETER_EXPRESSION
Rxmin,&xcen-w/2
Rxmax,&xcen+w/2
Rymin,&ycen-dp/2
Rymax,&ycen+dp/2
Rzmin,&zcen-h/2
Rzmax,&zcen+h/2
Rp_avg,&F/w/h
Rp_avg_ol,&rp_avg*2.0
Rasc_dt,&te/n_asc
Rbin_dt,&te/n_bin
*INCLUDE
../01_control/control_pat.k
../02_structure/structure_NC_2_fm.k
../02_structure/parts_N.k
*END

```

patch load analysis
simulations
page (1/3)

ice load patch and box definition
F = force [N]
w = width [m]
h = height (vertical) [m]
dp = depth of load box [m]
xcen, ycen, zcen = coordinates for center of load box [m]
pltpid = part id for shell plate (for pressure application)

outnidX = output nodes for measuring structural deformation (in ASCII file)

n_asc, n_bin, n_inf = number of outputs for ASCII, binary and interface force databases
te = total simulation time [s]
tssf = maximum stable timestep scale factor

sigy = material yield strength [Pa]
ey = young's modulus [Pa]
et = tangent modulus [Pa]

t_X = thicknesses for shell element parts [m]

shrf = shear correction factor
elform = 1 (Hughes-Liu shell elements)

expressions for load box dimensions (**xmin, xmax, ymin, ymax, zmin, zmax**), pressure (**p_avg**), and overload pressure (**p_avg_o**)

expressions to set sampling rates for ASCII (**asc_dt**), and binary (**bin_dt**) databases

additional k-files to include in simulation

control_pat.k — **control card for patch analysis simulations**

patch load analysis
simulations
page (2/3)

```

=====
$execution controls
=====
*CONTROL_MPP_IO_NODUMP
*CONTROL_TERMINATION
$  endtim  endcyc  dtmin  endeng  endmas
   &te    0      0.000  0.000  0.000

*CONTROL_TIMESTEP
$  dtinit  tssfacs  isdo  tslimt  dt2ms  lctm  erode  mslst
   0.000  &tssfacs  0      0.000  0.000  0      0      0

$  dt2msf  dt2mslc  imsc1
   0.000  0      0

*CONTROL_ENERGY
$  hgen  rven  slnten  rylen
   2      2      2      2

*CONTROL_ACCURACY
$#  osu  inn  pidosu
   0      2      0

*CONTROL_SHELL
$#  vrpang  esort  irnxx  istupd  theory  bvc  miter  proj
   20.000000  1      -1      0  selform  1      1      1
$#  rotasc1  intgrd  lamsht  cstyp6  tshell
   1.000000  0      0      1      0
$#  pstupd  sidt4tu  cntco  itsfig  irquad
   0      0      0      0      2
$#  nfail1  nfail4  psnfail  keepecs  delifr  drocpsid  drocpm
   0      0      0      0      0      0  1.000000

=====
$output controls
=====
*DATABASE_GLSTAT
$  dt  binary  lcur  ioopt
  &asc_dt  0      0

*DATABASE_MATSUM
$  dt  binary  lcur  ioopt
  &asc_dt  0      0

*DATABASE_BINARY_D3PLOT
$  dt  lcdt  beam  npitc  psetid
  &bin_dt  0      0      0      0
$  ioopt
  0

*DATABASE_SPCFORC
$  dt  binary  lcur  ioopt
  &asc_dt  0      0

*DATABASE_NODOUT
$  dt  binary  lcur  ioopt
  &asc_dt  0      0

*DATABASE_HISTORY_NODE
$  id1  id2  id3  id4 ...
  &outnid1 &outnid2 &outnid3 &outnid4

*DATABASE_EXTENT_BINARY
$#  neiph  neips  maxint  strflg  sigflg  epsflg  rltflg  engflg
   0      0      3      0      1      1      1      1
$#  cmpflg  ieverp  beamip  dcomp  shge  stssz  n3thdt  iaemat
   0      0      0      1      2      1      2      1
$#  nintsid  pkp_sen  scip  hydro  msscl  therm  intout  nodout
   0      0  1.000000  0      0      OSTRESS  STRESS
$#  dtbdt  resplt
   0      0

=====
$boundary conditions
=====
*BOUNDARY_SPC_SET
$#  nsid  cid  dof1  dof2  dof3  dof4  dof5  dof6
   1      0      1      1      1      1      1      1

```

execution controls

output controls

boundary condition
structural support (fixed)

control_pat.k (cont')

patch load analysis
simulations
page (3/3)

```

=====
$loading curve and load box
=====
*DEFINE_CURVE
$   lcid   sidr   sfa   sfo   offa   offo   dattyp
$       1
$       a1           o1
$       0.00         0.00
$       &st1         &p_avg
$       &ste         &p_avg_cl

*DEFINE_BOX
$   boxid  xmin  xmax  ymin  ymax  zmin  zmax
$       1   &xmin &xmax &ymin &ymax &zmin &zmax

*LOAD_MASK
$   pid   lcid  vid1  off  boxid  lcidm  vid2  inout
$   &pltpid 1     0     0     1     0     0     0
$   icycle
1000000
    
```

loading curve and load box

structure_NC_2_frm.k — FE mesh for hull structure (e.g. naval combatant)

```

*BOUNDARY_SPC_SET
$#   nsid   cid   dofX   dofY   dofZ   dofRX   dofRY   dofRZ
$   1       0     1       1       1       1       1       1

*SET_NODE_LIST_TITLE
NODESET (SPC) 1
$#   sid   da1   da2   da3   da4   solver
$   1     0.000 0.000 0.000 0.000MECH

$#   nid1  nid2  nid3  nid4  nid5  nid6  nid7  nid8
$   389   390   391   392   393   399   400   401
$   402   403   404   405   406   426   429   430

*ELEMENT_SHELL
$#   eid   pid   n1     n2     n3     n4     n5     n6     n7     n8
$   1     3     5467   5464   5466   5466   0     0     0     0
$   2     3     5473   5463   5472   5472   0     0     0     0
$   25    4     77     9315   78     78     0     0     0     0
$   26    4     9326   5499   9325   9325   0     0     0     0
$   27    4     9327   5499   9326   9326   0     0     0     0
$   55    6     11102  15512  57     57     0     0     0     0
$   56    6     15574  11102  57     57     0     0     0     0
$   57    8     15955  15960  16079  16079  0     0     0     0
$   58    8     8678   16170  16171  16171  0     0     0     0

*NODE
$#   nid   x       y       z       tc       rc
$   1     0.000  0.420812 -2.515940 0 0
$   2     0.000  0.420812 -3.468610 0 0
$   3     0.000  0.420812 -2.611210 0 0
    
```

boundary_spc_set and
set_node_list for
structural boundary
condition (fixed, id:1)

shell elements

nodes

part_N.k — parts and material for hull structure (e.g. naval combatant)

```

$material for structure
*MAT_PLASTIC_KINEMATIC
$#   MID   RHO   E       PR   SIGY   ETAN   BETA
$   1     7850.0 &EY  0.30000 &sigy &Et  0.000
$#   src   srp   fs     vp
$   &SRC  &SRP  0.000  0.000

$parts and sections
*PART
1
$   pid   secid  mid   eosid  hgid  grav  adpopt  tmid
$   1     1     1     0     0     0     0     0

*SECTION_SHELL
$   secid  elform  shrf  nip  propt  qr/irid  icomp  setyp
$   1     &elform &shrf  5.0  0.0  0.0  0
$   t1     t2     t3     t4     nloc  marea
$   &t_1   &t_1   &t_1   &t_1   0.0
    
```

material card
mat_plastic_kinematic
for structural material (id:1)

parts and sections
section_shell for
shell elements (id:1)

D.3 Ice-structure Interaction Analysis Simulations

ice-structure interaction
analysis simulations
page (1/3)

```

sim_N_101.k — main simulation file

*KEYWORD
*TITLE
N_101_ice350_centered_on_longi
*PARAMETERS
$initial impact location
Rxcen,1.016
Rycen,2.2574
Rzcen,-0.4557
Ipltpid,1
$output notes
Ioutnid1,203922
Ioutnid2,2363
Ioutnid3,29164
Ioutnid4,2361
$ice parameters
RP_o,5.7
Rh_ice,0.35
Rbeta,6
Rsigyi,1.2551E6
Rpen_y,-0.5
Rmov_y,0.02
$control parameters
In_asc,1000
In_bin,25
In_inf,100
Rt1,0.85
Rte,1.0
Rtssf,0.9
$material properties
Rsigy,550E6
Rey,204E9
Ret,1000E6
RSRC,0.0
RSRP,0.0
$shell thicknesses
Rt_1,0.009
Rt_2,0.005
Rt_3,0.009
Rt_4,0.007
Rt_5,0.008
Rt_6,0.005
Rt_7,0.008
Rt_8,0.005
$shell element parameters
Rshrf,0.8333333
Ielform,1
*PARAMETER EXPRESSION
Rasc_dt,ste/n_asc
Rbin_dt,ste/n_bin
Rinf_dt,ste/n_inf
*INCLUDE
../01_control/control.k
../02_structure/structure_NC_2_frm.k
../02_structure/parts_N.k
../03_ice/ice_350_123.k
../03_ice/mat_ice_ep.k
*END
    
```

xcen, ycen, zcen = coordinates for ice wedge [m]
pltpid = part id for shell plate (for contact between ice and structure)

outnidX = output nodes for measuring ice displacement and structural deformation (in ASCII file)

P_o = target nominal pressure-area term [MPa]
h_ice = ice thickness [m]
beta = frame angle [deg]
sigyi = ice material yield strength [Pa]
pen_y = total ice displacement depth (y-direction) [m]
mov_y = initial gap between ice and structure [m]

n_asc, n_bin, n_inf = number of outputs for ASCII, binary and interface force databases
t = time to max ice indentation [s]
te = total simulation time [s]
tssf = maximum stable timestep scale factor

sigy = structural material yield strength [Pa]
ey = young's modulus [Pa]
et = tangent modulus [Pa]

t_X = thicknesses for shell element parts [m]

shrf = shear correction factor
elform = 1 (Hughes-Liu shell elements)

expressions to set sampling rates for ASCII (**asc_dt**), binary (**bin_dt**) and interface force (**inf_dt**) databases

additional k-files to include in simulation

ice_350_123.k — **FE mesh for ice wedge** (e.g. 35cm thick, 123 deg phi angle)
(see previous appendices)

mat_ice_ep.k — **material for deformable ice model** (e.g. 35cm thick, 123 deg phi angle)
(see previous appendices)

structure_NC_2_frm.k — **FE mesh for hull structure** (e.g. naval combatant)
(see previous appendices)

part_N.k — **parts and material for hull structure** (e.g. naval combatant)
(see previous appendices)

control.k — **control card for ice-structure simulations**

ice-structure interaction
analysis simulations
page (2/3)

```

=====
$execution controls
=====
*CONTROL_MPP_IO_NODUMP
*CONTROL_TERMINATION
$  endtim  endcyc  dtmin  endeng  endmas
   &te      0      0.000  0.000  0.000

*CONTROL_TIMESTEP
$  dtinit  tssfacs  isdo  tslimt  dt2ms  lctm  erode  msist
   0.000   &tssfacs  0    0.000  0.000    0    0      0
$  dt2msf  dt2mslc  imsc1
   0.000    0      0

*CONTROL_ENERGY
$  hgen  rwen  slnten  rylen
   2      2      2      2

*CONTROL_ACCURACY
$#  osu  inn  pidosu
   0    2    0

*CONTROL_SHELL
$#  vxpang  esort  irnxx  istupd  theory  bvc  miter  proj
  20.000000  1    -1    0    &elform  1    1    1
$#  rotasc1  intgrd  lamsht  cstyp6  tshell
   1.000000  0    0    1    0
$#  psstupd  sidt4tu  ontco  itsflg  irquad
   0    0    0    0    2
$#  nfail1  nfail4  psnfail  keepsc  delifr  drocpsid  drocpm
   0    0    0    0    0    0  1.000000

=====
$output controls
=====
*DATABASE_GLSTAT
$  dt  binary  lcur  ioopt
  &asc_dt  0    0

*DATABASE_MATSUM
$  dt  binary  lcur  ioopt
  &asc_dt  0    0

*DATABASE_RCFORC
$  dt  binary  lcur  ioopt
  &asc_dt  0    0

*DATABASE_BINARY_D3PLOT
$  dt  lcdt  beam  npltc  psetid
  &bin_dt  0    0    0    0
$  ioopt
  0

*DATABASE_BINARY_INTFOR
$  dt  lcdt  beam  npltc  psetid
  &inf_dt  0    0    0    0

*DATABASE_EXTENT_INTFOR
$  NGLBV  NVELO  NPRESU  NSHEAR  NFORC  NGAPC  NFAIL  IEVERF
   -1    -1    1    -1    -1    -1    0    0

*DATABASE_SPCFORC
$  dt  binary  lcur  ioopt
  &asc_dt  0    0

*DATABASE_NODOUT
$  dt  binary  lcur  ioopt
  &asc_dt  0    0

*DATABASE_HISTORY_NODE
$  id1  id2  id3  id4 ...
  &outnid1  &outnid2  &outnid3  &outnid4

*DATABASE_EXTENT_BINARY
$#  neiph  neips  maxint  strflg  sigflg  epsflg  ritflg  engflg
   0    0    3    0    1    1    1    1
$#  cmpflg  ieverp  beamip  dcomp  shge  stssz  n3thdt  ialemat
   0    0    0    1    2    1    2    1
$#  nintsid  pkp_sen  sclp  hydro  msscl  therm  intout  nodout
   0    0  1.000000  0    0    OSTRESS  STRESS
$#  dtbd  resplt
   0    0

=====
$parts and sections
=====
*PART
H200 - Ice
$  pid  secid  mid  eosid  hgid  grav  adpopt  tmid
   200  200  200  0    0    0    0    0

*SECTION_SOLID
$  secid  elform  aet
   200  1    0
    
```

execution controls

output controls

parts and sections
section_solid for deformable
ice model (id:200)

control.k (con't)

ice-structure interaction
analysis simulations
page (3/3)

```

*PART
H201 - Ice Base
$  pid      secid      mid      eosid      hgid      grav      adpopt      tmid
   201      201      201      0          0          0          0          0

*SECTION_SOLID
$  secid      elform      aet
   201      1          0

*MAT_RIGID
$  MID      RHO      E      PR      N      COUPLE      M      ALIAS
   201      7850.0  200E9  0.30000  0          0          0          0
$  CMO      CON1      CON2
   0.000    0.000    0.000
$  A1      A2      A3      V1      V2      V3
   0.000    0.000    0.000    0.000    0.000    0.000

*SET_PART_LIST
$#  sid      da1      da2      da3      da4      solver
   200      200      201      0          0          MECH
$#  pid1     pid2     pid3     pid4     pid5     pid6     pid7     pid8
   200      201      0          0          0          0          0          0

*PART_MOVE
$#  pid      xmov      ymov      zmov      cid      iset
   200      &xcen    &yceen    &zcen    0          1
*PART_MOVE
$#  pid      xmov      ymov      zmov      cid      iset
   200      0.000    &mov_y    0.000    0          1

=====
$contacts
=====
*CONTACT_AUTOMATIC_SINGLE_SURFACE
$#  ssid      msid      sstyp      mstyp      sboxid      mboxid      spr      mpr
   0          0          0          0          0          0          1          1
$#  fs      fd      dc      vc      vdc      penchk      bt      dt
   0          0          0          0          0          0          1.0E20
$#  sfs      sfm      sst      mst      sfst      sfmt      fsf      vsf
   1          1          0          0          1          1          1          1
$#  soft      softscl  lcidab    maxpar    sbopt      depth      bsort      frfrfq
   2          0.1      0          1.025    2          2          0          1

*CONTACT_FORCE_TRANSDUCER_PENALTY_ID
$#  cid      title
   3          3
$#  ssid      msid      sstyp      mstyp      sboxid      mboxid      spr      mpr
   1          0          3          0          0          0          1          0
$#  fs      fd      dc      vc      vdc      penchk      bt      dt
   0.000    0.000    0.000    0.000    0.000    0          0.0001.0000E+20
$#  sfs      sfm      sst      mst      sfst      sfmt      fsf      vsf
   1.000000  1.000000  0.000    0.000    1.000000  1.000000  1.000000  1.000000

=====
$boundary conditions and ice position control
=====
*BOUNDARY_PRESCRIBED_MOTION_RIGID
$  sid      dof      vad      lcid      sf      vid      death      birth
   201      1          2          6          1.0    0          0          0
   201      2          2          7          1.0    0          0          0
   201      3          2          6          1.0    0          0          0
   201      5          2          6          1.0    0          0          0
   201      6          2          6          1.0    0          0          0
   201      7          2          6          1.0    0          0          0

*BOUNDARY_SPC_SET
$#  nsid      cid      dofz      dofz      dofz      dofz      dofz      dofz
   1          0          1          1          1          1          1          1

*BOUNDARY_SPC_SET
$#  nsid      cid      dofz      dofz      dofz      dofz      dofz      dofz
   2          0          0          0          1          1          1          0

*DEFINE_CURVE
$  lcid      sidr      sfa      sfo      offa      offo      dattyp
   6
$  a1          oi
   0.000      0
   ste        0
   1000.0     0

*DEFINE_CURVE
$  lcid      sidr      sfa      sfo      offa      offo      dattyp
   7
$  a1          oi
   0.000      0
   st1        &pen_y
   ste        0
   1000.0     0
    
```

parts and sections
section_solid for ice
base (id:201)

material card
mat_rigid for ice
support base (id:201)

part_move for ice
setting ice position

contact cards
automatic_single_surface
for ice-structure contact
force_transducer_penalty
for measuring contact
pressures

boundary conditions and ice
position control